Faculty of Science and Engineering
Department of Mechanical Engineering

Towards Application of Thermal Infrared Imaging in Medical Diagnosis: Protocols and Investigations

Daniel T. J. Arthur

This thesis is presented for the Degree of
Doctor of Philosophy
of
Curtin University

May 2014

Declaration

This thesis reports original work I carried out while working towards my Ph.D. in Mechanical Engineering degree at Curtin University. To the best of my knowledge and belief, this thesis contains no material that was previously published by any other person or organization. Due acknowledgments have been made for all cited works and illustrations.

Furthermore, this work contains no material that has been submitted or accepted for the award of any other degree or diploma in any university/institution.

Signature:_____

Daniel T. J. Arthur

Date:_____

Abstract

The current key goals of the Thermal Infrared Imaging (TIRI) research community are; exploiting its potential as a clinical tool, spreading awareness of the increased capability of TIRI technology, and encouraging medical practitioners to apply and develop TIRI in real clinical settings. The United States Department of Defence, the main developers and custodians of TIRI technology, recently conducted a technology transfer study to identify the major challenges that must be met for adopting TIRI as a clinical tool. The identified challenges include: (1) Developing objective protocols for clinical data acquisition, (2) Developing methods for useful quantitative interpretation of clinical TIRI data, and (3) Exploring the potential for pathophysiological aetiology of thermal signatures (Diakides, 2013). This thesis makes an integrated contribution to overcome the identified major challenges.

This work makes significant contributions towards transforming thermal infrared imaging into a reliable medical diagnostic tool through: 1) Development of clinical TIRI protocols; 2) Application and validation of the developed protocols through a clinical study; 3) Quantitative analysis of the thermographic data; and 4) Exploitation of the acquired data for determining the heat source depth using a recently developed mathematical model.

For conducting a series of interconnected investigations, this work began by objective characterization of the fundamental architecture of a clinical TIRI system with a view to facilitation of imaging protocol development, elucidation of the mechanism of human thermal infrared emittance and validation of TIRI as a diagnostic tool. A database of over 500 thermal infrared, magnetic resonance and scintigraphic images was developed for demonstrating the potential of intra and inter human tissue discrimination on the basis of thermographic data. The acquired TIR images were employed to investigate if the assumptions of universal grey-body emissivity and transmission of heat from subsurface tissue layers, as employed in heat transfer models, are acceptable for deploying TIRI in clinical investigations. Finally, using the acquired thermographic data, an attempt was made to determine the heat source depth in biological tissues for discriminating between healthy and unhealthy tissues. This step also helped in validating a newly proposed graphical method of determining depth of abnormal heat source in human body.

Unlike any of the previous works in this field, these interconnected studies, through exploitation of empirical data, demonstrate that TIRI has the potential to help

in distinguishing between thermal characteristics of normal and abnormal human tissues.

Acknowledgement

First and foremost, my deepest gratitude to Dr. Masood Mehmood Khan, for his encouragement, insight and always being graciously patient. I look forward to many more years of working with you and learning from you.

Bahut Bahut Shukriya

Thanks are also due to Associate Professor Tele Tan, Mr Luke Barclay, the ever supporting Head of the Department of Mechanical Engineering at Curtin University, Australian Defence Science & Technology Organisation, FLIR Systems Australia, the iVEC Supercomputing Facility, and the Western Australian Department of Health.

Contents

CHAPTER 1

BACKGROUND AND INTRODUCTION

This chapter outlines the developmental history of medical TIRI, and describes how the field has evolved from the first experimentation in the late 1950's, into its current state within the demanding world of evidence-based medicine. The chapter also presents the key challenges in making medical TIRI viable, and translates these key challenges into the problem definitions motivating this work. The chapter presents a plausible way to approach the identified problems, both as isolated challenges and as an integrated program of research. Finally, this chapter defines research objectives and describe contributions that were made to the field in the reaching of those objectives.

1. Background

1.1 Developmental History of Medical TIRI

Thermal infrared imaging (TIRI) is a technique in which heat-sensitive cameras produce images of temperature distribution across object surfaces. Because temperature distributions across human skin can give valuable insight to underlying physiological processes, and because TIRI is a non-contact, non-ionising technique, it has great potential as a diagnostic tool for clinical medicine and biometrics. The medical usefulness of tissue temperature information has been recognized since the days of Hippocrates ~400 BC, and medical TIRI is one of the latest in a long line of techniques designed to conveniently acquire this temperature information, and communicate it to physicians in a way that can helpfully guide their treatment decisions.

The earliest recorded explicitly medical use of TIRI occurred in 1959, when Francis Ring used a modified version of a prototype military TIRI camera called the 'Pyroscan' to create the first medical TIRI at Middlesex Hospital in London, Figure 1-1. By 1962, the 'Pyroscan 2' TIRI system (Figure 1-2) had been specifically developed for

medical applications, with the ability to acquire far better clinical images. The Pyroscan 2 had a slow mechanical scanning process that meant it took around five minutes to record a single image, and the final images were written line by line on electro-sensitive paper. In 1964, British surgeon K. Lloyd Williams showed that many tumours are hotter than their surrounding healthy tissues, and that the hotter the tumour, the worse the prognosis for the patient. This phenomenon of tumours as focal heat sources is now better understood and attributed to specific physiological mechanisms known as the 'Warburg Effect' and hyperactive 'angiogenesis' (Ring & Ammer, 2012; Arthur & Khan, 2011d, 2013). By the mid 60's, the images were displayed on a cathode-ray screen in black and white. Image processing by computer had not yet arrived so much discussion was given to schemes to score the images

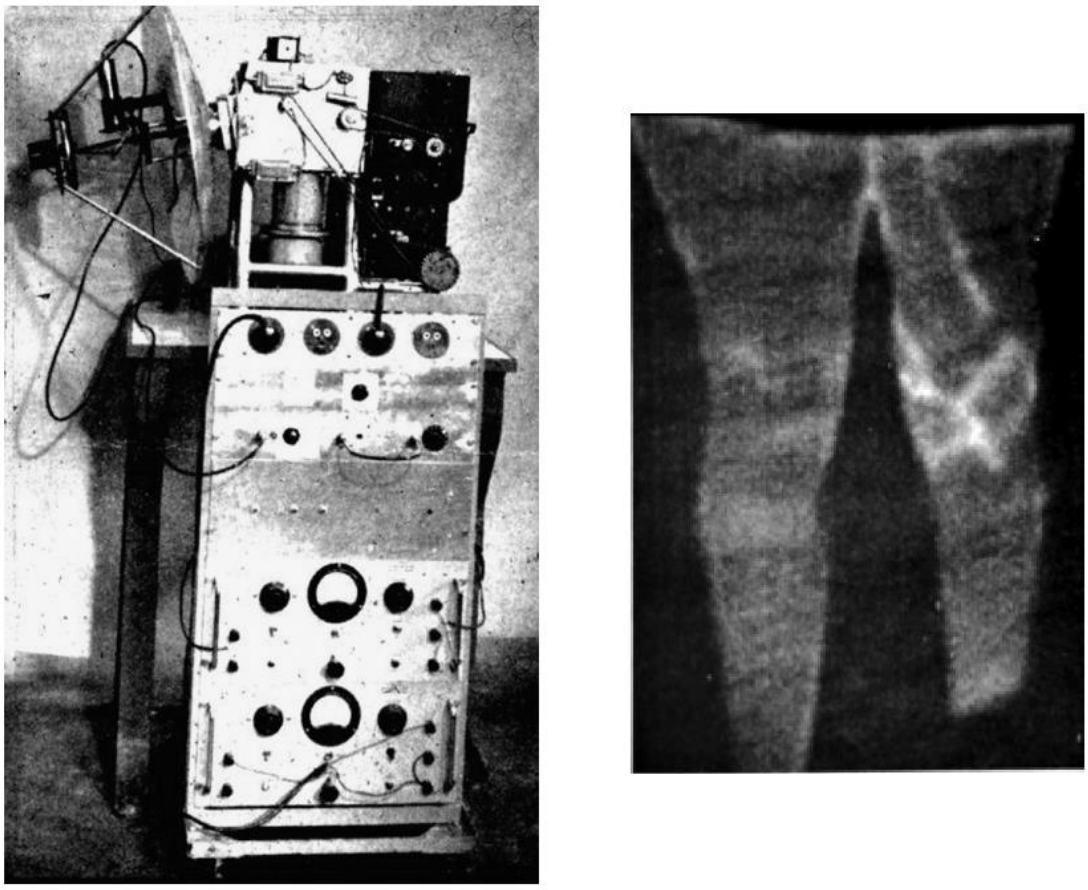

Figure 1-1. Left - The prototype 'Pyroscan' TIRI system, made for military applications in 1942, and Right - the first medical TIRI image revealing the obvious difference in appearance of the healthy right knee and the arthritic left knee, taken at Middlesex Hospital in 1959 by E.F.J. Ring.

subjectively, and to look for hot spots and asymmetry of temperature in the breast. Generation of false colour TIRI's was only possible by photography at this time, with a series of bright isotherms being Manually ranged across the temperature span of the image, each being exposed through a different colour filter and superimposed on a single frame of film (Ring & Ammer, 2012). By the mid 60's, the images were displayed on a cathode-ray screen in black and white. Computational image processing was not possible so discussions remained focused on the schemes to score the images subjectively, and on looking for hot spots and asymmetry of temperature in the breast. Generation of false colour TIRI's was only possible by photography at this time, with a series of bright isotherms being manually ranged across the temperature span of the

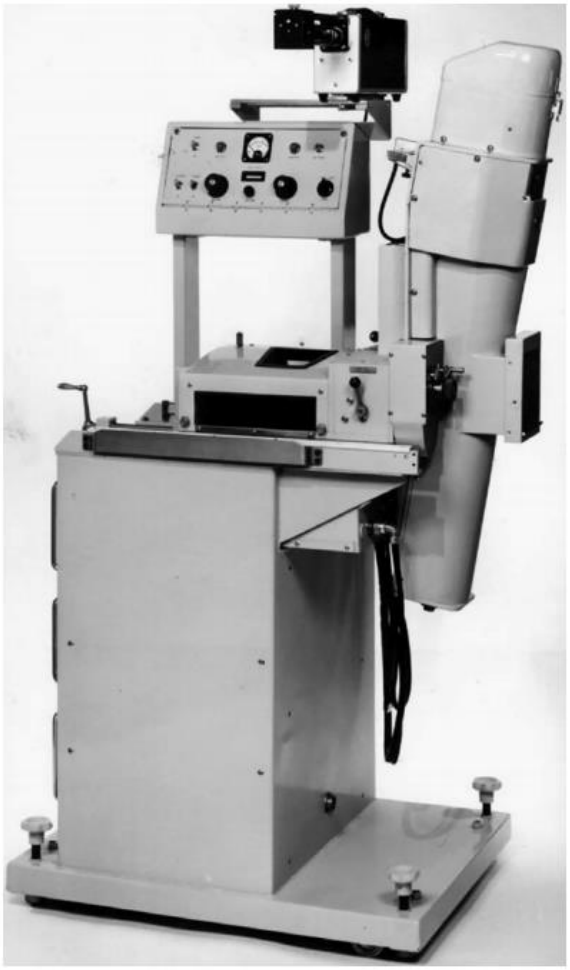

Figure 1-2. 'Pyroscan 2', the first Medical TIRI system. Middlesex Hospital UK, 1962.

image, each being exposed through a different colour filter and superimposed on a single frame of film (Ring & Ammer, 2012).

In Bath England, a medical imaging system originally developed for nuclear medicine in Sweden was adapted for medical TIRI, Figure 1-2. A colour screen was provided to display the digitised image, allowing selection of standard regions of interest, and approximate quantitative measurements of absolute skin temperature image, each being exposed through a different colour filter and superimposed on a from images obtained. In applied TIRI, our ability to make quantitative analyses is limited by how well we understand the emissivity behaviour of the object of interest – in medical TIRI we are nearly always concerned with the emissivity behaviour of human skin. Earlier work by the American physiologist J. Hardy in 1939 suggested that human skin is a highly efficient thermal radiator with an emissivity around 0.98, which is close to that of a perfect black body. Despite this high emissivity, the TIRI technology that was available in the early 1970's struggled to detect the intensity levels of emittance that radiate from human skin regions, which at average temperatures around 34°C is about 495 W/m^2 at peak frequency (~9.5μm), from areas of skin significantly smaller than 1 m^2 (Arthur & Khan, 2011d, 2013).

In the early 1970's, a cancer-driven surge of research interest led to several medical TIRI research centres emerging across Europe, the United States, and Japan (Ring & Ammer, 2012). Awareness that physiological mechanisms like the Warburg Effect and cancerous angiogenesis make regions of cancerous cells significantly hotter than healthy neighbouring cells, meant oncology was identified as an area of great promise for TIRI to contribute. Hopes that TIRI would revolutionise breast cancer screening provided the impetus for development of more sensitive TIR detectors, Figure 1-3.

In 1974 the European Thermographic Association was formed, with a charter to form guidelines for good practice in medical TIRI, and an inaugural conference in Amsterdam (Diakides et al., 2007). These guidelines were to include requirements for patient preparation, conditions for thermal imaging and criteria for the use of thermal

imaging in medicine and pharmacology. Release of these guidelines resulted in a recommended lexicon of clinical TIRI terms (Aarts, 1978), suggestions that optics and human skin emissivity should be investigated in greater detail as influential sources of thermometric error (Salter, 1976; Clark, 1976; Watmough, 1977), and some expert opinion-based recommendations for TIRI procedure in specific context of locomotor disease (Engel, 1979).

The early 80's saw more expert opinion recommendations for general image acquisition and analysis practices (Ring, 1983; Engel, 1984), and a guideline for analysis of TIRI's based on anatomic asymmetries was released by the American Academy of Thermology in 1986. The trajectory of the field of medical TIRI through the late 70's and all of the 80's was primarily driven by the market forces surrounding TIRI detector technology, Figure 1-3. The technical challenges that dictate the rate of TIRI camera development stem from the properties and attributes of their underlying

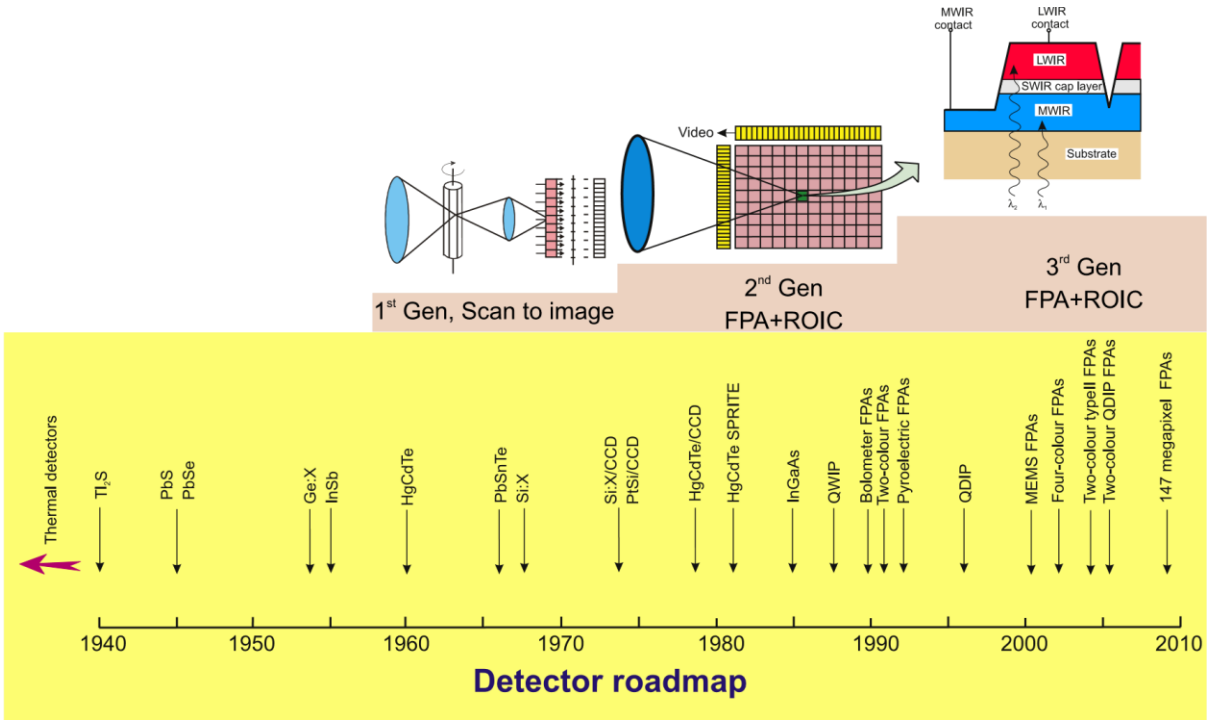

Figure 1-3. History of the development of infrared detectors and systems. Three generations of systems can be considered for principal military and civilian applications: 1st Gen (scanning

systems), 2nd Gen (staring systems – electronically scanned), and 3rd Gen (multicolour functionality and other on-chip functions) - (Rogalski, 2012).

IR detectors - Figure 1-3 (Rogalski, 2011). As it turned out, these market forces only recently allowed us to overcome the technical challenges that have hitherto prevented critical mass in biomedically-directed TIRI research (Diakides, Diakides, Lupo, Paul, & Balcerak, 2007).Specifically, the vast majority of 20th century TIRI research revolved around 'quantum detectors', i.e. detectors whose faculty for IR transduction comes from their propensity to exhibit photonic/quantum (*as opposed to 'thermal', or other types of*) physical phenomena. It should also be noted that this research was almost exclusively conducted by groups within the military, or in high-end industrial research laboratories that were funded by military programs.

Most groups pursued development of quantum-based TIRI because it was already a proven (*although not necessarily ideal or elegant*) technology, whereas *thermal*-type IR detectors required an unknown amount of research and development before acceptable sensitivity and response time performance would be achieved (Rogalski, 2012). However, as quantum detectors require cooling to prevent thermal generation of charge carriers from rendering their output signals unusably noisy, it is necessary to incorporate a cooling system into any quantum TIRI camera. This cooling functionality was/is best achieved by incorporation of components called 'Sterling cycle coolers' into TIRI cameras. As these cooling systems are significantly costly (*not to mention bulky and heavy*) and rarely last beyond 10,000 operating hours; hitherto, the only available TIRI systems with sufficiently well-developed performance for practical applications were prohibitively expensive for many would-be researchers (Rogalski, 2012). This prohibitive cost formed a barrier to entry for many new (*i.e. non-military*) promising fields of applied TIRI research, including us in biomedical (Ring & Ammer, 2012; Arthur & Khan, 2011d, 2013).

Of the relatively few research programs that *did* pursue uncooled (i.e. thermal detector-based) TIRI, it was those funded by the United States military that yielded the game-changing technology of vanadium oxide (VO_x) bolometers (Rogalski, 2012). The 1992 declassification and release of VO_x bolometer technology was a critical milestone

for the field of medical TIRI **(**Figure 1-4**),** allowing free industry to finally exert its powers of vertical integration and scale economy to produce a practical TIRI system with both research-worthy performance *and* accessible cost, removing the foregoing barrier to entry into biomedical TIRI research **–** see point 1990 in Figure 1-3. With subsequent advances in large-scale integration, micromachining, semiconductor technology and optics, the broader civilian research community now has access to high-quality low-cost TIRI systems, and excellent prospects of achieving critical mass in clinically-directed research (Arthur & Khan, 2011d, 2013). The newfound accessibility of TIRI technology in the early 90's caused a huge increase in the number of civilian TIRI camera owners, which in turn raised awareness of the general improvements in TIRI capability (speed, thermal sensitivity, spatial resolution) that had been made since the previous evaluation of TIRI for medicine that occurred in the late 70's, (Figure 1-3). The consensus that it was time to re-evaluate the utility potential of TIRI in medical applications led organisers of the 1996 IEEE EMBS conference to release a CD-ROM of seminal papers on medical TIRI. This CD was sponsored by the U.S. Office of Technology Applications and the U.S. National Technology Transfer Centre, and is available on request from the Medical Imaging Research Group at the University of Glamorgan (Plassmann, Ring, & Jones, 2006).

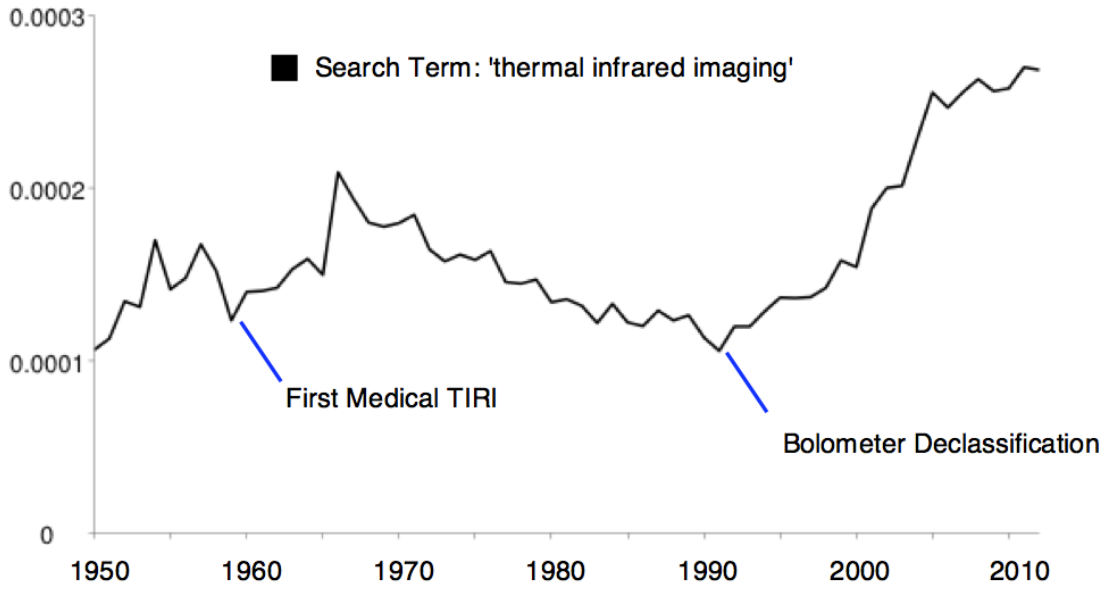

Figure 1-4. MedLine literature trending for appearance of 'Thermal Infrared Imaging in Medicine', in scholarly biomedical publications normalised by word count per year. Highlighted inflection points correspond to the first medical TIRI by Francis Ring in 1959, and the declassification of VOx bolometer technology in 1992 that made TIRI accessible.

This collection of papers emphasised the persisting need for development of objective image acquisition protocols, and development and demonstration of quantitative analytical techniques (Clark & Calcina-Goff, 1996). In 2001, the Glamorgan group launched a project to compile a database of healthy temperature profiles for all parts of the human body, which has since proven that standardised FOV's (fields of view) and ROI's (regions of interest) vastly increase the reproducibility of healthy clinical TIRI profiles (Ammer, 2001). Also in 2001, the US DOD held an important technology transfer workshop called "Tanks to Tumors" in Arlington, Virginia (Paul, 2002). The workshop was co-sponsored by the Office of the Director, Defense Research and Engineering, Space and Sensor Technology Directorate; the Deputy Assistant Secretary of the Army for Environment, Safety and Occupational Health; the Defense Advanced Research Projects Agency; and the Army Research Office. The purpose was to explore technological opportunities for integration of image processing, Web-based database management and development, and infrared sensor technology for the early detection of breast cancer (Paul, 2002).

The 'Tanks to Tumors' workshop was motivated by significant military advances in TIRI and automatic target recognition coupled with the medical understanding of abnormal vascularity (angiogenesis) offering the prospect of automated detection from one to two years earlier than other, more costly and invasive breast cancer screening methods. It was here that objective clinical image acquisition protocols, improved quantification ability through further understanding of skin emissivity, and case study demonstrations of successful pathological aetiology – were again identified as priority focus areas for ongoing research (Paul, 2002; Diakides, 2013).

In 2010, the IEEE EMBS chose '*Considerations for developers of new thermal imaging technologies*' as the theme for the workshop on 'Lessons Learned from Medical Systems Development' (Kong, Chbat, Haemmerich, Kroll, & Panescu, 2011). While

supporting thermal surgery guidance in the fight against cancer alone provides sufficiently compelling motivation for development of clinical thermal imaging technologies, image-guided thermal therapies are increasingly being used to also treat benign disease in the heart, liver, kidney, lung, prostate, brain, bone, uterus and other organs (Haemmerich & Laeseke, 2005). Moreover, transferrable applied research directed toward general advancement of insightful human thermal infrared imaging capability is of great interest to researchers in fields outside thermal therapies, including; affective computing (M. Khan, Ingleby, & Ward, 2006), diagnostic medical imaging (Çetingül & Herman, 2010b; de Weerd, 2010a), and human identification at distance (DARPA, 2000-2003; L. B. Wolff, Socolinsky, & Eveland, 2005). Current approaches to human TIRI can be broadly described as either 'classification', or 'bioheat inversion'.

The classification approach involves the use of human TIRI data to train robust classifiers for specific pattern recognition applications, within fields such as: affective computing (M. Khan et al., 2006; M. Khan, Ward, & Ingleby, 2009; Pavlidis et al., 2012), human identification at distance (DARPA, 2000-2003; L. B. Wolff et al., 2005), and diagnostic decision support (Çetingül & Herman, 2010c; de Weerd, 2010b). The classification approach has yielded several effective expert systems, with both classification robustness and specificity limitations stemming from the inherent spatial and convolutional abstraction layers (M. Khan et al., 2006; M. Khan, Ward, & Ingleby, 2009; Diakides et al., 2007; Wilson & Spence, 1988). The inherent nature of their intended operating environments means these pattern-recognising classifiers cannot rely on controlled image acquisition conditions and subject preparation protocols. Although absolute quantification of calibrated image content can give enhanced classifier performance and robustness, their principal function of spatial feature recognition means relative contrast with neighbouring pixels is more important (M. Khan et al., 2006; M. Khan, Ward, & Ingleby, 2009).

The bioheat inversion approach to human TIRI (detailed further below) requires development and use of bioheat transfer models, geometric models of anatomic milieu, and high fidelity inference and representation of several parameters. This approach and scope of appropriate application is still developmental, with

existing TIRI-compatible bioheat transfer models being Ill-posed, and excessively complex for analytical solution (Arthur & Khan, 2011d, 2013; Izhar & Petrou, 2012; Liu & Deng, 2009). In these bioheat transfer modeling approaches, quantification and absolute thermometric calibration is of fundamental importance. Efforts to date have not explored involvement of a complimentary thermal imaging modality (e.g. MRI) to enable joint inversion (Arthur & Khan, 2011d, 2013). Ability for quantification in applied TIRI critically depends on accuracy of characterization of emissivity behaviour of the imaged object's surface, which in the case of clinical TIRI and human skin presents significant room for improvement (Arthur & Khan, 2011d, 2013).

1.2 Problem Definition

As the goal of this project is to make a strategic contribution to the advancement of TIRI for clinical applications, the problem can be defined in terms of the challenges that must be overcome in order to achieve that goal. To recap, in 2001 the U.S. D.O.D. (the historical primary developers and custodians of TIRI technology) studied how to best approach the transfer of TIRI technology from military to medical applications (Paul, 2002). This study agreed with the consensus in the scholarly literature, identifying development of objective clinical image acquisition protocols, improved quantification ability, and demonstrations of successful pathological etiology as priority areas for focus of ongoing research efforts toward advancement of TIRI for medical applications.

The first aspect of the problem can be described as the lack of an organised systems architecture platform from which researchers can manageably and consistently develop protocols. To date, the published material that offers guidance for design and execution of new applied clinical TIRI research programs consists of expert opinion pieces, without visibility to the underlying physical, physiological, and optical considerations that led to the recommendations given. Moreover, the majority of this content is relatively high level, despite being given in context of specific disease states and anatomic locations. Decisions to set key experimental parameters (optical configuration, clinical procedure timings, ambient environmental controls) at certain

absolute values are often reported, but not accompanied by rationale or derivation from first principals – e.g. optical, physical, or physiological. This incompleteness of information has historically made it difficult for new researchers to decide how much of a given procedural recommendation is relevant or applicable to their envisaged application, and forces each experimental design from scratch.

This lack of a common science-driven starting point has led to a field of disparate studies, which hinders cross pollination of findings and progress. A possible reason that the field has evolved without this platform to date, is that in context of medical imaging technology, TIRI experiments are particularly challenging to design for control of functional variables as everything in the clinical setting is a source of potentially confounding TIR noise – i.e. everything in the clinical setting emits TIR radiation with similar wave properties to the subject of interest (human body), whereas the MRI coil, X-Ray tube, or ultrasound emitter are typically the only sources of the functional signal in an established radiographic suite. In the same way that effective design of an MRI suite is impossible without a comprehensive layout diagram showing functional characterisation of everything ferrous / magnetic in the vicinity, the absence of such a starting point for TIRI research designers has resulted in a field of inconsistent investigations with unknown levels of objectivity, and no common ground from which to discuss development of 'gold standard' practices, as enjoyed by researchers working in the established medical imaging modalities.

The second aspect of the problem, which follows directly from the first, is the lack of literature detailing examples of clinical TIRI protocol implementation. Detailed written accounts of how clinical protocols have been implemented in context of specific pathologies and patient populations serve 2 crucial purposes, 1) instil elevated levels of medical community acceptance of the technology by demonstrating that tests of TIRI's efficacy can be put into practice in compliance with accepted clinical trial standards for validity and reliability, and 2) provide a documented account of all lessons learnt and mistakes made, from which all subsequent investigators can learn and benefit when designing experiments and studies for further progress in the field.

The third aspect of the problem is centred on challenges to quantification of clinical TIRI data for aetiological analyses. In applied TIRI, ability for quantification is

predominantly driven and limited by how accurately the emissivity behaviour of the target body is understood. In the case of clinical TIRI, the emissivity behaviour of interest is that of human skin, which has historically been approximated at a constant value of 0.98 irrespective of anatomic location or any other variable factors. Moreover, these doubts surrounding quantification ability will not be resolved until clinically useful quantitative analysis have been demonstrated. The problem can therefore be described as a lack of accounts of validated quantitative analyses of clinical TIRI data that yield clinically useful information.

To summarise, the problem to be addressed by this thesis work may be defined in terms of the 3 major challenges to the advancement of TIRI for clinical applications, namely: lack of an organised and standardised clinical TIRI systems architecture from which researchers can manageably and consistently develop protocols, lack of literature documenting learnings gained through development and application of pathology-specific and anatomy-specific protocols, and insufficient understanding of human skin emissivity for quantitative aetiological analyses of clinical TIRI data obtained.

1.3 Approach and Rationale

As described in the previous section, the key challenges facing advancement of medical TIRI can be defined as a set of discrete but intrinsically related sub-problems. Accordingly, this doctoral program of research was designed as an integrated series of related phases of work. The most logical order in which to approach these sub-problems naturally emerges from their intrinsic relationships with each other, with completion of one phase prerequisite for commencement of another. Specifically, logic dictated addressing the sub-problems in the following order: systems architecture definition, protocol design, protocol application, and quantitative analysis (flow diagram below).

Mapping out an organised architecture for the clinical TIRI system was the logical first step, because prerequisite for objective design of clinical protocols. Similarly, protocol design was prerequisite for protocol application, and protocol application (aka data

collection) was prerequisite for quantitative data analysis (Arthur & Khan, 2011d). This sequential and integrated approach gave the added benefit of showing subsequent designers of clinical TIRI research programs a complete end-to-end example of how the various components flow into each other through the life cycle of a clinical TIRI research program.

Approaching the overall program of work as a sequence of discrete phases, made it possible to adopt a tailored approach to each individual phase that was best suited to the tasks involved. The goal of the first phase was to systematically map out and organise the architecture of the generic clinical TIRI system, to create a detailed and standardised platform from which clinical TIRI protocols can be developed. This first phase of the work was approached in the same way as a systems architecture project for a complex engineering system, starting with functional definition of the overall high-level systems architecture, then going into progressive levels of detail to describe the salient functional aspects of the various subsystems involved, and their functional (thermal / infrared) interactions with each other. Using this approach, the primary subsystems of the clinical TIRI system (namely: TIRI camera, human tissue volume, and ambient clinical atmosphere) and their interactions with each other were defined in a manner designed to be most helpful for the subsequent phase of clinical protocol design.

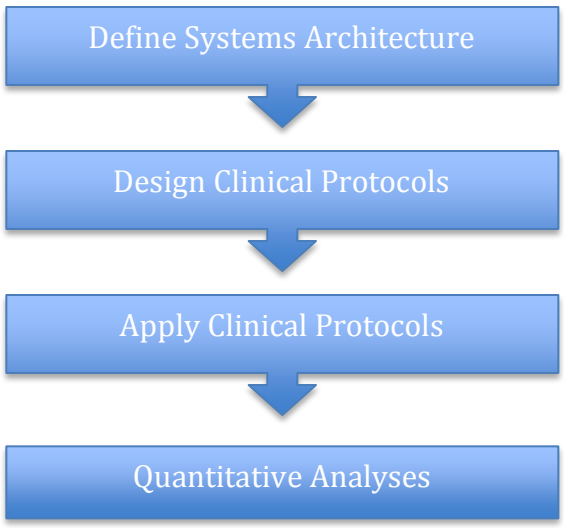

The second phase of work, designing clinical protocols, was approached in the same manner as one would investigate a new indication of an established radiological modality. This first involved literature review of the system's architecture in consultation with collaborating medical professionals to select a pathological context that would feature sufficient thermophysiological manifestation at a sufficiently superficial and thermodynamically homogenous anatomic location to warrant investigation by TIRI. Once tibial stress pathology had been identified, a similar exhaustive exercise was performed to identify a domestic Australian patient population that featured both a sufficiently high incidence of tibial stress pathology, and a controlled operating environment conducive to a longitudinal clinical study.

Once the Australian Army basic trainee population had been identified, it was then possible to identify a population-representative cadaver for deep thermodynamic characterisation of the anatomic context (the pretibial tissue volume) as would be done prior to investigation of a new indication in an established modality like MRI or X-Ray. Identification of the patient population also made it possible to extract the salient population-representative ergonomics (body dimensions) required to design the optical configuration for clinical data collection (average tibial dimensions drive lens-ROI distance, which in turn drives design of gantry and spatial resolution at the ROI surface (Arthur & Khan, 2011d, 2013).

The goal of the third phase of work was to apply the clinical protocols previously developed to evaluate their efficacy, highlight areas for possible improvement, and collect real clinical TIRI data under known controlled conditions for subsequent quantitative analyses. The approach to this logistical phase of work was extremely structured, and involved evaluation of TIRI against the already laid out ethical compliance practices normally applied to more established medical technologies. Although this phase of work was extremely applied, obtaining approval from both Curtin University and the Australian Defence Force, and implementing a three month clinical trial at a military hospital proved extremely valuable as both a learning exercise and demonstration of the seriousness of clinical TIRI research.
In order to capture the full value of this protocol application / clinical study phase as a learning opportunity for the medical TIRI community, the trial protocol was put

through the processes required for registered with both the WHO (World Health Organisation) and the ANZCTR (Australia New Zealand Clinical Trials registry). Clinical trial registry details are included in appendices. A full report of the trial's protocol, implementation, and early results was presented at the IEEE EMBC 2011, and published in proceedings which are available online. The goal of the fourth phase of work was to use the TIRI data collected during the previous clinical study to demonstrate a quantitative analysis with significant and obvious clinical utility. The thermophysiological concepts of the Warburg effect and oncological angiogenesis mean cancerous tumours are well known sources of abnormally focal heat.

Given the widespread use of tumour depth as a critical predictive factor for: staging of primary malignancy, the nature and degree of metastasis, appropriateness of resection, probability of upstaging, tumour control performance and general prognosis, combined with the high promise of successful TIRI-based heat source depth determination given by similar studies on tissue phantoms (Wang et al), it was decided to approach this phase of the work as an exercise in TIRI-based heat source depth determination, or 'HSDD'. This analytical phase of work was approached as one would approach a new indication with an established medical imaging modality, utilising HSDD via cadaveric dissection and MRI as the 'gold standard' validation techniques. This approach proved extremely successful, yielding some extremely encouraging results that successfully demonstrated a quantitative analysis of TIRI data with obvious clinical utility. Going through this phase of work toward advanced quantification prompted a supplementary investigation directed toward advanced characterisation of human skin emissivity, known to the be single most important physical parameter driving and limiting quantification ability in applied TIRI.

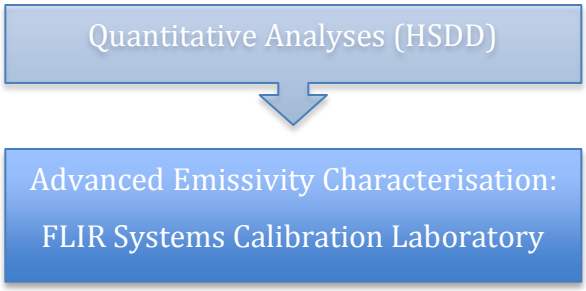

Having identified understanding of emissivity behaviour as the key factor determining quantification ability, the goal of this supplementary phase was to advance the current understanding of human skin emissivity behaviour, with a view to improved scope for quantitative deconvolution of human TIRI data, as found to be necessary during the HSDD phase of work. This phase was approached as a technical material characterisation study, and was accordingly conducted in collaboration with leading technical research staff from FLIR Systems Australia, at the FLIR Systems Calibration Laboratory in Melbourne, Victoria. The study was approached as any other emissivity behaviour characterisation study, observing the highest standards in blackbody radiometric calibration and atmospheric control, at the nation's leading dedicated TIRI camera calibration facility. This rigorous material characterisation approach was extremely successful, yielding interesting results which constituted the desired advanced understanding of human skin emissivity behaviour, which have since been published in the IEEE Journal of Biomedical and Health Informatics (Arthur & Khan, 2013). For completeness, this section also introduces the idea of thermometric MRI as a complimentary medical imaging modality for validation of clinical TIRI and inversion of TIRI-compatible bioheat transfer models. The author feels thermometric MRI should be a focus of ongoing work in advancement of clinical TIRI.

1.4 Objectives & Contributions

The following four items describe the specific objectives of this program of research work:

1. To objectively and systematically map out the architecture of the generic clinical TIRI setting as a controllable system, and define an organised meta-level system architecture, including salient TIR functional characterisation of both the primary subsystems and their functional interactions with each other.

Development and presentation of this systems architecture should be optimised for use as a helpful starting point for designers of clinical TIRI protocols and engineering solutions for experimental control measures.

2. Design objective protocols for acquisition of clinical TIRI data, demonstrating efforts to control all functional TIR variables as defined in the aforementioned systems architecture, and foster conditions for optimal data acquisition. These protocols should be developed in the context of a specific pathology, anatomic location, and patient demographic. The pathology and sample demographics should be chosen in careful consideration of conducive thermophysiology, known strengths and limitations of TIRI, and pragmatic realities of clinical study implementation (Arthur & Khan, 2011d, 2011e; Arthur, Khan, & Barclay, 2011a, 2011b).

3. Conduct a longitudinal clinical study to field-test the clinical protocols that have been developed, and to acquire clinical TIRI data for subsequent quantitative analysis. This clinical study should allow for evaluation and documentation of the efficacy of the clinical protocols, in terms of epidemiological consistency, specificity, temporality, and reversibility of the data obtained. The data obtained should be of a nature conducive to subsequent quantitative analyses, and also shed light on utility potential of TIRI in clinical management of the chosen pathology (Arthur & Khan, 2011d, 2011e; Arthur, Khan, & Barclay, 2011a, 2011b).

4. Carry out related quantitative analyses to:

   a) rigorously characterise human skin emissivity behaviour to evaluate the relative validity of the two conflicting bioheat transfer models conventionally used for interpretation of human TIRI data, namely; global greybody emissivity, and significant transmissivity in superficial tissue layers (Arthur & Khan, 2013) and;

b) demonstrate how clinically-useful TIRI-based measurements of skin temperature can lead to heat source depth determination (HSDD).

5. Examine if the acquired thermographic data would help in distinguishing between the normal and abnormal human tissue heat source depths or shape factors.

Each of the five objectives described above was successfully achieved, and in doing so, the following key contributions were made to the field of medical TIRI:

1. Developed objective protocols for clinical TIRI that guide consistent and standardised acquisition of high quality medical TIRI data;
2. Gained and published new and novel insight to the utility potential of TIRI in clinical management of osseous stress pathology.
3. Discovered and published an advanced understanding of human skin's emissivity behaviour that enables improved quantitative interpretation of clinical TIRI data.
4. Employed and validated an elegant technique for quantitatively determining the heat source depth (HSDD) from real clinical TIRI data, with several identified applications in clinical oncology.

1.5 Publications emanating from this work

Selected publications resulting from this thesis work on clinical TIRI:

1. D. Arthur and M. M. Khan. 'Quantitative Deconvolution of Human Thermal Infrared Emittance'. IEEE Journal of Biomedical and Health Informatics. Jan 2013, Vol.17, Issue 1, PP. 205 - 213. DOI 10.1109/TITB.2012.2225108.

2. D. Arthur, M. M. Khan, and L. C. Barclay. 'Image Processing for Pathological Visualization in Multitemporal Convoluted TIRI'. Proceedings of the IEEE-EMBS International Conference on Biomedical and Health Informatics, Hong Kong SH, Jan 2012. vol.1, pp. 725 – 728. DOI 10.1109/BHI.2012.6211685.

3. D. Arthur and M. M. Khan. 'Toward Validation of TIRI as a Next Generation Deployable Health System'. Journal of Military and Veterans' Health. Jan 2012, Vol. 20, No. 1, pp. 20-21. http://jmvh.org/issue/volume-20-no-1/.

4. D. Arthur and M. M. Khan. 'Infrared Interrogation of Osseous Stress Pathophysiology in Australian Army Recruits: a Three Month Clinical Case Study'. Journal of Military and Veterans' Health. Jan 2012, Vol. 20, No. 1, pp. 65-66. http://jmvh.org/issue/volume-20-no-1/.

5. D. Arthur, M. M. Khan, and L. C. Barclay. 'Thermographic Investigation of Osseous Stress Pathology'**.** Proceedings of the 33rd Annual International Conference of IEEE-EMBS, Boston, 2011, vol.1, p. 6250-53. DOI 10.1109/IEMBS.2011.6091543.

6. D. Arthur and M. M. Khan. 'Thermal Infrared Imaging: Toward Diagnostic Medical Capability'. Proceedings of The 33rd Annual International Conference of the IEEE-EMBS, Boston MA, Aug/Sep 2011, vol.1, pp. 6146-6149, DOI 10.1109/IEMBS.2011.6091518.

CHAPTER 1

THEORY OF CLINICAL THERMAL INFRARED IMAGING

Chapter Summary

This section provides a technical explanation of the thermal infrared imaging (TIRI) process, highlighting salient idiosyncrasies of using TIRI for diagnosing human conditions in a clinical setting. The TIRI process flow is described in terms of the following stages: thermo-active disease state; thermo-physiological process; radiative emission via the 'thermal' mechanism; infrared propagation; infrared detection; and quantitative interpretation.

Thermal Infrared Imaging

1.1 Thermophysiology

The premise for clinical utility of TIRI rests on subsurface tissue conditions manifesting themselves as characteristic temperature distributions across the skin's surface, via thermophysiological mechanisms like those in Table 0-1. As the human body generates heat via catabolism and muscle contraction, and blood is the primary medium of heat transfer within the body, disease states indicated for TIRI consideration must feature physiological mechanisms that modulate superficial perfusion and/or catabolism (Anbar 1998; de Weerd, 2010b).

The four main types of thermo-physiological mechanisms featured in the medical TIRI literature are vascular interruption, neurogenic vascular dysfunction, pathological nitric oxide production, and hypercatabolism (Table 0-1) (Arthur et al., 2011b; Çetingül & Herman, 2010a; Hooshmand, Hashmi, & Phillips, 2001; Swann & Black, 1984; Tkova, Foffova, Hudak, & Svelik, 2010). Interruptions to normal

Table 0-1 Physiological Mechanisms of TIRI-applicable Thermal Aberration.

Class of Mechanism	Instances of Mechanism	Host Pathologies *
Vascular Aberrations	Angiogenesis, Aneurysm, Embolism, Reactive hyperaemia, Reactive ischemia, Haemorrhage.	Deep vein thromboses, Stroke, Raynaud's, Cancer, Compartment Syndrome, Burns.
Neurogenic Vascular Dysfunctions.	Mechanical nerve damage, Chemical nerve irritation, Systemic disorders of the central nervous system.	Diabetes, Raynaud's syndrome, Complex regional pain, Cancers, Glaucoma, Heat burns.
Impaired Neurovascular Control – (caused by pathological nitric oxide production).	Osteocytic. Carcinogenic. Hyperalgesic.	CRPS, Cancer, Arthritis, SARS, Meningitis, Burns
Catabolic Dysfunction - (Hyper/hypo-catabolism).	Carcinogenic Traumatic, Infectious Systemic Endocrine.	Cancer, Osseous Fracture, Diabetes.

*Pathology list not exhaustive – limited to those reported in the clinical TIRI literature.

vasculature create foci of thermal contrast via; embolism, aneurysm, reactive hyperaemia and ischemia, angiogenesis, and haematoma following haemorrhage (Baglin, Crocker, Timmins, Chandler, & Boughton, 1991; Emery, Flavin, Nissen, & Mooney, 1996; Falk, Walther, Philippi, Autschbach, & Krieger, 1995; Friedlander AH, 1994; Garcia, Fernandez, Monge, & Gomez, 1996; Merin, Elami, & Zucker, 1995; Okudera, Kobasyashi, & Toriyama, 1994; Santori, Vitullo, Stopponi, Santori, & Ghera, 1994; Wheeler & Anderson, 1995).

The neurogenic class of mechanisms which includes mechanical nerve damage, chemical nerve irritation, and systemic disorders of the central nervous system - can impair neural control of peripheral vascular tone leading to pathological vasoconstriction or vasodilation (Groeneweg, Niehof, Wesseldijk, Huygen, & Zijlstra, 2008; Huh, Park, Ranson, Campbell, & Ravanbakht, 2009; Lang, Claus, & Handworker, 1995; Pascoe, Herrick, & Purohit, 1997; Tkova et al., 2010; Wasner, 2010). Several of these pathologies feature focal hypercatabolism as a diagnostic feature, perhaps best represented in the medical TIRI literature by the "Warburg effect" describing the propensity of cancerous cells to hypercatabolise glucose into lactic acid and produce a localised region of heat (Mathupala, Rempel, & Pedersen, 1995; Mullen, 1994; Reeves, Bauer, Capra, Davies, & Battistutta, 2004; Wolf, Agnihotri, & Micallef, 2011).

Various traumatic and infectious conditions are also known to feature TIRI – relevant hypercatabolism, as are the more distributed dysfunctions of the endocrine system (Cuthbertson & Tilstone, 1969; Schindeler, McDonald, Bokkoa, & Little, 2008; Schoettler, 1986). In addition, several dysfunctional physiological processes result in hyper-production of nitric oxide (NO), which induces relaxation in the smooth muscles of the vasculature, promoting vasodilation and perfusion, and inhibiting vasoconstriction (Anbar, 1995; Anbar & Gratt, 1997; Campero, Verdugo, & Ochoa, 1993; Fahi, Argiolas, Chiavarelli, & Del Basso, 1996; Garcia-Villalon, Garcia, Fernandez, Monge, & Gomez, 1996; Maigne, Treuil, & Chatellier, 1996; Takahashi, Takahashi, & Moriya, 1994). In summary, TIRI-detectable physiological mechanisms are a central feature of many diagnosable human disease states.

1.2 Thermal Emission

In medical TIRI, the phenomenon of thermal emission is what allows the thermal manifestation of the aforementioned pathophysiological processes to be detected by TIRI systems as spatial distributions of electromagnetic waves. Electromagnetic waves can be defined as self-propagating disturbances of perpendicular electric and magnetic fields, wherein both fields are perpendicular to the direction of propagation. The term 'electromagnetic radiation' refers to the physical phenomena within bodies of matter that involve emission and propagation of these waves. The term '*thermal* radiation' refers to the specific form of radiation in which the mechanism of emission is 'thermal', i.e. physically manifested by the translational kinetics of the emitting body's constituent charged particles.

To paraphrase, in every physical body, every atom and every molecule vibrates. The average kinetic energy of these vibrating particles is represented by the absolute temperature, described in units of Kelvin. According to the laws of electrodynamics a moving electric charge is associated with a variable electric field that produces an alternating magnetic field. This interaction is considered to produce electromagnetic waves that radiates from the body at the speed of light. The thermal radiation fundamental to medical TIRI is thus distinct from other forms of EMR that involve other emission mechanisms, such as synchrotron, maser, or Compton processes.

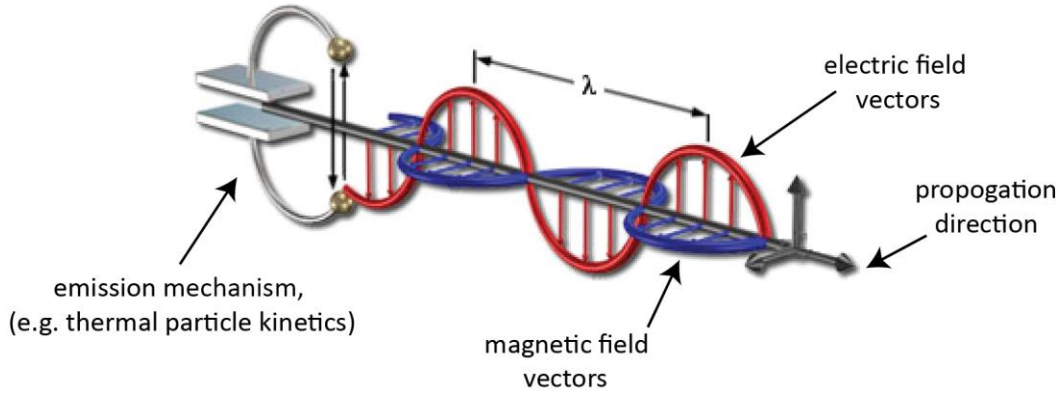

Figure 0-1. Radiation: the emission and propagation of electromagnetic waves (Spring, Inoue, Flynn, Sutter, & Davidson, 2006).

1.3 Infrared Propagation

Having outlined the physiological processes that TIRI can detect, and the phenomenon of thermal emission that allows the resulting skin temperature distributions to leave the human body; this section describes how those surface temperature distributions pass from the site of thermal emission at the skin's surface, to the medical TIRI system.

The term 'infrared radiation' refers to EMR involving waves that propagate with wavelengths ranging from approximately 0.75 μm to 1000 μm, as shown in Figure 0-2. The etymology of the infrared stems from proximity to the wavelengths our human eyes perceive as 'red', with *infra* meaning beneath. As shown in Figure 0-2 the sub-bands within the infrared band follow this nomenclature, with their exact upper and lower limits defined according to sensor response in subjective applications. As clinically relevant temperatures are well within the 1 - 1000K range (human surface euthermia ≈ 307 K) the associated thermal radiation will always involve infrared emittance.

More specifically, spectral variations in power distribution from physical bodies at clinical temperatures (Figure 0-3), transmittance of the clinical atmosphere (Figure 0-3 black), and sensitivity of available TIR detector technology - narrow our consideration to the MWIR (mid-wave infrared) and LWIR (long-wave infrared) sub-bands (Arthur & Khan, 2011d). Figure 0-3 illustrates the implications of conducting applied TIRI in this MWIR-LWIR spectrum, which translate to

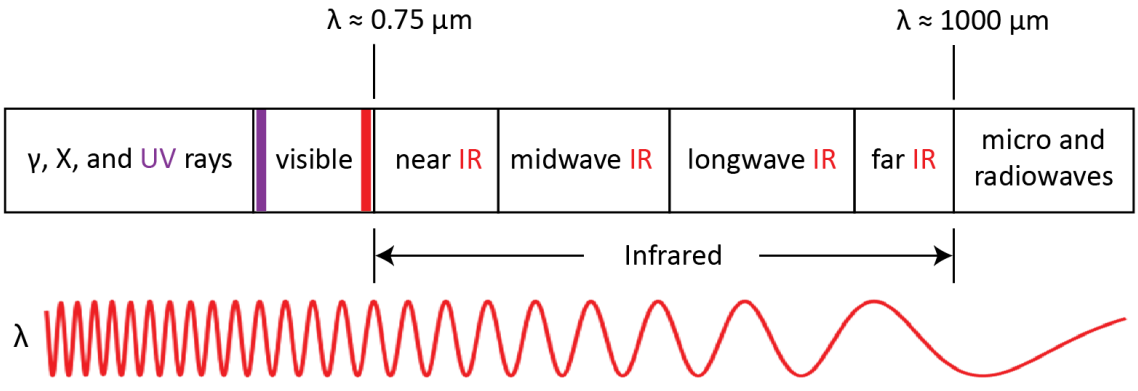

Figure 0-2: Placement of the infrared waveband within the electromagnetic spectrum.

engineering considerations when designing clinical TIRI protocols. Chief among these considerations is the fact that the water content of the 5-8 μm region within ambient clinical atmospheres creates sufficiently low transmittance to infrared propagation that there is no point developing detectors with sensitivity in that band.

As shown by the red curve passing through the 2-5 μm band, one must also consider how weakly the human body emits TIR radiation in the MWIR (0-25 $Wm^{-2}\mu m^{-1}$). This weak emittance is somewhat offset by the impressive sensitivity achievable with MWIR detector materials, which must be considered in context of the extra cost and cooling requirements of MWIR TIRI systems. So in summary, the wave properties of human thermal emittance, and the wave transmitting properties of clinical atmospheric conditions, drive the design decisions for medical TIRI systems.

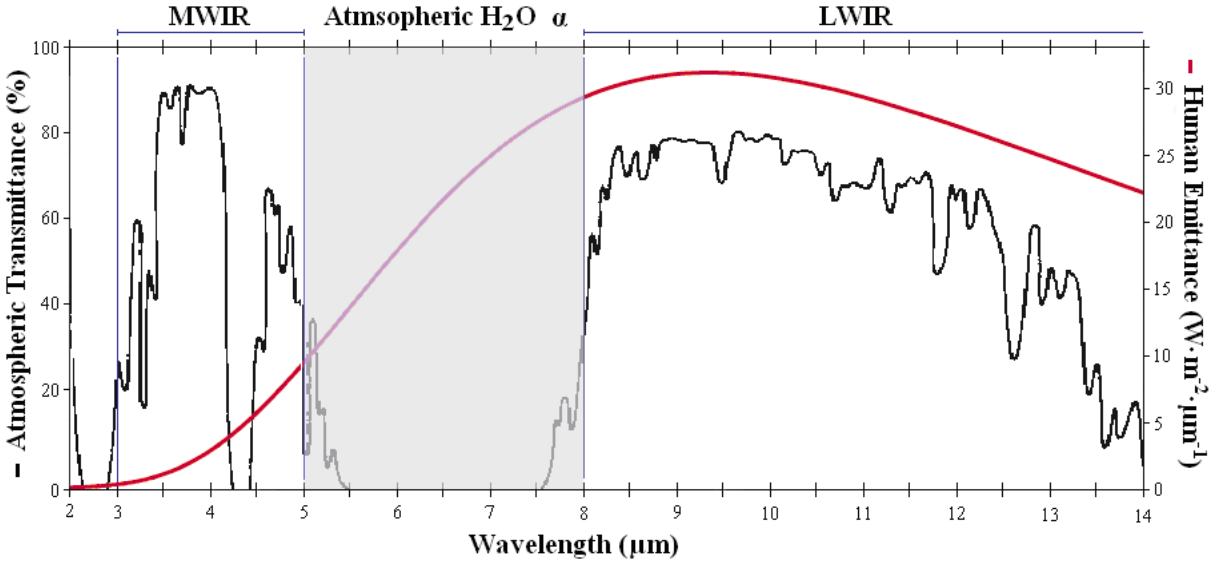

Figure 0-3: Red curve showing a clinically-relevant spectral power distribution; Black curve showing spectral variation in atmospheric transmittance; Grey rectangle showing region of zero transmissivity due to absorption of emittance by molecules of water vapour (Arthur & Khan, 2013).

1.4 Infrared Detection

Having described the physiological processes that TIRI can detect, and how the resulting skin surface temperature distributions pass to the TIRI system by thermal

emission and infrared propagation; this section now describes the fundamental physics that allow medical TIRI systems to convert that infrared emittance into a diagnostically useful digital image.

Several physical phenomena have been investigated for use in IR detection, most notably; impedance variation (bolometers), thermoelectric power (thermocouples), gas expansion (Golay cells), pyroelectricity (pyroelectric detectors), photon drag, the Josephson effect (Josephson junctions, SQUIDs), internal emission (PtSi Schottky barriers), fundamental absorption (intrinsic photodetectors), impurity absorption (extrinsic photodetectors), and low dimensional solid phenomena [superlattice, quantum well (QW) and quantum dot (QD) detectors] (Norton, 1999; Rogalski, 2012). Most IR detectors can be classified as either 'thermal' or 'quantum'; depending on the physical phenomena they exploit to transduce IR emittance.

In addition to certain performance and design implications for infrared imaging systems, the key functional difference between thermal and quantum

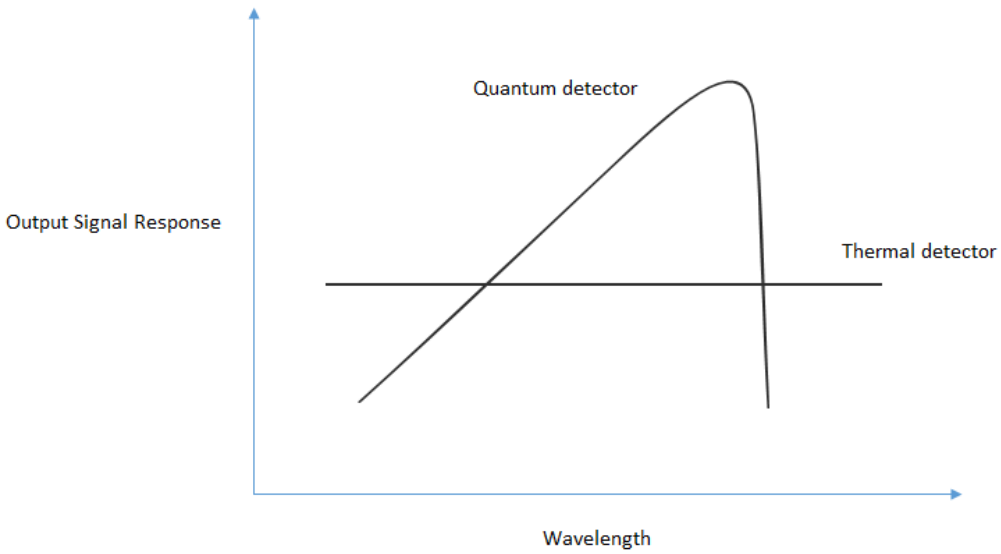

Figure 0-4. Wavelength-dependence of quantum-type IR detector response to irradiance, in context of the wavelength-*in*dependence of thermal-type IR detector response.

detectors is their relative spectral response characteristics. As illustrated in Figure 0-4, for a given irradiance, the electrical output signal observed from a thermal detector is

independent of the wavelength of that causal irradiance, whereas the electrical output response observed from a quantum detector varies selectively with wavelength.

When a 'thermal' detector material absorbs infrared irradiance, the temperature of the detector material changes, and this temperature change causes a corresponding change in a physical property of that material. The magnitude of this physical property change is used to generate a useful electrical output signal. The nature of the signal does not depend upon the photonic nature of the causative incident radiation. Thus, thermal effects are generally wavelength independent, and the observed electrical output signal depends upon the irradiance (incident Wm^{-2}), or rate of change in irradiance, but not upon the spectral content of that incident radiation (Figure 0-4).

Of all the thermal approaches to infrared detection, bolometers have found most widespread utility in TIRI. The key functional attribute of bolometers is their temperature-dependent impedance. Bolometers can be divided into several types (Figure 0-5), including semiconductor, metal, and superconductor bolometers. The

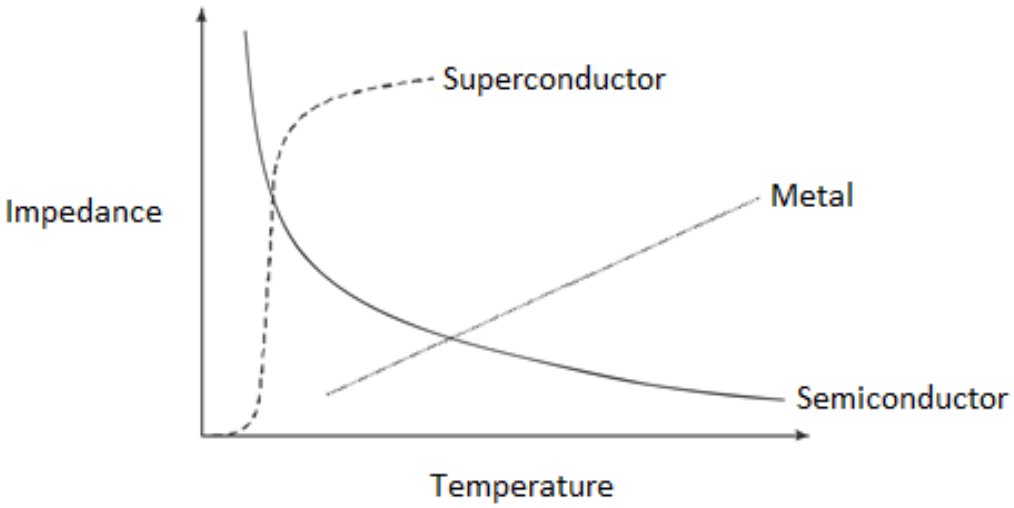

Figure 0-5. Bolometer types, shown in terms of output response to temperature change, as induced by infrared irradiance. Adapted from (Rogalski, 2012).

steeper gradients of the more recently developed semiconductor and superconductor types talks to advancements in thermal sensitivity that were critical to the recent increases in accessibility to TIRI technology.

In quantum detectors, irradiance is absorbed within the material by interaction with electrons. The observed electrical output signal results from the changes in electronic energy distribution via optical charge carriers. Quantum detectors exhibit wavelength-dependent response to irradiance (Figure 0-4), and when cryogenically cooled, can achieve excellent signal-to-noise and response time performance. Cooling is necessary to prevent the thermal generation of charge carriers that would compete with the functionally critical aforementioned optical charge carriers, and create unacceptable levels of noise in the output signal (Rogalski, 2012). The considerable cost involved in satisfying these cooling requirements is a major consideration in development and use of TIRI systems.

So in summary, thermal infrared waves (which hold skin temperature distribution information) can be converted into digital signals via either quantum or thermal phenomena; and the trade-off of quantum's superior sensitivity but greater cost (due to cooling requirements) which has historically been the main consideration, has become less important in recent years due to the introduction of high performance uncooled bolometers (which are thermal-type detectors).

1.5 Emissivity and Quantification

Once infrared emittance has been detected (as above), its quantitative deconvolution and interpretation (as required for thermometry) require application of several laws.

Planck's Law **(0.1)** describes the relationship between the temperature of a 'blackbody', and the wavelengths over which thermal emittance will propagate away from that blackbody. A blackbody is a conceptual (as opposed to real physical) body, which by definition exhibits the maximum possible thermal emittance for any given temperature (Planck, 1901). These blackbody spectral power distributions, or 'Planck curves' (Figure 0-6), provide a benchmark from which spectral power

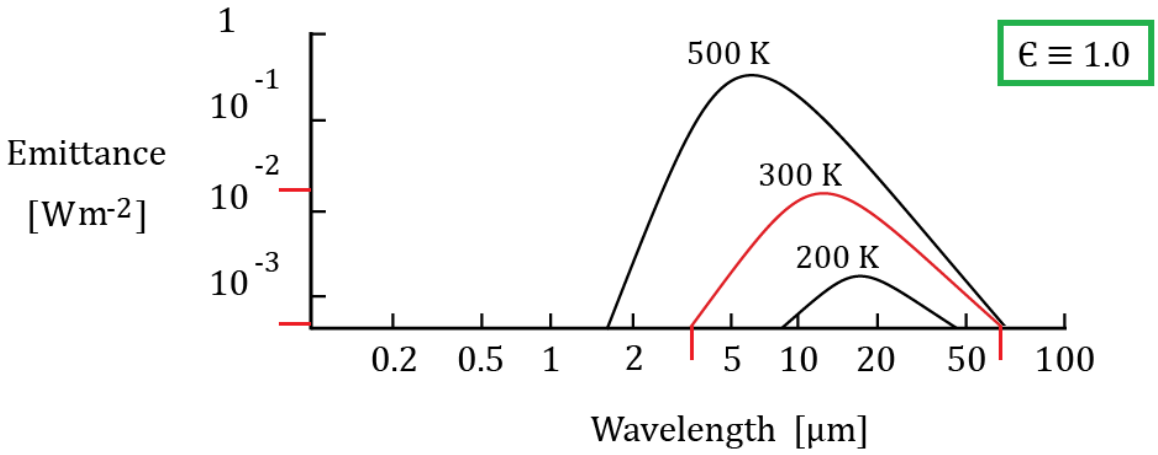

Figure 0-6: 'Planck Curves', hemispherical spectral power distributions corresponding to thermal emission from a blackbody at various thermodynamic temperatures ranging from 200 - 4000 K. Red curve indicating clinically-relevant temperatures for human euthermia.

distributions from real physical bodies can be quantified in context of specified wavelength (λ) and temperature (T) values.

$$B_{\lambda}(T) = \frac{2\pi hc^2}{\lambda^5(e^{\lambda kt} - 1)} \qquad \textbf{(0.1)}$$

Where:

B = spectral emittance [$Wm^{-2}m^{-1}$]

T = absolute temperature [K]

h = Planck's constant = 6.62 x 10^{-34} [Js]

c = the speed of light in vacuum = 3 x 10^{8} [ms^{-1}]

k = Boltzmann's constant 1.38 x 10^{-23} [JK^{-1}]

The Planck function has some useful properties which can be described by 'Wien's Displacement Law', 'The Rayleigh Jean Law', and 'Boltzmann's Law' (Brooker, 2008). Because the radiation process is statistical in nature and a large number of particles are involved, a range of wavelengths is radiated as shown in Figure 0-6. By equating the first derivative of Planck's function to zero with respect to wavelength 'λ', the wavelength around which most power is emitted is given by **(0.2)**:

$$\lambda_{max} = \frac{2898}{T} \quad [\mu m] \qquad \textbf{(0.2)}$$

This relation shows that high temperature bodies tend to emit more power at shorter wavelengths. In applied TIRI research it is useful to know the wavelength around which most power is emitted when designing image acquisition protocols.

$$B_\lambda \approx \frac{2\pi kcT}{\lambda^4} \quad [W \cdot m^{-2} \mu m^{-1}] \qquad \textbf{(0.3)}$$

At longer wavelengths (hc << λkT) the power density per unit wavelength becomes proportional to temperature, as represented by the Rayleigh-Jean Law **(0.3)**. The total power density Φ^0 within a particular bandwidth (which may be a specific section of a full power distribution from a blackbody) is determined by Integration of 'B_λ'over that bandwidth. This is normally solved numerically **(0.4)** or by approximation as there is no closed form:

$$\emptyset^0 = \int_{\lambda_2}^{\lambda_1} \frac{2\pi hc^2 \lambda^{-5}}{e^{hc/\lambda kT}} \delta\lambda \qquad [W \cdot m^{-2}] \qquad \textbf{(0.4)}$$

If the bandwidth under inspection includes more than 50% of the radiated power then the Boltzmann law **(0.5)** can be used to approximate the value:

$$\emptyset^0 = \sigma T^4 \qquad [W \cdot m^{-2}] \qquad \textbf{(0.5)}$$

Where 'σ' is the Stefan-Boltzmann constant (5.67×10^{-8} $Wm^{-2}K^{-4}$).

For any given combination of wavelength and temperature, the ratio of thermal emittance from a real body (W) to that from a blackbody (B) is referred to as that real body's 'emissivity', denoted 'ε', and expressed as shown in **(0.6)**.

$$\boldsymbol{\varepsilon_{\lambda}(T) = \frac{W_{\lambda}(T)}{B_{\lambda}(T)}} \qquad \textbf{(0.6)}$$

Where:

ε = emissivity [0 < decimal value < 1]

λ = wavelength under consideration [μm]

T = absolute temperature under consideration [K]

B = Blackbody emittance [W m^{-2} μm^{-1}]

W = Realbody emittance [W m^{-2} μm^{-1}]

Figure 0-7 shows emissivity as a function of wavelength. By definition, blackbodies always have an omnispectral emissivity of 1.0. Although blackbody emittance is isotropic by definition, it should be noted that real-body emissivity is subject to variation with emission angle 'φ'; making '$\varepsilon_{\lambda T\varphi}$' a more complete expression of

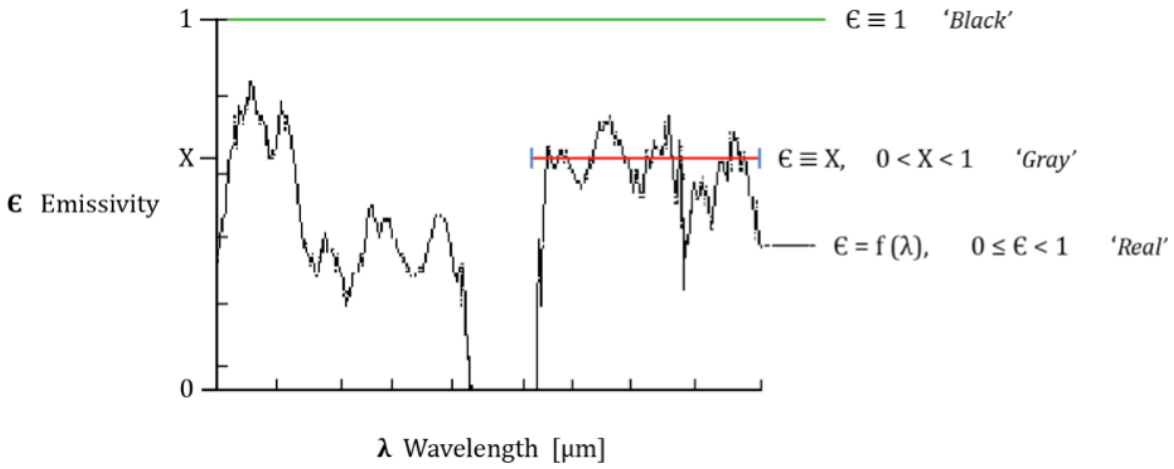

Figure 0-7: Spectral relationship between 'Black', 'Grey', and 'Real' emissivities; as correspond to a common temperature. Note how the 'Grey' characterisation approximates an emissively variable portion of the distribution to have constant emissivity over a finite spectrum.

Emissivity. In applied fields such as engineering however, it is customary to work with 'hemispheric' quantities (Figure 0-6), being those averaged over solid angles, i.e. '$\varepsilon_{\lambda T}$' (Arthur & Khan, 2013).

In summary, from a technologist's perspective, medical TIRI entails a sequence of physical processes; stemming from thermal physiology, to thermal emission, infrared propagation through a clinical atmosphere as an optical medium, to infrared detection (quantum or thermal) within a TIRI system, and ultimate deconvolution and quantification for diagnostic image analysis.

CHAPTER 3

THE INFRARED CLINICAL SETTING

CHAPTER SUMMARY

This chapter works through a description of the clinical TIRI setting as a system of elements that emit, reflect, absorb, or modulate infrared radiation. This infrared characterisation of the clinical setting is intended to make subsequent design of clinical protocols more manageable and objective (Arthur & Khan, 2011a, 2013).
The first section of this chapter discusses the IR characteristics of the overall clinical setting, with subsequent sections discussing protocol considerations surrounding individual components of the clinical setting.

2. The IR Clinical Setting

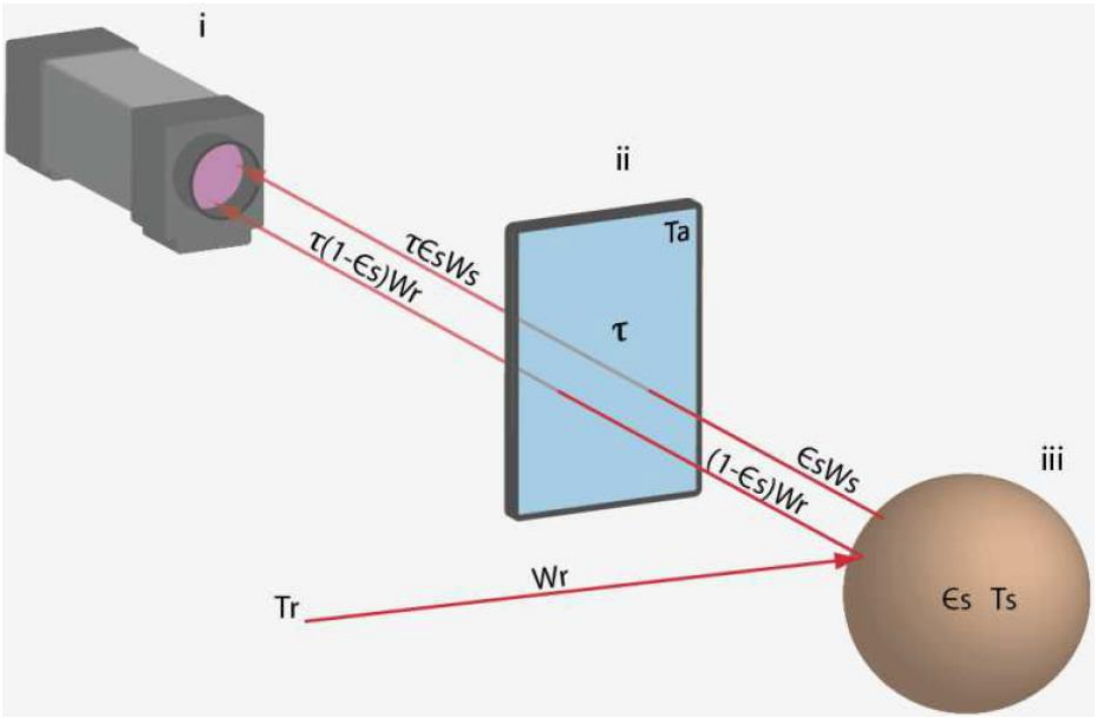

Figure 2-1. Abstraction of The Infrared Clinical Setting. i) TIRI camera (optoelectronics), ii) ambient clinical atmosphere, and iii) physioanatomy being imaged (Arthur & Khan, 2011d).

1.6 The Overall Clinical Setting

Figure 2-1 is a schematic of the overall clinical setting, showing the main infrared elements whose infrared behaviour should be accounted for in a clinical TIRI protocol (Arthur & Khan, 2011d). In Figure 2-1, the clinical setting is represented as a thermal infrared system comprised of three main subsystems, namely; a TIRI camera, the ambient clinical atmosphere, and the physioanatomy under examination. Protocol design considerations surrounding each of these three subsystems are discussed further in the following sections of this chapter.

In addition to the three main subsystems, Figure 2-1 also shows the key streams of radiation that pass between, and interact with, the subsystems. The symbols used in Figure 2-1 to represent these radiation streams and the parameters that drive them are explained as follows:

- Tr =combined effective temperature of ambient sources [K]
- Wr = IR emittance from ambient sources [W]
- (1-Ɛs)W = reflected IR emittance from ROI [W]
- ƐsWs = IR exitance from tissue volume [W]
- Ɛs = emissivity of tissue volume [0, 1]
- Ts = surface temperature of tissue volume [K]
- Ta = atmospheric temperature [K]
- τ = atmospheric transmittance [%]
- τƐsWs = IR emittance from ROI irradiating the lens [W]
- τ(1-ƐsWs)Wr = IR emittance from ambient sources irradiating the lens [W]

Being aware of all of these streams of radiation and spatially understanding how they interact enables more manageable and objective design of protocols to control these streams in a manner that best supports the goal of the clinical study. In most cases the goal of a clinical TIRI study protocol will be to create conditions that allow acquisition of image data containing maximum signal to noise ratio, where the 'signal' is ƐsWs (thermal infrared exitance from tissue volume [W]), and the 'noise' is τ(1-ƐsWs)Wr (TIR emittance from ambient sources irradiating the lens [W]), Figure 2-1.

In the field of ergonomics, where products are designed to function in harmony with humans, the design process begins with characterisation of human body part with which the product will interface, and proceeds by building the product's necessary functionality around that body part characterisation. The same principal applies to design of clinical devices and clinical device application protocols, which are both driven by the specific with which the device must interact. It follows that development of clinical TIRI protocols should begin with detailed thermoradiative characterization of the relevant physioanatomy, (item iii, Figure 2-1).

By the same logic, the subsystem that should be characterized second is the ambient clinical atmosphere. After the atmosphere has been characterized, as both an effector of physioanatomy and infrared signal propagation, it is possible to identify optimal TIRI camera specifications. In the order of phyisoanatomy, atmosphere, camera; the following sections walk through an infrared characterisation of the clinical setting, as a necessary precursor to objective development of clinical TIRI protocols.

1.7 Physioanatomy of Interest

For any given clinical TIRI study, the 'physioanatomy of interest' refers to a specific body part, in specific physiological circumstances; e.g. the anteromedial aspect of a lower leg (anatomy), with a suspected stress fracture in the tibia (physiology). Although the physioanatomy of interest will vary from one clinical TIRI case to another, the approach required to thermoradiative characterisation of the physioanatomy for the purposes of protocol design will be more uniform. As the goal of most clinical TIRI studies is to infer internal heat distribution from surface temperature distribution (in the form of a TIRI image), characterisation should be in terms of both heat transfer within the tissue volume, and external radiative heat transfer from the skin to the TIRI camera.

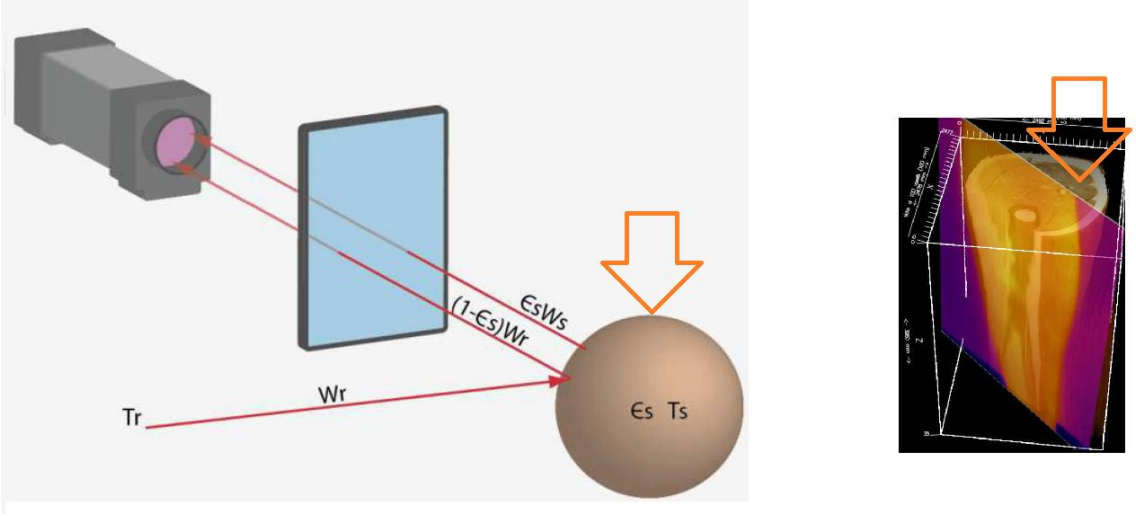

Figure 1-2-2. 3D Physioanatomy of Interest - highlighted in context of the overall clinical setting (left), and in relation to TIRI-obtained surface temperature distribution (right).

The task of inferring or predicting temperature distributions within unit volumes of tissue is typically achieved via computational heat transfer models based upon adaptations of Pennes' seminal 'Bioheat Equation' **(2.1)** (Pennes, 1948). Pennes' original equation, also known as the 'continuum model', has many limitations including a basic assumption that all heat transfer between the tissue and the blood occurs in the capillaries (Nelson, 1998).

$$\rho C \frac{\partial T}{\partial t} = k\nabla^2 T + \rho C_b \omega_b (T_a - T) + Q \qquad \textbf{(2.1)}$$

Where

- ρ = tissue density [kg·m^{-3}]
- C = specific heat of tissue [J·kg^{-1}·K^{-1}]
- T = unknown tissue temperature (*as inferred via TIRI*) [K]
- t = time [s]
- k = thermal conductivity [W·m^{-1}·K^{-1}]
- C_b = specific heat capacity of blood [J·kg^{-1}·K^{-1}]
- ω_b = blood flow rate [kg·m^{-3}·s^{-1}]

- T_a = arterial blood temperature [K]
- Q = volumetric metabolic heat generation rate of tissue [$W \cdot m^{-3}$]

Although many models based upon Pennes' equation are cited in the biomedical literature, this discussion is limited to those models developed for use in conjunction with TIRI, i.e. with 'TIRI-inferred skin surface temperature' as the intended input parameter. The general form of Pennes' equation given **(2.1)** describes the amount of heat transferred from subsurface sources (due to haemodynamics) to the outer surface of the tissue, as indirectly perceptible by a TIRI system. Under steady state conditions, Pennes' equation takes the form given in **(2.2)**

$$0 = k\nabla^2 T + \rho C_b \omega_b (T_a - T) + Q \qquad \textbf{(2.2)}$$

The three terms on the right-hand side of **(2.2)** represent the rate at which thermal energy is considered to enter or leave the unit volume in unit time, by conduction, perfusion, and metabolism respectively. This form is applicable where it is valid to assume; no large arteries or veins cross the volume of interest, and that the region is sufficiently large to make heat transfer to adjacent tissue volumes negligible (Nelson, 1998). High-fidelity modeling of heat transfer mechanisms in specific physioanatomic milieu may conceivably allow extraction of useful physiological parameters from TIRI data (Garbey, Merla, & Pavlidis, 2004; Herman & Çetingül, 2011; Pavlidis et al., 2007).

An example of this is described in (Pavlidis, 2003), where the authors developed an augmented version of Pennes' for use in conjunction with thermometric TIRI, for inference of haemodynamic perfusion rate (ω_b [$kg \cdot m^{-3} \cdot s^{-1}$]). It was argued that the heat produced by the body from metabolic processes is transported to the cutaneous level (surface of the skin) through conduction and convection, and is lost to the environment through radiation, evaporation, and air flow convection (Pavlidis, 2003). The TIRI-perceptible heat loss 'q_{rad}' was modeled as in **(2.3)**:

$$q_s = q_{rad} + q_{con} + q_{ev} \qquad \textbf{(2.3)}$$

Where:

- q_s = total heat loss from ROI [W·m^2]
- q_{rad} = radiative heat loss from ROI [W·m^2]
- q_{con} = convective heat loss from ROI [W·m^2]
- q_{ev} = evaporative heat loss from ROI [W·m^2]

Pennes' **(2.1)**was then extended to include these three mechanisms of heat dissipation from the ROI to the environment, as:

$$\rho C \frac{\partial T}{\partial t} = k\nabla^2 T + \rho C_b \omega_b (T_a - T) + Q - q_{rad} - q_{con} - q_{ev} \qquad \textbf{(2.4)}$$

This model assumes that the blood maintains arterial temperature (T_a) until it reaches thermal equilibrium with the skin tissue (Izhar & Petrou, 2012). The unknown tissue surface temperature 'T' is obtained via quantitative TIRI of the ROI. Using automated methods similar to those described in (Pavlidis, 2003) to evaluate physiological parameters (ρ, C, k, C_b, T_a) and heat components (Q, q_{con}, and q_{ev}), TIRI-based evaluation of 'q_{rad}' enables evaluation of blood perfusion rate ω_b.

An identified mathematical problem in TIRI-associated bioheat modeling is the retrieval of superficial blood vessel location, and the haemodynamic flow rate within those vessels from time-resolved thermometric TIRI data (Izhar & Petrou, 2012). Two legacy bioheat transfer models proposed to address the problem associated with the vascularity of the underlying tissue were also discussed by (Garbey et al., 2004) and (Pavlidis et al., 2007) - the continuum model expressed by **(2.4)** and the geometric model.

The continuum model relates haemodynamic perfusion rate to ROI surface temperature as a function of the effective conductivity and internal heat sources of the tissue VOI, whereas the geometric model strives for exhaustive description of

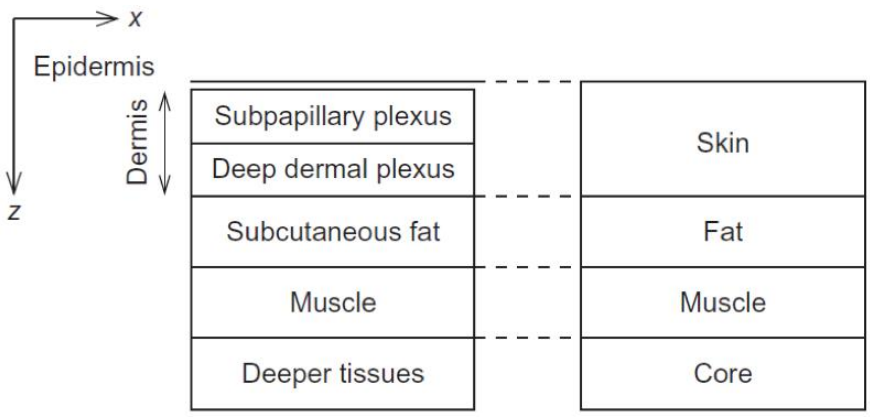

Figure 2-3. Geometrical models of anatomic context (xy plane corresponding to TIRI ROI) for bioheat transfer models used in conjunction with TIRI studies by (a) (Wilson & Spence, 1988), and (b) (Pavlidis, 2003). Figure adapted from (Izhar & Petrou, 2012).

the geometry of the vascularity. As one would expect, the major trade-offs include the inability of continuum models to represent the heterogeneity of vascular geometry, whilst the complexity and variability of superficial vasculature hinders generalization of the geometric approach. Hence, a general procedure to solve the problem by recovering missing information on vessel morphology and blood flow fluctuations was proposed (Garbey et al., 2004; Izhar & Petrou, 2012; Pavlidis et al., 2007).

With a view to capturing the advantages of both approaches (continuum and geometric), a hybrid model was formulated using a partial differential approach with specified boundary conditions (Izhar & Petrou, 2012). This directional model describes bioheat transfer of large superficial vasculature (in skin), with vessels characterised as volumetric heat sources embedded within a thermally passive four-layer tissue structure, Figure 2-3. Each tissue layer is assumed to be isotropic in terms of density, thermal conductivity, metabolic heat rate, and specific heat.

The new modelling approach allows scope to include naïve representations of: the geometry and the anatomy of tissues surrounding vasculature (with vasculature still considered the functional heat source component), the thermal properties of surrounding tissues, the general energy balance of vasculature, and vascular geometry – enabling bioheat transfer modelling with a fidelity more conducive to retrieval of

vascular location and haemodynamic information from TIRI image data corresponding to the superficial ROI.

To capture the advantages of both approaches (continuum and geometric), a hybrid model was formulated using a PDE approach with specified boundary conditions (Izhar & Petrou, 2012). This directional model describes bioheat transfer of large superficial vasculature (in skin), with vessels characterised as volumetric heat sources embedded within a thermally passive four-layer tissue structure, Figure 2-3. Each tissue layer is assumed to be isotropic in terms of density, thermal conductivity, metabolic heat rate, and specific heat.

The new modelling approach allows scope to include naïve representations of: the geometry and the anatomy of tissues surrounding vasculature (with vasculature still considered the functional heat source component), the thermal properties of surrounding tissues, the general energy balance of vasculature, and vascular geometry –enabling bioheat transfer modelling with a fidelity more conducive to retrieval of vascular location and haemodynamic information from TIRI image data corresponding to the superficial ROI.

The PDE describes the unit tissue volume as a Cartesian solid wherein the skin's surface lies in the XY plane, and the perpendicular Z axis extends into the depth of the body, Figure 2-3. Assuming universally isotropic thermal conductivity throughout the volume, the thermal conductivity 'k' term **(2.4)**, which represents

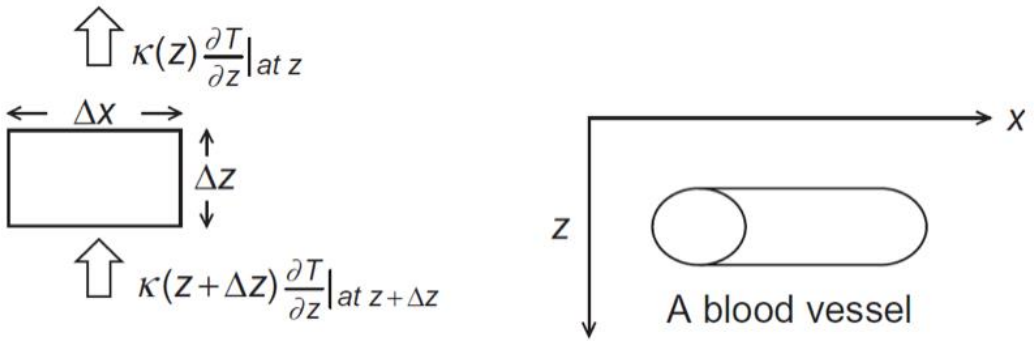

Figure 2-4 (a) An infinitesimal cross section of skin showing entry of heat from the deep muscle layer and loss of heat through the superficial epidermis layer. (b) A blood vessel is assumed to be cylindrical and at a constant depth z below the skin surface. Image reproduced from (Izhar & Petrou, 2012).

the spatial rate of change of the temperature, becomes:

$$k\left(\frac{\partial^2 T}{\partial x^2}+\frac{\partial^2 T}{\partial y^2}+\frac{\partial^2 T}{\partial z^2}\right) \qquad \textbf{(2.5)}$$

Considering a tomographic XZ-plane slice of the unit tissue volume as depicted in Figure 2-3b, thermal conductivity will vary with tissue type, which varies as a function of depth, i.e. k (z). Further considering an infinitesimal rectangular section of this XZ slice, of size ΔX × ΔZ, Figure 2-4, heat *entering* element 'ΔX × ΔZ' is given by **(2.6)**, and heat *leaving* element 'ΔX × ΔZ' is given as:

$$k(z+\Delta z)\frac{\partial T}{\partial z}\Big|_{z+\Delta z} k(z)\frac{\partial T}{\partial z}\Big|_{z} \qquad \textbf{(2.6)}$$

The difference in **(2.6)** represents the heat that remains within element 'ΔX × ΔZ', and contributes to temperature change over time, i.e. $\frac{\partial T}{\partial t}$. Normalising this difference by division over the length of ΔZ gives time-resolved temperature variation per unit length in the Z direction, which in context of an infinitesimal ΔZ gives **(2.7)**:

$$\lim_{\Delta z\to 0}\frac{k(z+\Delta z)\frac{\partial T}{\partial z}\Big|_{z+\Delta z} - k(z)\frac{\partial T}{\partial z}\Big|_{z}}{\Delta z}=\frac{\partial}{\partial z}\left(k(z)\frac{\partial T}{\partial z}\right) \qquad \textbf{(2.7)}$$

Similarly, the time-resolved temperature variation within element 'ΔX × ΔZ' per unit length in the X direction is given by $\frac{\partial}{\partial x}\left(k(z)\frac{\partial T}{\partial x}\right)$. Thus, the $k\nabla^2 T$ (thermal conductivity) term in the higher fidelity **(2.5)** representation of Figure 2-3b becomes **(2.8)**:

$$\frac{\partial}{\partial x}\left(k(z)\frac{\partial T}{\partial x}\right)+\frac{\partial}{\partial z}\left(k(z)\frac{\partial T}{\partial z}\right) \qquad \textbf{(2.8)}$$

Assuming that the ($\rho C_b \omega_b (T_a - T)$) term in **(2.1)** represents the heat transported by a blood vessel running along the x-axis at a constant depth below the epidermis-atmosphere interface, and denoting that heat flow by q_b (x, t), then the bioheat transfer in the unit tissue volume may be represented by **(2.9)**:

$$\rho C \frac{\partial T}{\partial t} - \frac{\partial}{\partial x}\left(k(z)\frac{\partial T}{\partial x}\right) - \frac{\partial}{\partial z}\left(k(z)\frac{\partial T}{\partial z}\right) = q_b(x,t) + Q(x,z) \qquad \textbf{(2.9)}$$

The right-hand side of this equation represents conduction of the heat produced through the control volume tissue and fluctuates over time as expressed by the spatial and time derivatives of the left-hand side of the equation (Pavlidis et al., 2007). In this model, the vessel acting as the heat source is assumed to be a cylinder centred on line Z = s (at constant depth *z,* Figure 2-4b), transferring heat as qb = u_b(t)r(x, z), where u_b(t) denotes haemodynamic flow rate, and r(x, z) is a function **(2.10)** modelling heat transfer *away* from the vessel:

$$r(x,z) \equiv \mu \exp\left(-\frac{(z - s(x))^2}{\pi v_{app}^2}\right) \qquad \textbf{(2.10)}$$

Where v_{app} is the apparent radius of the vessel, while μ is defined as in **(2.11)**

$$\mu \equiv \rho_b C_b \frac{A}{V}(T_a(x,z,t) - T(x,z,t)) \qquad \textbf{(2.11)}$$

Where A represents the cross sectional area of the blood vessel, and V is a normalising volume of tissue. For testing, the PDE model **(2.9)** was used in conjunction with a TIRI system to predict the time-varying haemodynamic flow rate in a major superficial blood vessel (Pavlidis et al., 2007), as useful in monitoring for heartbeat irregularities. The input to the model was the TIRI-inferred temperature 'T' of the skin overlying the carotid artery, and the output was the haemodynamic flow rate 'ω_b' within the vessel.

All other parameters required for inverse solution of **(2.9)** were either measured or assumed, and validation data Figure 2-5a) was obtained via contact blood flow meter.

The biometric utility of TIRI illustrated in Figure 2-5 has been investigated for diagnosis of several medical conditions and affective states (M. Khan et al., 2006; M. Khan et al., 2009). Ways in which this directional PDA model augments Pennes' original include:

- Use of a Gaussian **(2.10)** to model the heat transferred by the vessel, allowing adaptation to arbitrarily complex vascular geometries,
- Multilayer representation of the surrounding tissue,
- Assumed modulation of vessel heat power via control of haemodynamic flow rate,
- And fundamental representation of vessels as a heat sources.

In terms of radiative heat transfer from the outer surface of the skin (the ROI) to the TIRI system, there have been two modelling paradigms to date: the first representing superficial skin tissue on all parts of the body as a greybody emitter with emissivity ≈ 0.98 Figure 2-6a, and the second representing superficial tissue as having significant transmissivity 0.98 Figure 2-6b. The greybody (b) has conventionally been employed in applied human TIRI, such as the during the SARS and avian flu pandemics of 2003 and 2008, when several governments deployed

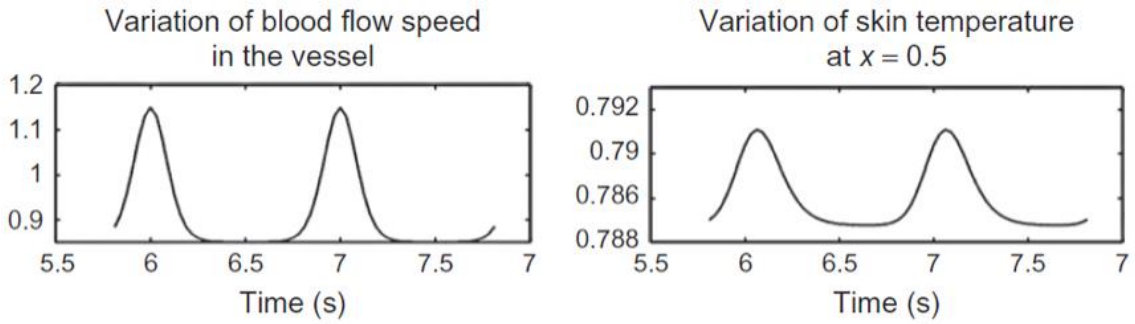

Figure 2-5 (a) time-resolved haemodynamic flow rate in the carotid artery according to contact blood flow meter (Vasimedics®), (b) Time-resolved temperature of skin surface directly overlying the carotid artery monitored in (b), according to a thermometric TIRI system. Reproduced from (Pavlidis et al., 2007).

quantitative thermometric TIRI systems to mass screen for febrile TIR emittance profiles in hospitals and at border control points (Çetingül & Herman, 2010c; Ng & Acharya, 2009; Ring & Ammer, 2012).

This model has been found sufficient in other such applications where tolerance of variable ambient conditions over large lens-object distances is required, efforts toward quantitative deconvolution of imaged human emittance are redundant. In controlled clinical or laboratory environments, however, one may consider more sophisticated modes of application that exploit TIRI's noncontact, noninvasive, and nonionizing features (Arthur & Khan, 2011d; Çetingül & Herman, 2010c; de Weerd, 2010b).

First, TIRI hardware may be readily configured to afford sufficiently stable spatial resolution at the region of interest (ROI) for meaningful pixel-based analyses (Arthur et al., 2011a; M. Khan et al., 2009) and second, controlled ambient conditions give scope for quantitative deconvolution of measured emittance via online inference and mapping of spatiotemporal variations in emissivity (Arthur & Khan, 2013). Departure from the greybody convention followed reports of greater emittance from a 305 K human face (a large inhomogeneous ROI) than from a 305 K radiometrically calibrated Ɛ > 0.99

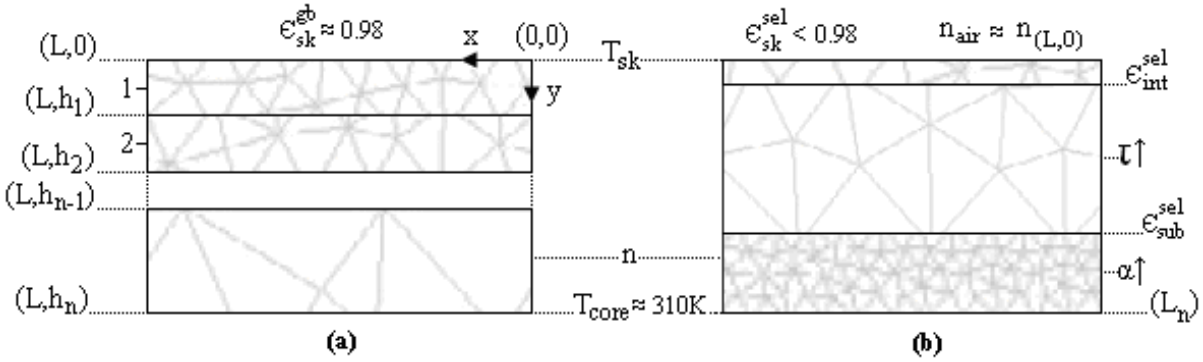

Figure 2-6. Schematic of the two prevalent TIRI-compatible bioheat transfer models, (a) The Greybody Model, featuring global omnispectral emissivity of 0.98 at (L, 0) with subsurface heat transfer entirely conductive and convective, as in (Çetingül & Herman, 2010b). (b) The Transmissive Model, with selective emissivity at the outer surface, a low index of refraction 'n' at the skin-air interface, significant TIR transmissivity in superficial tissue layers, significantly greater absorptivity (α) within the deepest tissue layer, and common skin temperature T_{sk} and core temperature T_{core} boundary conditions at (L, 0) and (L, n) (Arthur & Khan, 2013).

blackbody source during the DARPA HID program. By definition, a blackbody source exhibits greater emissive power at a given surface temperature than a real physical body at that same temperature, so the discrepancy was attributed to significant transmissivity of the superficial tissue layers to emittance from deeper sources.

These findings led to development of the model shown in Figure 2-6b, characterised by selective emissivity at the outer surface, a low index of refraction 'n' at the skin-air interface, significant TIR transmissivity in superficial tissue layers, significantly greater absorptivity 'α' within the deepest tissue layer, and common skin temperature T_{sk} and core temperature T_{core} boundary conditions at (L, 0) and (L, n).

It should be noted that as Kirchhoff's law stipulates that 'the emissivity of a body in thermal equilibrium will be equal to its absorptivity', such that a body with an emissivity ≈ 0.98 should also have an absorptivity ≈ 0.98, and given that reflection, absorption, and transmission of incident radiation are related as: $\rho_{\lambda T\varphi} + \alpha_{\lambda T\varphi} + \tau_{\lambda T\varphi} = 1.0$, (Figure 2-7) - that transmissivity tends to 0.0 as emissivity tends to 1.0. Even when the thermal equilibrium requirement is realistically relaxed, the fact that transmissivity tends to 0.0 as emissivity tends to

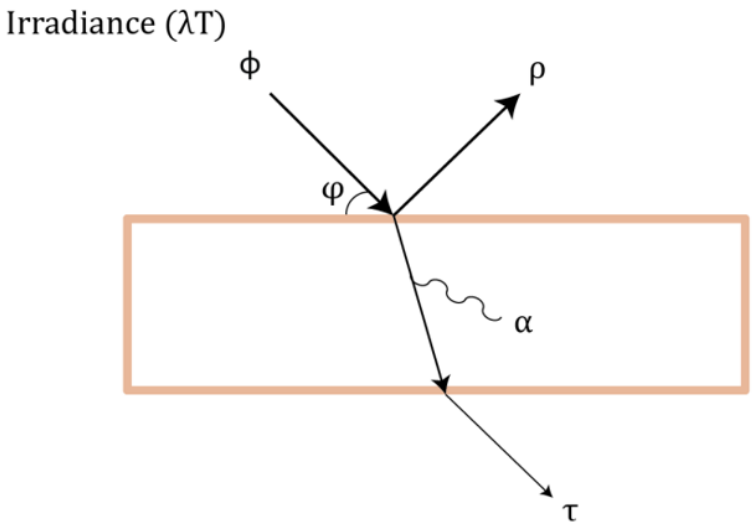

Figure 2-7. Relation of reflection (ρ), absorption (α), and transmission (τ) of a physical body to irradiance (Φ), illustrating the inverse proportionality of absorptivity and transmissivity, in context of the direct proportionality of absorptivity and emissivity (Ɛ), as applicable to the thermophysical representations of superficial tissues shown in Figure 2-6.

1.0 calls the validity of both radiative bioheat modelling assumptions (Figure 2-6) into question. It should also be noted that accurate characterisation of these thermophysical properties of superficial tissue is both critical to solution of the forward problem in clinical TIRI, and directly bounds the resolution of solutions to the inverse problem – thus, rigorous evaluation of the thermophysical characteristics of superficial human tissues is critical to the development of TIRI for clinical applications (Arthur & Khan, 2013).

1.8 Ambient Clinical Atmosphere

Characterisation of the ambient clinical image-acquisition atmosphere is a necessary precursor to protocol design, as the atmosphere constitutes; an optical medium for IR radiation streams, a stimulus to the physioanatomy of interest, and a source of TIR noise, as shown in Figure 2-8, where:

- T_a = atmospheric temperature [K]
- τ = atmospheric transmittance [%]
- $\tau\varepsilon_s W_s$ = TIR emittance from ROI irradiating the lens [W]
- $\tau(1-\varepsilon_s W_s)W_r$ = TIR emittance from ambient sources irradiating the lens [W]

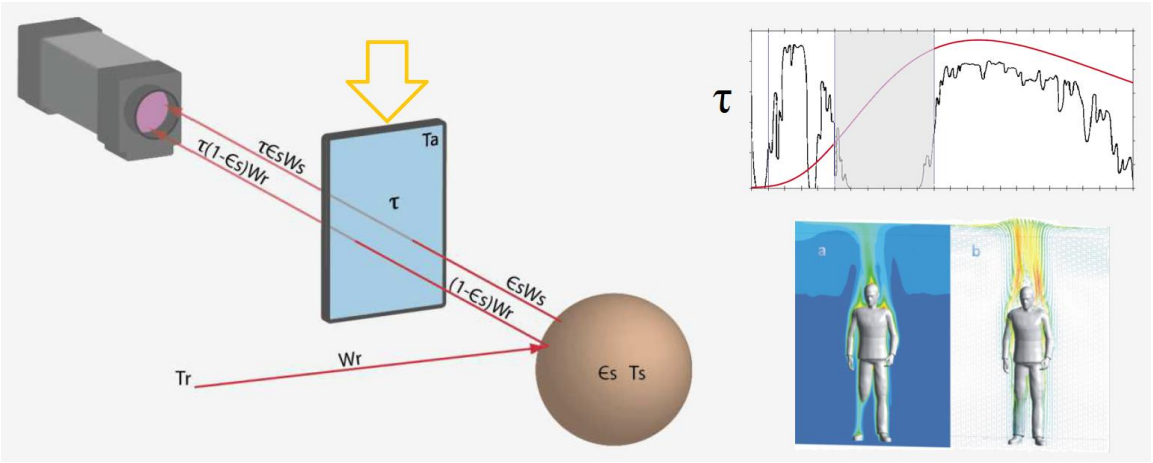

Figure 2-8. Ambient Clinical Atmosphere, in context of clinical setting (left), as an optical medium (upper right), and as a physiological stimulus (lower right).

Figure 2-9 characterises the ambient atmosphere as an optical medium to for human thermal infrared emittance (represented by the red curve). Due to the molecular composition of the atmosphere, the certain parts of the infrared spectrum allow passage of infrared emittance, whereas others are completely opaque; e.g. atmospheric H_20 molecules absorb 100% of emittance within the 5.4-7.6μm band, leading to 0% transmittance. Conversely, the 3-5μm MWIR (midwave infrared) and 8-14μm LWIR (longwave infrared) band exhibit both significant human emittance and transmittance, making these the most popular bands for effective clinical TIRI image acquisition.

Although there are regions beyond 14μm in which significant human emittance and atmospheric transmittance coexist, current availability of sensitive IR detector technology precludes them from consideration for clinical research applications (Arthur & Khan, 2011d; Rogalski, 2011). When characterising the ambient atmosphere as a source of IR noise, it should be noted that illumination invariance in the LWIR is not completely ideal, and identification of optimal illumination parameters requires further investigation (L. Wolff, Socolinsky, & Eveland, 2001). Characterisation of the atmosphere as a physiological stimulus to determine optimal ambient conditions for image acquisition is a critical aspect of

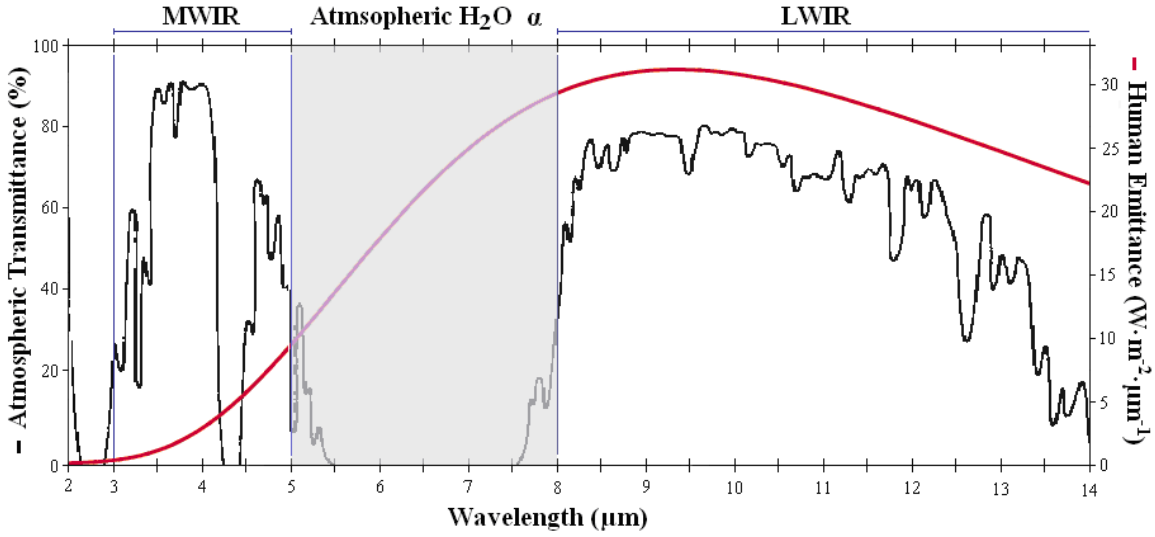

Figure 2-9. Spectral variations in atmospheric transmittance (black) to human thermal infrared emittance (red) (Arthur & Khan, 2011d).

clinical TIRI research that has received little attention in the literature (Borten, Ransil, Di Leo, & Friedman, 1984; Roy, Boucher, & Comtois, 2006; Zaproudina, Varmavuo, Airaksinen, & Närhi, 2008). In the majority of cases it will be desirable to foster thermoneutral conditions within which thermoregulation is actuated almost solely by peripheral vasomotion, with extremely limited perspiration, no shivering, and minimal catabolic thermogenesis (Arthur et al., 2011b). Recent approaches employ multi-node models of human thermoregulation to predict human thermophysiological and thermal sensation responses to wide ranging steady and transient boundary conditions, as illustrated in Figure 2-10 (Fiala et al., 2010).

Recent efforts to establish these conditions have coupled CFD indoor-environment models, with biocybernetic finite-element human thermoregulation models to simulate the overall thermal interaction between a human body and it's climate controlled host indoor environment (Fiala et al., 2010). Successive iterations of the IESD-Fiala model (Figure 2-10a) predict the thermal response of the body to the current ambient conditions provided by ANSYS CFX (Figure 2-10b). The resultant new skin surface properties are then fed back to CFX as inputs, with continued bidirectional iterations until a degree of convergence is reached, indicating thermoneutral conditions.

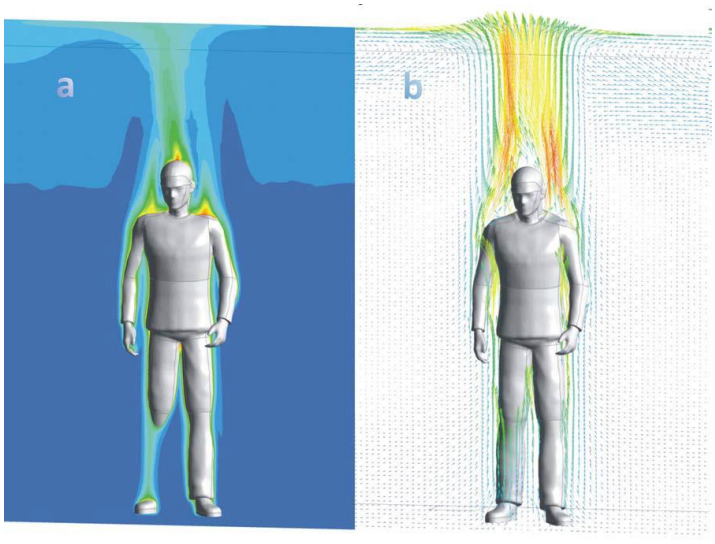

Figure 2-10 Temperature and (a) air velocity (b) distribution around a temperature-regulated human body predicted by coupled CFD-model simulation (Fiala et al., 2010).

1.9 Thermal Infrared Cameras

Having accurately characterised both the physioanatomic context and the ambient clinical atmosphere, it is possible to characterise a compatible TIRI camera system performance and associated optical configuration. Holistic characterisation of TIRI system performance with a view to use in research toward advancement of TIRI for clinical applications is most meaningfully done in terms of a figure of merit known as the 'noise equivalent temperature difference (Arthur & Khan, 2011d).

Noise equivalent temperature difference (NETD) is defined as the difference in temperature between two adjacent blackbody sources of significant lateral extent which, when viewed by the TIRI system, gives rise to a difference in signal-to-noise ratio of 1.0 in the electrical outputs of the two halves of the array (Niklaus, Vieider, & Jakobsen, 2008).

Infrared imaging systems based on uncooled bolometer arrays can reach NETD's below 25 mK with an F number (ratio, focal length : entrance pupil diameter) of 1.0 (Niklaus et al., 2008). For the aforementioned uncooled TIRI systems based on bolometer FPA's with column based ROIC designs, and assuming bolometer temperature is equal to ambient atmospheric temperature (Ta, Figure 2-1ii) the overall NETD can be expressed in terms of its constituent noise components (1/f, Johnson, thermal, and ROIC noise), as in **(2.12)**:

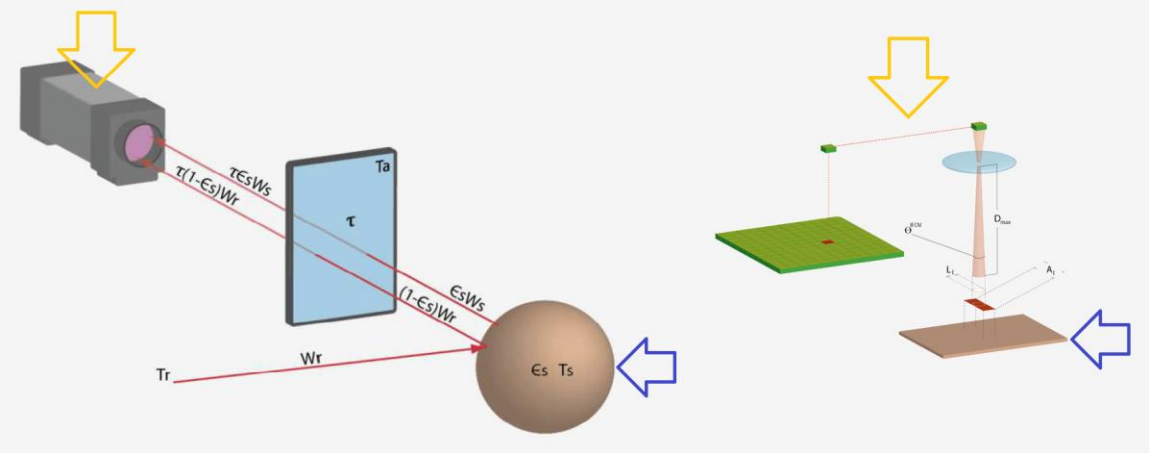

Figure 2-11. The TIRI camera system, in context of overall clinical setting (left) and as a focal plane array of IR detector elements with optics and a physioanatomic target (right).

$$NETD^2 = NETD_{\frac{1}{F}}^2 + NETD_{Johnson}^2 + NETD_{Thermal}^2 + NETD_{ROIC}^2 \quad \textbf{(2.12)}$$

Where:

$NETD_{1/f} = \frac{1}{f}$ noise form the bolometers, given by **(2.13)**:

$$NETD_{\frac{1}{F}} = \left(\frac{4F^2}{\left(\frac{\Delta P}{\Delta T}\right)\emptyset_{\lambda 1-\lambda 2}}\right) \cdot \frac{G}{\beta A \varepsilon_{\lambda 1-\lambda 2}} \cdot \frac{\sqrt{1+\omega^2 \cdot \left(\frac{C}{G}\right)^2} \cdot \sqrt{\frac{K}{v}} \cdot \sqrt{ln\left(\frac{x_1 \cdot f_i}{f_s}\right)}}{TCR} \quad \textbf{(2.13)}$$

$NETD_J$ = Johnson noise of the bolometers, given by **(2.14)**:

$$NETD_J = \left(\frac{4F^2}{\left(\frac{\Delta P}{\Delta T}\right)\emptyset_{\lambda 1-\lambda 2}}\right) 2\sqrt{k} \cdot \frac{\sqrt{T_1} \cdot G}{\beta A \varepsilon_{\lambda 1-\lambda 2}} \cdot \frac{\sqrt{x_l} \cdot f_i \sqrt{1+\omega^2 \cdot \left(\frac{C}{G}\right)^2}}{\sqrt{R_{bol}}^{-1} \cdot TCR \cdot U_{bias}} \quad \textbf{(2.14)}$$

$NETD_{thermal}$ = thermal fluctuation noise from the bolometers and heat exchange, given by **(2.15)**:

$$NETD_{Thermal} = \left(\frac{4F^2}{\left(\frac{\Delta P}{\Delta T}\right)\emptyset_{\lambda 1-\lambda 2}}\right) \sqrt{k} \cdot \frac{G}{\beta A \varepsilon_{\lambda 1-\lambda 2}} \cdot \frac{T_1}{\sqrt{C}} \quad \textbf{(2.15)}$$

and $NETD_{ROIC}$ = noise from the read-out integrated circuit (ROIC), given by **(2.16)**:

$$NETD_{ROIC} = \left(\frac{4F^2}{\left(\frac{\Delta P}{\Delta T}\right)\emptyset_{\lambda 1-\lambda 2}}\right) \cdot \frac{G}{\beta A \varepsilon_{\lambda 1-\lambda 2}} \cdot \frac{(R_{ROIC} + R_{bol}) \cdot \sqrt{1+\omega^2 \cdot \left(\frac{C}{G}\right)^2}}{TCR \cdot R_{ROIC} \cdot \boldsymbol{V_{ROIC}}^{-1}} \quad \textbf{(2.16)}$$

where;

$$\boldsymbol{V_{ROIC}} = \sqrt{V_{amp}(x_l \cdot f_i)^2 + \frac{V_Q^2}{12} + \left(\frac{R_{ROIC} \cdot R_{bol}}{R_{ROIC}+R_{bol}}\right)^2 \cdot I_{ROIC}(x_l \cdot f_i)^2}$$

and

- F = 'F number', = 'focal length : aperture diameter' ratio
- $\Phi_{\lambda 1\text{-}\lambda 2}$ = transmittance of optics in bandwidth λ1-λ2
- G = thermal conduction between each bolometer and surroundings
- C = heat capacity of bolometer pixel
- TCR = temperature coefficient of resistance of bolometer material
- K = $\frac{1}{f}$ noise constant of bolometer material
- v = volume of resistive bolometer material
- T_1 = bolometer membrane temperature
- R_{bol} = bolometer resistance at temperature T_1
- B = bolometer pixel fill factor
- A = bolometer pixel pitch (effective area)
- $\varepsilon_{\lambda 1\text{-}\lambda 2}$ = infrared absorbtion rate of bolometer membrane in waveband λ1-λ2
- x_i = number of bolometer pixels per column
- f_i = frame rate (readout frequency)
- f_s = array shutter correction frequency
- U_{bias} = bolometer bias frequency
- R_{ROIC} = ROIC input impedance
- V_{ROIC} = total noise voltage of ROIC
- V_{amp} = input reference noise voltage
- V_Q = input reference quantisation interval
- I_{ROIC} = current noise from ROIC input
- $\left(\frac{\Delta P}{\Delta T}\right)_{\lambda 1-\lambda 2}$ = temperature contrast in waveband λ1-λ2
- ω = modultation frequency of the IR biosignal from the tissue ROI
- k = Boltzmann constant = 1.381×10^{-23} m^2 kg s^{-2} K^{-1}

In addition to physics-based thermometric performance criteria, design of clinically-directed TIRI research also requires characterisation of TIRI cameras in terms of optical configuration requirements such that the instantaneous fieold of view yileds sufficient spatial resolution at the ROI, as shown Figure 2-12.

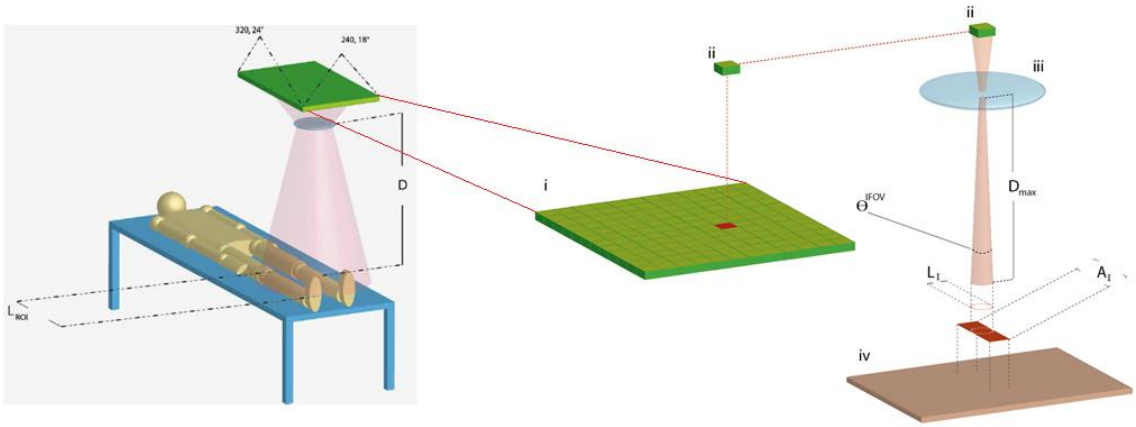

Figure 2-12. Schematic illustration of optical configuration design for IFOV (instantaneous field of view) in context of: clinical image acquisition setup, critical ROI anthropometry, FPA dimensions, and resulting spatial resolution on the surface of the tissue ROI (Arthur & Khan, 2011d; Arthur et al., 2011b).

In summary, the clinical TIRI setting can be characterised as a system of elements that emit, reflect, absorb, or modulate infrared radiation. Having a detailed understanding of heat transfer within the physioanatomy, and the clinical atmosphere as both an optical medium and physiological stimulus, allows selection and calibration of appropriate TIRI camera technology. This infrared characterisation of the clinical setting enables manageable design of objective clinical protocols, which can lead to acquisition of superior clinical data and ultimately to improved patient outcomes (Arthur & Khan, 2011a, 2013).

CHAPTER 4

DEVELOPMENT OF CLINICAL TIRI PROTOCOLS

CHAPTER SUMMARY

This chapter builds on the generalisable infrared characterisation of the clinical setting provided in chapter 3, to develop specific clinical protocols for a TIRI study into osseous stress pathology (OSP) in the tibia. Developing a protocol for a specific pathoanatomic context is valuable as an opportunity for learning general lessons about clinical TIRI protocol development, and delivers a protocol that can be implemented in clinic to give empirical insight to TIRI's utility in a promising application. Tibial OSP was chosen for its strong thermal component, superficial homogenous anatomy, high prevalence in an available test population, and a high-consequence differential diagnosis that could benefit from additional decision support. This chapter walks through the building of necessary understanding, and rationale for key design decisions made in development of a protocol for clinical study of TIRI's utility in management of tibial OSP in an Australian military basic trainee population.

3. Image Acquisition Protocols

The improved reproducibility of body positions and ROI locations has been shown to have a marked influence on both the accuracy and precision of temperature measurements obtained from clinical thermal infrared images (Ring & Ammer, 2012). Moreover, the historical lack of objective protocols for coherent clinical and laboratory-based data acquisition and processing has precluded clinical TIRI from establishing critical mass in epidemiological consistency, specificity, temporality, and reversibility (Ammer, 2008; Clark & Calcina-Goff, 1996; Plassmann, Ring, & Jones, 2006; Simpson, 2008).

Previous human TIRI systems can be functionally characterised as 'two-dimensional spatial classifiers of convoluted human emittance'. Because the

applications for which these expert systems are designed require robust operation under variable conditions, their underlying classifiers are trained with appropriately noisy human TIRI data, acquired under accordingly lenient image acquisition protocols such as those pertaining to febrile screening (IEC/DIS, 2008; ISO, 2009).

The envisaged advanced mode of clinical TIRI may be characterised as 'quantitative three-dimensional radiometry'. This quantitative physics-critical mode of application is tasked to achieve greater specificity than previous systems; despite being without the spatial and convolutional abstraction layers and more forgiving core task that gave previous systems their operational robustness. As advanced clinical TIRI will not be able to achieve this ambitious brief under the variable image acquisition conditions tolerated by legacy systems, development of objective image acquisition protocols is critical for advancement of clinical TIRI for clinical applications.

1.10 Approach to Protocol Development

The purpose of medical image acquisition protocols is to guide implementation of controlled conditions and practices that are most conducive to acquisition of high fidelity image data that contain as much clinically-relevant information as possible (Hawkes et al., 2010). The maturely developed protocols for image acquisition with established medical imaging modalities are multifaceted, with certain elements of these protocols being applicable every time a certain modality is used, and others only applicable when certain pathology or anatomy are involved in the imaging investigation (Abbey & Eckstein, 2012; Carver & Carver, 2010).

The more generally applicable aspects of medical image acquisition protocols often stem from the fundamental physics of the modality, in the form of measures taken to mitigate potential sources of spectral noise within the clinical image acquisition setting, and accentuate the signal of interest. Prior selection of a particular pathoanatomic context provides a helpful framework for subsequent protocol development, with the vast majority of protocols developed around a particular pathoanatomic context being applicable to all clinical investigations with the subjective imaging modality. Selection of a specific pathoanatomic context also allows for

experimental design and execution of real clinical studies, allowing discovery of practical image acquisition issues that might remain unconsidered in solely laboratory-based development, resulting in richer protocols with greater pragmatic utility, whilst generating valuable clinical data.

Accordingly, it was decided to approach the development of image acquisition protocols for clinical TIRI by first identifying a suitable pathoanatomic context, where suitability is primarily characterised by: a significantly thermoactive pathophysiological mechanism that is prevalent in a readily accessible population; and an anatomic setting that is both superficial and unoccluded by thermogenic anatomy (Arthur & Khan, 2011d; Arthur et al., 2011b; Pascoe, Mercer, & de Weerd, 2008). Preference was also given to host tissues (anatomic context) exhibiting static rigidity and low lipid concentration, as conducive to thermometric validation of clinical TIRI data via PRF (proton resonance frequency)-based MRI sequences (Arthur & Khan, 2013; Kagayaki, 2005; Rieke & Pauly, 2008; Taylor et al., 2011). P Pathologies with serious differential diagnoses that stood to gain from an additional diagnostic decision support tool were also prioritised. As detailed in (Arthur et al., 2011b), clinical TIRI image acquisition protocols were developed in pathoanatomic context of 'osseous stress pathology in the anteromedial aspect of the tibia' (described in detail below). To bring similar benefits of a focusing pathoanatomic context, the demographic context of the Australian Army Military Basic Trainee population was also specified prior to protocol development (Arthur & Khan, 2011b).

Following characterization of the implications of these contextual tissue ROI constraints (Figure 3-1iii) upon protocol development, and in alignment with the broader systems architecture (Figure 3-1), clinical TIRI image acquisition protocols were developed to technically address 'optical configuration' (Figure 3-1i) and 'atmospheric control' (Figure 3-1ii) considerations (Arthur et al., 2011b).

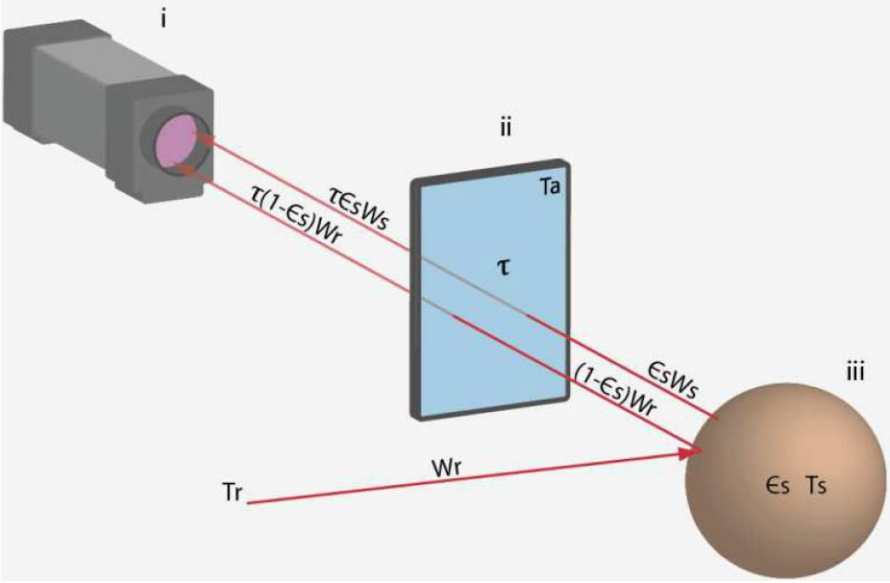

Figure 3-1. The infrared clinical setting (Arthur & Khan, 2011d).

1.11 Pathoanatomic Context

This section provides: rationale for the decision to develop clinical TIRI image acquisition protocols in pathoanatomic context of 'anteromedial tibial stress pathology' (Figure 3-1 iii), and, a characterisation of the aspects of tibial stress pathology relevant to TIRI image acquisition protocols. Osseous stress pathophysiology features focal thermodynamic mechanisms including hyperemia, and both osteocytic and hyperalgesic nitric oxide production (Saini, Yadav, & McCormick, 2011).

In anatomic context of the anteromedial aspect of the tibia (Figure 3-2 and Figure 3-3) where OSP is most prevalent (Itskoviz, Marom, & Ostfeld, 2011), these mechanisms occur within a thin superficial volume of thermodynamically determinate tissues (Arthur et al., 2011b), unoccluded by thermogenic anatomy or dissipative heat-sinking vasculature (de Weerd, 2010b; Pascoe et al., 2008).This contrasts with the complex network of tissues interstitial to the metatarsals (the second most prevalent OSI site) and the dorsal aspect of the foot, as shown Figure 3-3 (Itskoviz et al., 2011; Phillipson & Parker, 2009). Moreover, the pretibial tissue volume exhibits the static rigidity and low lipid concentration conducive to

Figure 3-2. Anteromedial pretibial tissue volumes excised from a cadaver at Curtin University School of Biomedical Sciences spanning mediolaterally from the thermophysical boundaries of the superficial posterior to the anterior compartments. Enlarged excision views (inset above) showing the thin homogeneous nature of tissue interstitial to the exposed periosteum.

thermometric validation of clinical TIRI data via PRF (proton resonance frequency)-based MRI sequences (Arthur & Khan, 2013; Kagayaki, 2005; Rieke & Pauly, 2008; Taylor et al., 2011).Osseous stress injury (OSI) is a significant cause of inactive downtime in athletic and military populations, constituting 10% of all athletic injuries (Goodman, Heaslet, Pagliano, & Rubin, 1985; Phillipson & Parker, 2009). The differential diagnosis of OSI includes extremely serious conditions that require significantly different treatment and management to OSI, such as osteoid osteoma and osteomyelitis in the younger patient and metastases in the older patient -

Figure 3-3. Exploratory dissection of pre-metatarsal tissues from a cadaveric specimen at Curtin University School of Biomedical Sciences, showing complex network of tissues interstitial to the metatarsals (a site of high OSI prevalence) and the dorsal aspect of the foot that would constitute the ROI in a clinical TIRI study. The relative vascularity and complexity of these tissues to those in Figure 3-2 illustrates the rationale for selection of the pre*tibial* tissues as pathoanatomic context for protocol development and clinical study.

-(Daffner et al., 2008; Dugert et al., 2010; E. Dugert, 2010; Heun & Jatoi, 2009; A. Khan, Chandramohan, Turnbull, & MacDonald, 2009; Lew & Waldvogel, 2004; Mader & Calhoun, 2000; Nagashima, Nishi, Yamane, & Tanida, 2010). The possibility of discovering TIRI's ability to improve the rate of correct OSI diagnoses (as suggested by (Goodman et al., 1985)) makes OSI an even more attractive pathophysiological context within which to develop clinical TIRI protocols.

The term 'osseous stress injury' describes the pathophysiological continuum of progressive rarefaction of bone by a physiological mechanism known as both 'active remodelling' and 'secondary bone formation' in accordance with 'Wolff's Law' Figure 3-4 (Schindeler et al., 2008; J. Wolff, 1986). Clinically significant points along this continuum include those of; 'stress reaction', when the volume of interest initially becomes hyperalgaesic following periods of load-bearing; 'stress change', when the sub-threshold physiological correlates of hyperactive remodelling first become apparent on imaging; and 'stress fracture', when the physiological or morphological

correlates of rarefaction evident on imaging are sufficiently significant to warrant a prescribed period of convalescent rest (Barclay, 2010; Daffner et al., 2008; Rae, 2010).

When a long bone is subject to mechanical stress, the ensuing deformation induces a flow in the interstitial fluid of the lacunar-canalicular system of the cortex, shown as 'q' in Figure 3-4 (Danova, Colopy, & Radtke, 2003; Knothe tate, Steck, Forwood, & Niederer, 2000; Mak, Qin, Hung, Cheng, & Tin, 2000; Piekarski & Munro, 1977; Tami, Schaffler, & Knothe tate, 2003; Wang, Ciani, Doty, & Fritton, 2004; Wang et al., 2005). Deformation is also thought to induce a piezoelectric charge gradient from the electronegative compression side 'x' to the electropositive tension side '-'of the cortex, Figure 3-4 (Baxter, Bowen, Turner, & Dent, 2010; Breithaupt, 1855; Fu, 2010; Fukada & Yasuda, 1957; Lakes, 2008; Webb & Tricker, 2000).

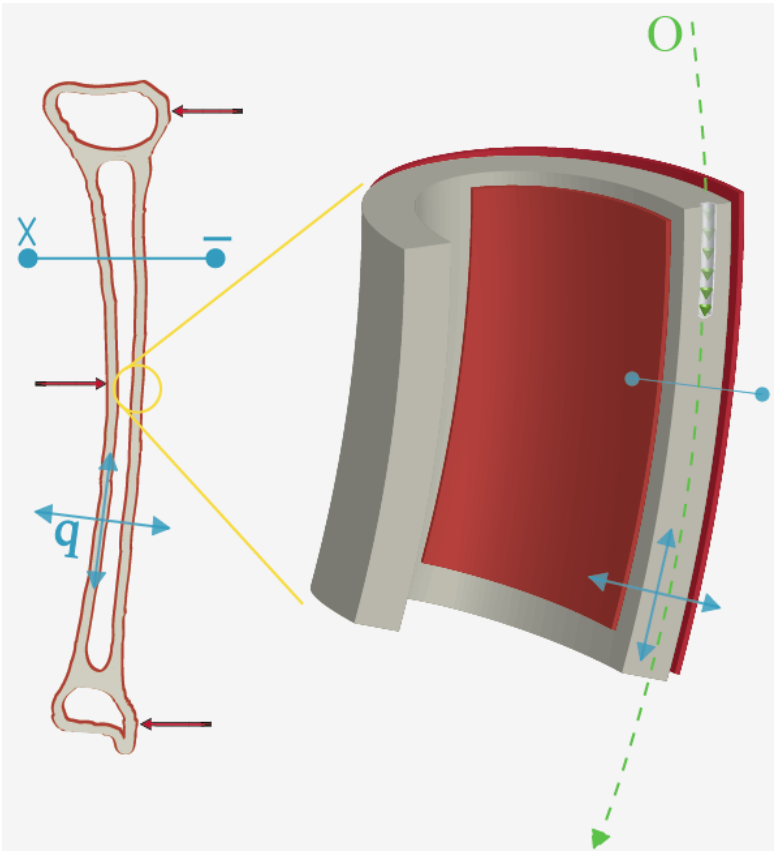

Figure 3-4. The mechanism of osseous stress pathology. Both pathogenetic and perpetuating through pathology – with stressing forces shown as red arrows; cortical bone shown in grey; endosteal and periosteal connective tissues shown as layers of red either side of the cortex; omnidirectional interstitial fluid flow 'q' shown in blue; piezoelectric charge gradient (X - -), also shown in blue; resorptive tunnelling action of osteoclastic effector cells shown in green.

The osteocyte cells of the cortex have been implicated as the osseous 'mechanotransducers', detecting these stress-induced changes, releasing RANKL and nitric oxide molecules, and activating local osteoclasts (Bacabac et al., 2008; Chen, Liu, You, & Simmons, 2010; Jacobs, Temiyasathit, & Castillo, 2010; Philips et al., 2008; Tan et al., 2007; Tatsumi et al., 2007). These conic osteoclasts (green 'O', Figure 3-4) then secrete proteolytic enzymes, drilling 3-10mm tunnels through the cortex normal to the axes of the inducing stress forces (Breithaupt, 1855; Engh, Robinson, & Milgram, 1970; Lech & Iwaniec, 2010).

Osteoblastic cells then fill these 'Haversian canals' with a mineral matrix, requiring approximately one week to structurally mature into new bone fibres, during which the periosteum becomes markedly inflamed (Albright & Brand, 1987; Li, Zhang, Chen, & Chen, 1985; Romani, Gieck, Perrin, Saliba, & Kahler, 2002). Continued stressful activity during this weakened period can exacerbate theperiosteal inflammation, induce oedema in the proximal marrow, and propagate cortical micro-cracks with potential for coalescence into clinical 'stress fracture' and marked local production of nitric oxide (Kidd et al., 2010; Phillipson & Parker, 2009; Sommer & Kress, 2004).

Although cortical bone itself does not contain any nociceptors, local hyperalgesia ensues via penetration of cortical fragments into the highly innervated proximal periosteum and endosteum (Figure 3-4), and pressure from resultant haemorrhage oedema (Athanasou, 2009; Wedro, 2009). The multiple routes to NO production, combined with the certainty of periosteal inflammation and potential for haemorrhage oedema, easily satisfy the criteria for TIRI applicability in the pathogenetic and initial clinical stages (Pascoe et al., 2008; Phillipson & Parker, 2009).

Despite the abundance of available epidemiological information pertinent to trauma-induced fracture in structurally sound bone, there is none objectively pertaining to the physiological mechanisms of repair specific to *stress* fractures, as any biopsy material obtained in differential diagnosis is typically discarded following tests for metastasis and osteomyelitis (Kidd et al., 2010; Mori, 2000). However, as stress fractures are non-displaced and feature near-perfect apposition with minimal necrosis, it is in-keeping with the literature to assume secondary bone formation and

compression osteosynthesis as the dominant mechanisms of repair (Athanasou, 2009; Einhorn, 1998; McKibbin, 1978; Mori, 2000).

Nonetheless, continued stressing of the symptomatic bone may compromise the stability condition, inducing some degree of the well documented, more inflammatory, and more hypercatabolic secondary mechanism of fracture healing (Athanasou, 2009; Einhorn, 1998; McKibbin, 1978; Mori, 2000; Schindeler et al., 2008). The lack of pertinent prior data preclude objective prediction of the potential benefit of TIRI in monitoring and staging of the healing process, yet it should be noted that (Goodman et al., 1985) reported a temporal correlation between the appearance of 'cold spots' and the point of safe return to activity, with the caveat that this occurred in a single subject on a single occasion.

1.12 Demographic Context

This section provides: rationale for the decision to develop clinical TIRI image acquisition protocols in demographic context of the 'Australian Defence Force Basic Trainee Population', and, a characterisation of the aspects of this population relevant to TIRI image acquisition protocols, in context of osseous stress pathology. As with pathoanatomy, selection of a specific population to whom protocols may be targeted facilitates protocol development, with the vast majority of protocols developed for a particular demographic applicable to clinical investigations of all populations with the subjective imaging modality.

Given pathoanatomic context, it should be noted that the debilitating pathology of OSI accounts for 10% of all athletic injuries (Phillipson & Parker, 2009), with prevalence as high as 20% in modern military basic training cohorts (Itskoviz et al., 2011). Moreover, increasing concerns surrounding adverse effects of radiology (Schenkman, 2011), combined with the 12.5% contribution of diagnostic imaging to Australian Medicare benefits paid in 2009-10 have prompted several programs directed toward alternative/adjunct electronic decision support systems (Hricak et al., 2011)(Medicare Australia Statistics, 2011).

Figure 3-5. Nurse unit manager and author (left) addressing a platoon of recruits (right) at the Australian Defence Force Health Centre, Kapooka Basic Training Facility, Blamey Barracks, NSW. Optical image acquisition configuration shown in the central background. Defence participants shown right.

The work described in this thesis coincided with two such initiatives, namely the third and ongoing phase of the Australian DMO (Defence Materiel Organisation) Joint Project 2060, and the current CMVH (Centre for Military & Veteran's health) research initiative addressing the acquisition and introduction of new health technologies that enhance deployable health capability (Arthur & Khan, 2011e; DMO, 2010). Diagnostic imaging is a DMO focus area, with Phase 2A and Block 1 seeing the introduction of portable ultrasound and digital X-ray systems, and Defence have demonstrated air-worthiness and TGA certification of TIRI systems as Medical Devices (GMDN 17888) (Arthur & Khan, 2011e; DMO, 2010).

Accordingly, the ADHREC (Australian Defence Human Research Ethics Committee) granted access to Defence medical facilities and cooperation of personnel for the development and testing of clinical TIRI image acquisition protocols, for interrogation of tibial osseous stress pathology in basic trainees (Arthur & Khan, 2011a, 2011b; Arthur et al., 2011b). Iterative development of the associated protocols

led to Curtin University HREC Protocol #62/2010, AHDREC Protocol #592-10, and Australian New Zealand Registered Clinical Trial #12611000623998 (M. Khan, 2011). It should be noted that the Australian Institute of Sport was also investigated as a potential testing population, but were found to have far lower incidence and prevalence of OSI than the ARTC (Australian Recruit Training Centre), and also lacked the experimental controls afforded by a military training environment. In order for a protocol #592-10 to be endorsed by the ADHREC, it was subject to methodological and scientific internal review within the DSTO (Defence Science & Technology Organisation).

These internal reviews are initially screened by DSTO Research Leaders with both higher authority on the science involved (medical imaging, experimental radiometry, pathophysiology), and independence from the subjective research project. In cases such as this where the protocol under review (592-10) is considered in context of an existing research initiative (DMO Project 2060), the protocol is reviewed by the existing SAC (Scientific Advisory Committee) assigned to that larger initiative. Iterations of the protocol were prepared in consultation with a diverse team of senior military and medical staff at Kapooka Health Centre and RAP (recruit aid post), including radiologists, nurse unit managers, physiotherapists, and relevant commanding officers.

The protocol was accepted as a pilot study into the utility potential of TIRI in detection and monitoring of stress-related bone pathology. The ADHREC were particularly interested in the utility potential of TIRI in guiding diagnosis and treatment of stress reactions / changes /fractures, and monitoring their healing to the point when it is safe for ADF basic trainees to resume activity. Stress fractures currently result in costly/disruptive downtime for military recruits and civilian athletes, so acceleration of identification / diagnosis, safe return to activity is invaluable.

In the case of ARTC, those recruits showing symptoms of stress injury are conservatively sent for MR and/or Bone Scan imaging at the cost of defence during scheduled training time. If imaging returns positive for stress “fracture” recruits are sent home for (a conservative) 6 weeks of convalescence leave, or if deemed ‘un-

repairable within 4 months', they are discharged (Barclay, 2010; Rae, 2010). If imaging returns negative for stress "fracture" but shows stress reaction/changes (*periostitis, hyperalgesia, marrow oedema, and osteoporosis*) the recruit is withdrawn from training and sent to the rehabilitation platoon.

Whilst on convalescence leave recruits heal at various points up to the 6 week mark but the cost, inconvenience, and ionising dose associated with repeated imaging make it more sensible for all convalescents to rest for the full 6 weeks. Those sent to the rehabilitation platoon are constantly monitored for improvements in symptoms and functionality, with repeated MRI or bone scan (nuclear scintigram) as deemed necessary, and at the cost of defence. Bone scans involve injections & high doses of ionising radiation, and both MRI and bone scanning are expensive, time-consuming, and require skilled operators and purpose-built immobile facilities. Thermal imaging has none of these disadvantages, and was deemed to have reasonable potential to provide sufficient information to guide treatment in a large proportion of cases. Understanding the utility of TIRI in this context requires longitudinal TIRI on recruits at the various stages through stress pathology, and comparison with clinical presentation, nuclear scintigraphy, and MRI (M. Khan, 2011).

Given the hierarchical nature of the ADF, ADHREC approval required justification for this research being conducted within Defence as opposed to the wider community. This justification stemmed from Kapooka Health Centre having the largest regular concentration of fatigue-type stress fractures in Australia, making it the ideal venue for this research. Moreover, in a civilian health centre there is no guarantee that any number of stress fractures will arise within a given period. Furthermore, as the health professionals at Kapooka are exposed to the greatest number of stress fractures it follows that they should be among the best at identifying and managing them, making their insights into our clinical practices and TIRI image acquisition protocols invaluable.

The highly organised nature of the ARTC physical training and rehabilitation schedules also allows researchers to cross-reference any physiological changes revealed in the thermal scan to the physical activities of the participants. The impact of physical fitness upon the careers of those within military populations (as with sporting

populations) requires protocols to pay particular attention to clear explanation of management options should an abnormality or unexpected result arise. Of particular concern to were avenues for functional trade tests and reallocation, as addressed in part 4e of protocol #592-10.

1.13 Optical Configuration

Given anatomic context of the anteromedial aspect of the tibia, and demographic context of the ADF basic trainee population, it is possible to design the optical configuration for clinical TIRI acquisition, Figure 3-6 (Arthur et al., 2011b). An ad-hoc camera mounting system was constructed to steadily maintain the lens to skin-surface distance ('D' Figure 3-6), with the optical axis normal to the patient bed. A FLIR ThermoVision™ A40V thermal infrared camera featuring a 7.5 to 13.0 μm uncooled bolometric FPA and thermal sensitivity of 0.08° C was used in the

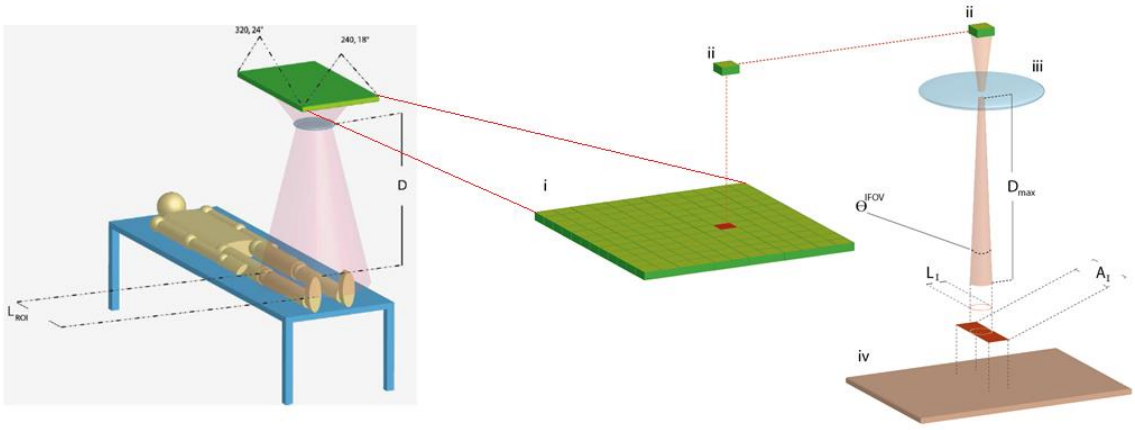

Figure 3-6. Schematic relationship between (Left) optical configuration for clinical image acquisition, and (right) exploded view of optical design parameters impacting spatial resolution achieved at the surface of the tissue ROI. Where: 'L_{roi} ' = ROI length (popliteal height), 'D' = Lens to ROI surface distance, 'i' = FPA, 'ii' = individual FPA element, 'Θ^{IFOV}' = instantaneous angular field of view of 'ii' element, 'iii' = lens, 'D_{max}' = maximum lens-ROI distance permissible for a given IFOV at ROI surface, 'L_1' = IFOV diameter at ROI surface, 'iv' = ROI surface. Enlarged view of optical configuration for clinical image acquisition (above Left) shown Figure 3-6. Enlarged view of optical design parameters impacting spatial resolution achieved at the surface of the tissue ROI (above Right) shown Figure 3-8.

configuration shown in Figure 3-6 (FLIR, 2004, 2011). The optical configuration was optimised for a longest dimension of the region of interest (L_{roi}) ≤ 515mm in accordance with 95th percentile 'popliteal height' as defined in ISO/TR 7250-2:2010 (ISO, 2010). Given the A40V's 320x240 FPA with Θ_{FOV} of 24°x18° (FLIR, 2004, 2011),

The lens to skin-surface distance shown 'D' Figure 3-6, was set to 1.30 m, providing a 553 mm x 412 mm coplanar field of view with instantaneous spatial resolution of 0.58mm^2 at the skin's surface (Arthur & Khan, 2011d; Arthur et al., 2011b). In addition to the basic optical configuration (as shown Figure 3-6), a high emissivity backing mat (Figure 3-9 left) was positioned immediately beyond the ROI during image acquisition to create a thermal chroma-key background with known and emissively-uniform thermo-optical properties for all clinical TIRI's acquired (Arthur et al., 2011b). This controlled and consistent background (Figure 3-10) was designed to introduce consistency, minimise back ground noise, and facilitate

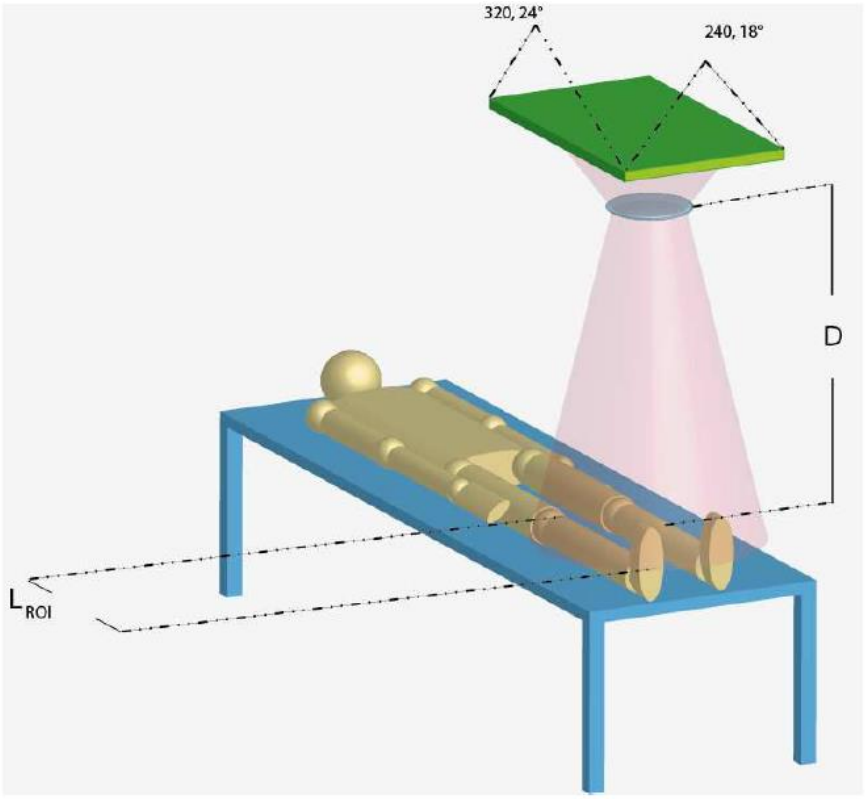

Figure 3-7. Optical configuration for clinical TIRI image acquisition. Where: 'L_{roi} ' = ROI length (popliteal height), 'D' = Lens to ROI surface distance.

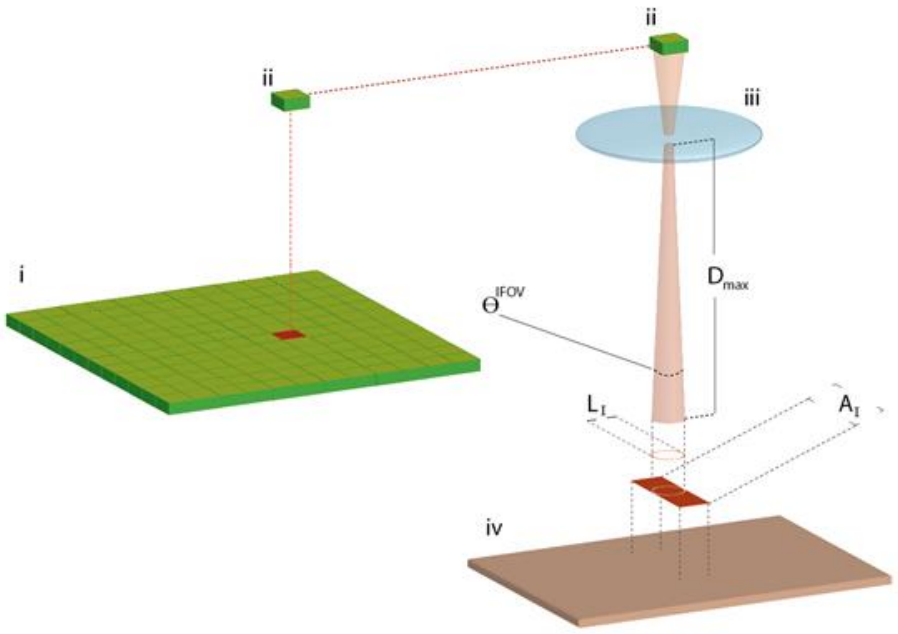

Figure 3-8 Optical parameters impacting spatial resolution at ROI. 'L_{roi} ' = ROI length, 'D' = Lens to ROI distance, 'i' = FPA, 'ii' = FPA element, 'Θ^{IFOV}' = instantaneous angular FOV, 'iii' = lens, 'D_{max}' = maximum lens-ROI distance permissible for a given IFOV at ROI surface, 'L_1' = IFOV diameter at ROI surface, 'iv' = ROI surface.

subsequent TIRI processing operations including: segmentation, inter-temporal calibration, in-ROI enhancement, and registration (Arthur et al., 2011a).
As shown in the TIRI and histogram of Figure 3-10 (corresponding to Figure 3-9 Left), the thermal chroma key mat exhibits highly uniform emittance over it's surface. Figure 3-11 illustrates how introduction of the human ROI (as in Figure 3-9 Right) allows acquisition of distinctly bimodal clinical TIRI's, enabling highly effective segmentation via the venerable threshold selection method (Arthur et al., 2011a; Otsu, 1979).

The algorithm entails an exhaustive search for the threshold grey level 'k' that yields optimal efficacy in segmentation of bimodal digital image data, in cases (*such as this*) where intensity-based segmentation is meaningful to the application. Specifically, if a TIRI features 'L' different grey levels in the range [1, L], with the number of pixels exhibiting grey level 'i' given by 'n_i', and the total number of pixels in the TIRI given by $N = n_1 + n_2 + ...n_L$; then the TIRI's normalised histogram (Figure 3-12) is evaluated as if it were a probability distribution, characterised by the following simple relations;

$$p_i = \frac{n_i}{N}\,, \qquad p_i \geq 0\,, \qquad \sum_{i=1}^{L} p_i = 1. \qquad \textbf{(3.1)}$$

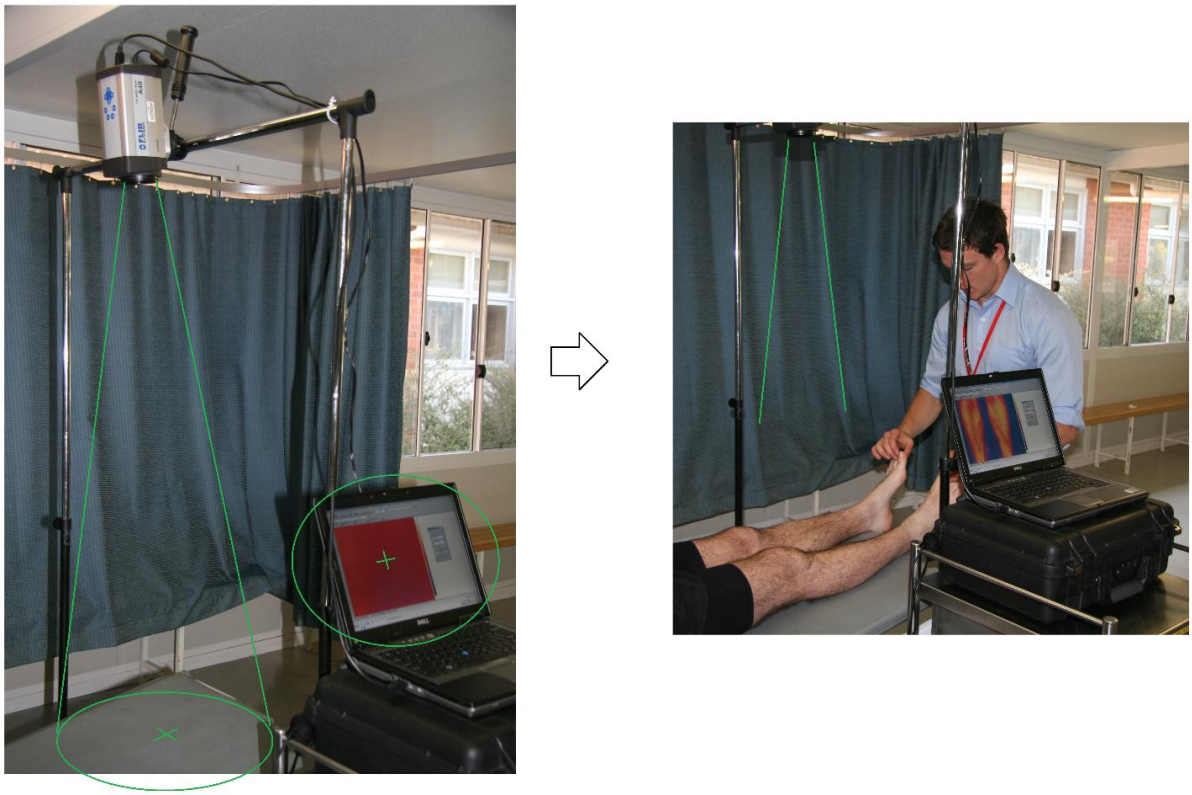

Figure 3-9. Actual optical image acquisition configuration used, FLIR A40V camera mounted on purpose-built gantry, grey TIR chroma-key surface in FOV, spatially uniform false colour display on DAQ laptop, corresponding to the uniform TIR output shown (Figure 3-10 Right). Calibration of optical configuration and image acquisition software parameters (ThermaCAM Researcher Professional) using in-vivo test subject at the Australian Army Health Centre – corresponding to the bimodal output shown Figure 3-11.

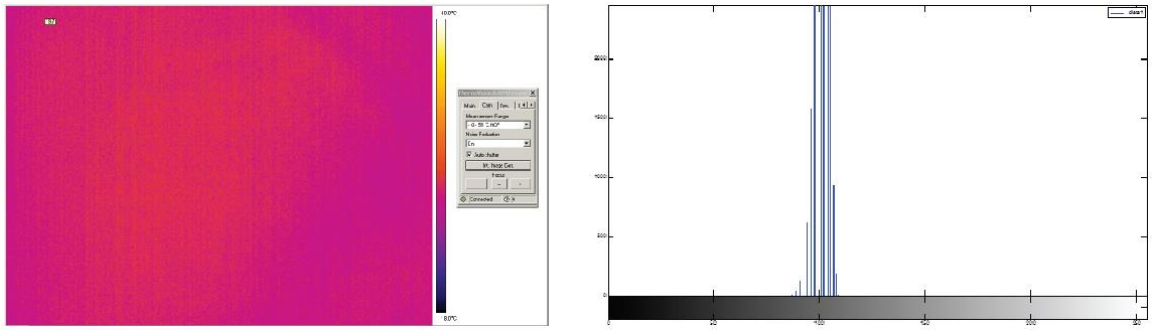

Figure 3-10: Two representations of backing mat emissive uniformity. TIRI shown left, and corresponding histogram shown right.

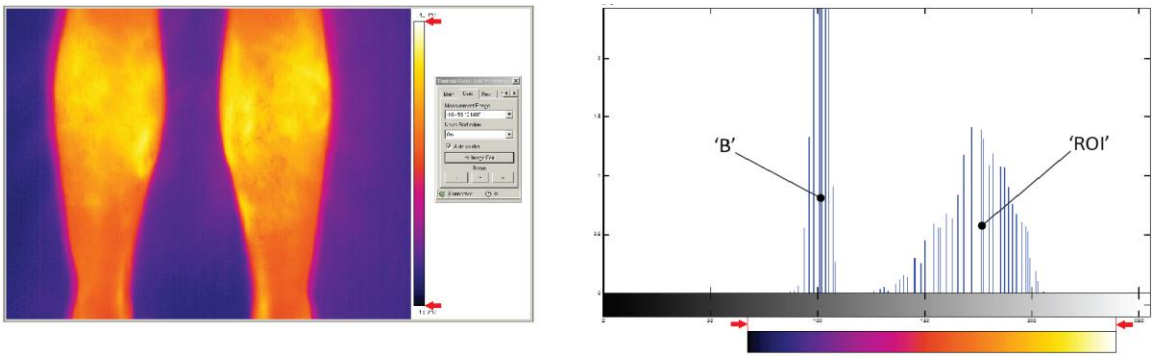

Figure 3-11: Left; TIRI showing uniform background and variable ROI (lower legs) foreground. Right; corresponding 0-255 greylevel histogram of TIRI shown left, illustrating quintessential bimodality of the clinical data, and correspondence to false colour scale.

In the case of the clinical TIRI data where, by design, ROI intensities are always greater than those of the background; pixels exhibiting levels greater than 'k' are classified as 'ROI', with all others classified as background 'B', Figure 3-11. In order to identify the greylevel threshold that yields greatest classification efficacy 'k*', Otsu's first evaluates the zeroth and first order cumulative moments of the TIRI's normalised histogram, (ω and μ values). Firstly, the probabilities of background class 'ω_B', and ROI class occurrence 'ω_{ROI}' occurrences are given by **(4.2)** and **(3.3)**, respectively.

$$\omega_B = \sum_{i=1}^{k} p_i = \omega(k) \qquad \textbf{(3.2)}$$

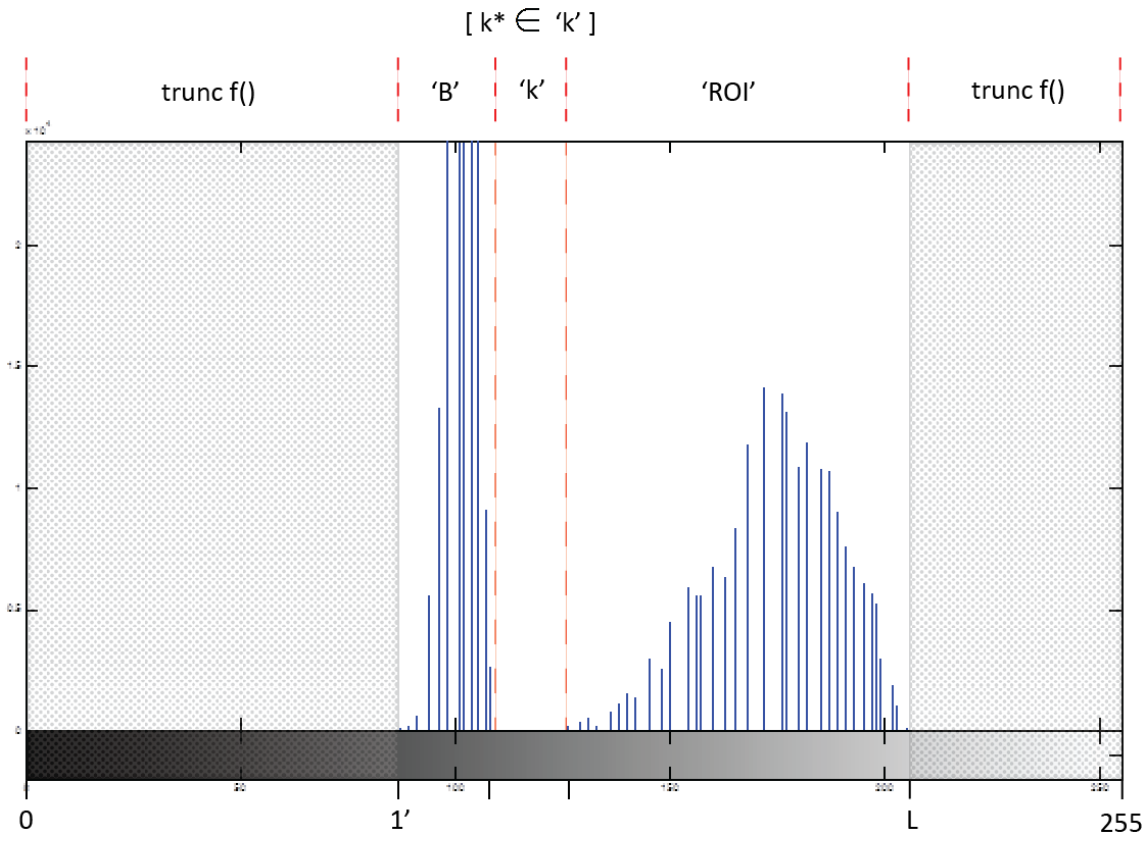

Figure 3-12: TIRI histogram for threshold selection algorithm, with; truncation of vacant grey levels from extrema, background signal 'B', threshold search space 'k', and tissue signal 'ROI'. Surface temperature of chroma key mat is kept below human euthermia to provide clear contrast and facilitate segmentation (width of region 'k' corresponds to ROI-B temperature difference), without causing a thermophysiological stimulus to the ROI.

$$\omega_{ROI} = \sum_{i=k+1}^{L} p_i = 1 - \omega(k) \qquad \textbf{(3.3)}$$

Secondly, mean 'μ' grey levels of the 'B' and 'ROI' classes are given by **(3.4)** and **(3.5)**, respectively:

$$\mu_B = \sum_{i=1}^{k} \frac{ip_i}{\omega_B} = \frac{\mu(k)}{\omega(k)} \qquad \textbf{(3.4)}$$

$$\mu_{ROI} = \sum_{i=k+1}^{L} \frac{ip_i}{\omega_{ROI}} = \frac{\mu_{ROI} - \mu(k)}{1 - \omega(k)} \qquad \textbf{(3.5)}$$

Evaluation of those moments described in **(3.3)** to **(3.5)** allows expression of interclass variance 'σ²', as in **(3.6)**. The greylevel 'k' that yields greatest interclass variance is identified as the optimal threshold 'k*', as in **(3.7)**. This scheme follows Otsu's conjecture that well thresheld classes are well separated in the greylevel domain, and thus, the greylevel 'k' that yields best class separation is identified as the optimum threshold level 'k*', as expressed in **(3.6)**.

$$\sigma^2 = \omega_B \omega_{ROI} (\mu_{ROI} - \mu_B)^2 \qquad \textbf{(3.6)}$$

$$\sigma^2(k^*) = \max_{1 \le k < L} [\sigma^2(k)] \qquad \textbf{(3.7)}$$

As follows, this conjecture holds true with the subjective clinical TIRI dataset (Arthur et al., 2011a). Clinical image acquisition (and processing) protocols that facilitate isolation of pixels corresponding to the ROI / pathoanatomic context have great utility in both classifier-based and advanced physics-based modes of human TIRI.

1.14 Atmospheric Control

As mentioned in the previous chapter, the ambient clinical image-acquisition atmosphere can be characterised as: an optical medium for interacting TIR signals, a source of TIR noise, and a set of thermophysiological stimuli to the tissue volume of interest (Arthur & Khan, 2011d). As atmospheric control gives little scope for favourable alteration of transmittance or emittance (as pertinent to optical medium and noise source characterisations), atmospheric control protocols are designed for optimal thermophysiological effects. Although characterisation of the atmosphere as a physiological stimulus is considered a critical and underdeveloped aspect of clinical TIRI research, it is desirable in this case to foster thermoneutral conditions within

which thermoregulation is actuated almost solely by peripheral vasomotion, with extremely limited perspiration, no shivering, and minimal catabolic thermogenesis (Borten et al., 1984; Roy et al., 2006; Zaproudina et al., 2008). Recent approaches to identifying subjectively thermoneutral conditions via multi-node models of human thermoregulatory response to a wide range of steady and transient boundary conditions have arrived at the thermoneutral conditions shown in Table 3-1 (Arthur & Khan, 2011d; Fiala, Lomas, & Stohrer, 2001; Fiala et al., 2010).

Table 3-1. Thermoneutral environmental conditions for human thermoregulatory response as per ANSYS CFX CFD model of flow and heat-transfer of air within a controlled indoor environment. Where: T_{air}, = ambient air temperature, T_{sr} = temperature of surrounding surfaces, V_{air} = ambient air velocity, Rh = relative humidity; ϵ_w, = average spectral emissivity of surrounding wall surfaces, act_{bas} = coefficient of metabolism due to physical exertion (Fiala et al., 2001; Fiala et al., 2010).

T_{air}, °C	T_{sr}, °C	V_{air}, m/s	Rh, %	ϵ_{wall},	act_{bas}, met
30.0	30.0	0.05	0.4	0.93	0.8

In summary, this chapter builds on the generic infrared characterisation of the clinical setting provided in chapter 3 to develop specific clinical protocols for a TIRI study into osseous stress pathology (OSP) in the tibiae of an Australian basic trainee population. Detailed investigations with the Australian Defence Science and Technology Organisation into pathophysiology and anatomy informed specific design decisions surrounding optical configuration and environmental control, which culminated in a detailed clinical TIRI protocol. The following chapter describes how this protocol was implemented at the Australian Army Health Centre to evaluate the protocol in a real clinical setting and collect valuable empirical data.

CHAPTER 5

IMPLEMENTATION OF CLINICAL TIRI PROTOCOL

CHAPTER SUMMARY

This chapter gives a detailed account of how the TIRI protocol designed in Chapter 4 was implemented over 3 months at an Australian Army Hospital, to evaluate performance of the protocol in a real clinical setting, and produce a dataset of more than 500 TIRI's tracking the shins of 120 recruits through basic training. A key finding from this dataset was the normal TIRI profile of a healthy shin, which is an important baseline in any image-based diagnosis. This chapter describes the key features of a normal shin TIRI, and then explains how those features are consistent with lower leg physioanatomy. Another key finding was the high processability of the dataset, which is necessary in cases of abnormal TIRI profiles. This chapter shows how a standard medical image processing routine can be used to extract diagnostically useful information from TIRI data obtained via this protocol. Finally, this chapter discusses opportunities to improve the protocol, and the specific potential of TIRI in diagnosis and management of osseous stress pathology.

Clinical Trial

1.15 Implementation of Protocol 539-10

The data collection methodology used in this three month clinical study was endorsed by: Curtin University Human Research Ethics Committee, the Australian Defence Human Research Ethics Committee, and registered with the Australian New Zealand Clinical Trials Registry - ACTRN12611000623998 (Arthur & Khan, 2011b; M. Khan, 2011). Military basic trainee populations are known for high incidence of tibial stress fractures, due to the sudden increase in high impact physical activity experienced by the recruits. For this reason, and given alignment with the strategic medical technology

capability goals of the DSTO (Australian Defence Science & Technology Organisation), the study was conducted at the ARTC (Asutralian Army Recruit Training Centre), Kapooka NSW. Upon arrival at the Australian Army Recruit Training Centre, three platoons of basic trainees consisting of 56, 48, and 43 recruits were given a comprehensive plain-language study briefing, and allowed 24 hours to anonymously deposit consent forms featuring medical questions pertinent to contraindication of TIRI into a sensitively located ballot box, Figure 0-1 (M. Khan, 2011).

Ethical considerations and participant safeguards are detailed in the full protocols included in appendices. Consenting participants were first thermally imaged during their initial inoculation parade, occurring prior to their first physical training session. Thermal infrared images were acquired prior to administration of any vaccines to avoid vasoactive artifacts (Arthur et al., 2011b). In absence of data pertinent to optimal conditions for pre-TIRI equilibration, participants remained seated, clad in loose fitting gym shorts and T-shirts, without shoes or socks, for a

Figure 0-1. Comprehensive plain-language study briefing to prospective participants with Defence Nurse Unit Manager present. Participants (foreground right) remove boots and socks to facilitate thermal equilibration. Optical configuration shown in the central background.

nominal 20-30 minute period, in a room with ambient conditions as listed in previous chapter.

During equilibration (prior to image acquisition) each participant's legs were visually photographed to screen potentially contraindicative superficial lesions. Following equilibration, patients lay stationary supine upon an unarticulated/flat LINAK OpenBus™ hospital bed, for no less than 3 minutes prior to image acquisition. Several 2cm thick dark grey matt-finish chroma-key mats were kept in redundancy, equilibrating on rotation to 20°C in an anteroom and used as a backing surface between the bed and each participant to prevent residual thermal artifacts from previous participants. An ad-hoc camera mounting system was constructed (Figure 0-1 centre, and Figure 0-2 left) to steadily maintain steady lens to skin-surface distance with the optical axis normal to the patient bed.

In absence of data concerning optimal ambient conditions for image capture, five wall-mounted Daikin FVXS71H ducted inverter units maintained conditions as close to thermoneutral as possible. Pending release of the IEC TC/SC/WG5 specifications for medical grade thermal infrared cameras, data collection was performed with a FLIR A40V ThermoVision™ TIRI camera, used in the configuration

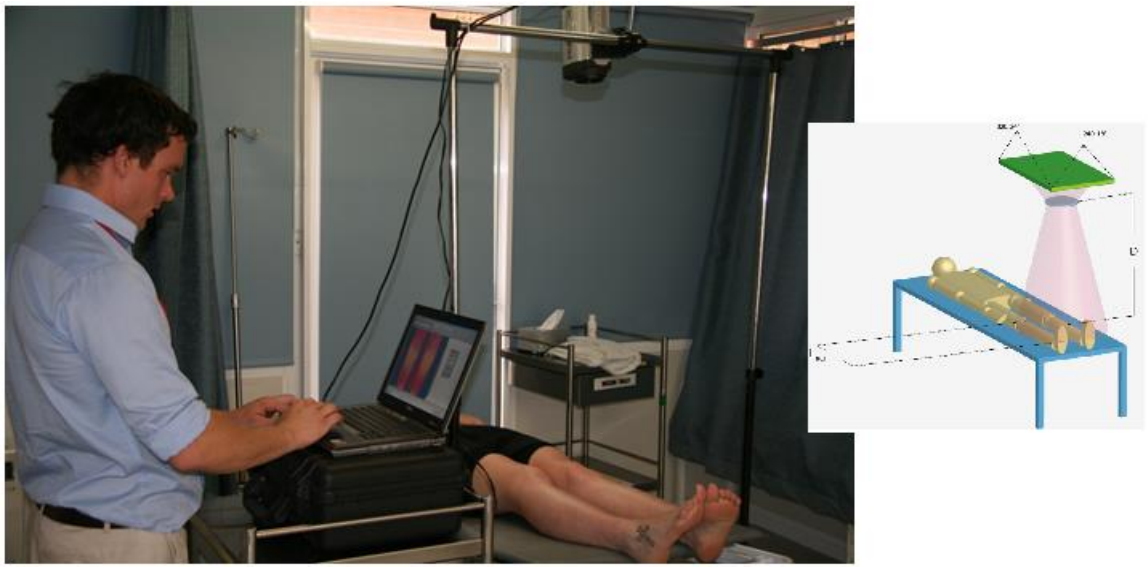

Figure 0-2. Implementing clinical TIRI image acquisition protocol #592-10 to acquire an anterior TIRI of the lower legs of an Australian Army recruit during week one of his basic training at the Australian Army Health Centre, NSW. (Arthur & Khan, 2011b; M. Khan, 2011).

shown in Figure 0-2. The Flir A40V is based around an uncooled array of microbolometer infrared detectors, which can detect temperature changes as small each participant. Participants were thermally imaged via the same protocol on three further occasions during their training continuum; in conjunction with scheduled medical check-up parades in weeks four, seven, and nine (Arthur & Khan, 2011b; M. Khan, 2011).

Any participants presenting consistently with osseous stress injury during the course of the study were withdrawn from physical training and subject to either MRI or nuclear bone scan in accordance with Australian Army SOPs. Additional TIRI's acquired from these symptomatic subjects within the two hour period immediately prior to MRI or bone scan procedures. Both MRI and Nuclear Scintigram (aka 'bone scan') image data were de-identified before use in comparison / validation of TIRI data. Subjects diagnosed with 'debilitating stress fracture' were sent home for 6 weeks of convalescent leave.

Table 2. Ambient clinical conditions during TIRI image acquisition (Arthur et al., 2011b).

	Thermoneutral	Experimental	Reference
Air Temperature	30°C	28°C ± 1°C	Vaisala HUMICAP® HM34
Relative Humidity	40%	46% ± 3%	Vaisala HUMICAP® HM34
Wall Emissivity	0.93	0.92-0.96	FLIR A40V®
Wall Temperature	30°C	Not Controlled	N/A
Air Velocity	0.05 m/s	Minimized	Vaisala HUMICAP® HM34
Basal Metabolic Rate	0.8	Minimized	N/A

*Optimal thermoneutral values as calculated via the IESD-Fiala human thermoregulation model with ANSYS CFX indoor environment program (Fiala et al., 2010).

1.16 The Normal Pretibial TIRI – Described and Explained

Among the 474 asymptomatic thermal images obtained, were 116 complete 4-image longitudinal intra-subject TIRI sets taken over the full ten weeks of basic training, allowing longitudinal change detection of emissive profile with a view to pathological staging. Analysis of these asymptomatic images also allowed characterisation of a 'normal' thermal topography for the asymptomatic anterior lower leg (Figure 0-3) with utility potential as a healthy baseline against which to compare potentially abnormal lower-leg TIRI's (Arthur et al., 2011b).

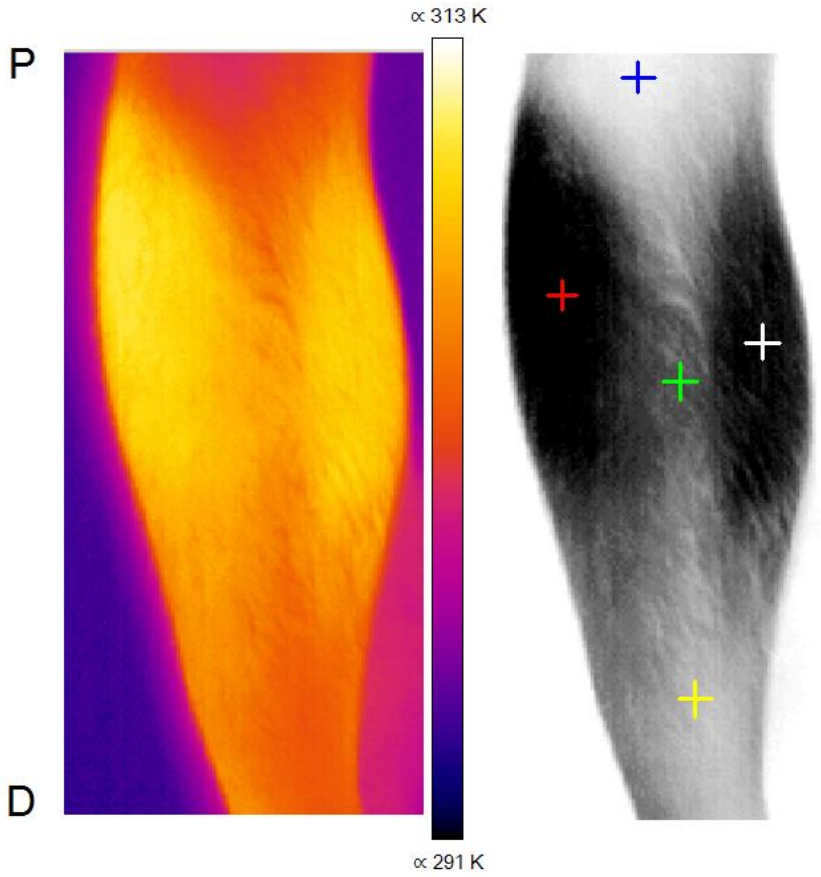

Figure 0-3. Archetypal anteroposterior view of the normal non-pathological 7.5 to 13.0 µm emissive profile of the lower leg, as perceived by TIRI. Left: false-colour TIRI display wherein colour is proportional to TIRI-inferred temperature assuming global greybody emissivity of 0.98, produced within FLIR ThermaCAM Researcher Professional v2.8. Right: partially-processed grey scale TIRI (segmented from chroma-key background and in-ROI image enhancement via histogram stretch), with coloured crosshairs marking the centroids of emissively distinct regions corresponding to thermophysically distinct underlying tissues.

Table 0-3. Thermal Characteristics of the Normal Shin TIRI.

n = 474	Mean	Mode	Standard Deviation	
Є = 0.98			Inter-subject	Intra-subject
Temp Max	31.0 °C	31.2 °C	0.6 °C	0.25 °C
Temp Min	28.0 °C	28.2 °C	0.4 °C	0.11°C

***Typical loci of maxima and minima indicated by the red and blue crosshairs in Figure 0-3 respectively.**

As with all medical imaging modalities (whether morphological or physiological) knowledge of normal healthy appearance is crucial. The apparent characteristic features of this 'normal / asymptomatic profile' correspond to the thermophysiology of the underlying anatomy Figure 0-4. As shown Figure 0-4, it was found helpful to characterise the healthy TIR profile as comprised of 5 emissively distinct regions. The blue crosshair in Figure 0-3 right marks the centroid of the funnel-shaped proximal region, most commonly found to be the site of least LWIR emittance (Arthur et al., 2011b).

As shown Figure 0-3, this coldest blue region overlies no thermogenic anatomy, is distal to the thermogenic muscle compartments, and as shown Figure 0-5, features the thickest layer of avascular interstitial osteocutaneous tissue (≈ 3.5 mm), supposedly insulating / attenuating the subsurface thermal profile from the TIRI-perceptible surface. The second row of Table 2 characterizes the average quantitative thermal characteristics of this region, as calculated from a dataset of 474 TIRI's acquired over a period of 3 months.

The red crosshair in Figure 0-3 marks the centroid of the almond-shaped lateral region, from which emittance is typically at a maximum. As shown in blue in Figure 0-4, this lateral region overlies the compartment of the highly thermogenic tibialis anterior muscle. Similarly, the white crosshair Figure 0-3, and the red regions in Figure 0-4 correspond to the thermogenic superficial posterior muscles. Figure 0-5 illustrates

the distal-proximal increasing gradients of both thickness and lipid concentration in pretibial tissue volumes. The green crosshair in Figure 0-3

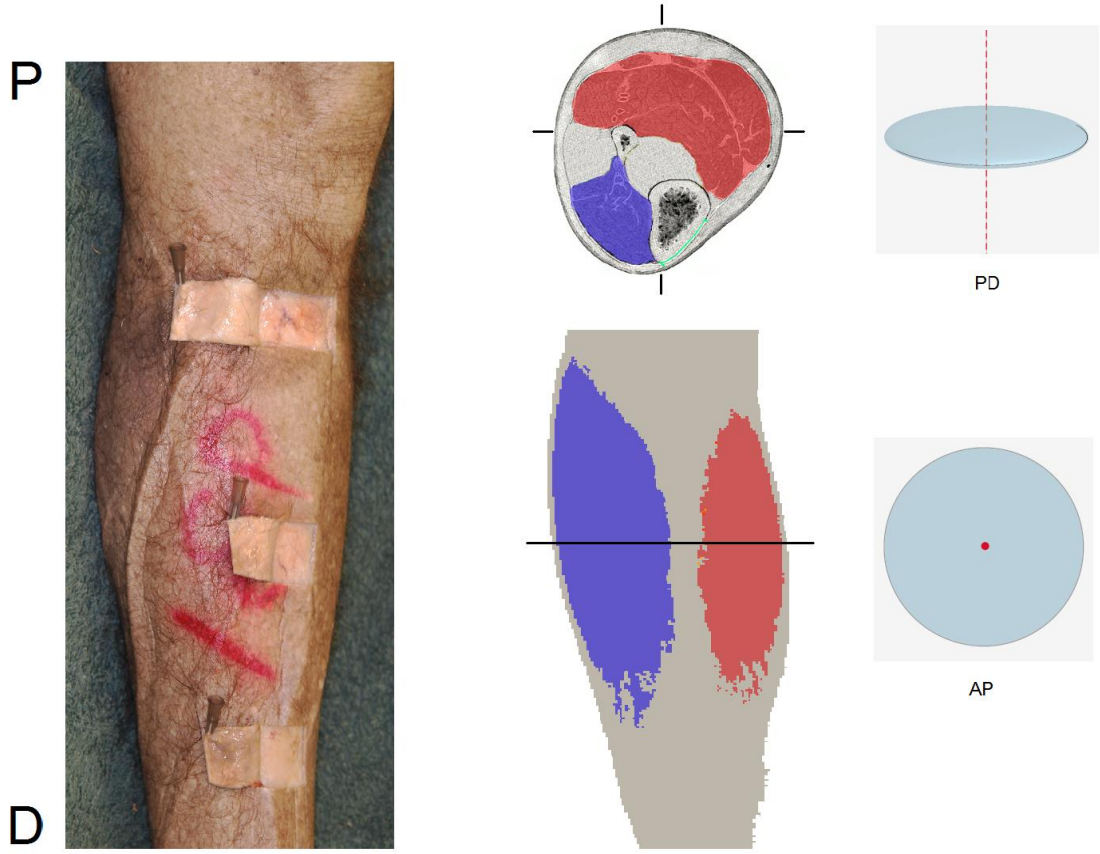

Figure 0-4. Anatomic explanation of 'normal' shin TIRI. Left: avascular interstitial tissue volumes, with P-D decrease in thickness and lipid content. Centre: anterior muscle compartment (blue), superficial posterior compartment (red).

corresponds to the area overlying an avascular osteocutaneous volume of medium thickness, bounded by both aforementioned thermogenic muscle compartments.

The yellow crosshair marks the region overlying the thinnest avascular volume of osteocutaneous tissue, most distal to thermogenic anatomy. Figure 0-5 provides a magnified view of the three osteocutaneous tissue volumes excised from the cadaveric specimen shown Figure 0-4 Left. Although all three volumes are avascular and thermophysically homogeneous, and without thermogenic anatomy; there are clear increases in both interstitial tissue thickness and lipid concentration from distal to

proximal – these gradients intuitively correspond to the healthy / asymptomatic AP profile shown Figure 0-3.

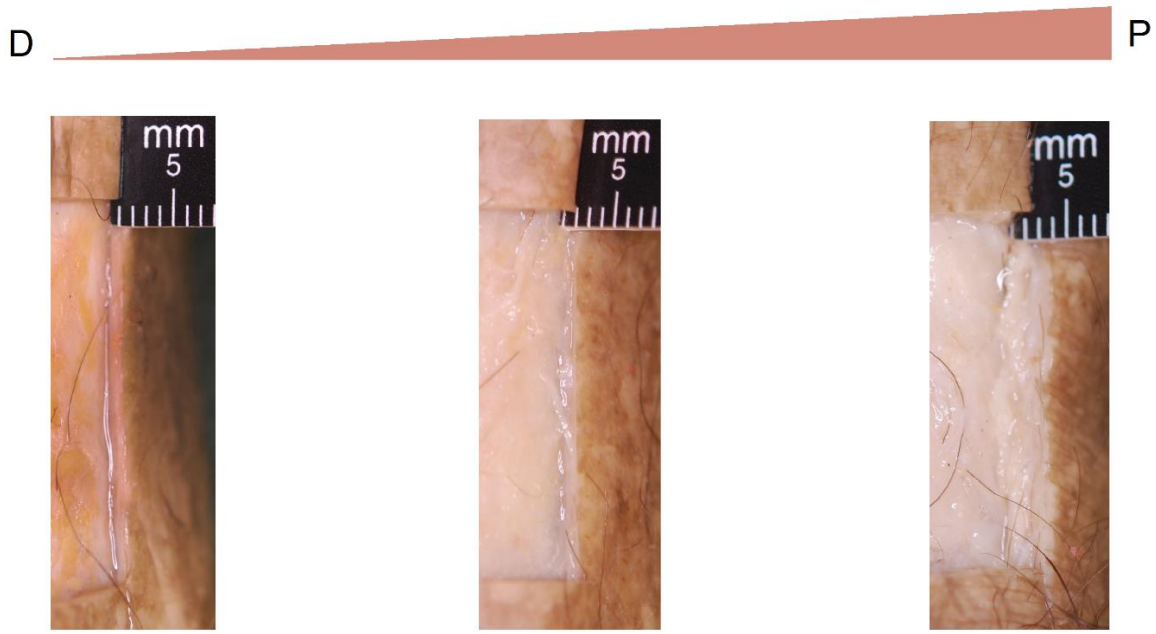

Figure 0-5. Magnified view of the three pretibial tissue volumes excised from the cadaveric specimen shown Figure 0-4 Left. Although all three volumes are avascular and thermophysically homogeneous, and without thermogenic anatomy; there are clear increases in both interstitial tissue thickness and lipid concentration from distal to proximal (D-P) – these gradients intuitively correspond to the asymptomatic AP profile shown Figure 0-3.

1.17 Processability of TIRI Data

In addition to description and explanation of the 'normal' TIRI shin profile, the 116 complete four-image longitudinal intra-subject TIRI sets (taken over the full ten weeks of basic training) were subject to an image processing routine designed to investigate the feasibility of staging osseous stress pathology via change detection over time, Figure 0-6. The clinical TIRI data collection protocols were intentionally designed to facilitate this subsequent extraction of clinically useful information from image data obtained. An example of this integrated experimental design and data processing is

highlighted in the first stage of the image processing routine shown Figure 0-6, where inclusion of chroma-key backing mats in the image acquisition protocol enables segmentation and inter-temporal calibration of image data during subsequent analysis stages.

The full image processing routine applied to the data obtained with the protocol is described in Figure 0-6. The image processing routine was designed to include all the basic processing steps used in standard medical image processing, namely; segmentation, quantitative calibration (in this case calibration of temperature), enhancement of ROI, identification of interest points, helpful description of interest points, and finally subtraction of subsequent images in a series to reveal change over time. This routine is particularly suited to the tracking / staging of osseous stress pathology over the course of basic training, and produced results (shown Figure 0-15) which are consistent with clinical theory, highlighting the area directly over the tibia as the area of most change during the course of basic training.

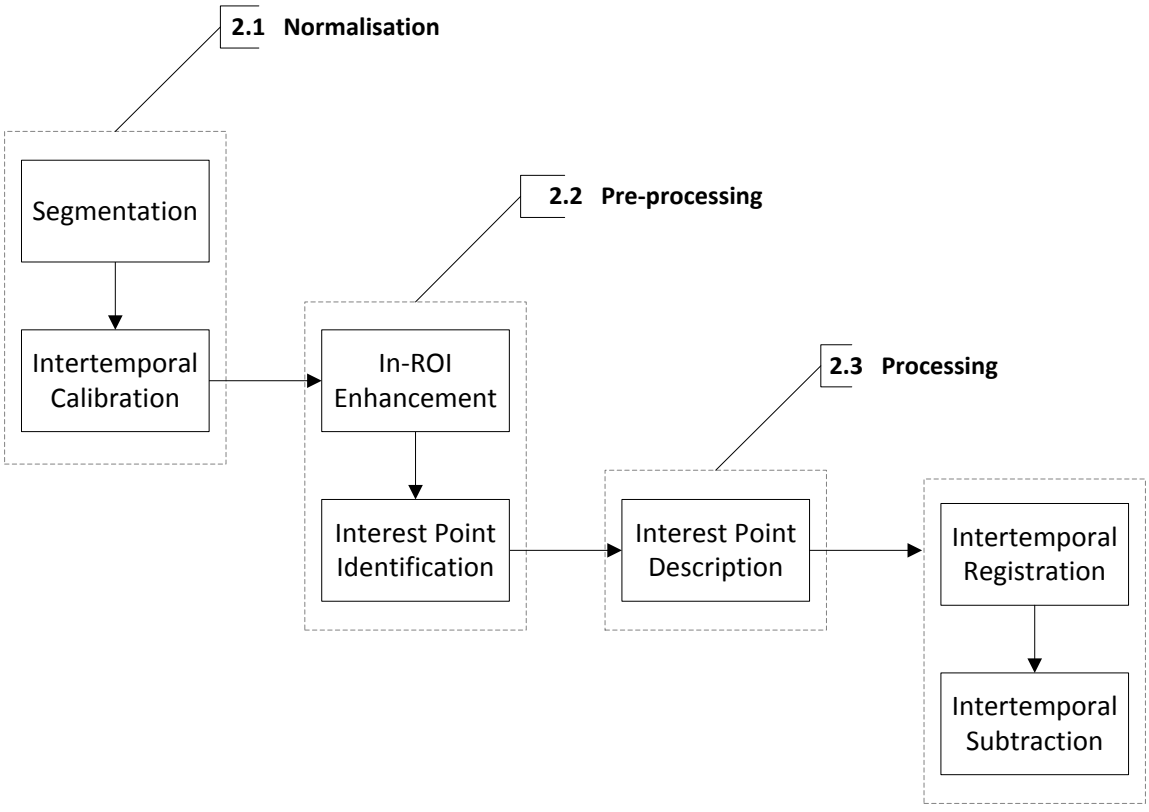

Figure 0-6. Image processing routine designed to explicate the feasibility of staging osseous stress pathology via TIRI-based temporal change detection. This routine was used to process four-image longitudinal data sets taken over the course of Australian Army basic training (Arthur et al., 2011a).

1.17.1 Segmenting TIRI Images

Segmentation is the process of partitioning an image into discrete sets of pixels that represent a specific part of the physical system being analysed. In medical imaging, segmentation usually involves partitioning an image into 'the human body' and 'the background', or partitioning discrete tissues within the imaged body part. In this clinical TIRI application, the TIRI image data is being segmented into 'the human body' and 'the background', so that subsequent image processing efforts can be focussed on the human body part of the image. The optical configuration and protocols used produced a dataset of bimodal images such as that in Figure 0-7, enabling effective segmentation via the threshold selection method (Arthur et al., 2011a; Otsu, 1979).

The thresholding algorithm described in Figure 0-7was implemented in Matlab 2011a, using 2D-array intensity image data and intra-class variance

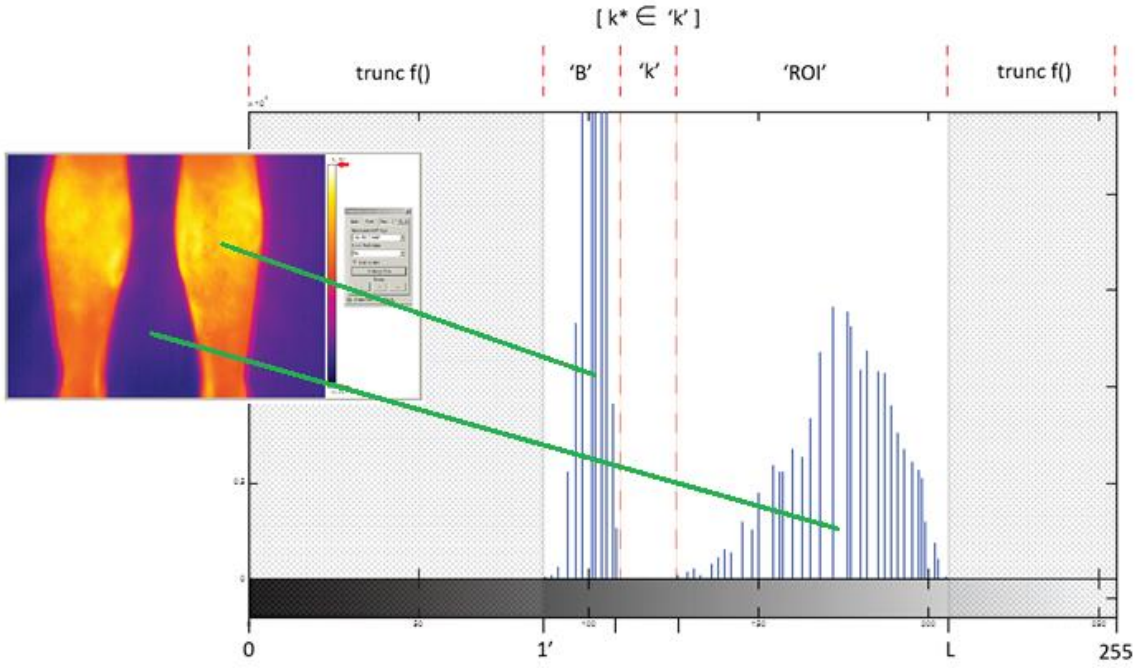

Figure 0-7. Left: false colour scale TIRI featuring uniform backing-mat background and variable ROI (lower legs) foreground. Right; corresponding 0-255 greylevel histogram regions pertinent to action of threshold selection algorithm upon clinical data, with; truncation of vacant grey levels from extrema, background signal 'B', threshold search space 'k', and tissue signal 'ROI'.

(equivalent to maximisation of interclass variance σ^2, as in Figure 0-7 right) as inputs, and outputting a normalised intensity value of 'k*' in the range [0, 1] (Figure 0-8 centre). The algorithm then takes the greyscale TIRI and 'k*' threshold level [0, 1] as two inputs, assigns a greylevel of 255 (white) to all pixels of the input image exhibiting exceeding the threshold, assigns greylevel 0 (black) to all other pixels, then outputs the resulting logical class (binary) image (Figure 0-8 right). When implemented as in Figure 0-8, input of a greyscale TIRI yields output of binary masks corresponding to the ROI and background, (code in appendix A.).

1.17.2 Time Series Image Calibration

As described in Protocol #592-10, recruits were imaged during weeks 1, 4, 7, and 9 of their basic training courses. Quantitative changes in tibial pathology over time translate to changes in; temperature, infrared emittance, and ultimately grey level in a TIRI. Quantitative detection of these time series changes requires inter-image calibration. As mentioned, the backing mats used during clinical image acquisition featured uniform emissivity across their entire surface, and were maintained at constant temperature during all imaging sessions. Actual 'background emittance' ($Wm^{-2}\mu m^{-1}$) was thus assumed to be equal in all images, and used as the

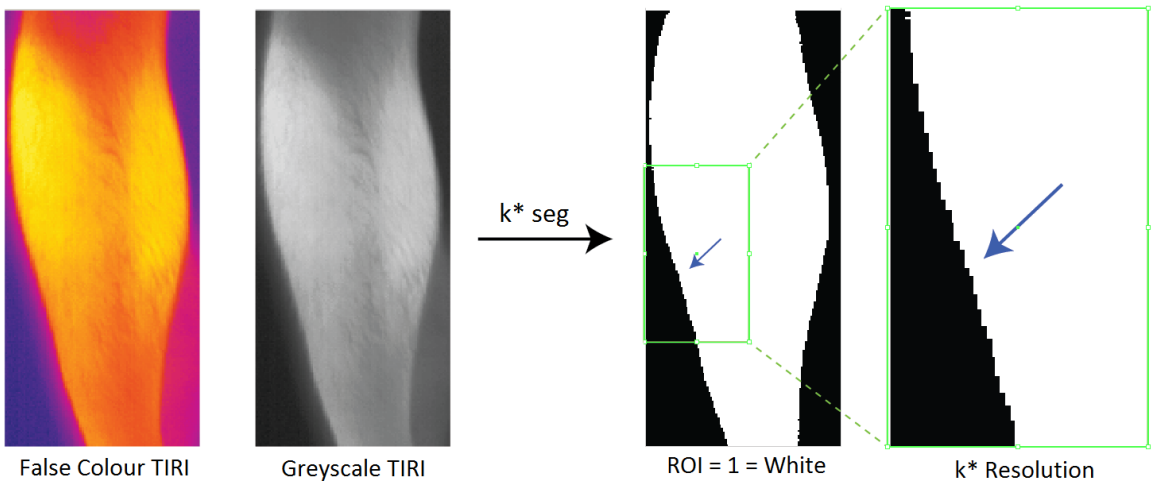

Figure 0-8: Visualisation of 'threshold selection' segmentation process. Image far right showing typical resolution achieved in clinical TIRI's, despite significant corona as shown in 'False Colour TIRI', far left.

basis/ground truth for cross-time-series image calibration. Following Figure 0-7 The mean greylevel value 'μ_B' of each TIRI's background region 'B' is readily available. These 'μ_B' values were used as the basis for evaluation of the global calibration offset to be applied to each TIRI (apart from the first in series), as illustrated Figure 0-9.

1.17.3 In-ROI Contrast Enhancement

During clinical image acquisition, the TIRI system is set to detect emittance in a range closely encompassing ROI characteristic variation, corresponding to 'L' different grey levels in the range [1', L]. Following segmentation and subsequent masking of the background to a greylevel of zero; the variance of each TIRI's histogram in a multitemporal set was expressed as a fraction of that of the widest

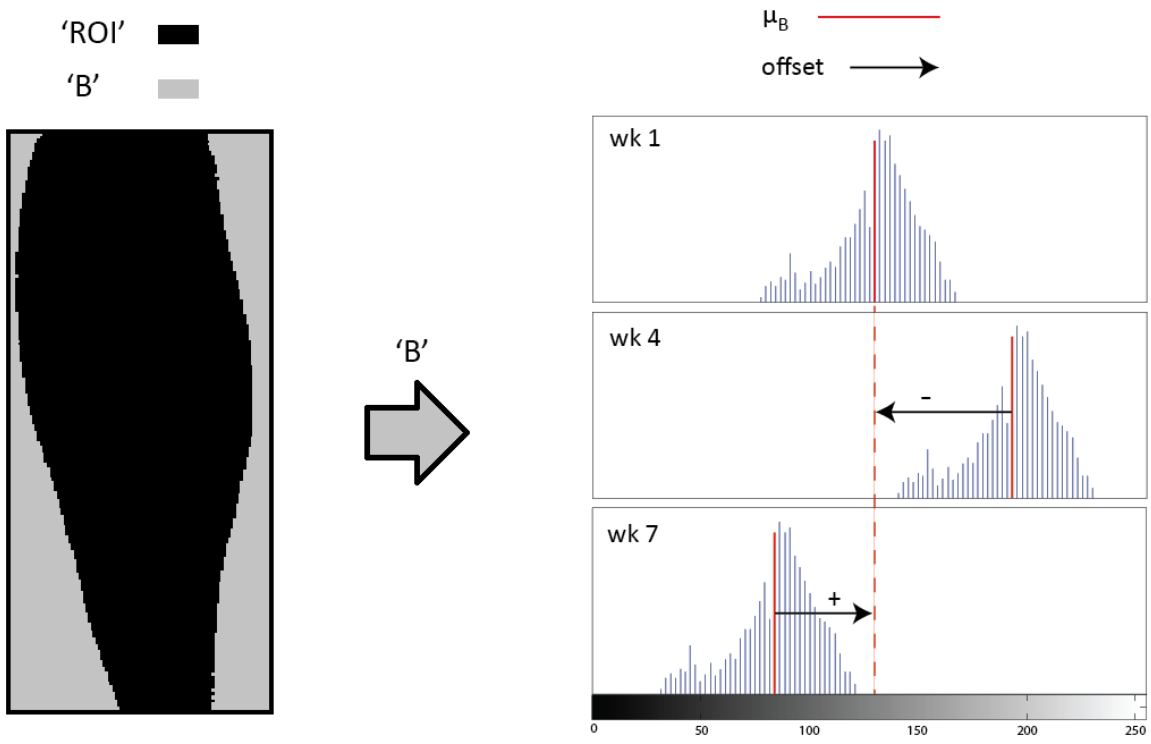

Figure 0-9. Intertemporal image calibration via global linear greylevel offset making all background regions have the same greylevel. As the backing mats have demonstrated uniform emissivity across their surfaces and their surface temperatures were maintained at a constant value throughout the study, they constitute a valid and helpful ground truth for calibration (Arthur et al., 2011a, 2011b).

histogram in that set (Arthur et al., 2011a, 2011b). This fraction was then used as a coefficient for a linear contrast stretch over all greylevels except 0, which remains occupied by the masked background, Figure 0-10. Following this *selective* normalization operation, each image was subject to contrast-limited adaptive histogram equalization (CLAHE). The CLAHE operates on small regions in the TIRI, called 'tiles', rather than the entire image. Each tile's contrast is enhanced, such that the histogram of the output region approximately matches a user-defined histogram. The neighbouring tiles are then combined using bilinear interpolation to eliminate artificially induced boundaries. Contrast in homogeneous areas was limited to avoid amplification of noise (Arthur et al., 2011a).

1.17.1 Interest Point Identification

The interest point identification process is a search for correspondences in discrete TIRI's, as the initial phase in the registration process. The most valuable property of

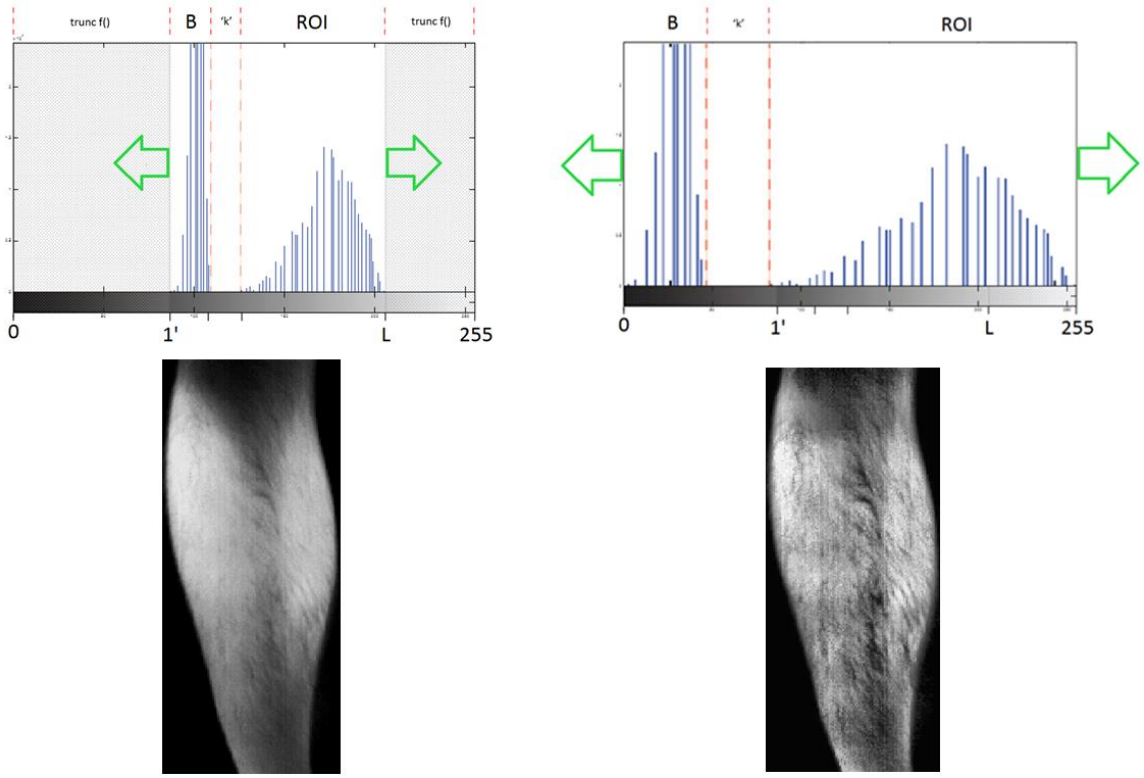

Figure 0-10. Illustration of selective normalisation operation for within-ROI contrast stretching of 'L' different grey levels in the range [1', L], to occupy greylevels [1-255].

an interest point detector is its repeatability, i.e. whether it reliably finds the same interest points under different viewing conditions. Given the nature of the image acquisition process, interest points in the 592-10 TIRI's were detected using OpenSURF's variant of the SURF fast Hessian detector, with excellent illumination and rotation invariance (Evans, 2011). The fast Hessian reduces computational expense in interest point detection via box-filter approximation (Figure 0-11, right) of the Hessian's discriminant via the Laplacian of Gaussians (Evans, 2011; Gossow, Decker, & Paulus, 2011).

Figure 0-12 illustrates application of the detector to a pre-processed sample TIRI from the 592-10 database (left), with circle-bounded interest points superimposed (right) (Arthur et al., 2011a). Rather than using a different measure for selecting the location and the scale (as in the Hessian-Laplace detector (Bay, Ess, Tuytelaars, & Van-Gool, 2008)), SURF uses the determinant of the Hessian for both for both (Bay, Ess, Tuytelaars, & Van-Gool, 2008). Given a point **x** = (x, y) in an image 'I', the Hessian matrix H(x, σ) in **x** at scale σ is defined as **(0.1)**, Where L_{xx} (x, σ) is the convolution of the Gaussian second order derivative **(0.2)**, of the image I at point **x**, and similarly for L_{xy} (x, σ) and L_{yy} (x, σ) (Arthur et al., 2011a).

Rather than using a different measure for selecting the location and the scale (as in the Hessian-Laplace detector (Bay, Ess, Tuytelaars, & Van-Gool, 2008)), SURF uses the determinant of the Hessian for both. Given a point **x** = (x, y) in an image 'I', the Hessian matrix H(x, σ) in **x** at scale σ is defined as in **(0.1)**, Where L_{xx} (x, σ) is the convolution of the Gaussian second order derivative **(0.2)**, of the image I

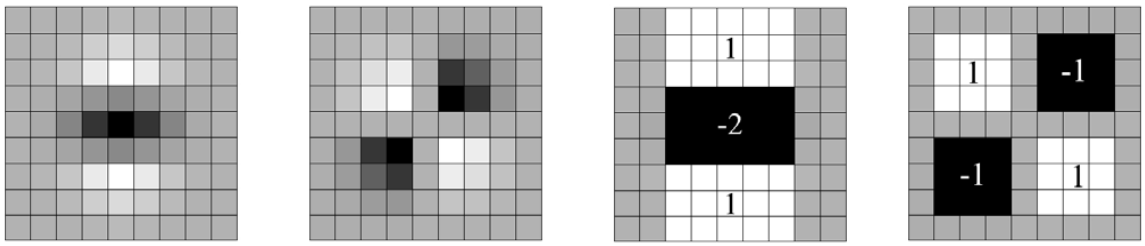

Figure 0-11 Left: discretised and cropped Gaussian second order partial derivatives in y-direction and xy-direction, and right; 9x9 box-filter approximations of the Gaussian second order derivatives (0.2 **) where 9x9 corresponds to a σ value of 1.2, as used in processing of the 592-10 TIRI database. The grey regions are equal to zero. Adapted from (Gossow et al., 2011).**

at point **x**, and similarly for L_{xy} (x, σ) and L_{yy} (x, σ) (Arthur et al., 2011a).

$$H(x,\sigma) = \begin{bmatrix} L_{xx}(x,\sigma) & L_{xy}(x,\sigma) \\ L_{xy}(x,\sigma) & L_{yy}(x,\sigma) \end{bmatrix} \qquad \textbf{(0.1)}$$

$$\frac{\partial^2}{\partial x^2} g(\sigma) \qquad \textbf{(0.2)}$$

Although Gaussians are optimal for scale-space analysis, in practice they must be discretised and cropped (Figure 0-11 ,left), and induce aliasing upon sub-sampling of the resultant images, Figure 0-12 centre. The 9 × 9 box filters in Figure 0-11 far right, are approximations of Gaussian second order derivatives, with σ = 1.2, which

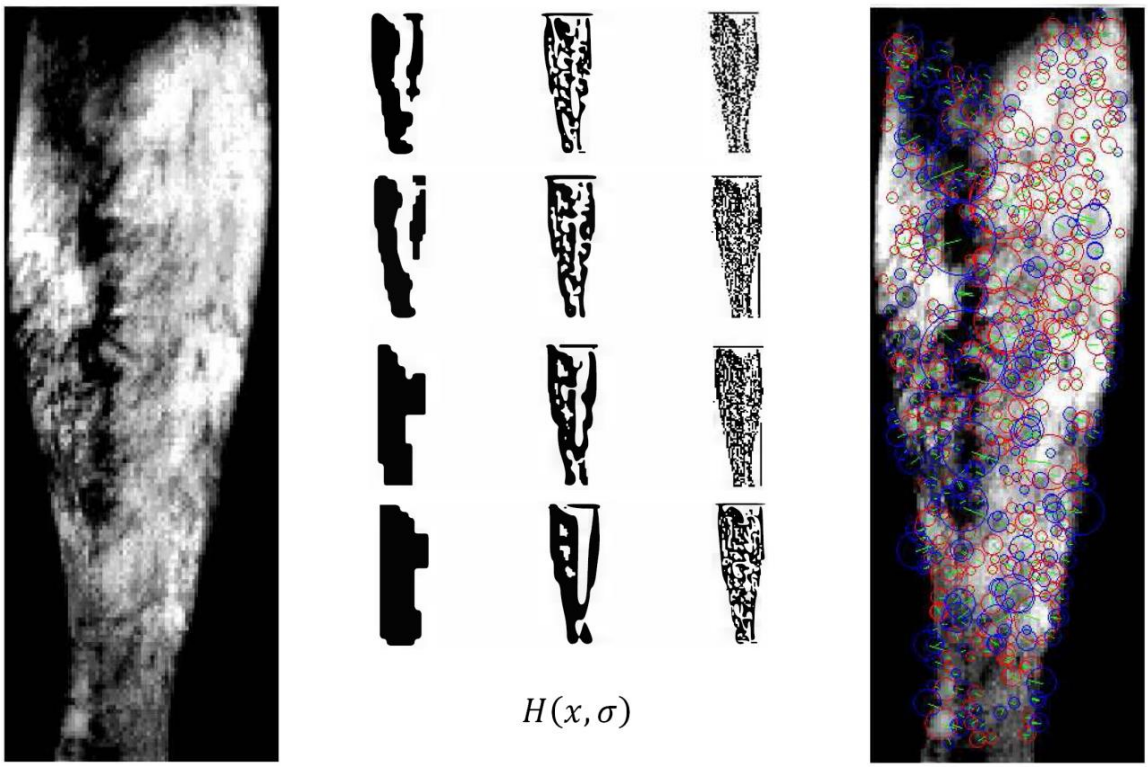

Figure 0-12. Fast Hessian interest point detector. Left; lower limb following pre-processing, Centre; staged convolution through to interest point detection, Right; superimposition of detected interest points on the original TIRI. Interest points lie at centre of circular regions from which their descriptors are subsequently extracted; green radial lines define reference abscissa from which the descriptor wavelets operate, Figure 0-13. (Arthur et al., 2011a).

corresponds to the spatial resolution used in processing of the 592-10 images. Dxx, Dyy, and Dxy denote approximations. Weights applied to the rectangular regions are kept simple for computational efficiency, using the 0.9 derived in **(0.3)**, to balance the relative weights in the expression for the Hessian's determinant,
(0.4) where |x|F is the Frobenius norm:

$$\frac{|L_{xy}(1.2)|F|D_{xx}(9)|F}{|L_{xx}(1.2)|F|D_{xy}(9)|F} = 0.912 \simeq 0.9 \qquad \textbf{(0.3)}$$

$$\det(H_{approx}) = D_{xx}D_{yy} - (0.9D_{xy})^2 \qquad \textbf{(0.4)}$$

1.17.2 Interest Point Characterisation

Once detected, interest points are characterized via local distribution, as classified by Haar wavelets, Figure 0-13. A sub-region's descriptor represents the nature of the underlying intensity pattern. In Figure 0-13 left, in the case of a homogeneous region, all values are relatively low. Figure 0-13 centre; in presence of frequencies in the x direction, the value of Idxl is high, whilst dx, dy, and |dy| remain low. Where intensity increases gradually in the x direction, both values dx and Idxl are high. Hence, each sub-region has a four-dimensional descriptor vector **v** for its underlying intensity structure. This results in a descriptor vector for all 4 x 4 sub-regions of length 64.

The wavelet responses are invariant to a bias in illumination (offset). Invariance to contrast (a scale factor) is achieved by turning the descriptor into a unit vector (Bay et al., 2008). When applied to the TIRI's, the descriptor's performance improved significantly following segmentation and contrast enhancement (Arthur et al., 2011a). Once interest points in temporally contiguous images are characterized, those of most statistical similarity are assigned to each other in pairs, as shown in Figure 0-14 left.

$$\boldsymbol{V} = \left(\sum dx\,, \sum |dx|\,, \sum dy, \sum |dy|\right) \qquad \textbf{(0.5)}$$

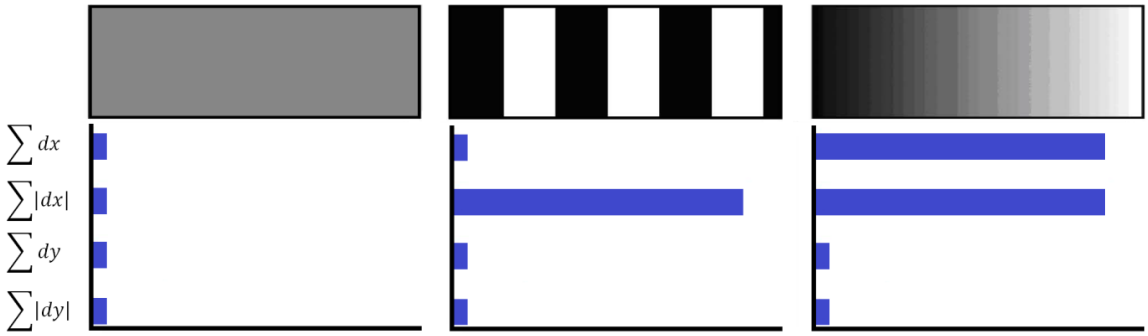

Figure 0-13. Illustration of the way the descriptor characterises each interest point based upon four properties (dx, |dx|, dy, and |dy|). These dimensions are based upon Haar Wavelet sampling.

1.17.3 Image Differencing

Once interest points have been identified and characterized, they can be used as control points in registration, as in Figure 0-14. As shown in Figure 0-14 right 'wk_l_warp', the algorithm provides an excellent warp with minimal distortion to the original. Following such a high fidelity registration, it is meaningful to perform subtractive change detection, as in Figure 0-14 below. Figure 0-14 shows consistency in the site of most emissive change over time; namely, the anteromedial aspect of the tibia. This localization of change conforms to intuitive agreement with current understanding of osseous stress pathophysiology (Goodman et al., 1985; Pascoe et al., 2008; Phillipson & Parker, 2009; Rae, 2010), and the thermophysiology of the underlying anatomy Figure 0-4.

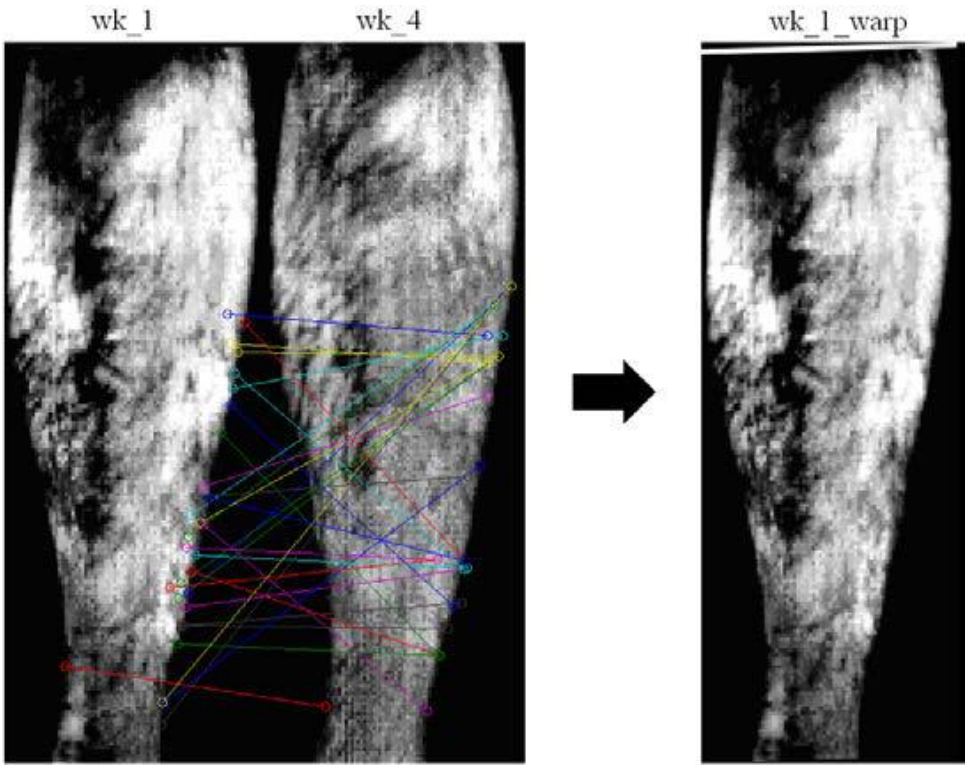

Figure 0-14. OpenSURF-based generation of point correspondences and resultant warp of 'wk_I' image onto a 'wk_4' base image (Arthur et al., 2011a).

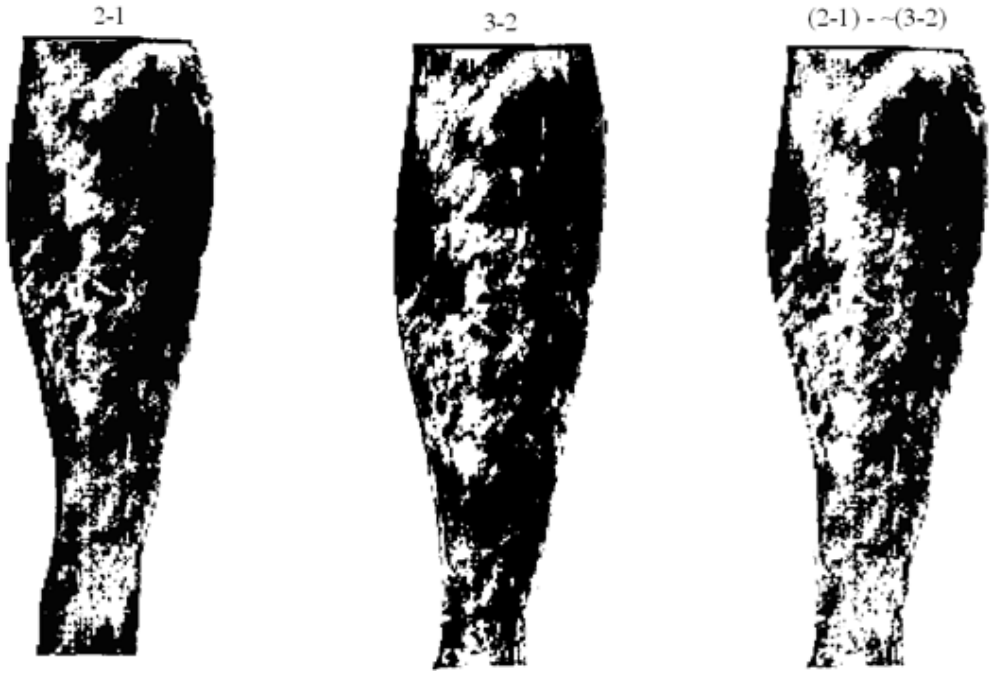

Figure 0-15. Longitudinal difference imaging in a progressing pathological subject (wherein white indicates site of change, black indicates consistency over time), showing a consistent site of emissive change overlying the anteromedial aspect of the tibia (Arthur et al., 2011a).

In summary, this chapter described how the TIRI protocol designed in Chapter 4 was implemented at the Australian Army Training Centre, introduced and explained the normal TIRI profile of a healthy shin, and demonstrated extraction of diagnostic information from TIRI data via standard medical image processing operations. Although this study demonstrates significant potential for TIRI as an initial screening tool for osseous stress pathology, it also highlights the need to explore deeper analyses of clinical TIRI data that have potential to provide high-specificity clinical decision support. The following chapter explores how analysis of clinical TIRI data can be used to determine the depth of subsurface heat sources, such as osseous stress fractures and cancerous tumours.

CHAPTER 6

HEAT SOURCE DEPTH DETERMINATION

CHAPTER SUMMARY

This chapter demonstrates successful practical application of a technique proposed by (Wang et al, 2011) for recovering the depth of a focal heat source within the body from analysis of a TIRI of the overlying skin surface. The first section of this chapter explains the theoretical basis for this technique, and the second accounts successful use of the technique to recover heat source depths from 30 TIRI's obtained in the clinical study described in the previous chapter. In demonstrating this 'quantitative clinical TIRI analysis with greater diagnostic specificity than screening', this chapter satisfies; the need identified in the previous chapter, and a key prerequisite for medical community adoption of TIRI identified by the U.S. Defence TIRI Technology Transfer Study.

4. Determining Depth of Tissue Abnormalities

The clinical significance of heat source depth determination via a non-invasive non-ionising technique like TIRI can be best appreciated in context of oncology, where the

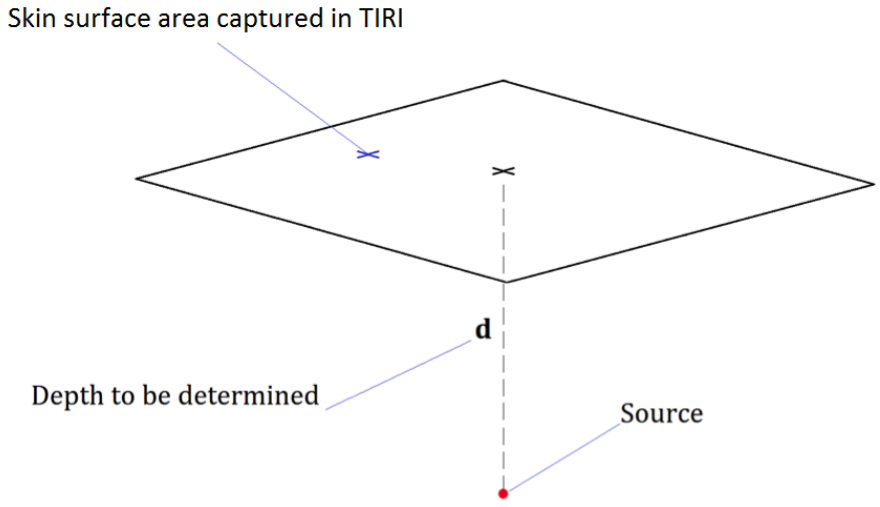

Figure 4-1. The heat source depth determination problem - determine source depth d from skin surface temperature distribution captured in a TIRI.

depth of a focal heat source in the form of a tumour is an established predictor of; primary malignancy, metastasis, appropriateness of resection, probability of upstaging, tumour control performance, and general prognosis. All of these measures provide critical decision support in management of a pathology that seriously affects millions of patients each year. In addition to biopsy, this tumour depth determination is currently performed with MRI, X-Ray CT, and ultrasound; all imaging modalities for which TIRI would be a rapid, low cost, non-contact, and non-ionising alternative.

As represented in Figure 4-1, TIRI-based heat source depth determination (HSDD) is a 3D heat conduction boundary value problem, in which the temperature distribution across the skin surface is the key boundary value that can be found via TIRI, and the problem is to solve for the heat source depth given the heat transfer properties of the source and interstitial tissues. The mathematical tool that enables solution of 3D heat conduction problems is a delta function, which represents the heat source as an idealised point in space, Figure 2. A Dirac delta function is a pulse of infinite magnitude and infinitely short duration, defined as (1.1):

$$\frac{1}{2a}[H(t+a) - H(t-a)] \qquad \textbf{(4.1)}$$

As the width of the pulse tends to zero (a→0), we get (1.2):

$$\delta(t) = \lim_{a \to 0} \frac{1}{2a}[H(t+a) - H(t-a)] \qquad \textbf{(4.2)}$$

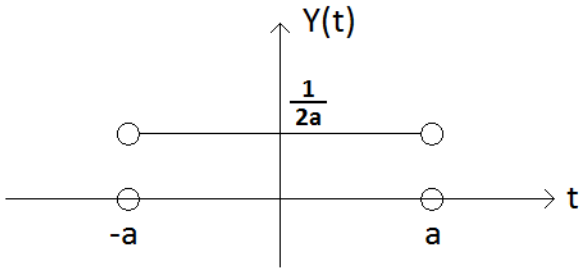

Figure 2. Dirac Delta Function - a pulse of infinite magnitude and infinitely short duration. This mathematical tool critically enables TIRI-based HSDD, representing the heat source as a point.

In standard terms (1.2) is not a function, but a distribution, where a distribution is a generalisation of a function's concepts. By taking the Fourier transform of the pulse, it can be shown that the Fourier transform of the Delta function is identically 1. By putting δ(t) formally through the convolution it can be seen that the delta function behaves like the identity under convolution.

When we use the Dirac delta function to represent the source as a point combined with a practical shape function, the surface temperature distribution captured in the TIRI is considered a convolution of the temperature distribution generated by the point source, with, the practical shape function. Accordingly, the temperature distribution captured within the TIRI must be deconvoluted via Fourier deconvolution scheme, before the source depth can be found from it via a graphical method exploiting the Fourier transform identity suggested by Wang et al, as demonstrated and explained through detailed examples using real clinical TIRI data below.

1.18 Graphic Determination of Heat Source Depth

Development of this algorithm for software implementation and practical application involves the following steps:

1. Define an expression for the temperature distribution seen by TIRI on the skin's surface as a function of: the temperature of a subsurface heat source that is a single point within the tissue, and, the heat transfer properties of the tissue between the heat-source and the skin's surface.
2. Enhance the expression to describe surface temperature distribution as the result of a subsurface heat source with realistic shape and size, as opposed to an idealised point in space.
3. Incorporate a Fourier deconvolution scheme to circumvent the need for a-priori heat source geometry information (Wang et al, 2011).
4. Implement the algorithm in Matlab for evaluation of its performance with real clinical TIRI data.

As mentioned in the description of bioheat transfer through human tissues in chapter 3**,** heat transfer from subsurface sources to the skin's outer surface may be modelled via augmented forms of the heat equation, as expressed in **(4.3)**:

$$\phi c \frac{\partial t}{\partial \tau} + \nabla(-k \nabla t) = Q_v \qquad \textbf{(4.3)}$$

Where Φ**,** c, and k, are the density, heat capacity, and thermal conductivity tensor of the tissue, respectively; t is the temperature of tissue, T is the time variable, and Q_v is the sub-surface heat source (stress fracture / tumour). Using a spherical co-ordinate system, and assuming steady-state heat transfer, isotropic conductivity and a point heat source, **(4.3)** can be expressed as in **(4.4)**:

$$\nabla \cdot \nabla \mathrm{t} = \frac{1}{r^2} \frac{d}{dr}\left(r^2 \frac{dt}{dr}\right) = -\frac{1}{k} Q \cdot \delta(r) \qquad \textbf{(4.4)}$$

where δ(r) is the Dirac delta function of the heat source's radius, which is used to represent the sub-surface heat source as an idealized point mass. When r ≠ 0, **(4.4)** can be expressed more simply as in **(4.5)**,

$$\frac{1}{r^2} \frac{d}{dr}\left(r^2 \frac{dt}{dr}\right) = 0 \qquad \textbf{(4.5)}$$

Solution to **(4.5)** for t looks like **(4.6)**, where C1 and C2 are constants (*evaluated below*)We now think of the heat source as a small sphere 'Ω' with radius □ (□ → 0^+), centered at point O, as shown in Figure 4-3.

$$t = -\frac{C_1}{r} + C_2 \qquad \textbf{(4.6)}$$

of **(4.4)** over V (volume of the heat source), and substitute a value of t (temperature at a point on the skin's surface obtained from **(4.6)**, gives **(4.7)** where dV is the element volume of sphere **(4.6)**, gives **(4.7)** where dV is the element volume of

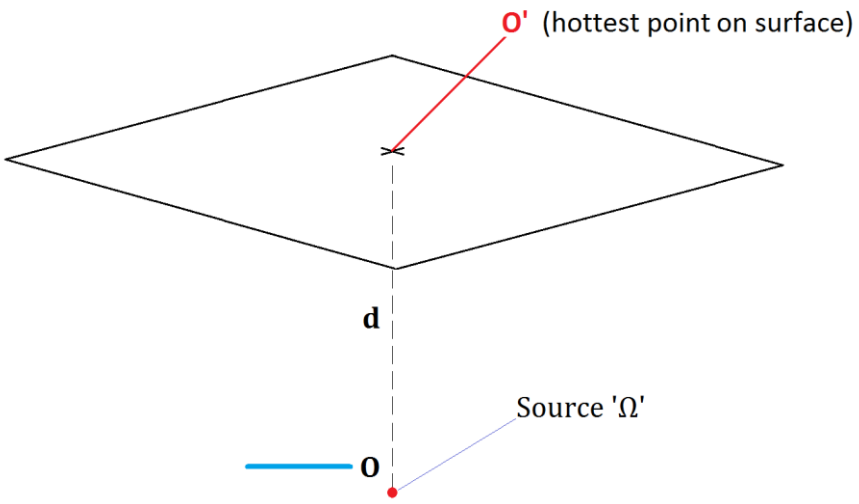

Figure 4-3. Representing the heat source as an infinitesimal red sphere 'Ω' located at point 'O'.

sphere Ω, and Σ is the outer boundary of the closed domain Ω, rearranged to make C1 the subject, as in **Error! Reference source not found.**:

$$\iiint_{\Omega} (\nabla \cdot \nabla t)\mathrm{dV} = \oiint_{\Sigma} \nabla t \cdot dS = \oiint_{\Sigma} \frac{C_1}{r^2} \cdot dS = 4\pi C_1 = -\frac{Q}{k} \qquad \textbf{(4.7)}$$

$$C_1 = -\frac{Q}{4\pi k} \qquad \textbf{(4.8)}$$

To then evaluate the other constant (C2), the hottest point on the skin's surface is assumed to lie directly above the centroid of the heat source. This hottest point on the surface is labeled O' as shown in Figure 4-3. Assuming the temperature of the sub-surface heat source at point O is t_m, from **(4.6)** gives **(4.9)**,

$$C_2 = t_m - \frac{Q}{4\pi k d} \qquad \textbf{(4.9)}$$

$$t = t_m - \frac{Q(r-d)}{4\pi k d r} \qquad \textbf{(4.10)}$$

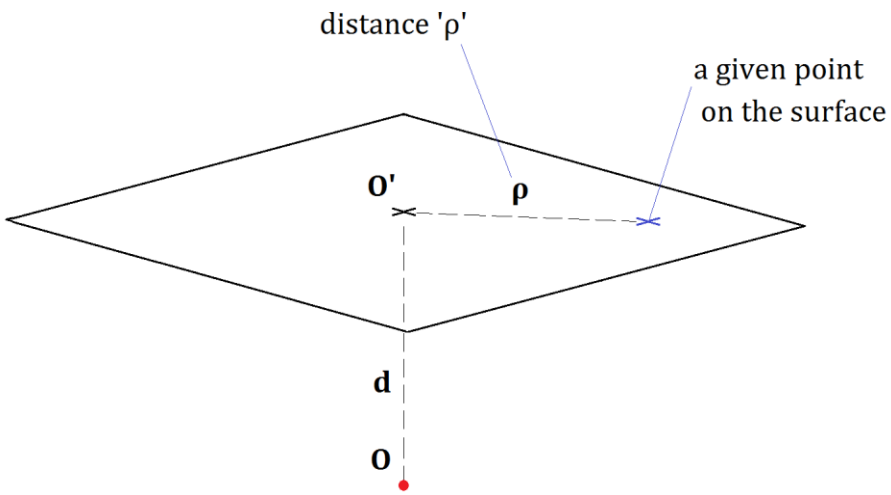

Figure 4-4. Introducing ' ρ ', the distance from a given point on the surface to the hottest point within the ROI. The hottest point on the surface is referred to as O'.

Using **(4.10)** the temperature at any given point on the skin's surface is calculated as a function of distance from the hottest point on the surface, which in the case of a simple spherical sub-surface heat source and uniform interstitial tissue will occur at O' in the centre of the ROI. The distance of a given point on the surface from point O' is expressed as a new parameter called ρ, as shown Figure 4-4. In order to now extract heat source depth 'd' from the surface temperature distribution, the new function **(4.11)** is defined:

$$f(\rho) = \frac{\rho^2}{t_m - t} \qquad \textbf{(4.11)}$$

When this new function f(ρ) is plotted using parameter values in the range relevant to human physiology, it takes a shape similar to that shown in Figure 4-5.

As ρ appears as ρ^2 in **(4.11)**, it is helpful to notice from Figure 4-6, the Pythagorean relationship of ρ to depth d, as $\boldsymbol{\rho^2} = r^2 - \mathbf{d^2}$. Substituting **(4.10)** into **(4.11)**, gives **(4.12)**:

$$f(\rho) = \frac{4\pi k d}{Q}(\rho^2 + d^2 + d\sqrt{\rho^2 + d^2}) \qquad \textbf{(4.12)}$$

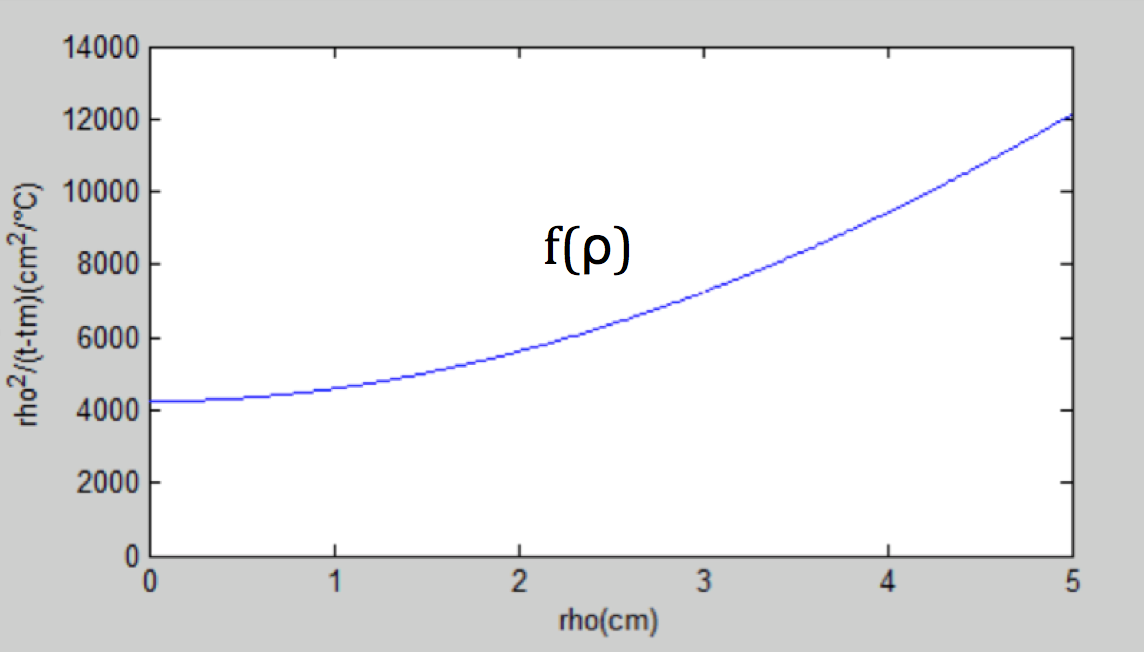

Figure 4-5. A plot showing the shape of f(ρ), equation (4.11), as a function of 'rho', the distance of a point on the surface from the hottest point (O') on the skin's surface (cm).

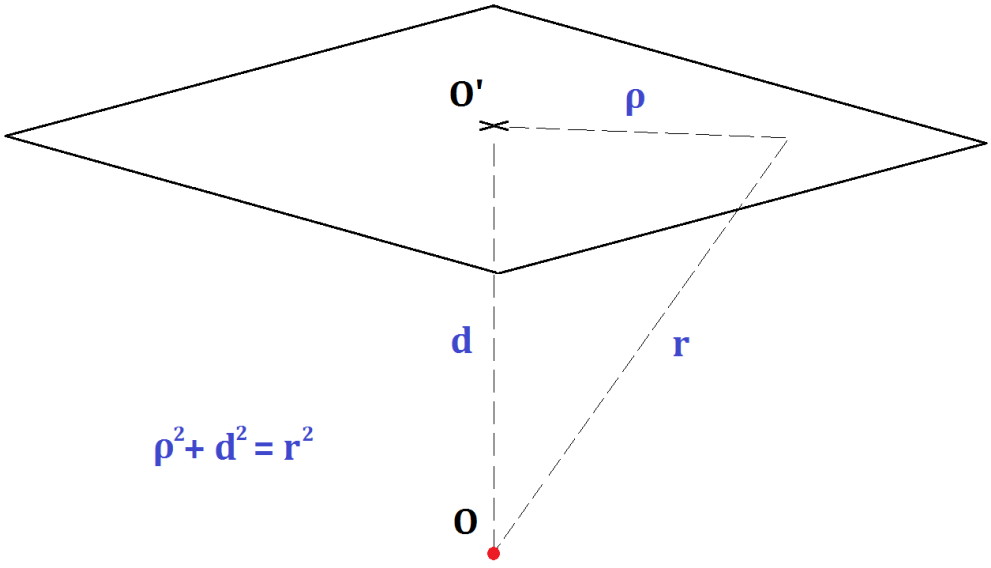

Figure 4-6. Pythagorean triangular relationship of depth 'd' with distance 'ρ' and distance 'r'

From **(4.12)** it is possible to obtain the limit and value for f(ρ) at ρ = 0 and **ρ = d**, via **(4.13)** and **(4.14)** respectively,

$$\lim_{\rho \to 0} f(\rho) = 8\pi k d^3 \qquad \textbf{(4.13)}$$

$$f(\rho)\rfloor_{\rho=d} = 4\pi k d^3 (2 + \sqrt{2}) \qquad \textbf{(4.14)}$$

Combining **(4.13)** and **(4.14)**, gives **(4.15)**,

$$f(\rho)\rfloor_{\boldsymbol{\rho=d}} = \left(1 + \frac{\sqrt{2}}{2}\right) \lim_{\rho \to 0} f(\rho) \approx \mathbf{1.707} \lim_{\rho \to 0} f(\rho) \qquad \textbf{(4.15)}$$

The significance of equation **(4.15)** lies in the constant 1.707 coefficient value shown in bold. This constant of 1.707 is key to the graphical method for determining source depth from plots of f(ρ) like Figure 4-5, namely, that the value of f(ρ) when ρ=0 is always approximately 1.707 times smaller than the value of f(ρ) at ρ=d, where d is the depth of the heat source. Exploiting this 1:1.707 relationship is the crux of the graphic depth determination method, which is done as follows:

1. Plot f(ρ) vs ρ (as shown Figure 4-5), and identify the value of f(ρ) at ρ=0, as shown in Figure 4-7.
2. Multiply the value f(ρ) at ρ=0 by a factor of 1.707, to find the point on the Y axis from which to draw a horizontal line, also shown in Figure 4-7.
3. Draw a horizontal line from this new point on the Y axis, in the positive x direction, until the line intersects curve f(ρ), Figure 4-9.
4. At this point where the horizontal line meets the curve, ρ = d (as shown Figure 4-8) draw a vertical line down from the intersection of the horizontal line and curve f(ρ), to identify the value of ρ at the point where ρ = d, and therefore finding d.

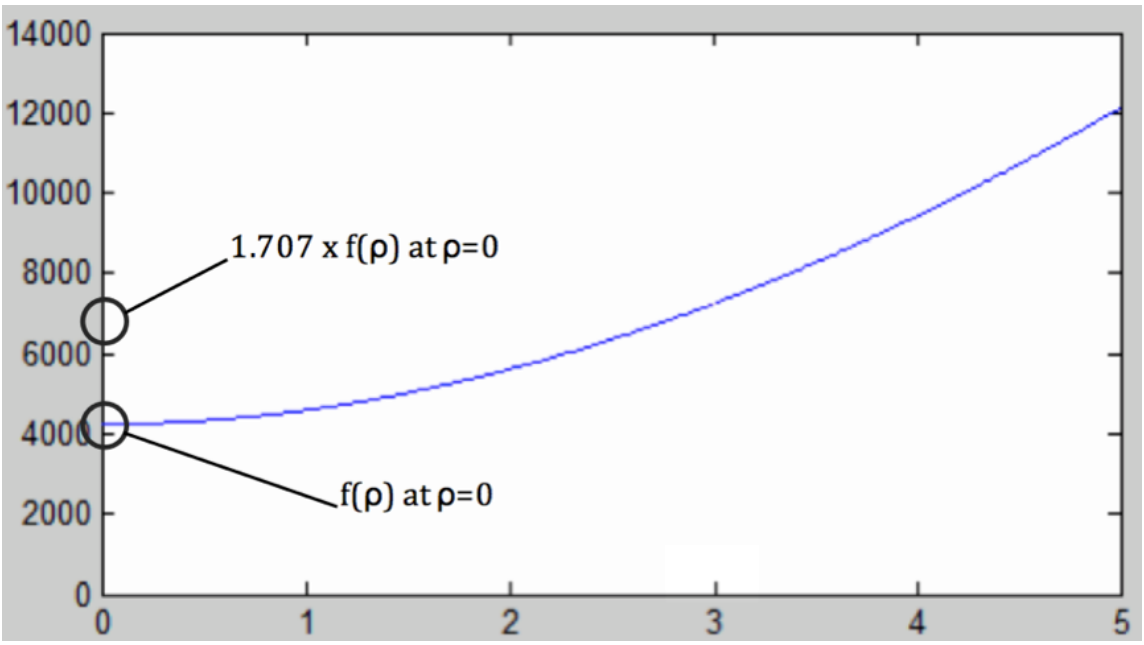

Figure 4-7. Steps 1 and 2 of the graphic heat source depth determination method – identifying the value of f(ρ) at ρ=0, and multiplying that value by 1.707 to find the point on the Y axis from which to draw a horizontal line across to the curve f(ρ).

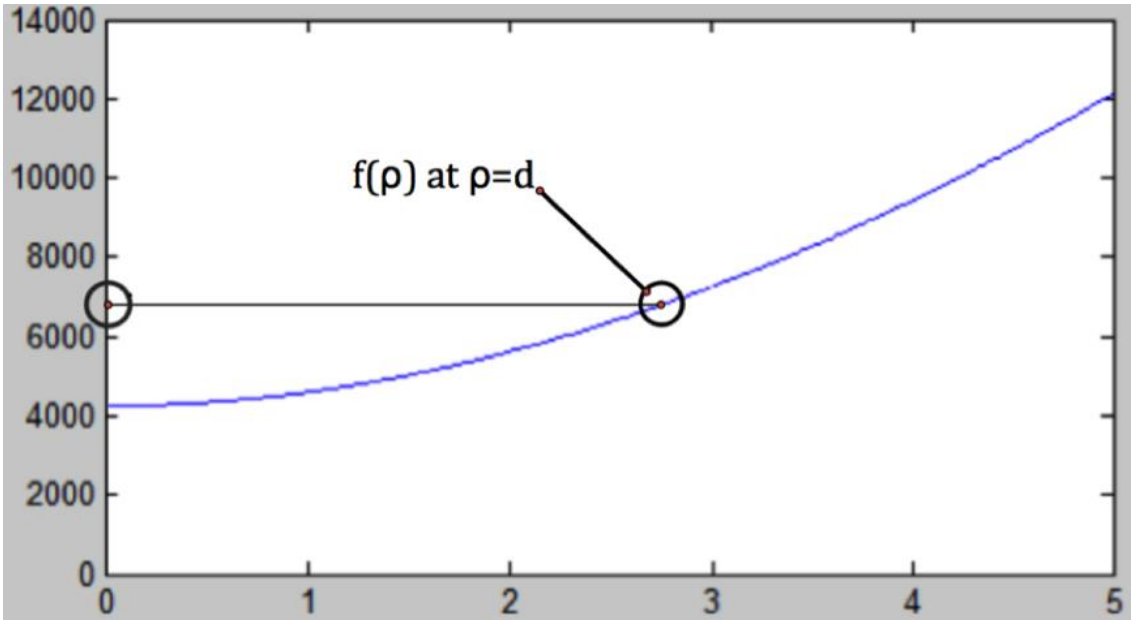

Figure 4-8. Step 3 of the graphic heat source depth determination method – drawing a horizontal line from the point on the Y axis at which f(ρ) = 1.707 x [f(ρ) at ρ=0], across to the point on curve f(ρ) at which ρ = d.

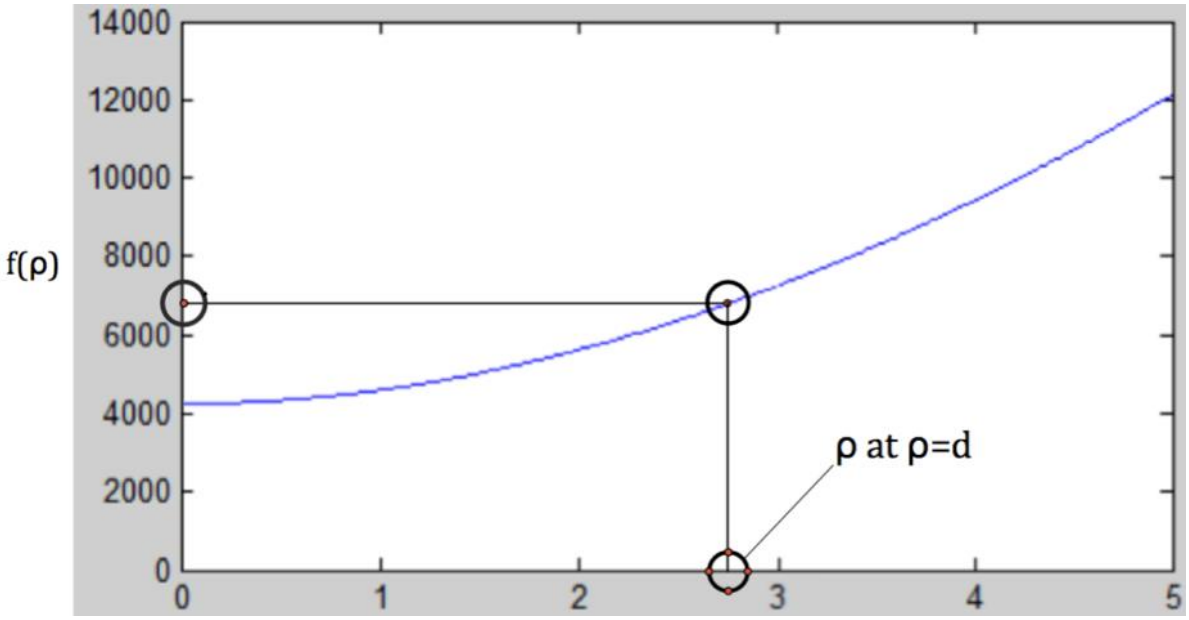

Figure 4-9. Step 4 of the graphic heat source depth determination method – drawing a vertical line down from the intersection of the horizontal line and curve f(ρ) to the X axis, to identify the value of ρ at the point where ρ = d, and therefore finding d.

1.19 Deconvolution of Surface Temperature Distribution

As mentioned above, in clinical cases where a real heat source is involved (as opposed to the theoretical *point* source considered hitherto) the stress fracture or tumor (for example) will have a non-zero shape and size. The thermal distribution pattern on the skin's surface that results from this real heat source can be termed 'g', and expressed as shown in **(4.16)**:

$$g = t \otimes h + \mathcal{E} \qquad \textbf{(4.16)}$$

Where 't' is the surface temperature resulting from a *point* source, as given by **(4.10)**, 'h' is the shape function of the source (Figure 4-10), 'ε' is the noise, and '⊗' is the convolution operator. To make the aforementioned graphic method useful in real clinical applications, it is necessary to deconvolute expression **(4.16)**.

In cases where the shape 'h' of the heat source is known and well defined, it is possible to perform a deterministic deconvolution of **(4.16)**, and use the graphical

method to determine source depth. In practical clinical TIRI, however, the shape of the source 'h' will usually be unknown – requiring deconvolution via blind Fourier transform. The critical property of Fourier transforms that makes this possible, is the fact that 'the Fourier transform of the convolution of two functions is equal to the product of their individual transforms'. In the absence of noise, the Fourier transform representation of **(4.16)** is as shown in **(4.17)**:

$$G(u) = T(u)H(u) \qquad \textbf{(4.17)}$$

Where the uppercase letters in **(4.17)** represent the Fourier transforms of the corresponding functions. The basic blind deconvolution scheme can be written as shown in **(4.18)** to **(4.25)**, Where the superscript 'k' denotes the number of iterations, 'abs' denotes the absolute value function, 'medfilt' is the median filtering operator, and 'F' and 'F^{-1}' denote the Fourier transform and inverse Fourier transform, respectively. Equation **(4.21)** ensures production of a shape function, and **(4.25)** uses a median filter to reduce the effects of noise.

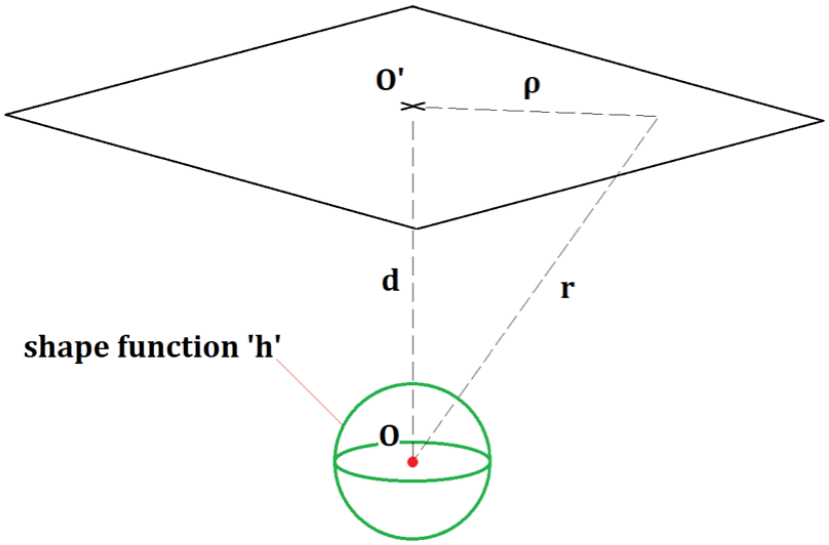

Figure 4-10. Representation of heat source shape function 'h'. In the case of clinical TIRI, the exact shape of the heat source will probably be unknown, but will have significant impact upon the fidelity of depth recovery from surface TIRI data – hence the need for deconvolution of the distribution as obtained by TIRI.

$$T^{(k)}(u) = Ft^{(k)}(\rho) \quad \textbf{(4.18)}$$

$$H^{(k)}(u) = G(u)/T^{(k)}(u) \quad \textbf{(4.19)}$$

$$h^{(k)}(\rho) = F^{-1}H^{(k)}(u) \quad \textbf{(4.20)}$$

$$h^{(k)}(\rho) = \frac{1}{2}\{h^{(k)}(\rho) + abs[h^{(k)}(\rho)]\} \quad \textbf{(4.21)}$$

$$H^{(k)}(u) = Fh^{(k)}(\rho) \quad \textbf{(4.22)}$$

$$T^{(k)}(u) = G(u)/H^{(k)}(u) \quad \textbf{(4.23)}$$

$$t^{(k)}(\rho) = F^{(-1)}T^{(k)}(u) \quad \textbf{(4.24)}$$

$$t^{(k)}(\rho) = \frac{1}{2}medfilt\{t^{(k)}(\rho) + abs[t^{(k)}(\rho)]\} \quad \textbf{(4.25)}$$

This is an iterative scheme so it is repeated a number of times until two functions with the convolution are found. One is the shape function and the other is the point source temperature.

Implementation of this algorithm requires substitution of a nonnegative-valued initial estimate of temperature distribution $t^{(0)}(\rho)$ into deconvolution scheme **(4.18)** to **(4.25)**, with successive iterations until two positive functions with the required convolution g (ρ) have been found. Figure 4-11 illustrates the effect of the blind deconvolution scheme upon the shape of the temperature distribution that the source depth determination algorithm considers – where skin surface temperature is considered as a function of rho, distance from the hottest point in cm.

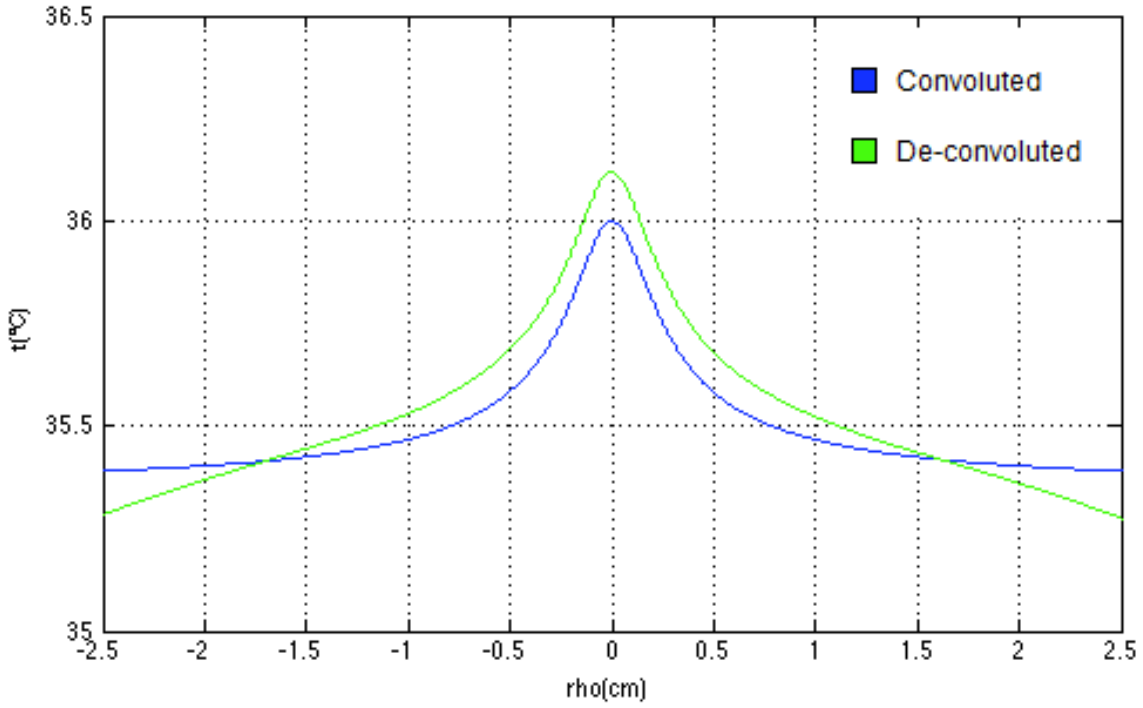

Figure 4-11. Effect of the blind deconvolution scheme upon the temperature distribution considered across the skin's surface, with temperature as a function of rho (cm).

1.20 Computer Implementation

The heat source depth determination algorithm described in the previous section was implemented in MATLAB, using the code shown in appendices. The code translates input values of TIRI-measured surface temperature profiles into output graphs of ρ^2 / (t_m – t) as a function of ρ, from which heat source depth may be recovered via the graphic method. For implementation, it is necessary to supply the code with enough information to estimate an initial temperature distribution $t^{(0)}(\rho)$ to initiate the iterative deconvolution loop from **(4.18)** to **(4.25)**:

```
%Assign initialising parameter value estimates

tmeas=32.4;    %TIRI-Inferred Surface Temperature
ts=36;       %Assumed Point Source Temperature (blood-perfused periosteum)
d1=0.3;      %Point Source Depth
d2=0.4;      %Extended Source Depth
Q1=1;        %Magnitude of Point Source
Q2=0;        %Magnitude of Extended Source
k=0.6;       %Thermal conductivity of Human Tissue
```

```
rho=-3:0.001:3;  %Define range of surface distances
No_Iterations=200;  %Number of iterations

Point_Source=ts-
(rho.^2./(((4*k*pi*d1)/Q1).*(d1^2+rho.^2+d1.*sqrt(d1^2+rho.^2))));%Define
Point Source Distribution

Extended_Source=tmeas-
(rho.^2./(((4*k*pi*d2)/Q2).*(d2^2+rho.^2+d2.*sqrt(d2^2+rho.^2))));%Define
Extended Source Distribution
```

The loop then repeats until two positive functions with the required convolution g(ρ) have been found, remembering that 'g' represents the heat distribution data measured on the skin's surface by clinical TIRI, as in **(4.16)**.

```
for i=[1:No_Iterations];%Blind Deconvolution loop

   T=fft(Point_Source); %Convert point source to Fourier domain

   G=fft(Extended_Source); %Convert extended source to Fourier domain

   H=G./T; %Define shape function in Fourier domain

   h=ifft(H); %Convert shape function to temperature domain

   h=(1/2).*((h)+abs(h)); %Check that shape function is positive

   H=fft(h); %Convert shape function back to temperature domain

   T=G./H; %Define next value of point source temp in Fourier

   Point_Source=ifft(T); %Convert next value of point source into
temperature domain

   Point_Source=0.5.*medfilt1((Point_Source+abs(Point_Source)),1);%Median
Filtering Command
end

ts=max(Point_Source); %Find max value of new temp distribution

fp_deconv=(rho.^2./(ts-Point_Source)); %Define f(p) for new temperature
distribution
```

The Matlab implementation was then tasked to recover the depth of the dominant heat source within the tibial tissue volume examined during the clinical study (the blood-filled periosteum) from skin surface temperature data acquired via TIRI. Figure 4-12

shows the heat source depth situation relevant to the clinical study and associated TIRI data. The left side of the figure shows cadaveric excision of the pretibial thickness/depth of tissue overlying the distal third of the tibia, through which heat must pass from the blood-perfused periosteum to reach the skin's surface.

The right side of the figure is a schematic of the blood-perfused periosteum (red) in relation to the tibial cortex (grey). During dissection of a cadaveric specimen that was representative of the sample population examined in the clinical study, the thickness of tissue overlying the tibial periosteum, which corresponds to the heat source depth to be retrieved from the clinical TIRI data obtained, varied from approximately 1mm at the distal third of the tibia, to approximately 3 mm at the proximal third. A sample of 10 TIRI's containing 30 tibial ROI's (3 per tibia) was selected from the database of images acquired during the clinical trial described.

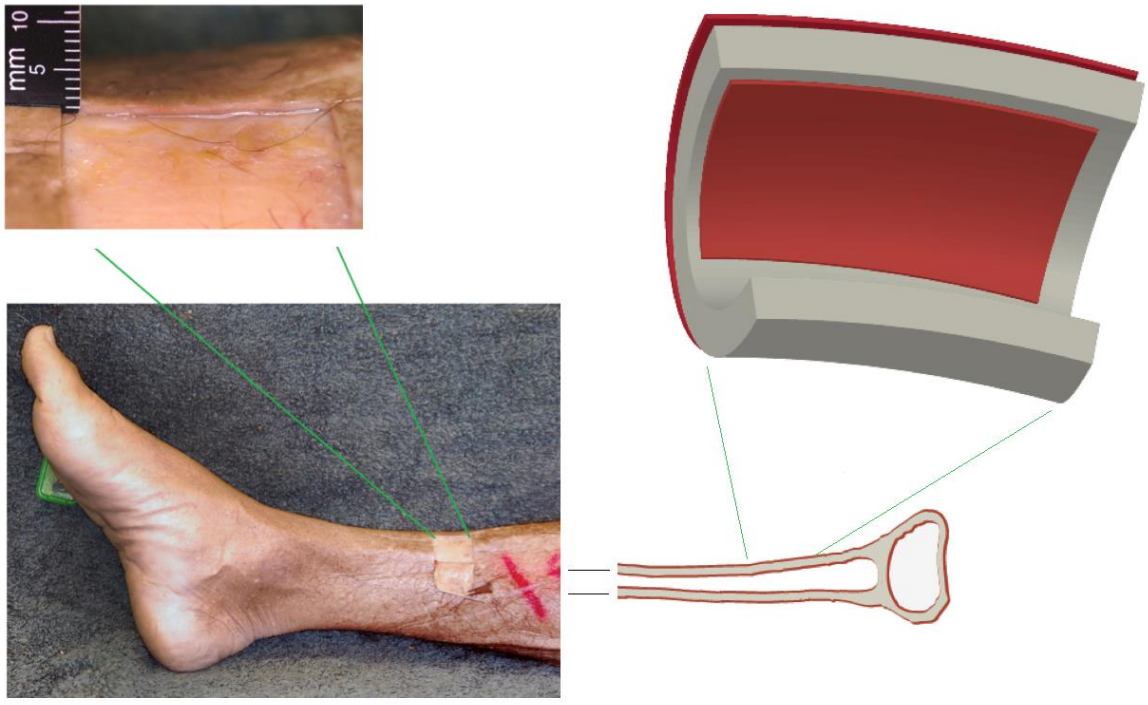

Figure 4-12. The heat source depth situation relevant to the clinical study. Left: cadaveric excision of the 1mm thick pretibial tissue (ROI_3) overlying the distal third of the tibia, through which heat must pass from the blood-perfused periosteum to reach the skin's outer surface seen by TIRI. Right: schematic of the blood-perfused periosteum (red) in relation to the tibial cortex (grey) shown for clarity.

The TIRI's selected correspond to healthy participants who did not develop any symptoms during the study. The TIRI's were imported into FLIR Systems' proprietary software environment for analysis, Thermovision Professional V2.8. As the Matlab implementation of the heat source depth determination algorithm requires skin surface temperature as the input from which to recover heat source depth, the 'spotmeter' tool was used to extract the surface temperature distributions from the three ROI's within each of the 30 radiometrically-calibrated TIRI's, as shown in Figure 4-13.

As detailed above, these ROI's were selected to provide representative thermal characterisation from the thermophysiologically-distinct thirds of the tibiae. The absolute surface temperature distributions obtained from the analyses shown in Figure 4-13 are given in Figure 4-14.

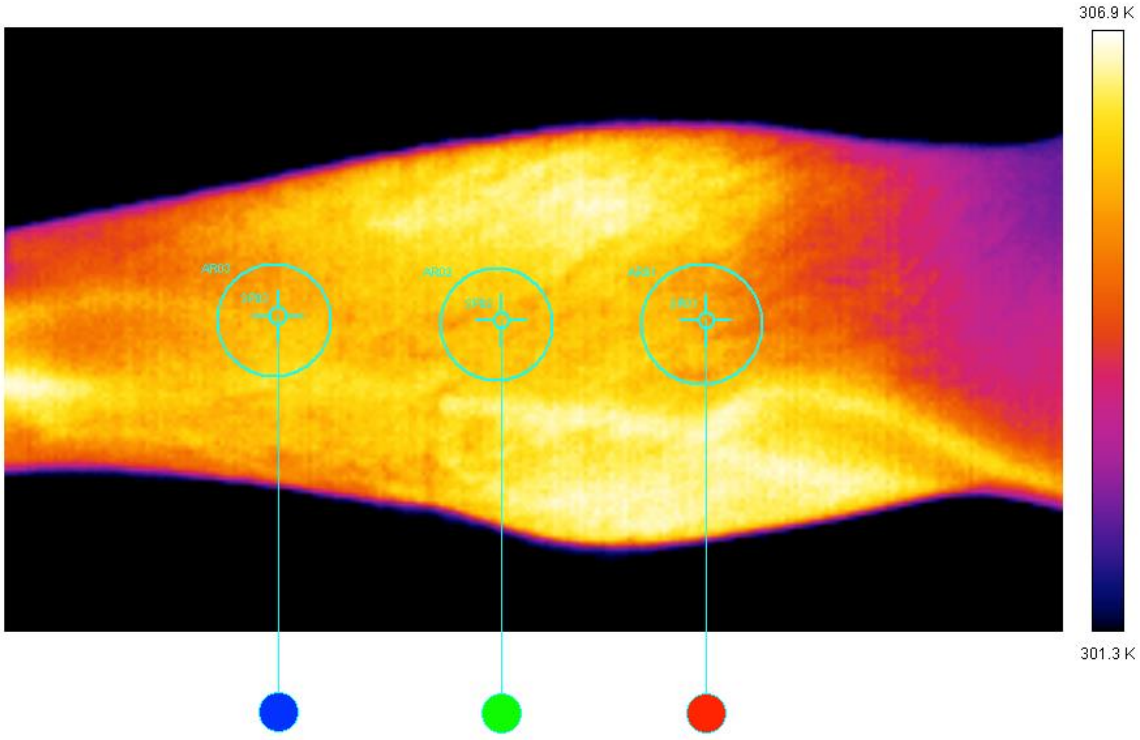

Figure 4-13. Radiometric TIRI, being analysed within FLIR Thermovision Professional v2.8. The temperature values obtained via this software were used as the surface temperature inputs to the Matlab heat source depth determination code. It is these temperatures (1-3) that are considered the convolution of the periosteum heat source at depth 'd' beneath the imaged surface.

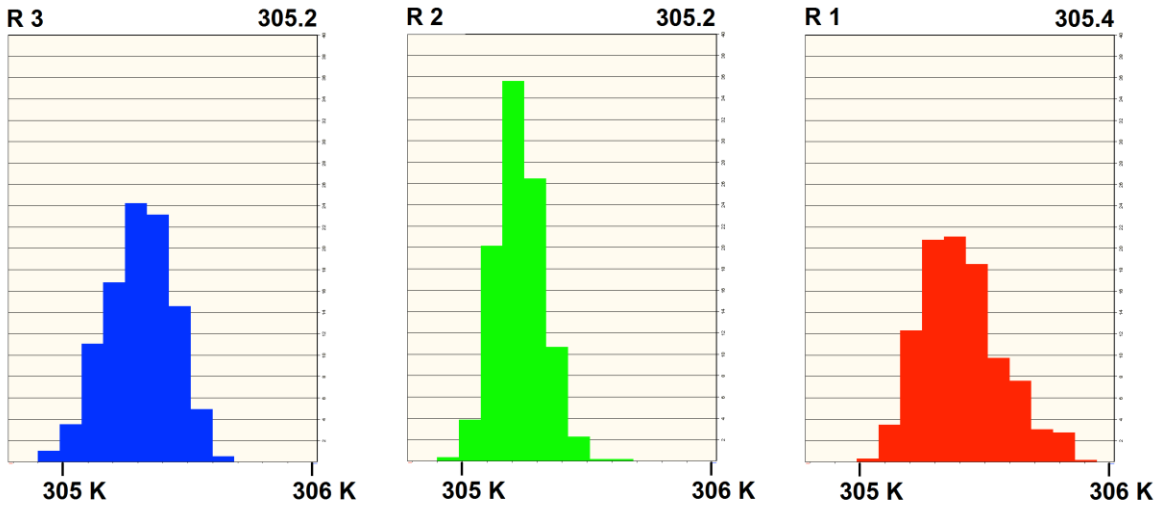

Figure 4-14. Surface temperature distributions across the ROI's shown in Figure 4-15. R3 (blue), R2 (green), and R1 (Red) correspond to the distal, medial, and proximal ROI's shown in Figure 4-15, respectively. The mean absolute temperature for each ROI is shown top right of each distribution.

Following extraction of surface temperature distributions from the clinical TIRI's, via the method shown in Figure 4-13 and Figure 4-16, the mean absolute temperature from each ROI distribution was obtained, and entered into the Matlab code as the initial temperature distribution $t^{(0)}(\rho)$ to initiate the iterative deconvolution loop from **(4.18)** to **(4.25)**. Figure 4-15 shows the resulting graph of t (ρ) corresponding to the proximal ROI_2, shown in green in the centre of Figure 4-13 and Figure 4-14.

From inspection of Figure 4-15, it is clear that the code produces a surface temperature distribution with the expected shape and features corresponding to a spherical heat source as described in Figure 4-10. Although this shape function is not an accurate representation of a distributed heat source like the periosteum would be in the real case, the model still produces acceptable results for determination of source depth.Figure 4-16 is a plot of $\rho^2 / (t_m - t)$ as a function of ρ, corresponding to central ROI_2, marked green in the clinical TIRI of Figure 4-13.

The depth of the subsurface heat source (periosteum) leading to the temperature distribution across ROI_2 in Figure 4-13, may be recovered from Figure 4-16 via application of the graphic method. The red rectangle extending out to the right from the origin marks the region within which the graphic method can be applied. It

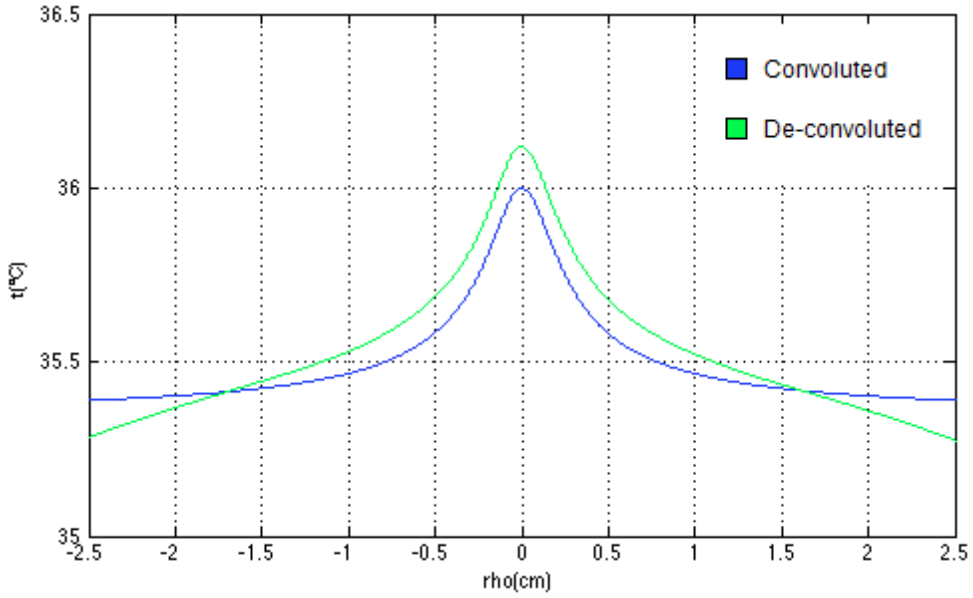

Figure 4-15. Skin surface temperature as a function of rho (distance from point on the skin's surface overlying the centroid of the heat source), representing the temperature distribution extracted from ROI_2, shown green and centred in TIRI Figure 4-13 and Figure 4-14. The green curve represents the blue distribution (extended source) adjusted via the deconvolution scheme.

should be noted that the green spike at rho = 0 is an artefact of the Dirac delta function within **(4.4)**, and is not driven by a constitutive property of the physical heat transfer system. Figure 4-18 illustrates application of the graphic method to correctly determine the depth of the heat source beneath the skin surface of ROI_2 in Figure 4-13. As shown, f (ρ) intersects the y axis at 'A', where Y = 0.1206. As per the graphic method detailed above, horizontal line BC is then drawn, such that OB = 1.707 OA = 0.2109, and 'C' lies on curve f (ρ). Vertical line CD is then drawn vertically down to intersect the X axis at D, indicating the depth of the heat source, namely 0.2109 cm.

The small photograph inset bottom right of Figure 4-18 shows an actual pretibial tissue volume excised from a proximal tibial ROI corresponding to ROI_2 in in Figure 4-13, and analysed here. As can be seen from inspection of the photograph, the surface of the periosteum (heat source) is approximately 2mm beneath the skin's surface, in excellent agreement with the heat source depth value obtained via the graphic method above. Figure 4-17 and Figure 4-19 illustrate successful use of the technique to recover heat source depth from the other tibial ROI's, with photos inset.

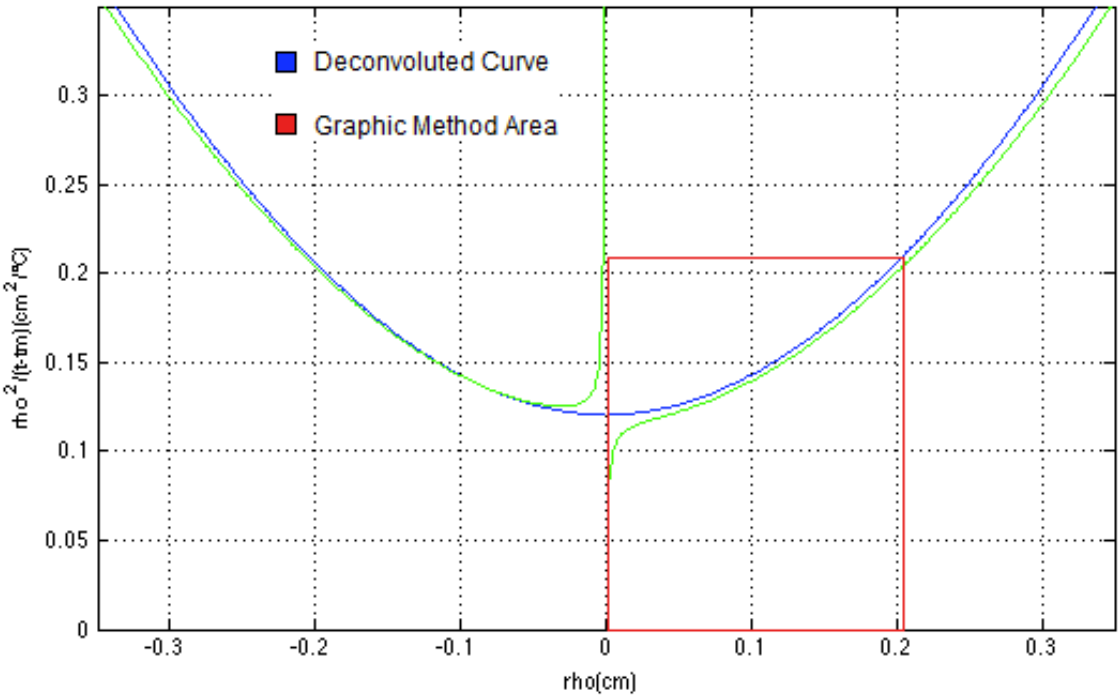

Figure 4-16. Plot of ρ^2 / (t_m – t) as a function of ρ, from which the depth of heat source beneath ROI_2 may be recovered via the graphic method.

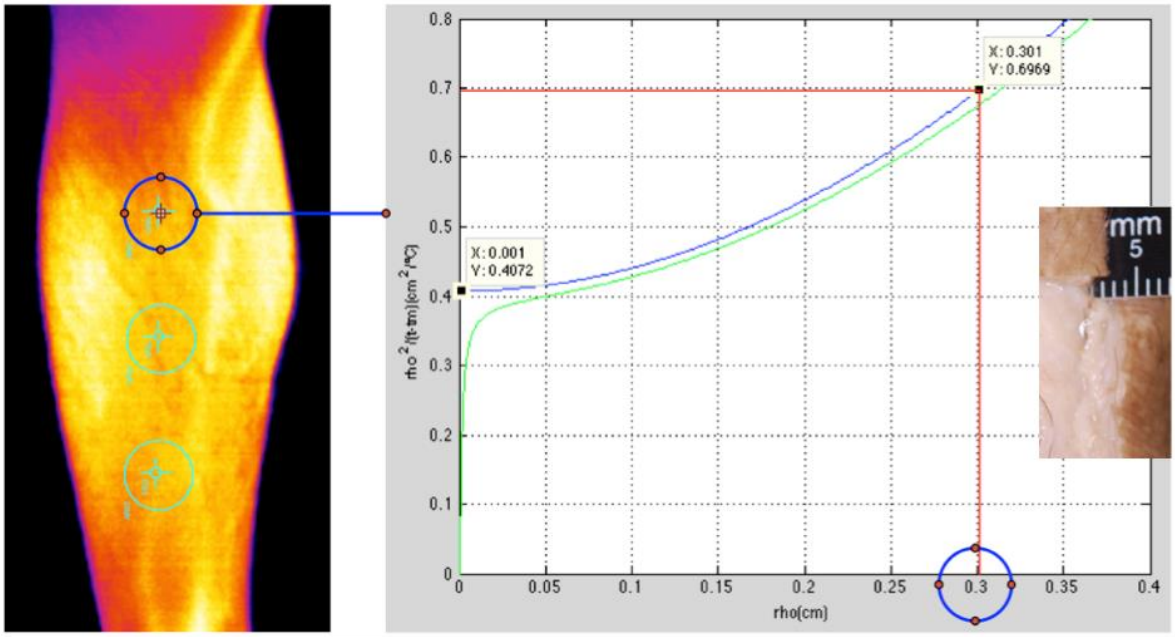

Figure 4-17. Successful recovery of heat source depth (≈ 3mm) from TIRI of tibial ROI_1. Photograph inset bottom right shows the actual tissue depth involved (also ≈ 3mm), taken during dissection of a population-representative pretibial tissue volume. Note that the interstitial tissue beneath ROI_1 is a lot more fatty than the tissue in ROI_2, so a lesser thermal conductivity value should be applied.

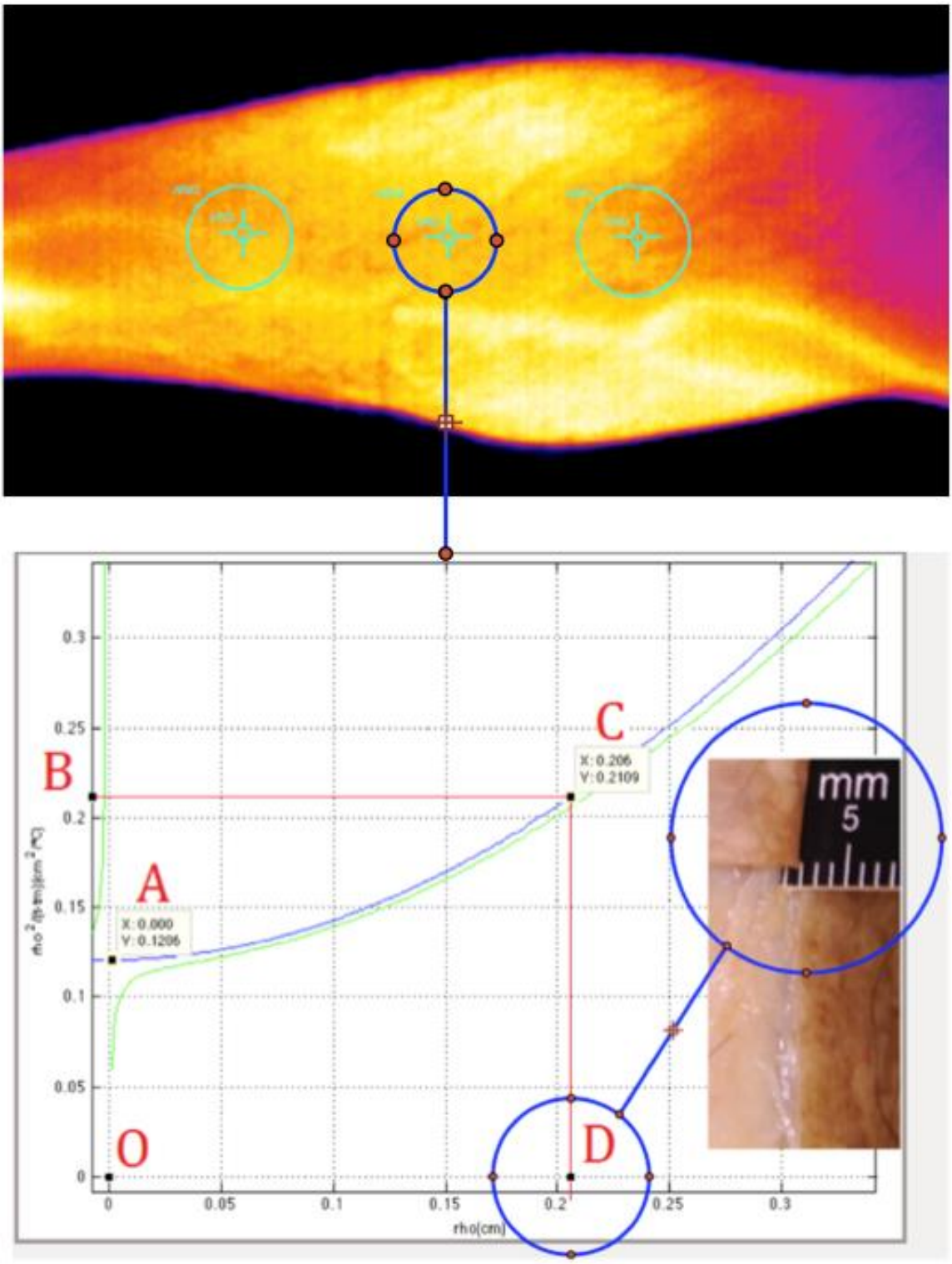

Figure 4-18. Successful heat source depth determination on real clinical TIRI data of tibial ROI_2. The source depth recovered by the graphic method is indicated where line CD intercepts the X axis at point 'D', corresponding to a source depth of approximately 0.2 cm. The photograph inset bottom right shows the actual tissue depth involved (also ≈ 2mm), taken during dissection of a representative pretibial tissue volume, as detailed in 'Pathoanatomic Context' above.

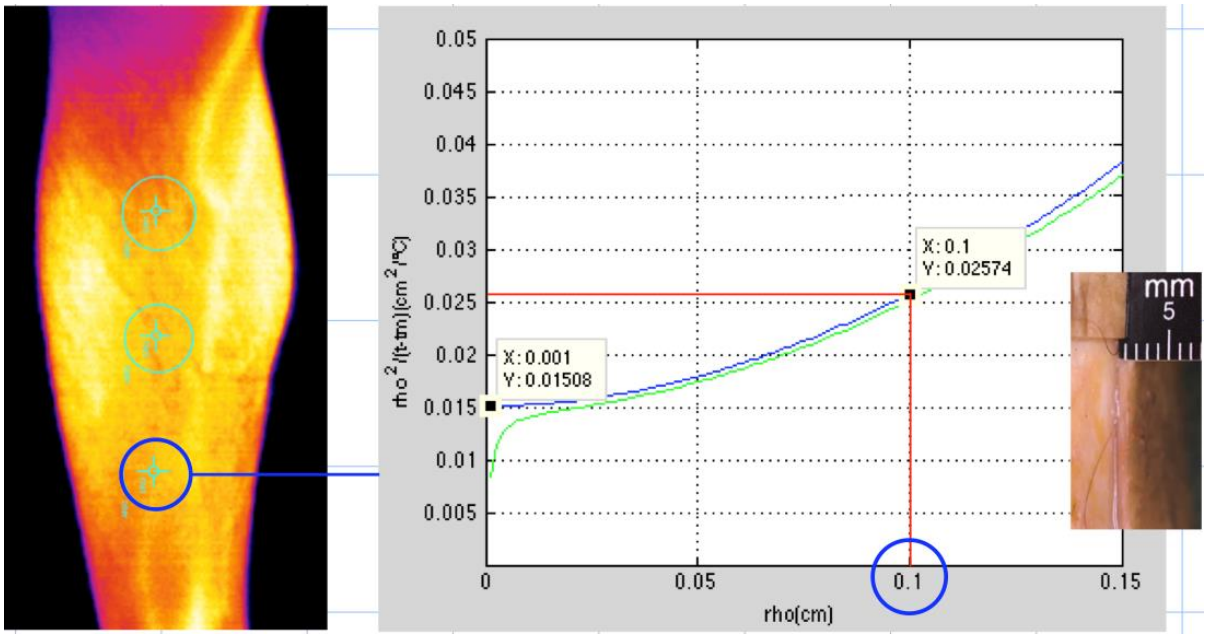

Figure 4-19. Successful recovery of heat source depth (≈ 1mm) from TIRI of tibial ROI_3. The photograph inset bottom right shows the actual tissue depth involved (also ≈ 3mm), taken during dissection of a population-representative pretibial tissue volume. Note that the interstitial tissue beneath ROI_3 is a lot less fatty than the tissue in ROI_1 and ROI_2, so a greater thermal conductivity value should be applied.

1.21 Results & Discussion

This heat source depth determination technique was applied to a total of 30 tibial ROI's, taken from 10 TIRI's obtained during the aforementioned clinical study. Table 4-1 and Figure 4-21 to Figure 4-26 summarise the heat source depth recovery results and the surface temperature data used to produce them. Because mean ROI temperature (as determined by clinical TIRI, assuming small ρ) was the sole parameter varied in study of this depth recovery technique, evaluation of the technique's efficacy is based upon consideration of whether the depth values obtained made sense when compared to depths obtained via dissection of the actual tissue volume in a representative human cadaver (Figure 4-20) – rather than sensitivity analysis of the technique to constitutive elements of the heat transfer model and deconvolution scheme. Statistical comparisons are made across groups of corresponding ROI's in different participants.

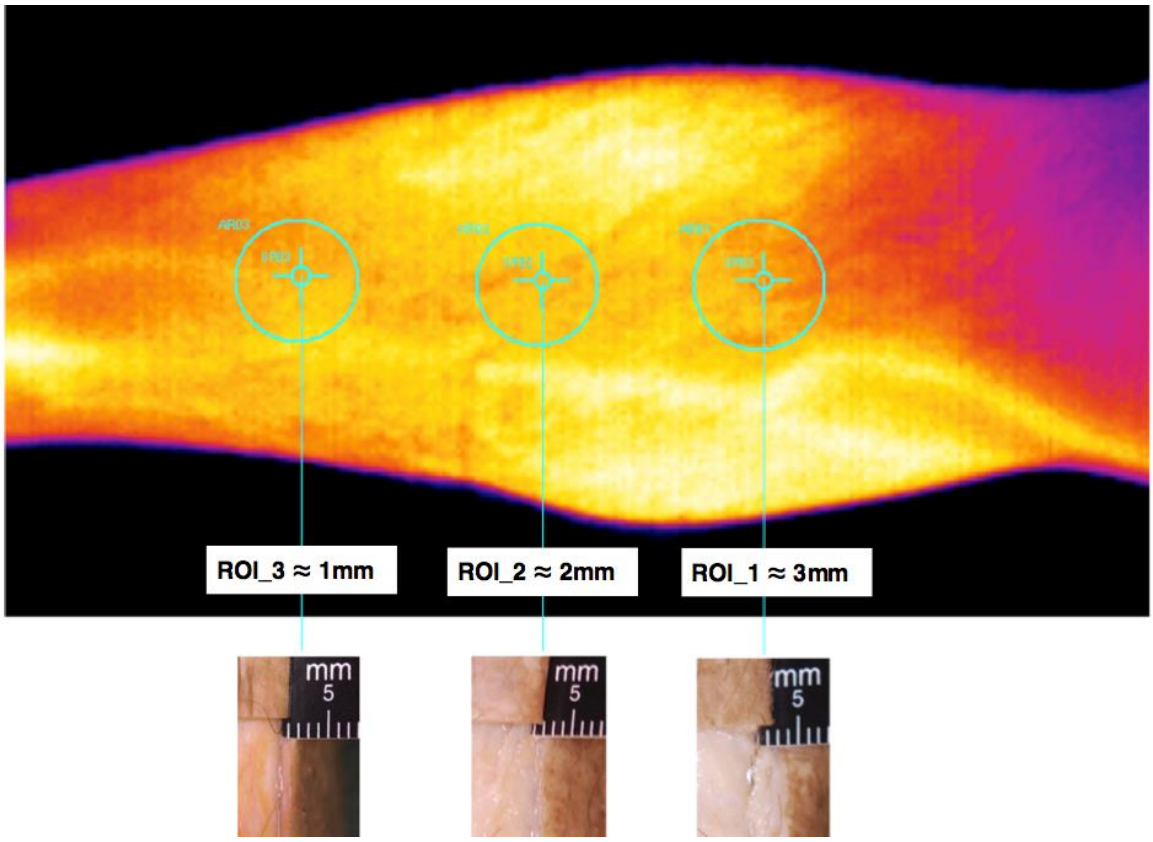

Figure 4-20. Reminder of the objective – to determine heat source depth from TIRI of the surface. Shown are the three ROI's and associated tissue depths excised from the cadaveric specimen shown Figure 0-4 Left. Although all three volumes are avascular and thermophysically homogeneous, and without thermogenic anatomy; there are clear increases in both interstitial tissue thickness and lipid concentration from distal to proximal (D-P).

Overall, this study found that when real clinical TIRI-obtained pretibial skin surface temperature distributions are entered into the aforementioned heat transfer model that features physiologically-representative heat transfer parameter values, the heat source depth determination technique described above (graphic method plus blind deconvolution) produces heat source depth values that are consistent with the relevant thermoanatomy, as determined by investigative dissection - Table 4-1, and Figure 4-20. This claim assumes that: the primary heat source driving the temperature distribution seen by TIRI across the pretibial skin's surface is the blood-perfused tibial periosteum, and that the cadaver used for investigative dissection of the actual tissue depths corresponding to each tibial ROI was representative of the population studied (Early 20's Australian Caucasian male, representing Australian Army Recruits).

Table 4-1. Skin surface temperature values and heat source depths recovered from TIRI's of tibial ROI's during clinical study. *TIRI # 1 corresponds to Figure 4-13 used in the example above. *Recovered depths should be compared to actual tissue sections shown in Figure 4-20.

TIRI #	ROI_#	Surface Temperature [K]			Recovered Depth* [mm]
		Min	Max	Mean	
1*	1	305	305.9	305.4	3.1
	2	304.8	305.7	305.2	2.1
	3	304.8	305.7	305.2	1.1
2	1	305.2	306.1	305.6	2.9
	2	304.9	305.7	305.6	1.9
	3	304.8	305.9	305.3	1.1
3	1	304.9	305.9	305.5	3.1
	2	305.4	306.1	305.7	1.9
	3	305.2	306.2	305.6	0.9
4	1	304.9	305.9	305.4	3.1
	2	304.6	305.9	305.3	2.1
	3	304.9	306	305.3	1.1
5	1	304.7	305.7	304.9	3.2
	2	304.5	305.4	305	2.2
	3	304.4	305.1	304.8	1.2
6	1	304.8	305.6	305.1	3.1
	2	304.9	305.7	305	2.2
	3	305.1	305.3	305	1.2
7	1	305.8	306.3	306.1	2.8
	2	305.5	306.3	306	1.8
	3	304.8	305.9	305.4	1.1
8	1	304.8	306	305.3	3.1
	2	304.8	305.7	305.2	2.1
	3	305.2	305.9	305.5	1.1
9	1	305.2	306	305.4	3.1
	2	304.7	305.7	305.2	2.1
	3	305	305.7	305.2	1.1
10	1	305.2	306.1	305.6	2.9
	2	305.7	306.3	306	1.8
	3	304.8	305.7	305.3	1.1

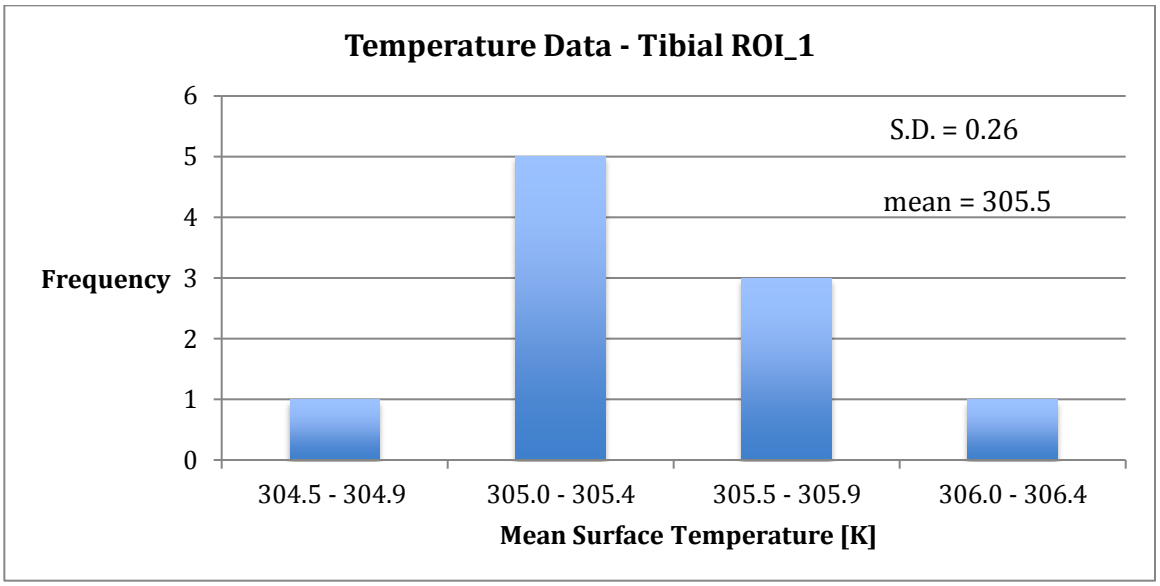

Figure 4-21. Distribution of mean surface temperatures across tibial ROI_1 acquired from TIRI analysis of a sample of 10 clinical study participants. The fact that all participants presented with temperatures inside a tight range (S.D. = 0.26) suggests that ROI_1 temperatures found outside of this range could be indicative of dysfunction.

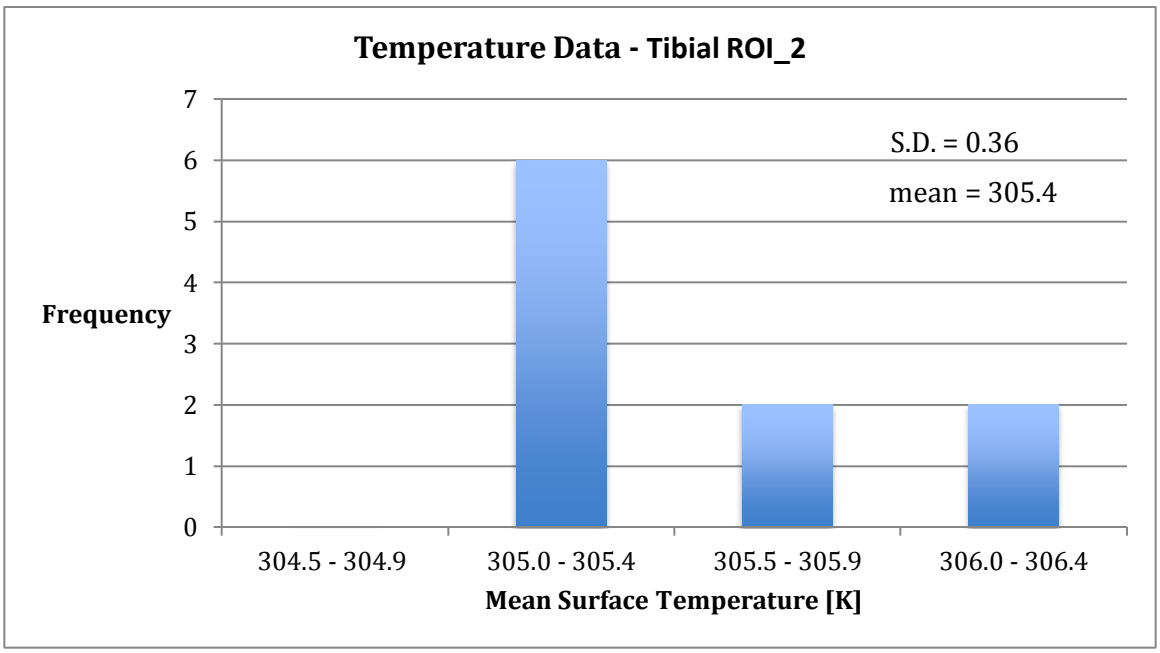

Figure 4-22. Distribution of mean surface temperatures across tibial ROI_2 acquired from TIRI analysis of a sample of 10 clinical study participants. All participants presented with ROI_2 temperatures inside a tight range (S.D. = 0.36) suggesting that ROI_2 temperatures found outside of this range could be indicative of dysfunction.

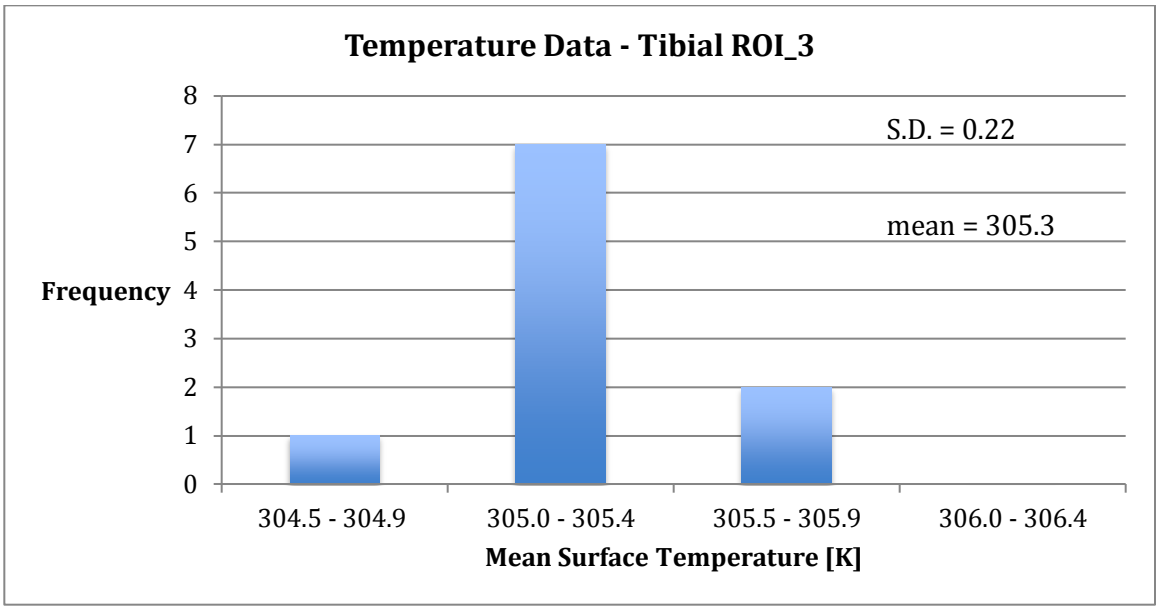

Figure 4-23. Distribution of mean surface temperatures across tibial ROI_3 acquired from TIRI analysis of a sample of 10 clinical study participants. All participants presented with ROI_3 temperatures inside a tight range (S.D. = 0.22) suggesting that ROI_2 temperatures found outside of this range could be indicative of dysfunction.

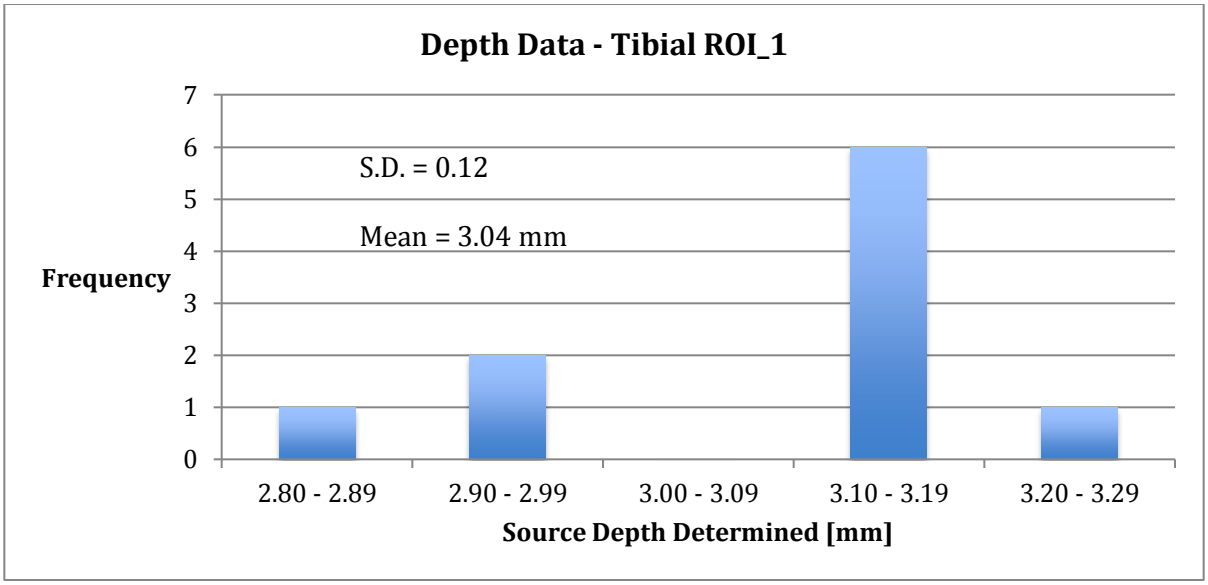

Figure 4-24. Distribution of heat source depths obtained from analysis of all ROI_1 TIRI's. Mean depth value of 3.04 mm is consistent with the expectation of 3 mm.

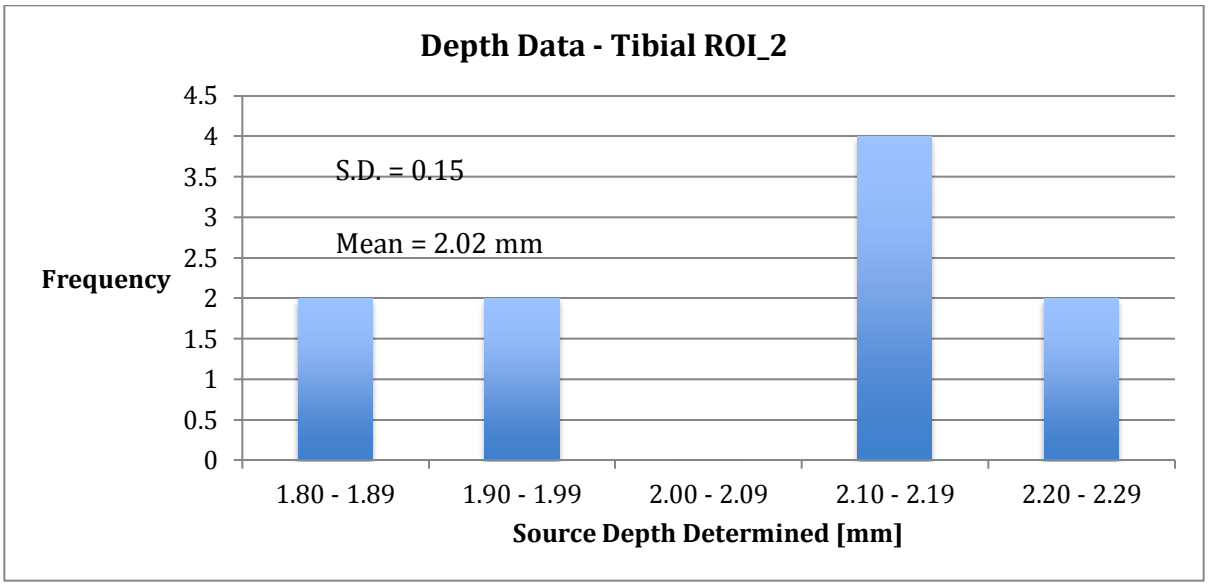

Figure 4-25. Distribution of heat source depths obtained from analysis of all ROI_2 TIRI's. Mean depth value of 2.02 mm is consistent with the expectation of 2 mm.

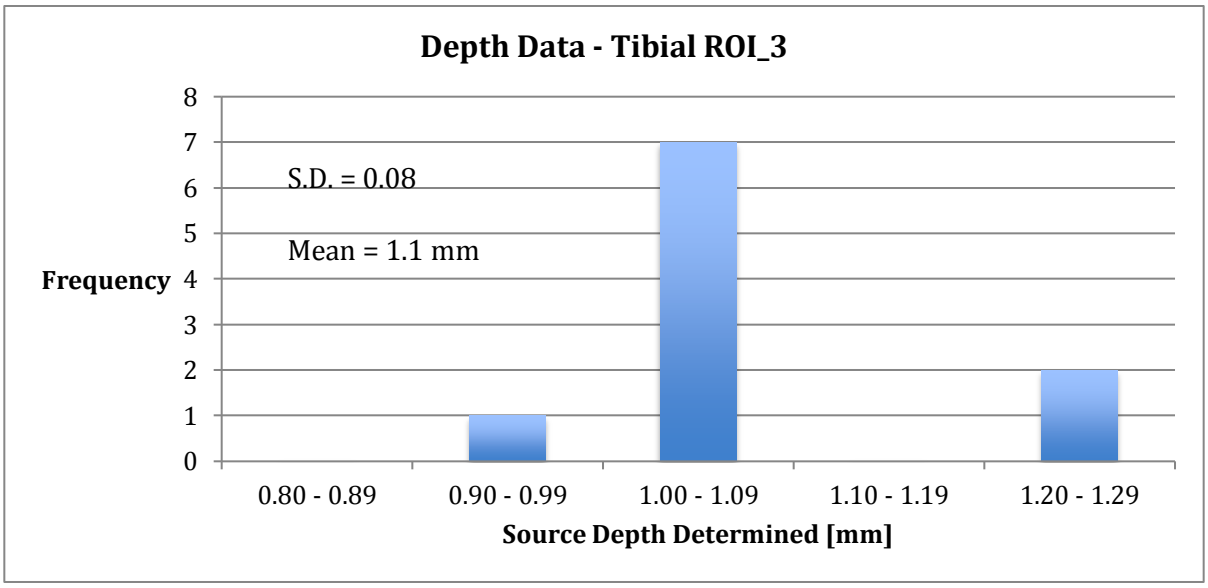

Figure 4-26. Distribution of heat source depths obtained from analysis of all ROI_3 TIRI's. Mean depth value of 1.1 mm is consistent with the expectation of 1 mm.

These encouraging preliminary results warrant further efforts to test and improve the validity and robustness of the approach and HSDD technique, i.e. devising ways to make the technique fail, and learning from the nature of those failures how the technique can be made more robust. For example, a tissue phantom of known heat transfer properties and dimensions, and with an embedded controllable heat source, could be used to test the robustness of the technique's ability to distinguish a 'smaller hotter deeper' source from a 'larger and cooler but shallower' source, that produces a similar surface temperature distribution. Although the current algorithm does protect against this type of failure by allowing the researcher to prescribe initial parameter value estimates, a more physically valid approach would be preferable. This type of work using tissue phantoms with embedded know heat sources also gives opportunity for development of improved thermometric MRI sequences, which could provide an invaluable validation modality for ongoing TIRI studies.

Another area recommended for further investigation is the sensitivity of the model to the aforementioned initial parameter estimates. The fact that the code recovers source depths consistent with anatomic expectations (ranging from 1 to 3 mm) for all ROI's in all participants, despite surface temperatures being extremely similar for all ROI's in all participants (S.D. for entire sample = 0.31, ranging from 304.8K – 306.1K) suggests that the current implementation of the algorithm may be too sensitive to initial parameter estimates (Arthur & Khan, 2013). Future implementations should strive to ensure that clinically obtained surface temperature distributions have significantly greater influence over final depth results than operator determined initial parameter estimates.

Although the stark difference in fat content between the different tibial ROI's is apparent from inspection of the dissection photos inset in Figure 4-20, the lack of variation in the range of human tissue thermal conductivity values reported in the literature (~ 0.45 - 0.55) suggests there is little performance / robustness to be gained from efforts to use ROI-specific thermal conductivity values in future implementations of the algorithm.

The successful demonstration of the clinical protocols developed and promising results of subsequent data analysis encourage further efforts toward the fulfilment of

TIRI's potential in clinical decision support. Although encouraging, the specificity and therefore clinical utility of TIRI as used in the clinical study described is limited by the absence of: a gold standard thermal imaging modality for validation of results obtained, and corresponding high-fidelity bioheat transfer models. As the biosignal detected by TIRI (thermal emittance, wm^{-2}) is multivariate in nature, a step-change advancement in specificity and clinical utility critically depends on high-fidelity quantitative deconvolution of human thermal infrared emittance – which is driven by our understanding of the nature of human emissivity.

Progressive definition of human thermophysical properties, and development of TIRI-based thermometric capability, requires successive iterations of empirical measurement and validation from an appropriate benchmarking modality. Moreover, the information attainable by TIRI alone is insufficient for generation of inverse bioheat transfer solutions with sufficient fidelity for the demanding clinical applications that stand to gain from TIRI's fulfilment of its potential. Without infusion of thermometric information from an appropriate complementary modality, cross-constraint of the inverse problem and generation of solutions with clinically acceptable fidelity will remain intractable.

Accordingly, a logical next step toward the advancement of TIRI for clinical applications is a highly controlled laboratory study to provide a deep understanding and characterisation of the nature of human skin emissivity. In turn, this deeper understanding will enable us to design better image acquisition protocols. In summary, this chapter has demonstrated successful TIRI-based HSDD on real clinical TIRI data, and motivated the goal of the following chapter, which entails a detailed laboratory-based investigation to further our understanding of human skin emissivity as the salient factor both driving and limiting specificity in clinical TIRI (Arthur & Khan, 2013).

CHAPTER 7

REASSESSING THE EMISSIVITY MODEL

CHAPTER SUMMARY

This chapter investigates whether the conventional model of regime-independent emissivity is adequate for use in the more temperature-critical next generation applications such as heat source depth determination. This chapter describes experiments conducted in a controlled environment at FLIR Systems Calibration Laboratory which showed that human skin emissivity varies significantly across clinically-relevant regimes of wavelength and skin type (Arthur & Khan, 2013). These findings motivate a change of practice toward use of regime-specific emissivity models in clinical TIRI applications where absolute temperature accuracy is critical.

5. Emissivity in TIRI

Temperature 'T' [K] is a measure of the energy with which the constituent particles of a material perform a certain type of vibration, specifically, the type of vibration that gives rise to emittance of infrared waves of energy. The Stefan-Boltzmann law **Error! Reference source not found.**) describes an *idealised* relationship between these two related energies; the energy of the particle vibrations 'T' [K], and the energy of the emitted waves 'j' (Wm^{-2}) - where

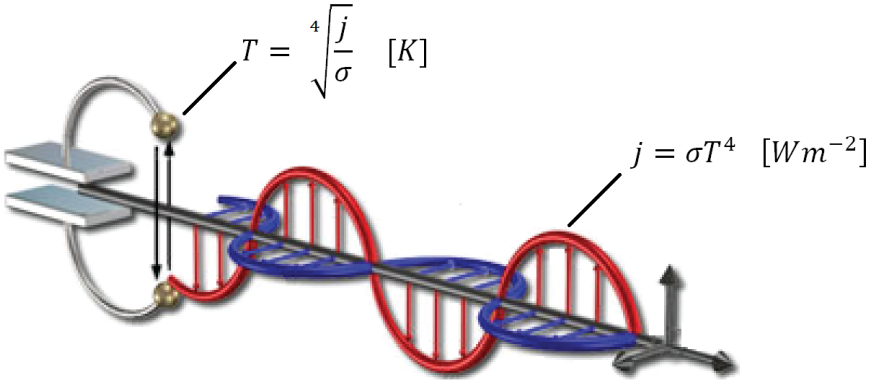

Figure 5-1. Stefan-Boltzmann law relating temperature 'T' (energy of particle vibrations) and emittance 'j' (energy of TIR waves). Image modified from (Spring et al, 2006).

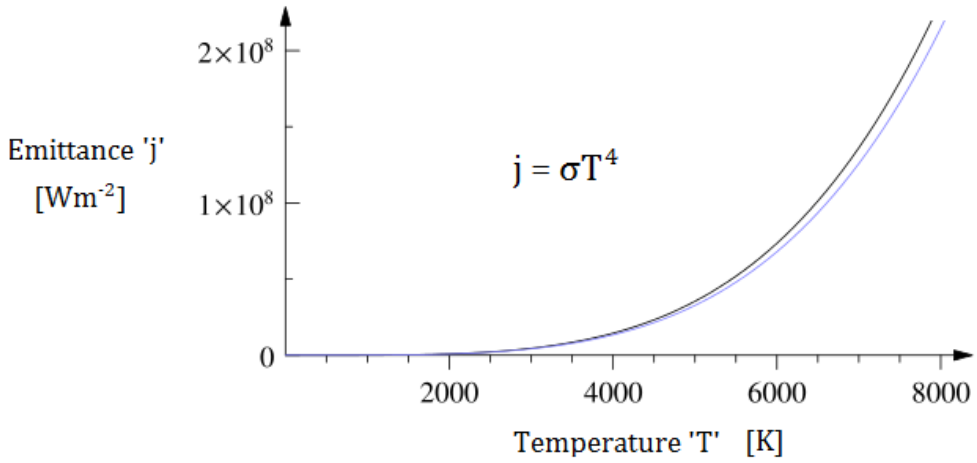

Figure 5-2: Idealised relationship between the temperature and emittance of a perfect 'blackbody' radiator, according to the Stefan-Boltzmann law, Error! Reference source not found..

'σ' is Boltzmann's constant 5.67×10^{-8} [$Wm^{-2}K^{-4}$], derived from the idealised physics of thermal radiation.

Clinical TIRI systems measure 'j' directly, then use the version of the Stefan-Boltzmann law shown **(0.1)** which has been *non-idealised* by inclusion of the emissivity coefficient 'Є', to calculate tissue temperature 'T' [K]. Emissivity is defined as 'the ratio of the energy radiated from a real material 'j' (Wm^{-2}) to that which would be radiated from an idealised 'blackbody' material (**Error! Reference source not found.**) under the same regime of temperature, waveband and viewing conditions. Emissivity is expressed as a dimensionless number with a value between 0.0 and 1.0, where 1.0 represents the idealised emission described by the idealised law in **Error! Reference source not found.**.

$$j = \varepsilon\sigma T^4 \quad [Wm^{-2}] \qquad \leftrightarrow \qquad T = \sqrt[4]{\frac{j}{\varepsilon\sigma}} \quad [K] \qquad \textbf{(5.1)}$$

As the definition implies, regime-dependency is one of the defining characteristics of emissivity, and real non-idealised materials like human tissues can and do exhibit a variety of different emissivities under different regimes of temperature, wavelength, and surface condition. Figure 0-7 illustrates the regime-dependency of a real and idealised objects emissivity in context of the wavelength parameter of a TIRI regime.

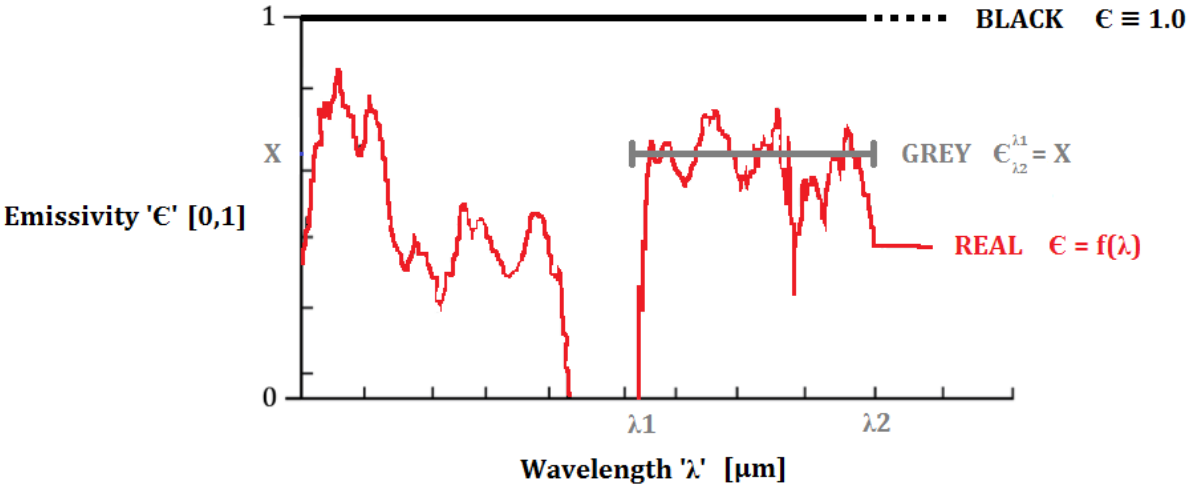

Figure 5-3: Emissivity of real, black, and grey bodies, as a function of wavelength.

In Figure 0-7, the fluctuating red line illustrates the non-linear variability of a real materials emissivity as a function of wavelength, on the clinically-relevant μm scale. Emissivity also varies as a function of multiple other variables which make up a TIRI regime. The key implication of emissivity being multivariate and non-linear, is that emissivity values to be used in **(0.1)** as part of a TIRI application must be empirically measured in the regime of the intended TIRI application, rather than predicted by a mechanistic model.

Conversely, the blackbody emissivity described by the straight black line in crossing all wavelength regimes along the top of Figure 0-7 *was* derived from the mechanistic model described in Figure 5-1 and Figure 5-2. The important difference is that the blackbody model relies upon idealised assumptions of thermodynamic equilibrium and no net flow of energy, which allow it to define a useful baseline from which the emissivities of real materials can be defined, and provide a framework for applied TIRI to produce quantitative absolute image data.

Figure 0-7 also illustrates the 'grey body' model of emissivity, in which a constant emissivity value is used to approximate the real emissivity of a real material over a finite waveband. This grey body model is the emissivity model most commonly used in applied TIRI, including clinical TIRI hitherto. Because emissivity measurement requires a controlled environment and specialised equipment, it is not always possible

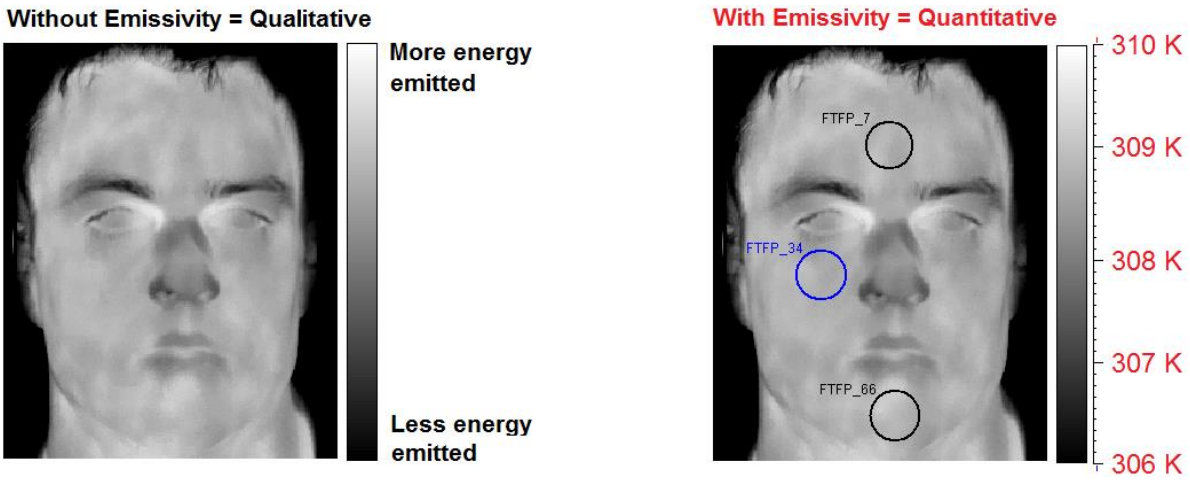

Figure 5-4. The benefit of knowing a materials emissivity – elevates TIRI from qualitative emittance mapping (left), to far more useful absolute temperature mapping (right).

or practical to measure the real emissivity of the specific ROI before each TIRI is acquired in an applied setting. Accordingly, the emissivity values that get used in applied TIRI tend to come from a look-up table, having previously been measured in a controlled environment under an application-relevant regime of TIRI conditions. Although TIRI without emissivity has use in certain screening-type applications for which absolute thermometric accuracy is not critical, the quantification capability that comes with accurate emissivity knowledge allows TIRI to realise its significant potential in far more clinical applications, Figure 5-4.

1.22 The Conventional Emissivity Model in Clinical TIRI

This section describes the conventional model of emissivity used in clinical TIRI hitherto, and explains why it may not be adequate for use in advanced clinical applications in which accuracy of absolute tissue temperature measurements is

critical. The conventional model of emissivity use in clinical TIRI can be summarised as 'a regime-independent greybody model with a value of 0.98'. Although this model has been applied across variations in all regime parameters, the most frequently and significantly varied are waveband (MWIR vs LWIR), and surface condition (i.e. skin type from on anatomic location to another).

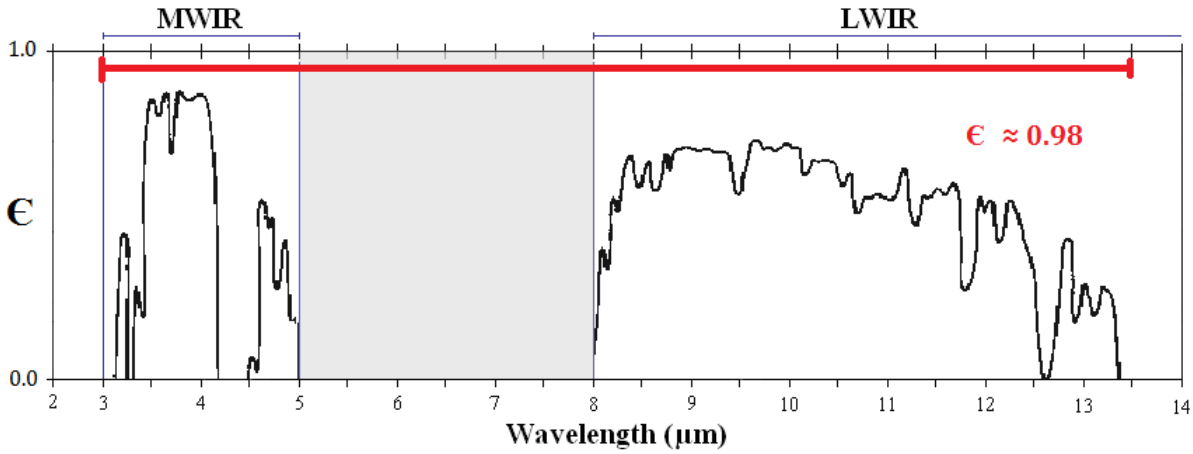

Figure 5-5. Conventional emissivity model - regime-independent greybody value of 0.98.

This conventional model has use in applications where precise mapping of tissue temperature were not critical, such as mass screening for febrile temperature profiles within crowds of people at airports during the recent SARS and avian flu pandemics. An isolated departure from this conventional model was explored during the DARPA HID (Human Identification at Distance) program (DARPA, 2000-2003), in which a model of selective emissivity was integrated as a surface boundary condition into a more comprehensive bioheat transfer model of human skin, with significant transmissivity in the most superficial layers, and significant absorptivity in the deepest tissue layers, Figure 5-6 (b).

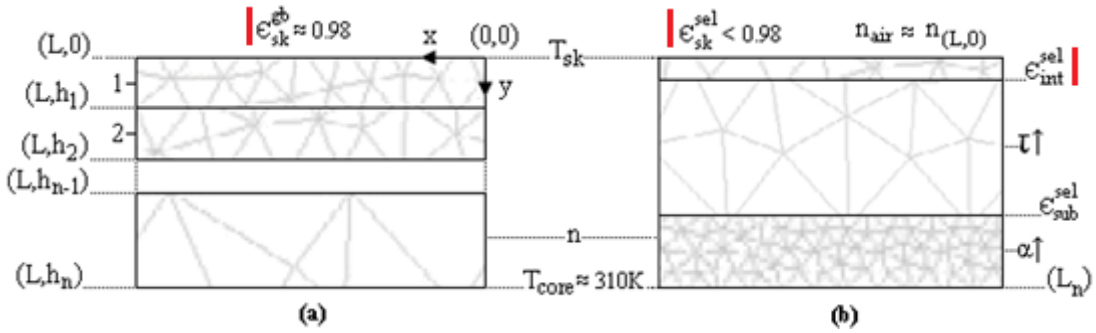

Figure 5-6. The two leading bioheat transfer models of human skin featuring the conventional regime-independent skin emissivity model at (L, 0) with all subsurface heat transfer considered conductive and convective, as in (Çetingül & Herman, 2010b), (b) Selective emissivity and low index of refraction 'n' at the(L, 0), significant transmissivity in superficial tissue and absorptivity (α) in the deepest tissue layer, as in (DARPA, 2000-2003). Figure (Arthur & Khan, 2013).

The potential inadequacy / limitation of this conventional model can be explained in context of TIRI-guided thermal ablation therapy, which has been identified as one of TIRI's most promising next generation medical applications of the heat source depth determination algorithm demonstrated in the previous chapter (Oley et al., 2009). Thermal ablation therapy is a technique for inducing coagulation necrosis (cell death) within cancerous tumours by precise application of heat with a needle-like applicator. Figure 5-7 illustrates thermal ablation therapy in terms of the delicately temperature-sensitive cellular processes involved.

The role of a TIRI system in a thermal ablation procedure would be to allow the surgeon to observe the increasing temperature of the tumour gradually increasing in real time, making it possible to deliver a far more controlled and accurate heat, whilst minimising damage to healthy surrounding tissue. As shown in Figure 5-7, an error of

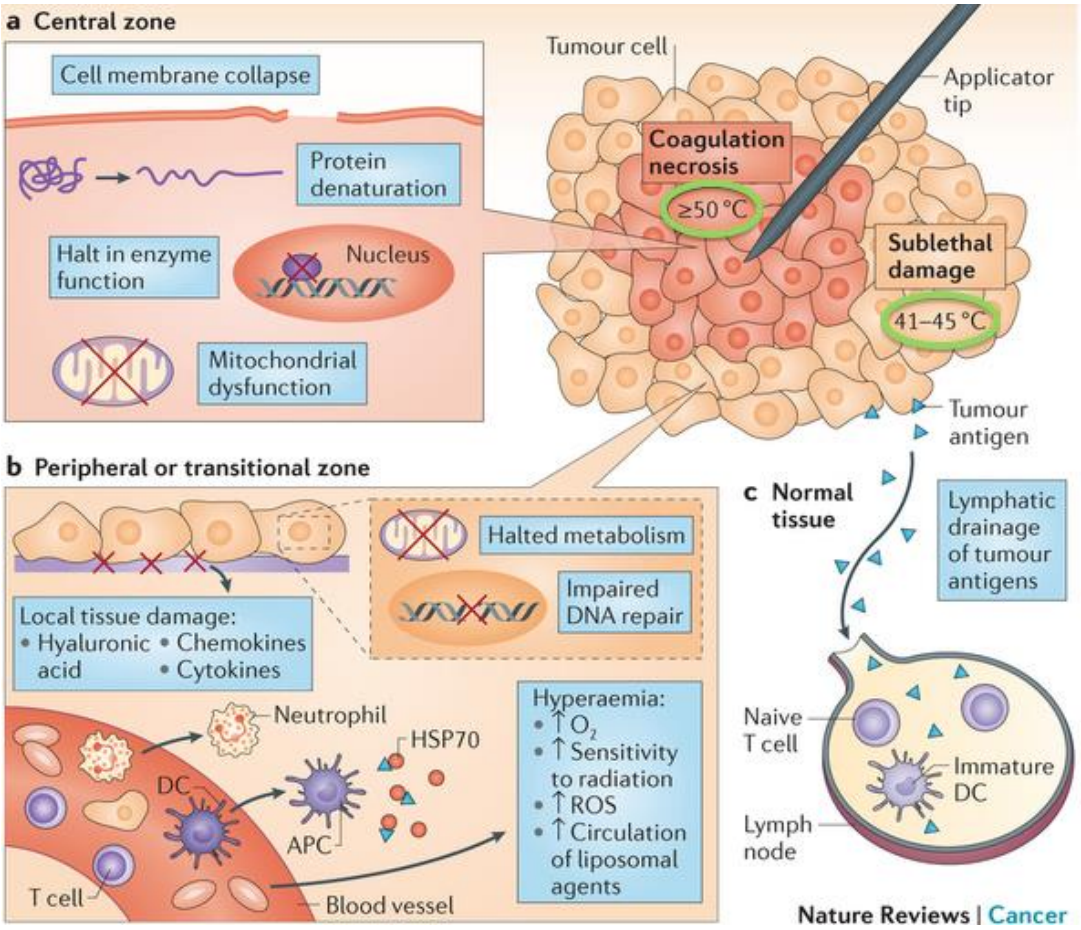

Figure 5-7. Thermal ablation - reproduced with permission from (Chu & Dupuy, 2014).

5°C in absolute tissue temperature measurement (≥50°C vs 41-45°C) can make the difference between successful induction of coagulation necrosis in a malignant cell cluster, and mere induction of sublethal damage which leaves the patient at risk of further potentially fatal metastasis.

Thermal ablation is just one example among many clinical applications in which the physiological significance of a specific absolute temperature makes emissivity critical, such as; cancer diagnostics, intraoperative haemodynamic monitoring, and affective computing (Çetingül & Herman, 2010c; de Weerd, 2010b; M. Khan et al., 2006; Ng & Acharya, 2009). Accordingly, evaluation of the conventional models adequacy for next generation temperature-critical applications requires controlled empirical measurement of skin emissivity across clinically-relevant TIRI regimes.

1.23 Experimental Design

This section documents the process of designing experiments to accurately measure any variations in the emissivity of human skin ROI's that may occur as a result of clinically-relevant changes in TIRI regime. The most clinically-relevant changes in TIRI regime come from changes in the parameters of 'imaging waveband' and 'ROI location'.

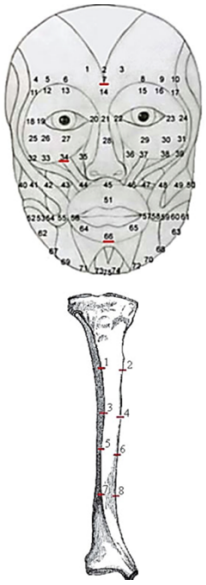

Regime 1: 3.6 - 5.0 µm (MWIR) Facial Skin ROI 308.5 - 310.1 K	**Regime 2:** 7.5 - 13.0 µm (LWIR) Facial Skin ROI 308.5 - 310.1 K
Regime 3: 3.6 - 5.0 µm (MWIR) Pre-Tibial Skin ROI 304.8 - 305.8 K	**Regime 4:** 7.5 - 13.0 µm (LWIR) Pre-Tibial Skin ROI 304.8 - 305.8 K

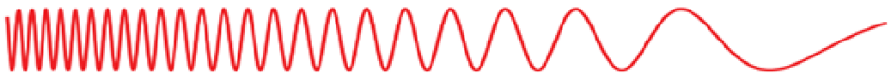

Figure 5-8. Clinically-relevant TIRI regimes across which skin emissivity will be measured.

Due to currently available IR detector technology and associated camera specifications, clinical TIRI can be expected to occur within one of two waveband regimes for the foreseeable future, namely; MWIR (~ 3-5µm), or LWIR (~ 8-13 µm). Accordingly, the waveband parameter will be varied between these to create two clinically-relevant classes of TIRI regimes in which human skin emissivity can be measured, Figure 5-8.

Emittance measurement in regimes 1 and 2 (MWIR) will be performed with a via FLIR SC660 TIRI camera, featuring a 640 x 480 array of uncooled microbolometer IR detectors, an NETD < 30mK, and an IFOV of 0.65 mRad (FLIR, 2009b). Emissions within the 7.5 – 13.0 µm waveband were measured via FLIR 550, featuring a 320 x 240 FPA of Stirling cooled platinum-silicide IR detector elements, NETD < 30 mK, and an IFOV of 1.10 mRad (FLIR, 2009a). Immediately prior to image acquisition, both

cameras were subject to two-point radiometric cavity-blackbody calibration at 298K and 318K (Arthur & Khan, 2013). Detailed manufacturers datasheets for both cameras can be found in the appendices.

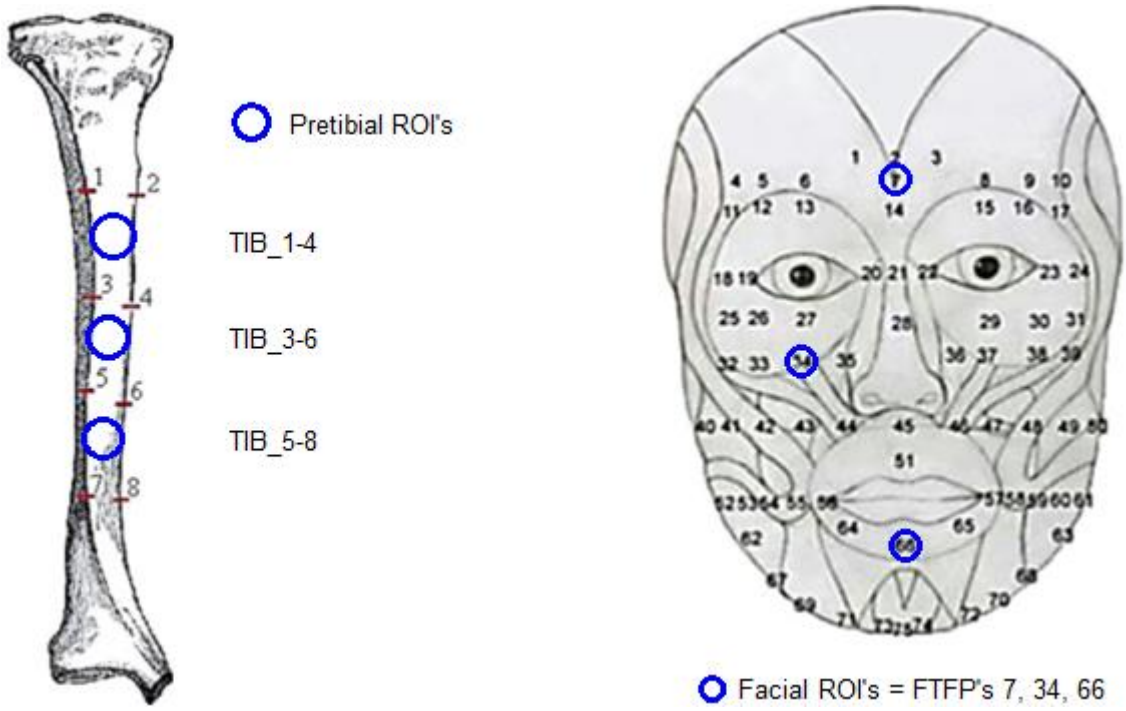

Figure 5-9. ROI's for MWIR and LWIR emissivity measurement. Pretibial ROI's (left) correspond to ADHREC clinical study protocol. Facial ROI's (right) chosen to represent a cross-section of skin types among the FTFP's used in automated affect classification (M. Khan et al., 2006).

With potential for even more variation than the waveband parameter is the anatomic location of the ROI. In context of TIRI regimes, a change in ROI location most importantly constitutes a change in radiating surface material (skin) properties, and to a lesser extent in ROI surface temperature range. In order to meaningfully capture emissivity variance due to ROI location and remain within the scope of this study, it was decided to measure the emissivity of two anatomically-distinct skin ROI's, creating two further classes of TIRI regime, Figure 5-9. These ROIs were identified given the significant differences in emissivity-relevant surface properties of skin at these two locations, the principal investigators' deep experience in handling the idiosyncrasies of facial and pretibial TIRI acquisition and analysis.

Collectively, measurements obtained within each of the 4 regimes in Figure 5-8 should provide sufficient insight to the variability of human skin emissivity across a representative cross-section of clinically-relevant TIRI scenarios to indicate whether or not the conventional regime independent emissivity model is adequate for use in temperature-critical applications going forward. As previously mentioned, accurate measurement of emissivity requires a suitably controllable environment, and specialised equipment.

Moreover, there are two leading techniques for emissivity measurement in the literature, namely; measuring reflectivity and invoking Kirchhoff's law, or by acquiring a TIRI of the ROI next to a radiation source with known emissivity and temperature and directly comparing their emittance. Each of these techniques have advantages and disadvantages. The reflectance technique requires assumption of thermal equilibrium in the ROI. This assumption allows application of Kirchhoff's law **(5.11)**, stating that the emissivity of a body ($\varepsilon_{\lambda T\psi}$) in thermal equilibrium is equal to its absorptivity ($\alpha_{\lambda T\psi}$), Figure 5-10.

$$\varepsilon_{\lambda\psi T} = \alpha_{\lambda\psi T} \qquad \textbf{(5.2)}$$

Considering irradiation of the ROI with emittance of known wave properties from a controlled synthetic source (Sanchez-Marin, 2010); this irradiance must be reflected (ρ), absorbed (α), or transmitted (τ) as described in **(5.3)**:

$$\rho_{\lambda\psi T} + \alpha_{\lambda\psi T} + \tau_{\lambda\psi T} = 1 \quad \xrightarrow{yields} \quad \alpha_{\lambda\psi T} = 1 - \rho_{\lambda\psi T} - \tau_{\lambda\psi T} \qquad \textbf{(5.3)}$$

Substituting **(7.1)** into **(5.3)**, allows expression of emissivity (Ɛ) in terms of reflectivity (ρ) and transmissivity (τ), **(5.4)** and Figure 5-10:

$$\varepsilon_{\lambda\psi T} = 1 - \rho_{\lambda\psi T} - \tau_{\lambda\psi T} \qquad \textbf{(5.4)}$$

$$\tau_{\lambda\psi T} = 0 \quad \xrightarrow{yields} \quad \varepsilon_{\lambda\psi T} = 1 - \rho_{\lambda\psi T} \qquad \textbf{(5.5)}$$

Assuming zero transmissivity in the ROI, then gives emissivity in terms of reflectivity (ρ) as in Figure 5-11:Considering clinical TIRI of a human ROI in absence of the aforementioned applied irradiance, the total TIR flux incident upon the array of infrared detectors inside the TIRI camera 'Φ_0' is a combination of: emittance from the human ROI 'j_{ROI}', direct irradiation by the ambient atmosphere Φ_{atm}, and indirect atmospheric irradiance via reflection from the ROI $\rho\Phi_{atm}$, as in Figure 5-13:

$$\emptyset_0 = j_{ROI} + \emptyset_{atm} + \rho\emptyset_{atm} \qquad \textbf{(5.6)}$$

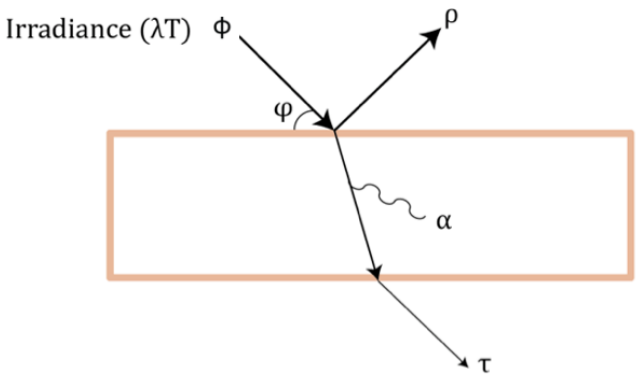

Figure 5-10. Relationship of reflection (ρ), absorption (α), and transmission (τ) to irradiance (Φ), applicable to the L0 air-skin interface in the radiative bioheat transfer models shown Figure 5-6.

Following introduction of the aforementioned synthetic irradiance 'Φ_L', the total irradiance of the FPA may be given by **(5.7)**:

$$\emptyset_1 = j_{ROI} + \emptyset_{atm} + \rho\emptyset_{atm} + \rho\emptyset_L \qquad \textbf{(5.7)}$$

Subtraction of **(5.6)** from **(5.6)** gives the reflectivity of the ROI in terms of flux values that are either already known or readily measurable, as in **(5.8)**

$$\emptyset_1 - \emptyset_0 = P\emptyset_L \quad \xrightarrow{yields} \quad \rho = \frac{\emptyset_1 - \emptyset_0}{\emptyset_L} \qquad \textbf{(5.8)}$$

Substituting **(5.8)** back into **(5.5)** then gives emissivity (**Ɛ**) in terms of these readily measurable and known infrared flux values, as in **(5.9)**:

$$\varepsilon_{\lambda\psi T} = 1 - \frac{\emptyset_1 - \emptyset_0}{\emptyset_L} \qquad \textbf{(5.9)}$$

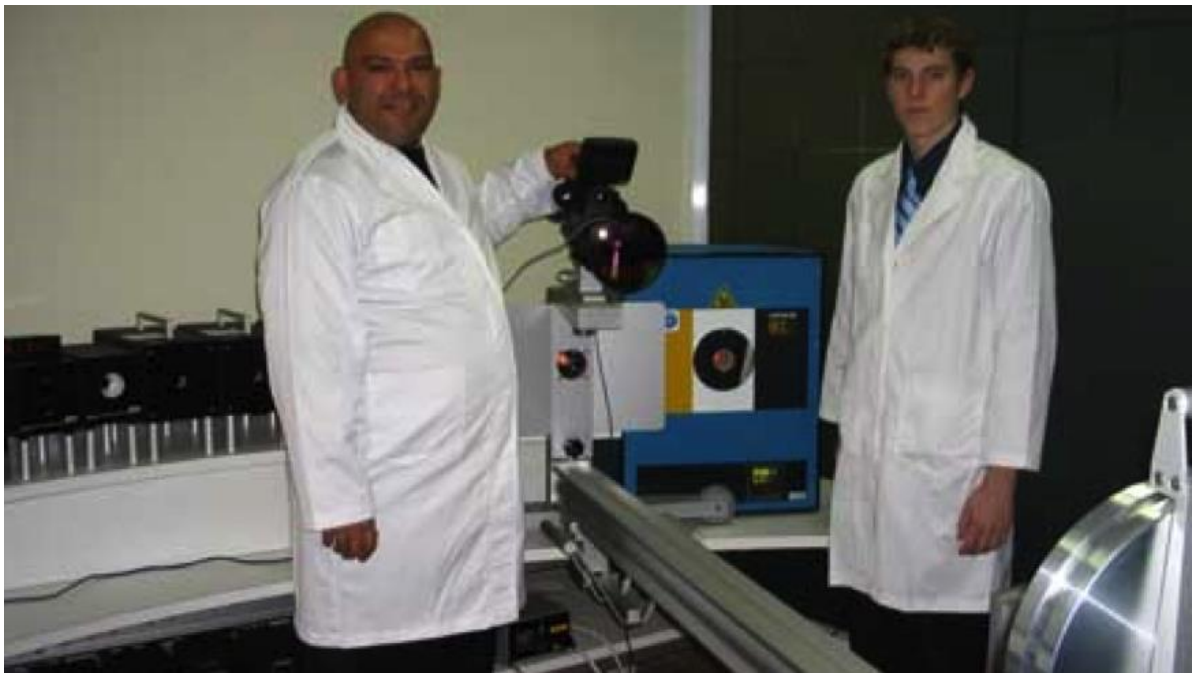

Figure 5-11. Flir Systems Calibration Laboratory, Melbourne Australia. Rigid lens-object distance gantry among a series of greybody emittance sources with controllable surface temperature.

Despite the non-contact benefits of the reflectance technique, the need to assume zero transmissivity in the ROI is undesirable given the model proposed in Figure 5-6b. Emissivity measurement via the greybody comparison technique requires no such assumption, and is preferred by our research partners at FLIR Systems Calibration Laboratory, Figure 5-11. The greybody comparison technique involves the following steps (Figure 5-11):

1. The ROI is placed next to a synthetic greybody radiation source which has known calibrated emissivity (≈1.0) and controllable surface temperature.
2. ROI surface temperature is measured with a calibrated contact thermometer.
3. Greybody temperature is set to be equal to ROI surface temperature.
4. A single TIRI capturing emittance from both the greybody and ROI is acquired.
5. Because intensity differences between ROI and greybody pixels are entirely due to emissivity difference, and the emissivity of the greybody is known, emissivity of the ROI is easily recovered.

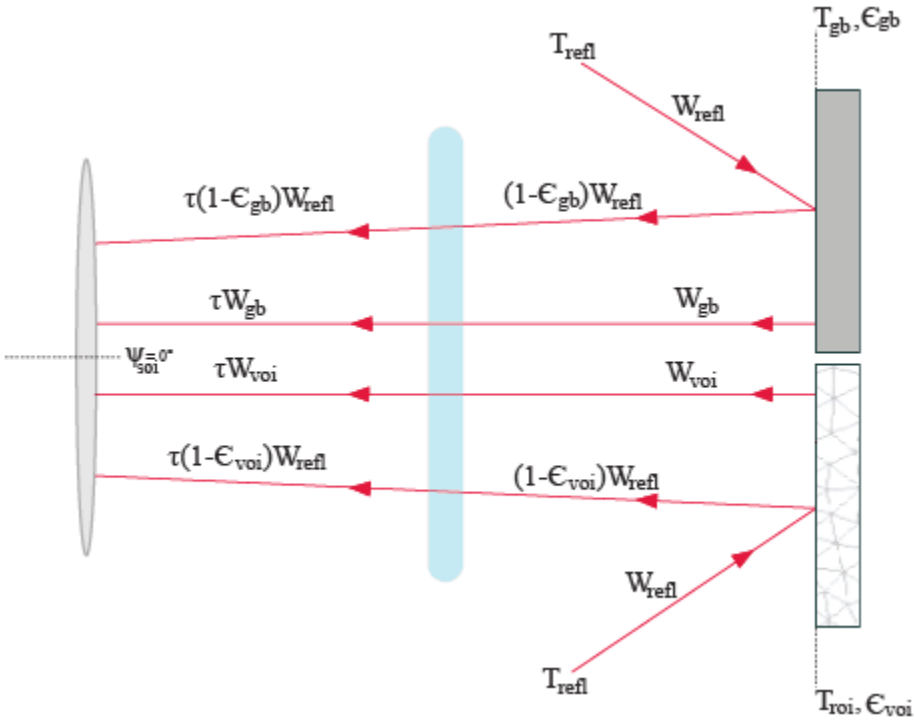

Figure 5-12. Setup for emissivity measurement via simultaneous measurement of emittance from the ROI and a source with known emissivity and temperature (Arthur & Khan, 2013).

Figure 5-12 illustrates the experimental setup for emissivity measurement via the greybody comparison technique. The skin ROI is represented by the white rectangle shown bottom right, and temperature and emissivity of the skin ROI are represented by T_{roi} and ϵ_{roi}, respectively. The product of T_{roi} and ϵ_{roi} is the thermal infrared emittance from the ROI, which is represented as W_{roi}. Similarly, the synthetic greybody

radiation source with known emissivity and controllable temperature is represented by the dark grey rectangle adjacent to the skin ROI shown upper right, and the temperature and emissivity of the greybody are represented by T_{gb} and ϵ_{gb}, respectively.

At the time of image acquisition, greybody temperature (T_{gb}) ROI temperature (T_{roi}) and are equal. The temperature of and emittance from any sources in the lab other than the ROI and the synthetic greybody are collectively represented by T_{refl} and W_{refl}. The blue region in the centre of **Error! Reference source not found.** represents the ambient image acquisition atmosphere, with τ representing % transmittance, which is the % of MWIR/LWIR emittance that is not absorbed by the molecules in the atmosphere and can pass through the atmosphere over short distances.

A contact probe (Figure 5-13) was constructed for optimal stand-alone measurements of Tsk (skin surface temperature) and T_{bb} (blackbody temperature). A

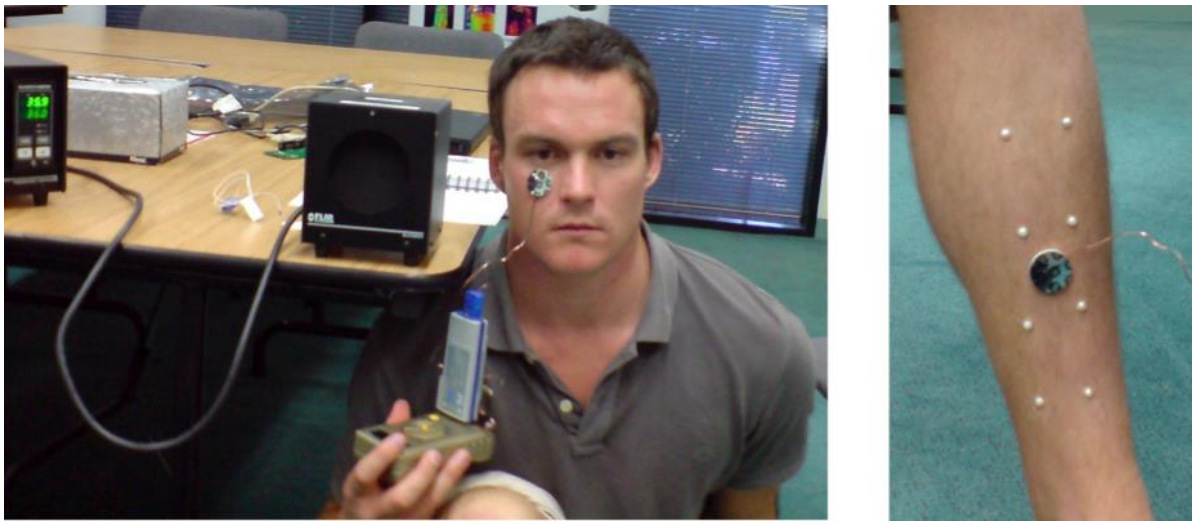

Figure 5-13. Purpose built contact probe for measuring ROI and greybody surface temperature in greybody comparison technique for emissivity measurement (Arthur & Khan, 2013).

25-mm diameter circular M1024222 GE-Health skin contact pad was used to affix the sensor head to the skin and blackbody surface ROIs. The M1024222 contact pad features hypoallergenic non-irritating non-sensitising adhesive, light flexible 3mm thick foam body, and a Mylar backing surface to eliminate ambient interference. The

potential for introduction of TIR artefacts due to application and removal of the contact pad was evaluated and dismissed via visual inspection of ROI TIRIs taken pre and post -pad application.

A type-T, 32 standard wire gauge PVC-coated Dural thermocouple was used as the embedded temperature sensor. A Super-MCJ Omega Engineering thermocouple-to-analogue connector was used to relay the measured surface temperatures to an Agilent U1272 a digital multimeter, giving readings to 0.1K. The human subject was allowed a nominal 30-minute period to equilibrate to ambient laboratory conditions at seated rest prior to measurement. During said period, facial and tibial ROIs were left uncovered, and periodically observed under real-time LWIR TIRI to qualitatively assess emissive stability.

Following equilibration, contact T_{sk} measurements were made at the subjective ROI. The contact probe was then removed from the skin ROI and applied to the surface of the greybody emitter; T_{bb} was then adjusted until achieving $T_{bb} = T_{sk}$. The ambient atmospheric conditions were entered manually into the camera to facilitate accurate compensation via online proprietary FLIR algorithms, and scene emittance was then measured in both MWIR and LWIR bands.

In accordance with thermoneutral conditions prescribed by the cybernetic 'IESD-Fiala ANSYS CFX' model of human thermoregulation in controlled indoor environments, ambient laboratory air temperature, humidity, and velocity were maintained at 294 (± 1.0) K, 46 (± 1.0) %, and < 0.1ms^{-1}, and monitored via Vaisala HUMICAP® HMP155 and DANTEC FiberFlow®, respectively. Immediately prior to image acquisition, emissivity and surface temperature values of the surrounding wall and ceiling surfaces were recorded at 0.92-0.96 and 293-296K respectively, as calculated via 2-point calibrated FLIR SC660 TIRI camera.

1.24 Results: Regime Dependence of Skin Emissivity

This section presents the results of experiments to measure the regime-dependent emissivity of human skin in the form of TIRI image data and energy distribution histograms showing emittance from the synthetic greybody and human ROI's within

each of the four regimes. The histograms show each ROI's emittance in terms of a non-calibrated unit called Object Signal (OS) which is proprietary to FLIR Systems. Because OS is proportional to the amount of energy incident upon the detectors of the particular TIRI camera being used, it allows for direct comparative imaging with calibrated greybody sources in any given waveband, and creates a level playing field for this type of experiment without being influenced by the idiosyncrasies of a particular TIRI cameras responsivity (FLIR, 2004, 2009a, 2009b).

Because MWIR TIRI was performed using a camera with photonic platinum silicide (PtSi) detectors, the MWIR Object signal shown in the histograms below was linear with respect to incident MWIR photons per m^2 of detector per second, as shown **(5.10)**. Similarly, LWIR OS values obtained via the vanadium oxide microbolometers are linear with respect to incident Wm^{-2}. Integration of **(5.10)** or **(5.11)** with respect to wavelength gives the total energy emitted from the ROI at known surface temperature, and thus emissivity, as exemplified in the context of FTFP 34 in **(5.12)**:

$$W_{T\boldsymbol{\lambda}\varphi} = \varepsilon_{T\boldsymbol{\lambda}\varphi} \frac{2\pi hc}{\lambda^5 (e^{\frac{hc}{\boldsymbol{\lambda kt}}} - 1)} \left[W \cdot m^{-2}\right] \qquad \textbf{(5.10)}$$

$$Q_{T\boldsymbol{\lambda}\varphi} = \varepsilon_{T\boldsymbol{\lambda}\varphi} \frac{2\pi hc}{\lambda^5 (e^{\frac{hc}{\boldsymbol{\lambda kt}}} - 1)} \left[\gamma \cdot m^{-2} \cdot sec \cdot \mu m^{-1}\right] \qquad \textbf{(5.11)}$$

$$\rightarrow \varepsilon_{\lambda,309K}^{FTFP\_34} = \frac{W_{7.5-13.0\mu m}^{FTFP\_34}}{\int_{7.5}^{13.0} \frac{2\pi hc^2}{\lambda^5 (e^{\frac{hc}{k309K}} - 1.0)} \delta\lambda} = 0.92 \qquad \textbf{(5.12)}$$

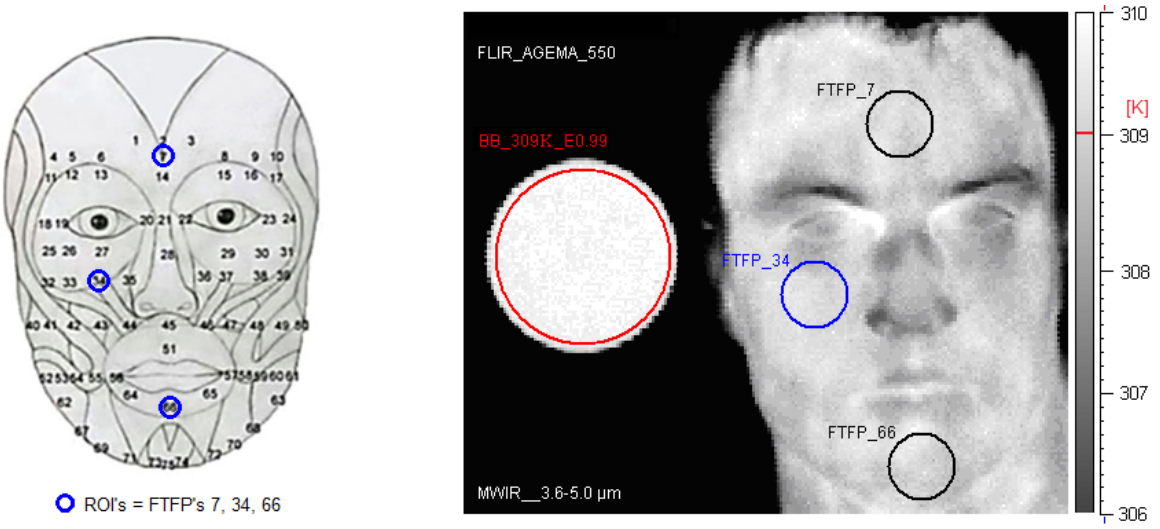

Figure 14. TIRI acquired in regime 1 to measure MWIR emissivity of facial skin ROI's.

Figure 14 shows a TIRI of 3.6-5.0µm emittance from a 309K greybody with emissivity of 0.99 and a 309K facial ROI with emissivity to be determined. The difference in pixel intensity between the greybody and skin ROI is obvious, and corresponds to an emissivity difference of 0.05 (= 0.99 - 0.94), but energy differences ~100 OS, as shown in Figure 5-16 to Figure 5-18. This contrasts with the 7.5 – 13.0 µm LWIR situation in Figure 5-15, characterised by a less obvious brightness contrast from greybody to facial ROI, and ΔOS values between LWIR greybody and facial energy distributions on the order of ~10, as visible in Figure 5-19 to Figure 5-21.

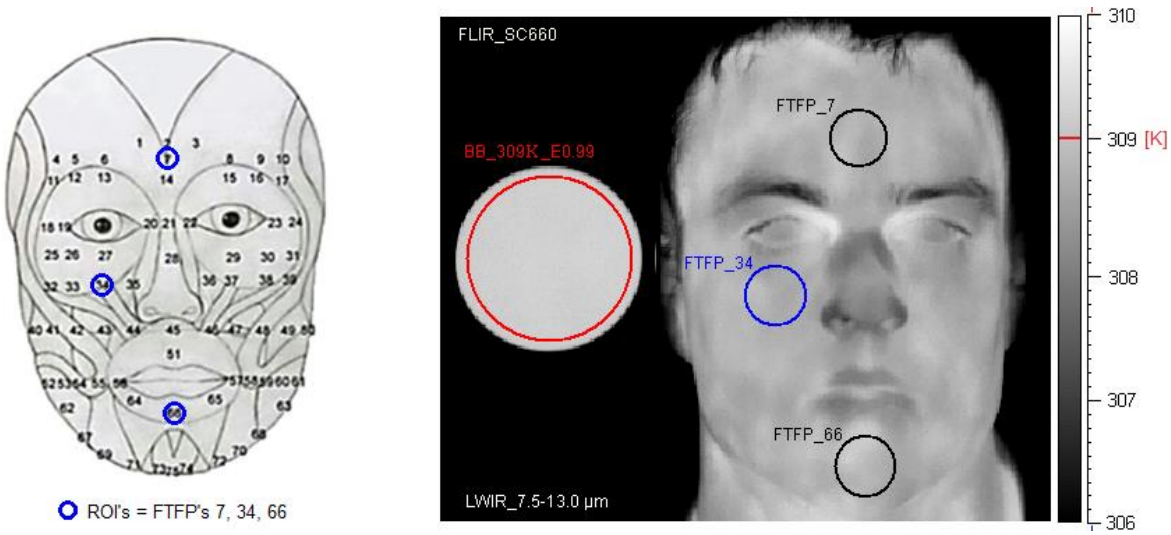

Figure 5-15. TIRI acquired in regime 2 to measure LWIR emissivity of facial skin ROI's.

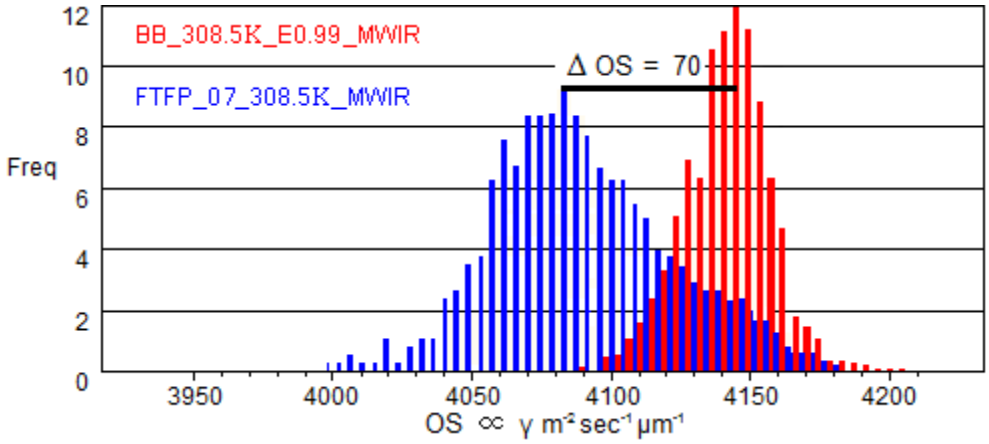

Figure 5-16. MWIR Emittance Histogram from FTFP_7 and an equal temperature greybody.

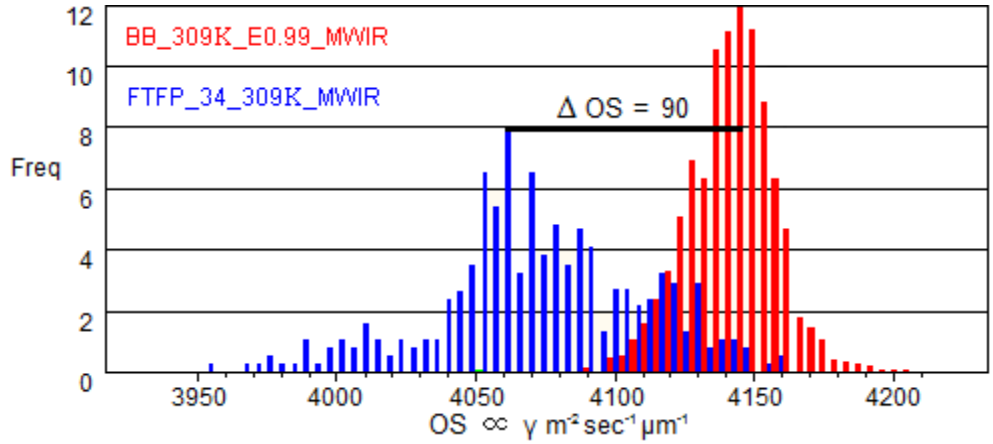

Figure 5-17. MWIR Emittance Histogram from FTFP_34 and an equal temperature greybody.

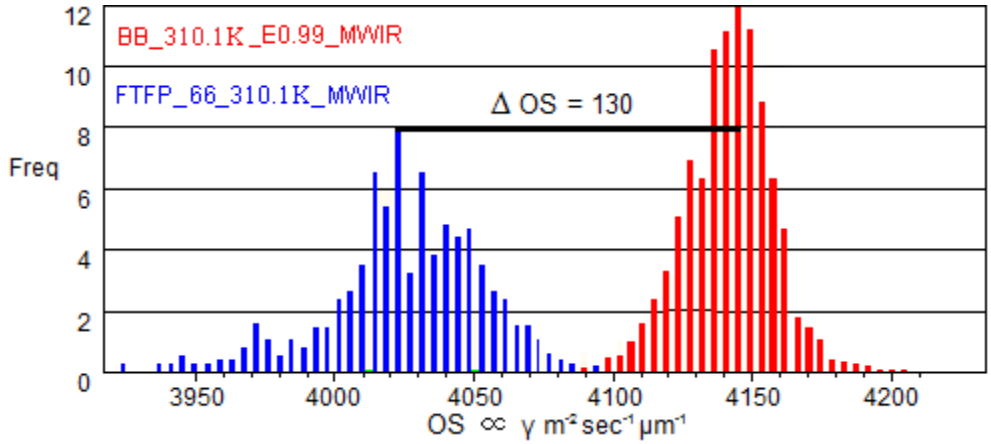

Figure 5-18. MWIR Emittance Histogram from FTFP_66 and an equal temperature greybody.

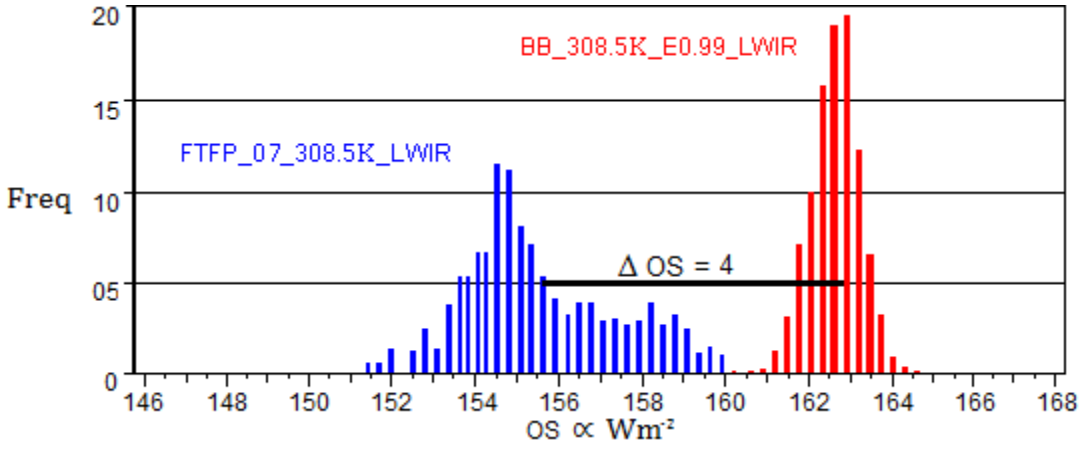

Figure 5-19. LWIR Emittance Histogram from FTFP_7 and an equal temperature greybody.

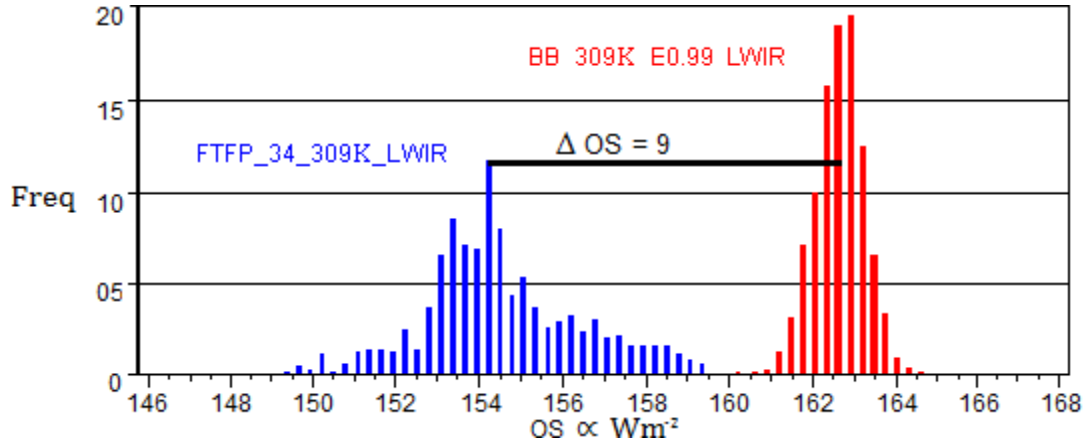

Figure 5-20. LWIR Emittance Histogram from FTFP_34 and an equal temperature greybody.

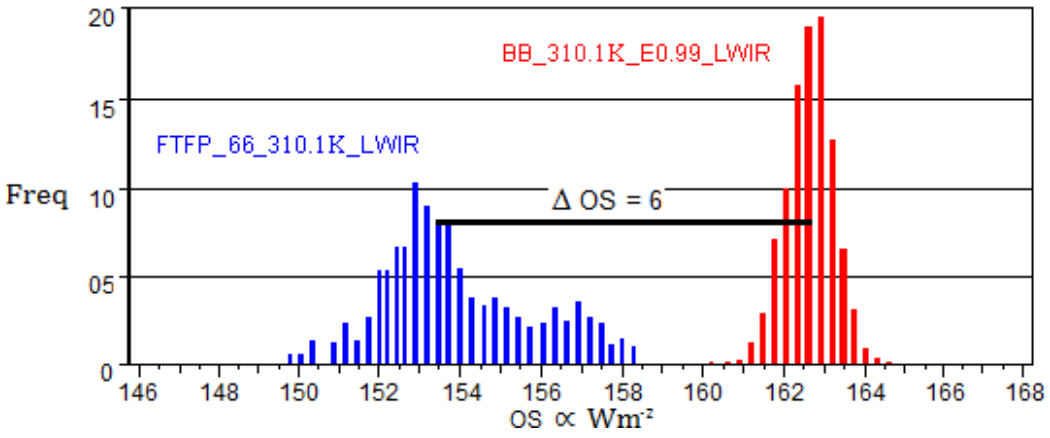

Figure 5-21. LWIR Emittance Histogram from FTFP_66 and an equal temperature greybody.

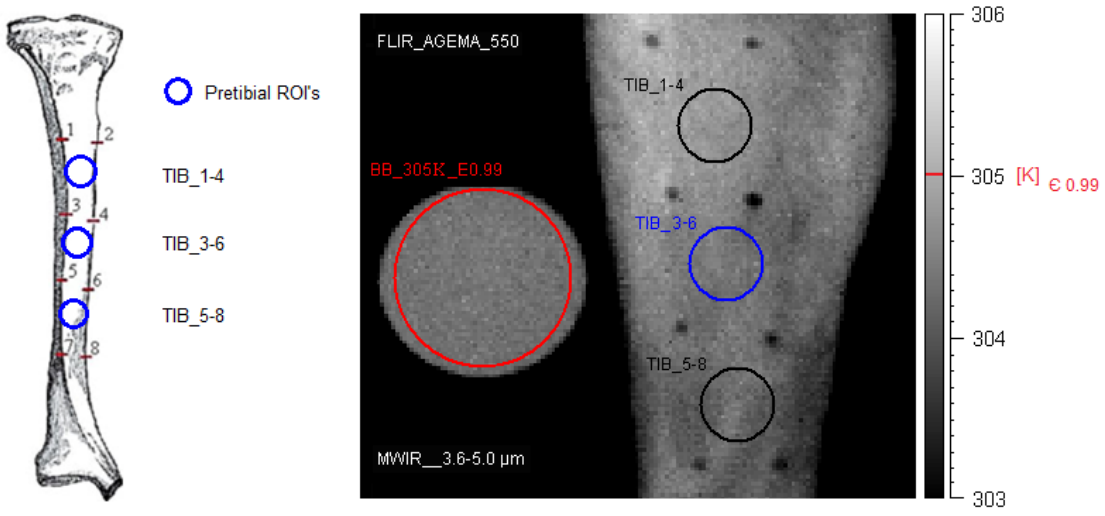

Figure 5-22. TIRI acquired in regime 3 to measure MWIR emissivity of Pre-Tibial skin ROI's

The indistinguishable pixel intensities the ROI's and greybody in Figure 5-22 suggest that the MWIR emissivity of the tibial ROI's is extremely close to the known 0.99 emissivity of the controllable greybody source. Moreover, the emittance histograms in figures Figure 5-24, Figure 5-25, and Figure 5-26 are almost completely overlapping. The LWIR emissivity however is characterised by clear intensity difference in Figure 5-23, and clear ΔOS separation in the emittance distributions shown in

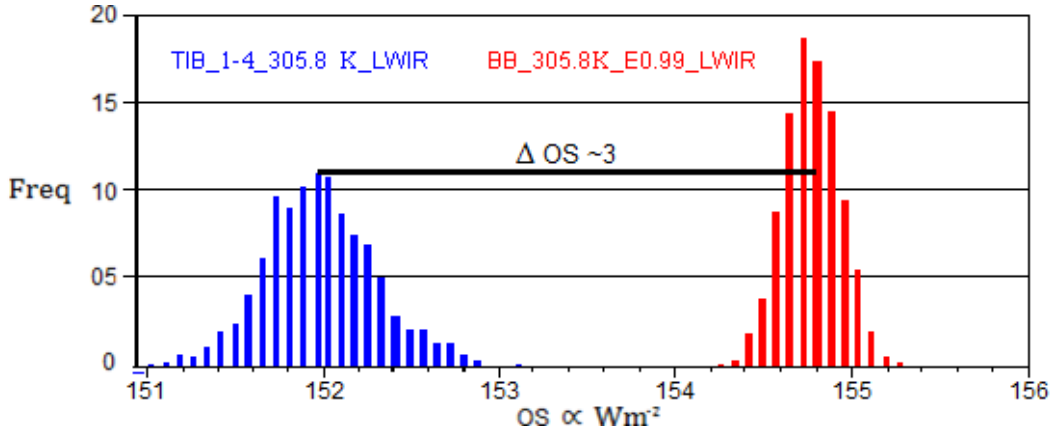

Figure 5-27, Figure 5-28 and Figure 5-29.

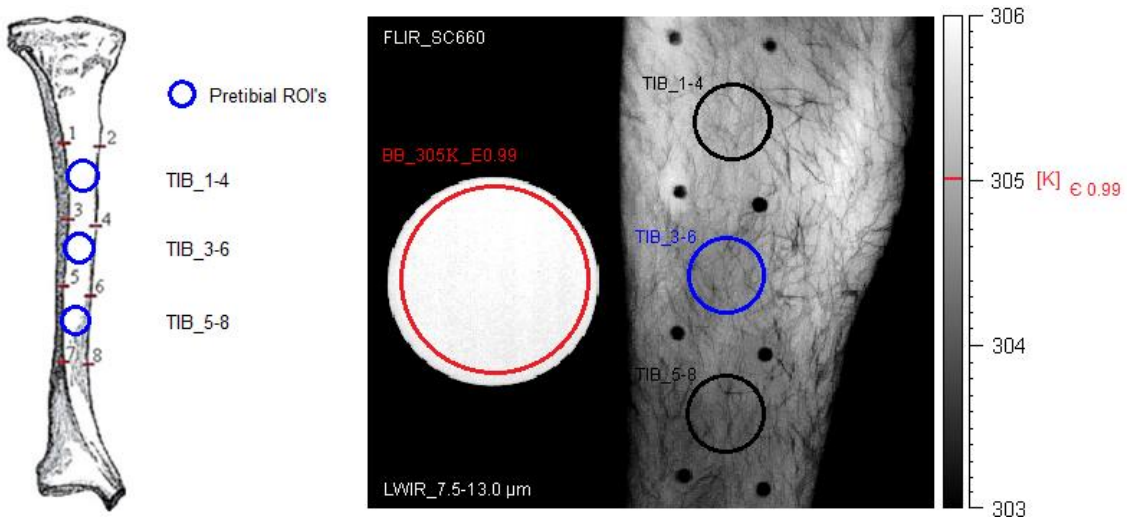

Figure 5-23. TIRI acquired in regime 4 to measure LWIR emissivity of Pre-tibial skin ROI's.

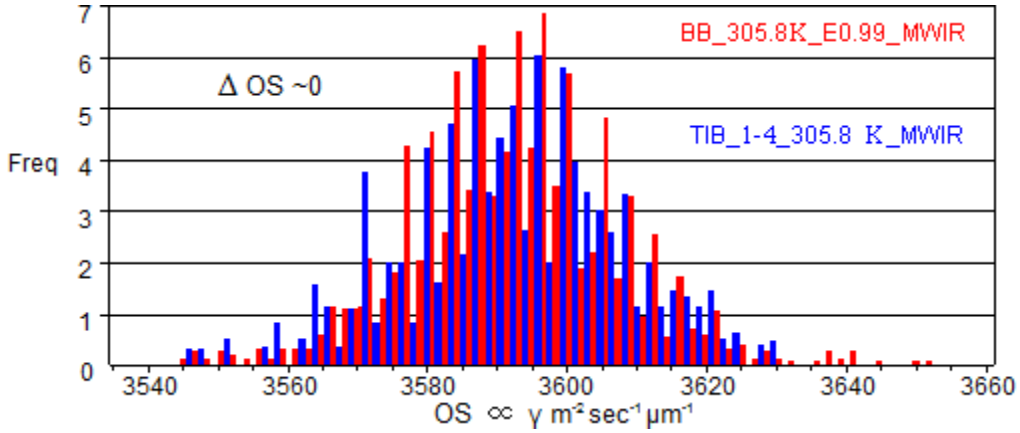

Figure 5-24. MWIR Emittance Histogram from TIB_1-4 and an equal temperature greybody.

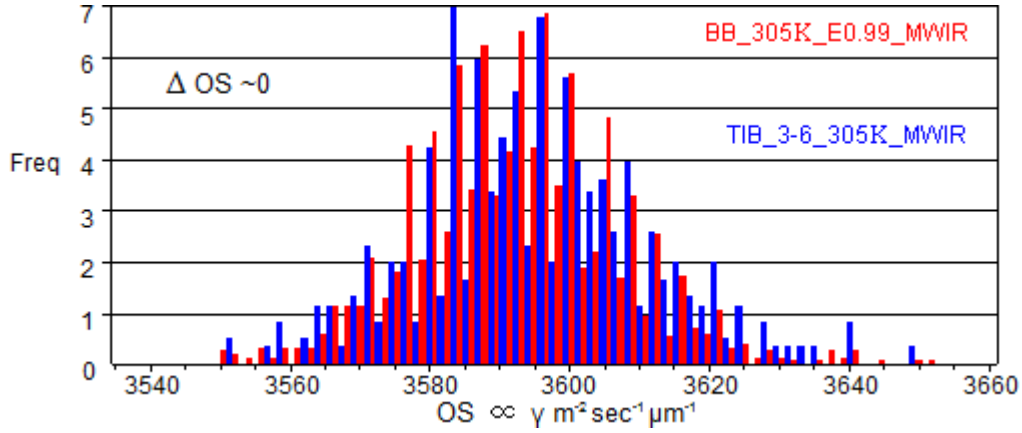

Figure 5-25. MWIR Emittance Histogram from TIB_3-6 and an equal temperature greybody.

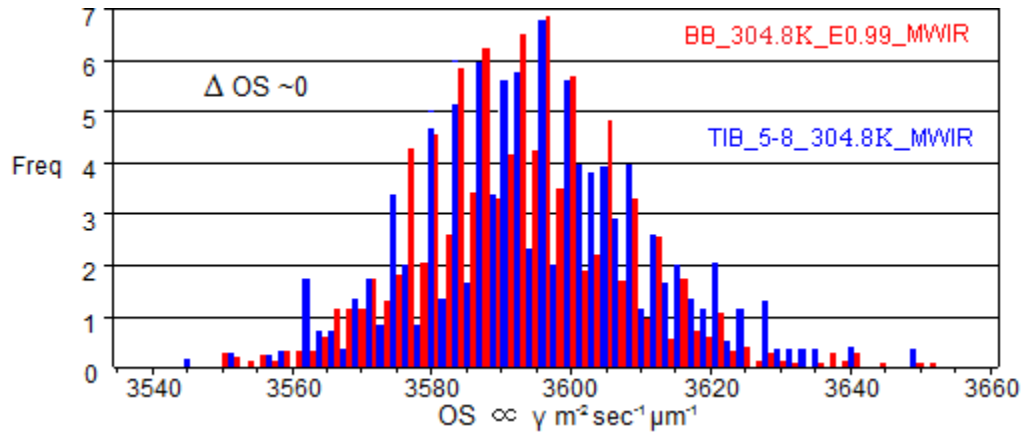

Figure 5-26. MWIR Emittance Histogram from TIB_5-8 and an equal temperature greybody.

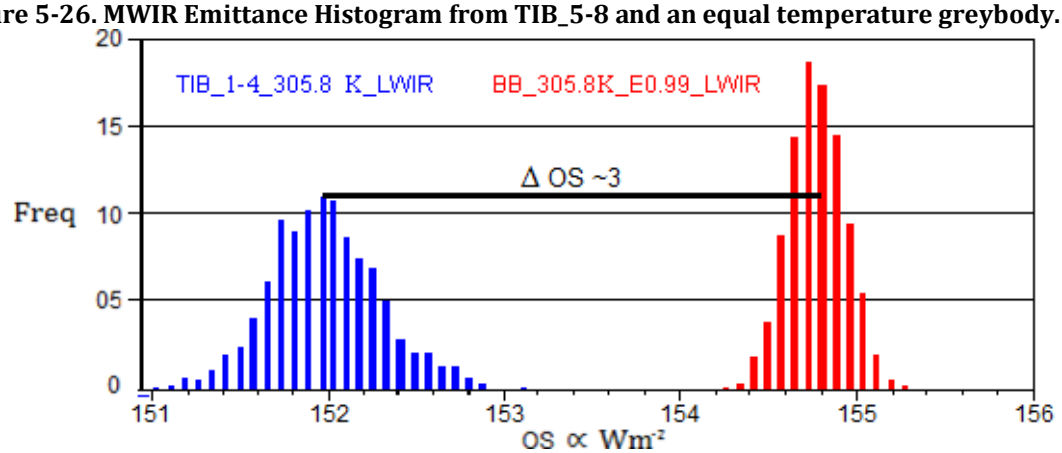

Figure 5-27 LWIR Emittance Histogram from TIB_1-4 and an equal temperature greybody.

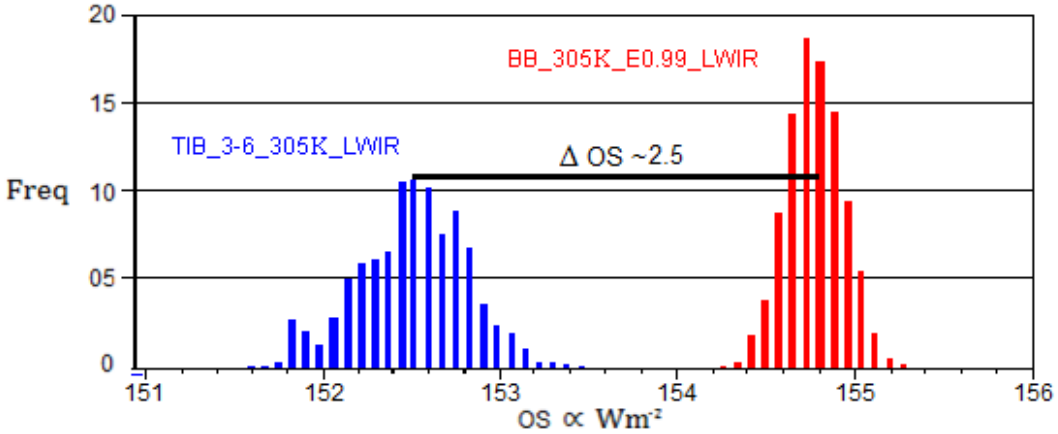

Figure 5-28. LWIR Emittance Histogram from TIB_3-6 and an equal temperature greybody.

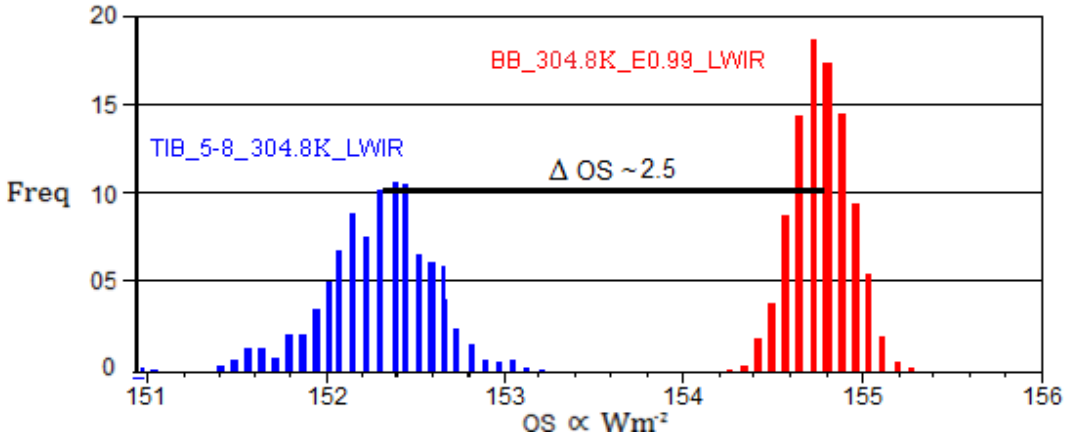

Figure 5-29. LWIR Emittance Histogram from TIB_5-8 and an equal temperature greybody.

Table 5-1. Experimentally determined emissivity (ε) values.

Spectral ROI	Temp Contact [K]	Temp TIRI [K]	SD	ε [0, 1]
FTFP_07 MWIR	308.5	308.4	0.2	**0.98**
FTFP_07 LWIR	308.5	308.1	0.2	**0.96**
FTFP_34 MWIR	309	308.5	0.3	**0.94**
FTFP_34 LWIR	309	308.1	0.2	**0.92**
FTFP_66 MWIR	310.1	308.5	0.2	**0.85**
FTFP_66 LWIR	310.1	308.3	0.3	**0.87**
TIB_1-4 MWIR	305.8	305.6	0.1	**0.98**
TIB_1-4 LWIR	305.8	304.1	0.1	**0.83**
TIB_3-6 MWIR	305	305	0.1	**0.99**
TIB_3-6 LWIR	305	303.8	0.1	**0.86**
TIB_5-8 MWIR	304.8	304.8	0.2	**0.99**
TIB_5-8 LWIR	304.8	303.4	0.2	**0.85**

To boost the statistical power of

Table 5-1's clinically relevant insights into emissivity variation, radiometric analyses were performed upon a random sample of 10 clinical TIRI data sets taken from the #592-10 data base acquired at the Australian Army Medical Centre, Figure 5-30 (Arthur et al., 2011b). For each image, skin surface temperature and contact-inferred emissivity corresponding to three left-leg ROIs (TIB_1–4, TIB_3–6, and TIB_5–8) were calculated as per the mean energy and ROI emissivity equations **(5.13)** and **(7.13)** proposed in (DARPA, 2000-2003; L. B. Wolff et al., 2005). In **(5.13)** and **(7.13)**, $\bar{e}_{s\_LWIR}$ represents the mean LWIR energy detected as emittance from the ROI, $\bar{e}_{BBTs}$ represents blackbody energy at skin temperature, $\bar{T}_s$ is

Table 5-2. Contact-measured skin surface temperature and emissivity at 3 tibial ROI's.

Participant #	Tibial ROI	TIRI Temperature [K]	Emissivity (ε)
1	**TIB_1-4 $_{LWIR}$**	303.4	**0.94**
	TIB_3-6 $_{LWIR}$	301.6	**0.92**
	TIB_5-8 $_{LWIR}$	300.4	**0.91**
2	**TIB_1-4 $_{LWIR}$**	305.1	**0.95**
	TIB_3-6 $_{LWIR}$	302.3	**0.93**
	TIB_5-8 $_{LWIR}$	301.2	**0.92**
3	**TIB_1-4 $_{LWIR}$**	302.3	**0.93**
	TIB_3-6 $_{LWIR}$	301.6	**0.92**
	TIB_5-8 $_{LWIR}$	300.7	**0.91**
4	**TIB_1-4 $_{LWIR}$**	304.1	**0.94**
	TIB_3-6 $_{LWIR}$	303.2	**0.94**
	TIB_5-8 $_{LWIR}$	302.7	**0.93**
5	**TIB_1-4 $_{LWIR}$**	304.1	**0.94**
	TIB_3-6 $_{LWIR}$	302.8	**0.93**
	TIB_5-8 $_{LWIR}$	301.9	**0.92**

6	**TIB_1-4 LWIR**	302.8	**0.93**
	TIB_3-6 LWIR	302	**0.92**
	TIB_5-8 LWIR	301.3	**0.92**
7	**TIB_1-4 LWIR**	303.1	**0.93**
	TIB_3-6 LWIR	302.6	**0.93**
	TIB_5-8 LWIR	302	**0.92**
8	**TIB_1-4 LWIR**	302.9	**0.93**
	TIB_3-6 LWIR	302.1	**0.93**
	TIB_5-8 LWIR	301.3	**0.92**
9	**TIB_1-4 LWIR**	303.3	**0.94**
	TIB_3-6 LWIR	302.5	**0.93**
	TIB_5-8 LWIR	301.4	**0.92**
10	**TIB_1-4 LWIR**	304.7	**0.95**
	TIB_3-6 LWIR	303	**0.93**
	TIB_5-8 LWIR	302.1	**0.93**

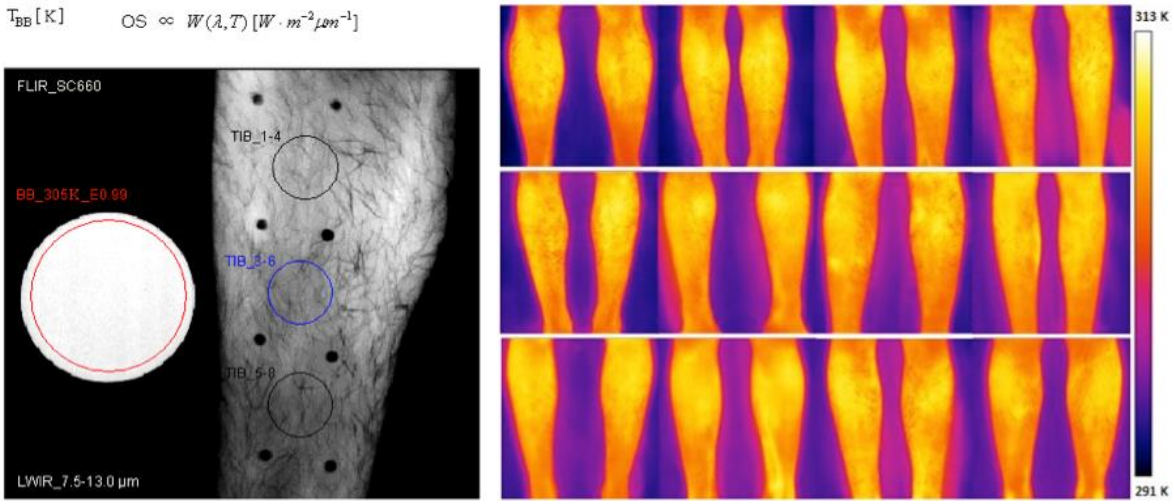

Figure 5-30. (a) Laboratory data, (b) clinical validation data - radiometrically calibrated blackbody-temperature TIRI's of 12 recruits used in the validation. For clinical data, total emissive energy and contact-inferred emissivity at TIB_1–4, TIB_3–6, and TIB_5–8 were calculated with the method reported in (DARPA, 2000-2003; L. B. Wolff et al., 2005).

average skin temperature in the ROI, $T_{BB\bar{T}_S}$ means blackbody temperature, Q represents ROI radiant energy, and λ shows wavelength (L. B. Wolff et al., 2005).

$$\bar{e}_{s\_LWIR} = \bar{e}_{BBT_s} + \frac{\bar{T}_s - T_{BB\bar{T}}}{T_{BB\bar{T}_s}} \quad \textbf{(5.13)}$$

$$\varepsilon_{s\_LWIR} = \frac{\bar{e}_{BBT_s}}{\int_{7.5}^{13.0} Q(\lambda, \bar{T}_s)\delta\lambda} \quad \textbf{(5.14)}$$

$$e_{\lambda b}(\lambda, T) = \frac{2\pi c_1}{\lambda^5 \left(e^{\frac{c_2}{\lambda T}} - 1\right)} \quad [wm^2 \mu m^{-1} sr^{-1}] \quad \textbf{(5.15)}$$

Wherein C_1 and C_2 represent constants in Planck's spectral energy distribution with respective values of 0.59992 x 10^8 W·µm^4 / (m^2 ·sr), and 14387.69 µm·K.

1.25 Discussion and Conclusions

As evident in Table 5-2, the calculated ROI emissivity values differ significantly from the conventionally accepted 'close to blackbody' or '≈ 0.98' emissivity of human skin. The previous calculations are aligned with the generalization of Planck's equation proposed for the LWIR region in (L. B. Wolff et al., 2005) which assumes $C_2/\lambda T << 1$, and expresses emissive power ($e_{\lambda b}$) as in (5.15 **). As illustrated in the TIRI's and emittance histograms above, and summarised in**

Table 5-1, the emissivity of human skin varies considerably across clinically relevant regimes of both regimes of waveband and anatomic ROI location.

Interestingly, it can be seen that both MWIR and LWIR emissivity values obtained via this greybody comparison technique applied at the forehead (FTFP 7) and skin region overlying orbicularis oculi (FTFP 34) agree with those in the literature, as might be expected given that the forehead constitutes a conventional anatomic site for clinical contact thermometry (Arthur & Khan, 2013). It is also interesting to note that emissivity values obtained for non-traditional ROIs differ significantly from those in the literature; the published values empirically derived from contact based and

reflective media display less wavelength dependence, with FTFP_66 (Orbicularis Oris) being consistently less emissive then other FTFP's in both the MWIR and LWIR spectra, ranging from 0.971 to 0.99 (Sanchez-Marin, 2010; Togawa & Saito, 1994).

These observations reinforce the need for calculation of regime-specific emissivity values for use in critical clinical applications. It is also interesting to note the consistency of the wavelength-dependence of tibial emissivity with; all tibial MWIR values within 0.98-0.99, and LWIR values from 0.83-85. In contrast, less wavelength dependence was observed at facial ROI's, with FTFP_66 being consistently less emissive then other FTFP's in both the MWIR and LWIR.

In terms of waveband-specific considerations, the far greater energy densities involved in the MWIR than the LWIR should be considered when designing the thresholds for regime-specific emissivity values. This significant difference in energy density (and perhaps regime size sensitivity) can be noticed from inspection of the absolute OS (object signal) values along the x axes of the emittance histograms above. To quantify the clinical significance of the emissivity variations discovered at FLIR Systems Calibration Laboratory, one can consider the case of pretibial emissivity in the 7.5-13μm LWIR region as in Figure 5-31. A TIRI Illustrating emissivity - the ratio of the energy radiated from a blackbody (left, circular) to a human skin ROI (right, shin) at the same temperature (32°C) and wavelength (LWIR, 7.5-13μm) and under the same viewing conditions. This ROI has an emissivity of 0.83. In application context of TIRI for monitoring of an oncological thermal ablation procedure, use of the conventional model of a 0.98 emissivity value instead of the empirically determined 0.83, translates into a 16% difference in the tissue temperature displayed to the surgeon, which in the case of a 50°C target temperature equates to about ±8°C. If the tumour only reaches 42°C, the cells remain active and harmful to the patient (Figure 5-7), and if the tumour is heated to 58°C there will be unnecessary damage to healthy tissue surrounding the tumour (Figure 5-7).

As the goal of this chapter was to investigate whether the conventional model of regime-independent emissivity is adequate for use in more temperature-critical next generation, the findings motivate a change of practice toward use of regime-specific emissivity models in clinical TIRI applications where absolute temperature accuracy is

critical. Moreover, it is recommended that the transition toward this new practice involve accurate measurement of emissivity at strategic anatomic ROI locations, which are likely to be imaged on many occasions in context of specific clinical TIRI applications. Finally, it is recommended that the scope of this investigation be extended to include measurements of the emissivity of internal tissues, as applicable to open surgical applications.

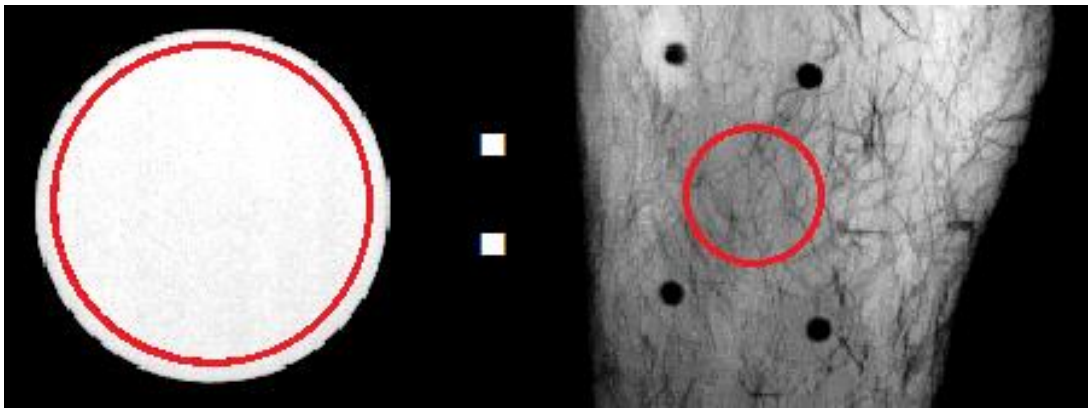

Figure 5-31. A TIRI Illustrating emissivity - the ratio of the energy radiated from a blackbody (left, circular) to a human skin ROI (right, shin) at the same temperature (32°C) and wavelength (LWIR, 7.5-13µm) and under the same viewing conditions. This ROI has an emissivity of 0.83.

CHAPTER 8

KEY FINDINGS & RECOMMENDATIONS

CHAPTER SUMMARY

This chapter discusses the main findings from this thesis work and explains their implications for the future of clinical TIRI. Topics discussed include; clinical protocols, heat source depth determination, and emissivity models. By demonstrating the benefit of objective clinical protocols, this thesis motivates change of practise in both research and application, and expands the scope of clinical TIRI to now include applications requiring the greater specificity that objective protocols afford. By objectively defining the infrared profile of the healthy pre-tibial tissues, this thesis provides the baseline

for TIRI-based management of osseous stress injury, and provides precedent to investigate the usefulness of TIRI in management of similarly superficial thermo-active pathologies.

By demonstrating successful TIRI-based heat source depth determination, this work motivates further research to rigorously evaluate TIRI's potential as a replacement for existing clinical depth determination tasks, such as biopsy-based tumour depth determination. By demonstrating that human skin emissivity varies significantly across clinically-relevant regimes of wavelength and skin type (Arthur & Khan, 2013), this thesis motivates change of practice toward the use of regime-specific emissivity models in all clinical TIRI applications where absolute quantitative accuracy is critical. In addition to discussing the key implications of the aforementioned findings, this chapter also provides specific recommendations for next steps in clinical TIRI research and development.

1.26 Clinical Protocols

This work demonstrated an objective approach to the development of clinical TIRI protocols, and also demonstrated the benefit of using those protocols over a three month clinical study. Like TIRI, the established medical imaging modalities (MRI, X-Ray, etc.) essentially rely on their ability to detect delicate waveform attenuations in order to build useful images. Unlike TIRI however, the established modalities now benefit from being used under strict clinical protocols inside purpose built image acquisition facilities designed to maximise signal to noise ratio. In MRI for example, significant resources are invested in purpose-built MRI suites that feature; active vibration damping, magnetic and acoustic shielding, temperature and humidity control, DC lighting, and quench duct routing. So far, the clinical usefulness of TIRI has

been judged on the basis of data acquired by stand-alone TIRI cameras used without proper protocols, in uncontrolled clinical environments.

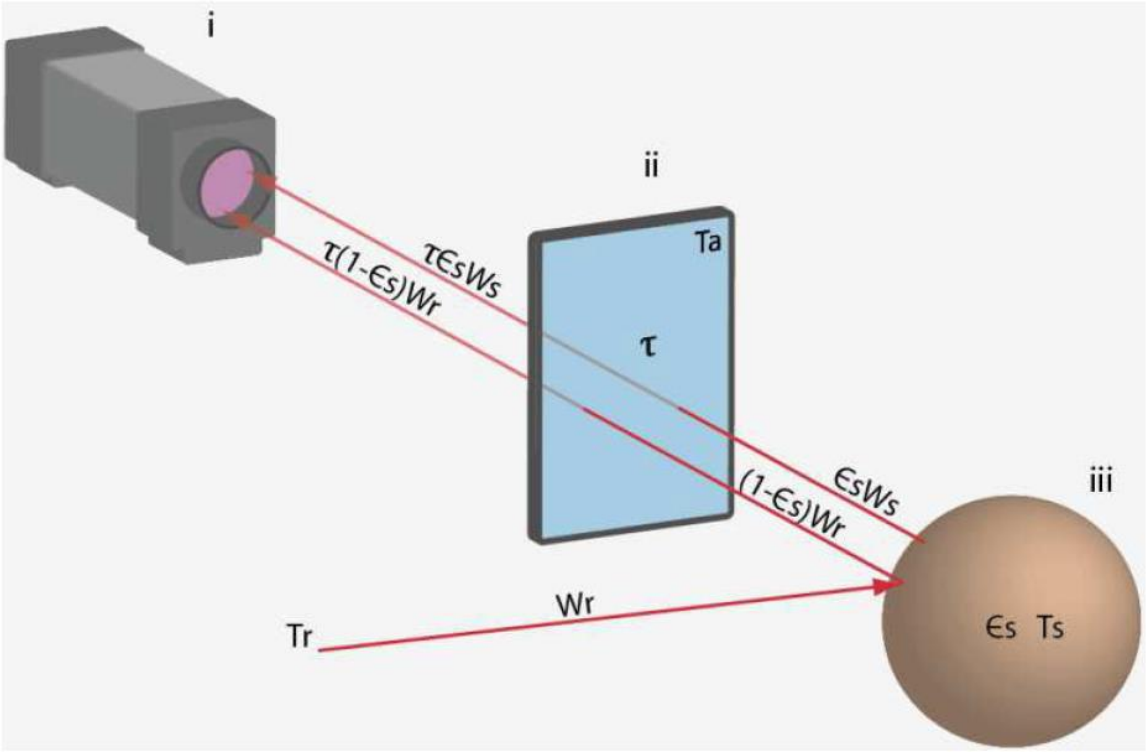

Figure 32. Key elements and variables in the infrared clinical setting that must be accounted for in clinical protocols i) TIRI camera, ii) ambient atmosphere as an optical medium and noise source, and iii) human tissue under investigation (Arthur & Khan, 2011d).

Clinical protocols for TIRI image acquisition are now well recognised by the clinical TIRI research community as a prerequisite for objective evaluation of TIRI's usefulness in medicine. Figure 32 provides a simple layout of the clinical setting in terms of the infrared elements that should be considered and accounted for in any objective clinical TIRI protocol. Future clinical TIRI studies can use this framework as a starting point for the design of any clinical or laboratory-based TIRI study to ensure a complete picture of all the controlled and uncontrolled variables involved. As demonstrated in this thesis work in specific context of osseous stress pathology, clinical studies conducted with this level of variable control and attention to image acquisition

protocols deliver TIRI data containing significantly more diagnostic information that is readily extractable via standard image processing operations.

In addition to showing that development and use of objective clinical protocols should be adopted as standard practice in clinical TIRI from now onwards, another outcome of the protocol aspect of this thesis work is the expanded scope of clinical TIRI applications. Objective clinical protocols expand the scope of clinical TIRI applications because they make it possible to achieve greater specificity (accuracy, precision, reliability, repeatability), and therefore make it feasible to investigate TIRI's usefulness in applications that were previously ruled out due to seemingly unachievable specificity requirements.

An example of a high-potential clinical application that might only receive competitive research and development funding when evaluated in context of an objective clinical protocol is 'heat source depth determination', as applicable to cancerous tumours. In tumour depth determination, TIRI has to accurately calculate an absolute quantitative parameter value that will directly influence the choice of treatment for a patient with a life threatening disease. Applications characterised by objective quantitative decision support are those in which TIRI can realise its fullest potential as a clinical tool.

Among TIRI's quantitative decision support applications, those involving significant amounts of image processing particularly stand to gain from protocols designed with the image processing component in mind from the outset. An example of a particular protocol feature that illustrates this point is the infrared

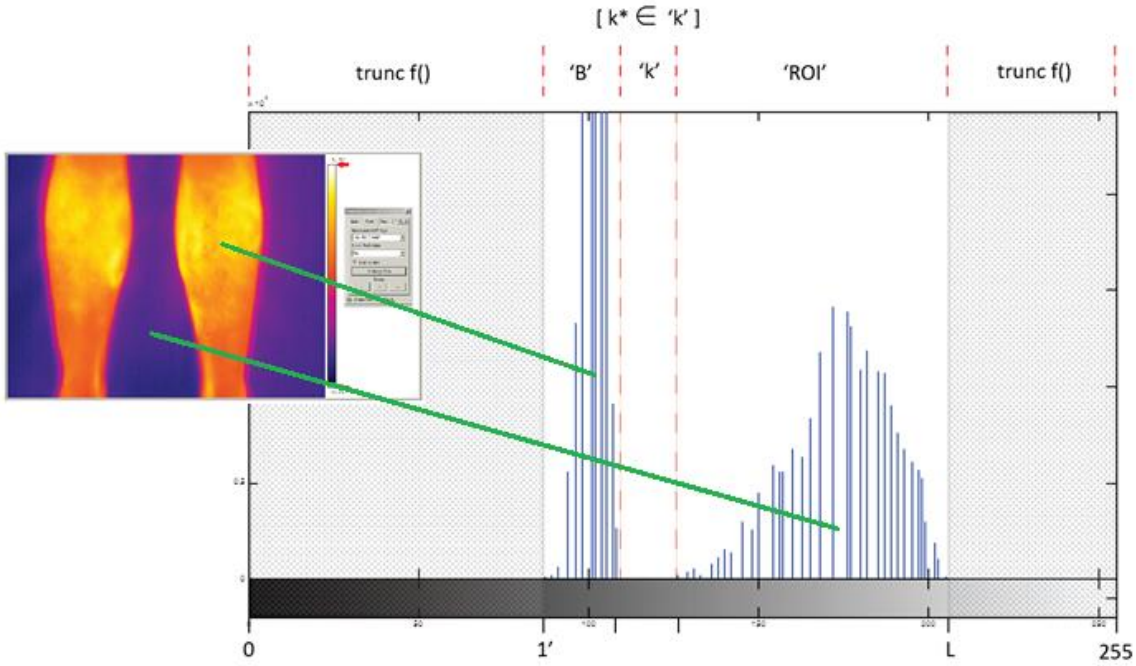

Figure 33. The clinical protocol for investigation of TIRI in stress fracture diagnosis included use of a 'chroma key' background surface to facilitate subsequent image processing operations like segmentation of the measured signal into backing surface 'B' and region of interest 'ROI', and and also facilitated quantitative absolute temperature calibration.

chroma key technique incorporated into the clinical protocol for investigation of TIRI's application in stress fracture diagnosis with the Australian Army, Figure 33. The foresight to incorporate a chroma key background surface into the protocol (a mat of uniform and known emissivity and temperature placed beneath the patients' legs) facilitated subsequent segmentation and quantitative calibration of the image data obtained. Protocols incorporating strategic features that consider the entire data processing and diagnostic decision making context from the outset can make or break a clinical trial that forms the basis for evaluation of TIRI's usefulness in a particular application.

In addition to highlighting the benefit of foresight in protocol design, the protocol aspect of this work also demonstrated the value of early thermal characterisation of the relevant anatomy, physiology, and pathology. In the stress fracture study with the Australian Army, the efforts made to understand and characterise the thermoanatomy and thermophysiology of the lower limb in context of tibial osseous stress pathology (Figure 34) paid enormous dividends, both during

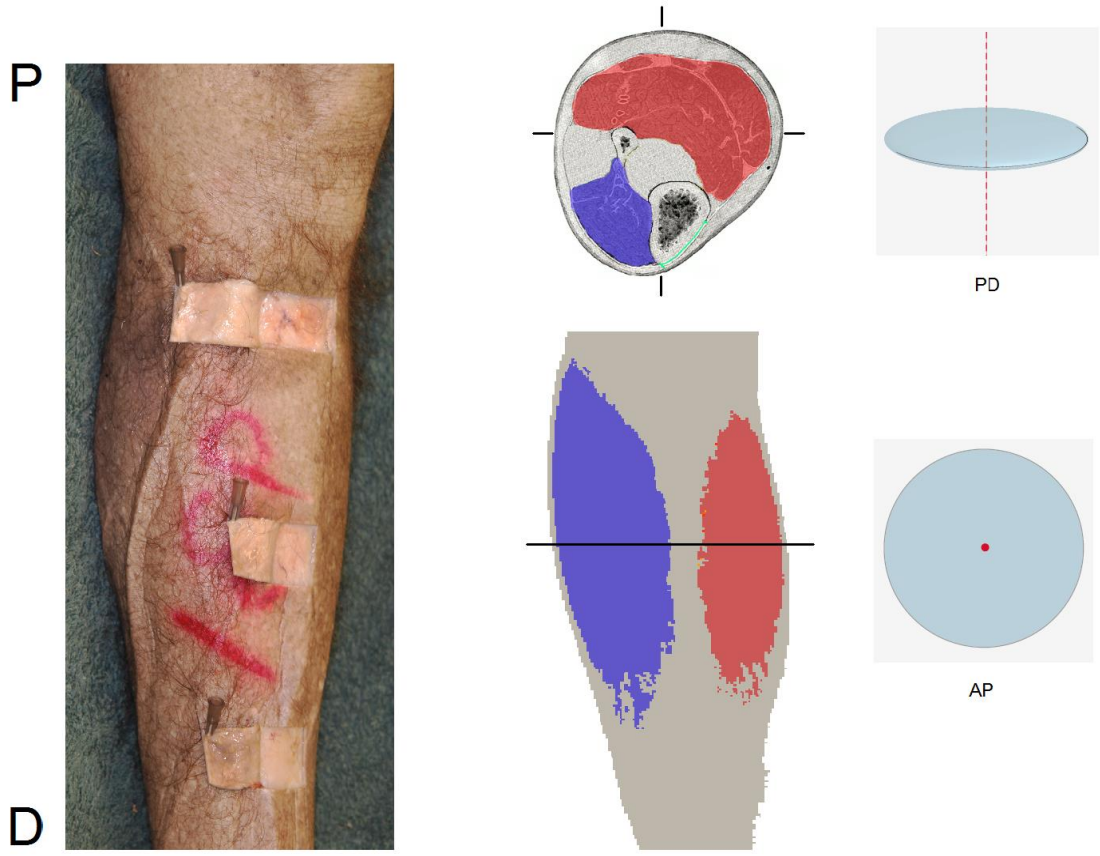

Figure 34. Anatomic explanation of 'normal' shin TIRI. Left: avascular interstitial tissue volumes, with P-D (proximo-distal) decrease in tissue thickness and lipid content. Centre: anterior muscle compartment (blue), superficial posterior compartment (red).

application of the protocol through the three month clinical trial at the Australian Army Hospital, and also during subsequent data analysis at Curtin University and Flir Systems Calibration Laboratory. This thermal understanding of the relevant anatomy, physiology, and pathology had a positive impact on all aspects of the study design, including clinical hardware, environmental control parameters and even image processing sequences. A particularly helpful exercise enabled by this a priori thermal characterisation work was prediction of how healthy and pathological pretibial tissues would likely present in a TIRI image. In studies like this one which investigate brand new clinical applications of TIRI, defining what the tissue looks like to TIRI in both healthy and unhealthy states is a critical goal, that a thermal understanding of the relevant anatomy and physiology makes far easier to achieve.

In summary, clinical TIRI has enormous potential as a diagnostic decision support tool, and its usefulness in any given application should only be evaluated on the basis of data collected under objectively developed protocols. This work describes an approach to development of such clinical TIRI protocols that ensures the critical issues are considered to an appropriate level of rigour, Figure 32, Figure 34. Protocols should be designed strategically, considering the physio-anatomic context and ultimate diagnostic decision from the very outset. Protocols should never lose sight of the ultimate goal which is to support a treatment decision, and that ultimate purpose should remain front of mind throughout the design and implementation of any clinical TIRI study, and particularly during evaluation of TIRI's usefulness in any given context.

1.27 Heat Source Depth Determination

As detailed in Chapter 6, TIRI can be used to successfully determine the depth of focal heat sources within human tissues (Figure 35). This section discusses the key technical challenges for development of TIRI-based HSDD (heat source depth determination), and suggests future research work to overcome them. This section also discusses the case for making tumour depth determination a target application for ongoing research, and outlines key steps along the technology roadmap from the current 'proof of concept' stage to useful clinical application. Among the possible applications of TIRI-based HSDD, tumour depth determination stands out as one of the most technically feasible and clinically impactful.

The technical feasibility of TIRI tumour depth determination stems from the fact that tumours are ideal heat sources, naturally occurring as focal, highly metabolic, vascularised cell clusters, within relatively cool and thermally homogenous healthy tissues. Situations characterised by a focal heat source within a relatively cool and thermally homogeneous surrounding material are ideally suited to TIRI-based HSDD. The main threats to the technical feasibility revolve around a potential discrimination failure mode (Figure 36), and the validity of the single bioheat transfer model across various anatomic locations. These technical challenges and possible solutions are discussed further below.

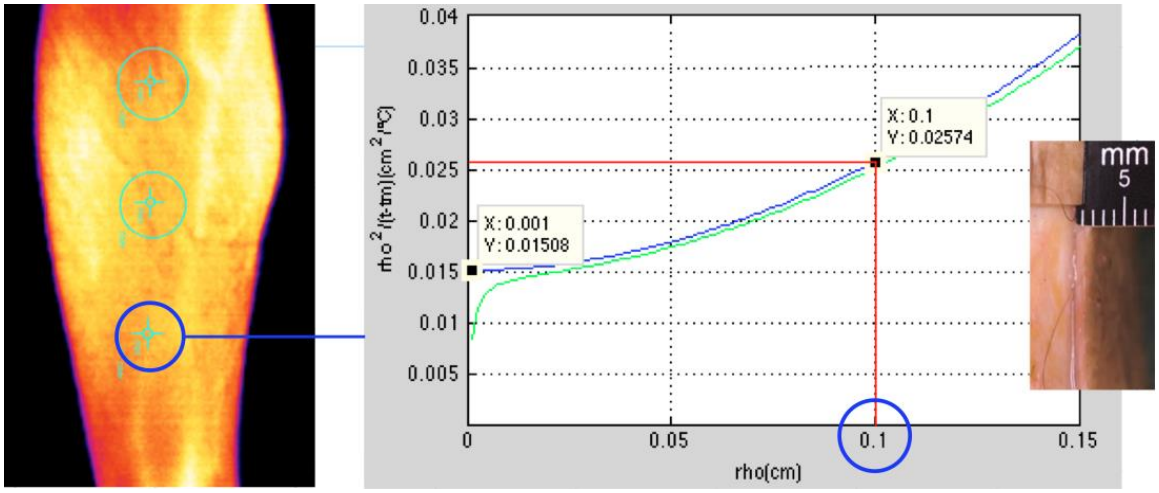

Figure 35. Successful recovery of heat source depth (≈ 1mm) from TIRI of distal tibial ROI.

The clinical impact potential of a robust TIRI-based tumour depth determination system stems from; the critical role of tumour depth in oncological prognosis, the invasiveness of current tumour depth determination techniques, and the huge global health burden of applicable cancers. As a key factor in oncological prognosis, tumour depth has a major influence on important treatment decisions at several stages through a cancer patient's care. Formerly known as 'Breslow's Depth' in recognition of pathologist Alexander Breslow's work to objectively translate tumour depth measurements into useful prognostic factors (Breslow, 1970), tumour depth is now a key foundation of the AJCC (American Joint Committee on Cancer) system for staging melanoma.

Subsequent clinical trials have validated tumour depth as a continuous variable correlating with prognostic factor, being particularly useful in prediction of lymph node metastasis with deeper tumours more likely to have spread to the lymph nodes (Breslow, 1970; Buttner et al., 1995; Buzzaid et al, 1997; Balch et al., 2001, Rousseau et al., 2003). With tumour depths currently determined via highly invasive biopsies and time consuming costly pathology lab work, development of a non-invasive, rapid, inexpensive alternative is highly desirable. Critical to this development will be a solution to the potential failure mode illustrated in Figure 36. This potential failure mode surrounds the technique's ability to distinguish between

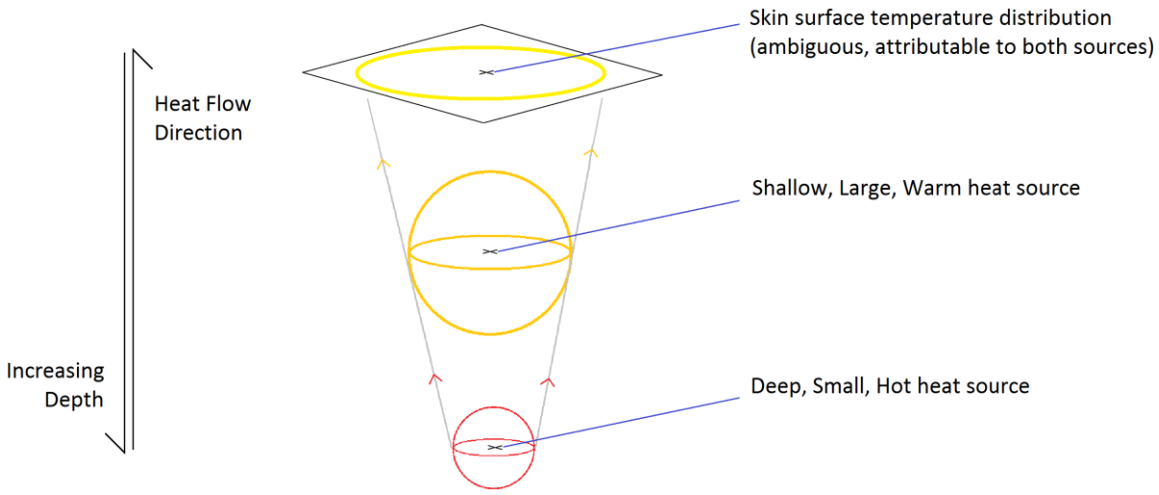

Figure 36. Possible Depth Determination Failure Mode - sources at different depths could project the same surface temperature distribution - current technique unable to discriminate.

skin surface temperature distributions caused by 'deep hot small' sources and 'shallow warm large' sources. In this scenario, both heat sources could project identical temperature distributions on the skin's surface, as seen by TIRI.

In the current algorithm, accurate initial estimates of key parameters like source temperature and source depth provide some safeguard against this failure mode. More robust and physically valid protection against this failure mode may be achieved via empirical TIRI research surrounding an articifical heat source embedded within an artificial tissue phantom. Specifically, a program of TIRI research within a controlled environment surrounding a controllable and known heat source embedded within a tissue phantom of known heat transfer properties.

This experimental setup will allow investigation of the sensitivity of the algorithm to the aforementioned initial parameter estimates. The fact that the code recovers source depths consistent with anatomic expectations (ranging from 1 to 3 mm) for all ROI's in all participants, despite surface temperatures being extremely similar for all ROI's in all participants (S.D. for entire sample = 0.31, ranging from 304.8K – 306.1K) suggests there is opportunity to improve the current implementation of the algorithm by reducing sensitivity to initial parameter estimates (Arthur & Khan, 2013).

Future implementations should strive to ensure that clinically obtained surface temperature distributions have significantly greater influence over final heat source depth results than operator determined initial parameter estimates. One way to facilitate the necessary technique improvements is to ensure that any experimental tissue phantom hardware is MRI-compatible, enabling development of TIRI compatible thermometric MRI sequences. Although thermometric MRI is highly valuable as a standalone clinical modality/technique, empirical research that simultaneously combines TIRI and thermometric MRI could provide a validation modality for future TIRI research, and also reveal fundamental TIRI-MRI dynamics that could enable TIRI to support thermometric MRI research in turn.

Although both modality-specific and multi-modality tissue phantoms are commercially available (e.g. medimgsys), development of a tissue phantom that is thermodynamically representative of human tissues with high fidelity in both TIRI &

MRI context would be a valuable research contribution in itself. Although high fidelity representation of heat transfer properties is crucial for any thermal tissue phantom, the HSDD findings in chapter 6 suggest that investing research efforts in maximising the precision of a phantom's heat transfer properties would be less valuable than work to more accurately characterise the general thermodynamics required for clinical decision support. Specifically, despite the significant differences in the fat content of the 3 tibial ROI's investigated, the lack of variation in the range of human tissue thermal conductivity values reported in the literature (~ 0.45 - 0.55) suggests there is little performance to be gained from efforts to use ROI-specific thermal conductivity values in future implementations of the algorithm.

In summary, this work has demonstrated that TIRI can be extremely useful in determining the depth of focal heat sources within human tissues, and it is recommended that future research efforts be specifically directed toward application in tumour depth determination. Tumour depth determination stands out as an ideal application to work towards in terms of both technical feasibility (tumours occur as focal heat sources) and potential for positive public health impact (focal cancers currently impose a huge global disease burden).

Specifically, it is recommended that the next steps in research and development focus on robustness of the technique to common failure modes, via integrated empirical TIRI-MRI studies on tissue phantoms which are thermodynamically representative in both modalities. As we move into a world where initiatives like ObamaCare are placing extreme and necessary pressure on the medical device industry to deliver both diagnostic and therapeutic technologies that take cost out of the health care system, low-cost high-utility technologies like TIRI will receive more research funding and attention.

1.28 Emissivity in Clinical TIRI

Emissivity 'Ɛ' converts measurements of energy radiated from a particular material 'j' (Wm^{-2}) into measurements of that particular materials temperature based on the energy that would be radiated from an 'blackbody' material under the same regime of temperature, waveband and viewing conditions **(0.1)**. As the definition implies, emissivity is highly regime-dependent, and this thesis work showed that human skin emissivity varies significantly across clinically-relevant regimes of wavelength and skin type (Figure 37). This finding motivates change of practice toward use of regime-specific emissivities in applications where absolute temperature accuracy is critical (Arthur & Khan, 2013).

$$j = \varepsilon\sigma T^4 \quad [Wm^{-2}] \qquad \leftrightarrow \qquad T = \sqrt[4]{\frac{j}{\varepsilon\sigma}} \quad [K] \qquad \textbf{(0.1)}$$

An important next step will be to quantify the magnitude of the risk that emissivity variation poses in context of some specific TIRI-supported clinical decisions. For example, in context of a TIRI-guided thermal ablation procedure, use of the nominal

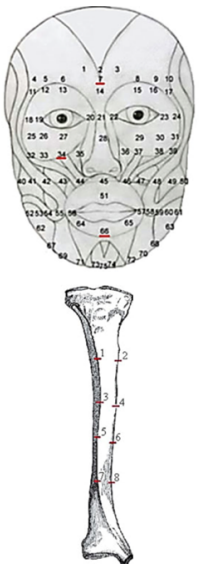

Regime 1: 3.6 - 5.0 µm (MWIR) Facial Skin ROI 308.5 - 310.1 K	**Regime 2:** 7.5 - 13.0 µm (LWIR) Facial Skin ROI 308.5 - 310.1 K
Regime 3: 3.6 - 5.0 µm (MWIR) Pre-Tibial Skin ROI 304.8 - 305.8 K	**Regime 4:** 7.5 - 13.0 µm (LWIR) Pre-Tibial Skin ROI 304.8 - 305.8 K

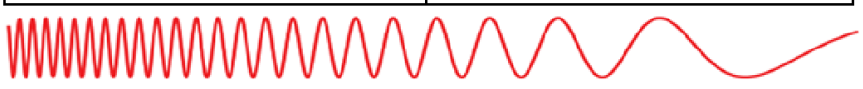

Figure 37. Clinically-relevant TIRI regimes across which skin emissivity was measured.

0.98 emissivity value when the tumour's actual emissivity is 0.83 (the lowest value calculated during the Flir study), translates to a 16% error in temperature readings displayed to the surgeon. In the case of a 50°C target temperature, as is typical in thermal ablation of cancerous tumours, a 16% thermometry error equates to ±8°C. The emissivity error would then lead to the kill zone being raised to 58°C, killing an unnecessarily large area of healthy tissue surrounding the tumour. Conversely, an 8°C underestimate in emissivity would cause the surgeon to prematurely cease heat application once the tumour had actually only reached 42°C, failing to induce thermal cell death through the entirety of the tumour mass, causing the procedure to fail, and leaving the patient at serious risk.

Thermal ablation is just one example among many clinical applications in which the physiological significance of a specific absolute temperature makes emissivity critical, such as; cancer diagnostics, intraoperative haemodynamic monitoring, and affective computing (Çetingül & Herman, 2010c; de Weerd, 2010b; M. Khan et al., 2006; Ng & Acharya, 2009). Accordingly, a recommended next step for research is investigation of the impact of realistic emissivity errors on the clinical decision being supported by TIRI in other promising clinical applications outside of thermal ablation. The experiments to measure the impact of emissivity errors upon the clinical decision being supported by TIRI should be conducted in realistic context of regime (waveband & ROI), disease state, clinical image acquisition conditions, data-processing circumstances, and physician decision making.

It is also recommended that research be carried out to investigate the relative merits of different techniques for measurement of emissivity in-situ. As mentioned in chapter 7, the two main classes of technique are based upon direct reflectance measurement and direct blackbody comparison. Although reflectance-based techniques are non-contact and do not require a costly blackbody source, real-world considerations like the shift from Lambertian (matte / diffuse) to specular (shiny) reflectance with perspiration may compromise their reliability. Consideration of the relative merits of each technique should include the practical ease with which emissivity readings can be integrated into clinically-obtained TIRI's.

In summary, recommended next steps with regard to the treatment and use of emissivity in clinical TIRI revolve around two questions; how significantly will emissivity errors impact the clinical decisions being supported under realistic conditions, and, how should in-situ emissivity be practically measured and integrated into clinical TIRI data. To ensure that in-situ emissivity measurement is not redundant, this research should be accompanied by quantification of uncertainty in absolute temperature measurement via TIRI due to all sources of uncertainty found in the practical clinical setting.

1.29 Overall Recommendations

This program of research work investigated clinical applications of thermal infrared imaging, and produced interesting findings concerning clinical TIRI protocols, emissivity of human tissues, and heat source depth determination. First and foremost, it is recommended that future clinical TIRI research programs invest significant effort into developing and adhering to data acquisition and processing protocols, in the manner described in this thesis. Protocols should be designed with facilitation and optimisation of the entire process flow in mind, from initial clinical image acquisition through to data processing and the ultimate diagnostic decision being supported by the TIRI data. Only in the presence of such protocols can we properly evaluate TIRI's potential usefulness in any given application.

Clinical TIRI has its greatest potential in quantitative decision support applications, and as emissivity accuracy is the fundamental driver of performance in those applications, it is recommended that future research aims to better understand the nature and significance of emissivity in specific clinical TIRI applications. Although this work revealed emissivity variations with both waveband (MWIR/LWIR) and anatomic location, it is recommended that future emissivity research focusses on variations due to anatomic location, and constrain investigations to the LWIR. With significantly lower costs and comparable performance, it seems inevitable that LWIR systems will dominate the future of clinical TIRI.

Finally, it is recommended that future research be strictly constrained to applications that have realistic promise of being useful in a real world clinical setting. Heat source depth determination is a great example of such an application, having significant significant PTRS (probability of technical and regulatory success), and real potential to improve clinical outcomes for large numbers of patients requiring important services like malignancy staging, metastasis prediction, resection guidance, tumour control monitoring and general prognostics. Similarly, osseous stress injury management exemplifies another class of appropriate clinical TIRI research, based around superficial thermo-active pathologies.

With a global trend toward value-based healthcare exemplified by the introduction of the affordable care act (ObamaCare), the biomedical engineering community will face increasing pressure to prioritise technology affordability, both in diagnostics and therapeutics. Accordingly, TIRI will be among the low cost, simple to operate technologies deservedly receiving increasing research and development funding and attention as time goes on.